UNIVERSITÀ DEGLI STUDI DI ROMA
"TOR VERGATA"

FACOLTÀ DI SCIENZE MATEMATICHE, FISICHE E NATURALI

DOTTORATO DI RICERCA IN ASTRONOMIA

XXI ciclo - a.a. 2008/2009

EXPECTATIONS AND PERSPECTIVES OF X-RAY PHOTOELECTRIC POLARIMETRY

Fabio Muleri

Docente Guida\Tutor:	Dott.	**Enrico Costa**
	Dott.	**Paolo Soffitta**
	Dott.ssa	**Angela Bazzano**
Coordinatore\Coordinator:	Prof.	**Pasquale Mazzotta**

Rome (Italy), February 2009

Contents

Introduction

Polarimetry of an electromagnetic wave consists in the measurement of the orientation of its electric field and consequently of its magnetic component: radiation is called partially polarized when an ordered component of the electric field emerges. Its direction defines the plane of polarization, while the fraction of the "ordered" field with respect to the total (to the square) is the degree of polarization.

Polarimetry has been developed mainly from radio to optical wavelengths and nowadays it has a primary role in a large number of applications, spanning from the characterization of materials to that of objects detected by radar systems. In general it is performed with instruments (polarimeters) which can exploit very different designs, the simplest one being the use of a filter able to transmit only the polarized component in a certain direction. In this case a measurement of the incident radiation beyond the filter is basically a measurement of polarization. However much more sophisticated techniques, such that presented in this thesis, are possible and may be required for specific purpose.

The knowledge of the Universe has been significantly improved thanks to polarimetry. Polarization basically emerges where a preferred direction is present and in fact the presence of an order magnetic field, an axis of symmetry or some special emission processes produce polarized radiation. The informations collected with polarimetry are accessible only in same cases and less straightforwardly when compared to other observations such as spectroscopy, imaging and timing.

Unfortunately polarimetry of astrophysical sources has been extensively exploited only from radio to optical so far. This is the direct consequence of the difficulties encountered in the development of sensitive polarimeters at higher energy, even for other applications. The smaller wavelength makes problematic the construction of the optical elements, such as filters or wave plates, that allow the easy manipulation of polarized signals in optical or radio. This adds to the intrinsic difficulty of performing any reliable measurement of polarization. Firstly the detection of the degree of polarization is definite positive, namely a certain polarization depending on the statistical fluctuations of the signal is always measured. Secondly a polarization at the level of only a few % is often expected in astrophysical contexts and this small fraction must be distinguished from the much stronger unpolarized signal and its statistical fluctuations. This implies that any realistic polarimetric measurement requires much more data than the detection of a new source, a normal light curve or a measurement of a spectrum.

The unsuccessful development of X-ray polarimetry has been particularly painful in the study of compact sources, basically white dwarf, neutron stars and black holes. They

emit mostly in X-rays and can show up as a large number of classes of objects: pulsars, X-ray binaries, magnetars, isolated neutron stars, cataclysmic variables, gamma ray burst, active galactic nuclei and blazars are only some examples. The extreme magnetic and/or gravitational fields near these objects often origin violent phenomena, revealing as non-thermal and possible high energy emission, strong asymmetric ejection of matter or sudden increase of luminosity of several orders of magnitude. As a consequence of these behaviors, a significant polarization should emerge in the emission of compact sources.

A wide literature has been developed on this subject from the beginning of X-ray astronomy, almost fifty years ago. X-ray polarimetry is ultimately able to unveil the signature of peculiar emission processes and, in particular, it is a privileged probe for the study of magnetic field. Synchrotron and cyclotron emissions produce highly polarized radiation and polarimetry provides direct informations on the orientation of the magnetic field and its intensity. The strong magnetic field near neutron stars and magnetars should deeply affect the radiation transfer and interesting signatures on polarization emerge. Peculiar quantum electrodynamic effects are expected to play an important role in these natural laboratories.

Polarization is also the signature of scattered radiation. It traces the geometry of the system and can reveal, for example, the configuration of the accretion into compact objects. This allows a meaningful comparison among competitive models and an important example in this context is the measurement of (optical) polarized radiation from active galactic nuclei. This has allowed to derive the geometry of the now widely accepted unified model for the emission from these sources.

Both special and general relativistic effects influence the polarization of the emission near black holes or neutron stars. Polarimetry has indeed been identified as a sensitive probe to investigate general relativity in the strong field regime. Moreover, it is one of the most powerful tool to study the spin of black holes.

Recently it has been emphasized that polarimetry can also explore intriguing topics of fundamental physics. These include matter under extreme conditions of density, gravitational and magnetic field or quantum gravity theories. As an example, the degree and the plane of polarization of the emission which emerges from the surface of neutron stars is very sensitive to its magnetic and gravitational fields. The latter is related to the ratio between the mass and the radius of the object and eventually this depends on the equation of state of matter at supranuclear densities.

The first attempts to measure linear polarization were performed at the beginning of X-ray astronomy with sounding rockets. Unfortunately, after these pioneering instruments, X-ray polarimeters have been systematically descoped from the major missions, e.g. *Einstein*, *XMM-Newton* and *Chandra*. Indeed the devices based on the classical techniques of measurements, i.e. Bragg diffraction and Thomson scattering, didn't reach a sufficient sensitivity to justify their inclusion in the focal planes of large observatories. Indeed polarimetry would be limited to brighter sources, while instruments devoted to spectroscopy, imaging and timing could provide huge improvements of sensitivity.

The Gas Pixel Detector (GPD hereafter) is a new generation X-ray polarimeter which is based on the photoelectric absorption. It is basically a proportional counter which has

the (almost) unique capability to finely resolve the track of photoelectrons in a gas. This allows to reconstruct their initial ejection direction which brings significant memory of the polarization of the absorbed photon.

The GPD is devoted to the measurement of the linear polarization, nevertheless it can also perform imaging, timing and spectroscopy with moderate energy resolution. The current prototype is optimized between 2 and 10 keV and the air absorption of X-rays in this energy range makes mandatory the use of the instrument on-board space satellite. The GPD promises to reach a sensitivity by far higher than instruments built so far thanks to the larger efficiency of detection, which has been the main limiting factor of the classical techniques.

The underlying theme of this thesis is the characterization and the development of the GPD toward the space use and its original contribution to this project is extremely diversified, being divided into four main points. The first one is the construction and the use of a facility for the complete characterization of the instrument in the maximum sensitivity energy range with polarized and unpolarized radiation. The latter is produced with radioactive sources or commercial X-ray tubes, while polarized photons are generated with a source based on Bragg diffraction at nearly 45°. This is one of the classical technique for the measurement of polarization in X-rays and it is commonly used in spectroscopy and crystallography. A first prototype is described in Chapter. 3; afterwards an improved version was built and that is presented in Chapter 4. A mechanical assembly, accurately tuned in accordance with the requirements of the calibration of the GPD, was also designed and built within this thesis to control the position and the inclination of the polarized and unpolarized sources. This is presented in Chapter 4.

The second important contribution is the first measurement of the low energy response of the GPD to polarized radiation, presented in Chapter 5. Today the GPD is a project in an advanced state of development, but its calibration was affected by the lack of a polarized source readily available at energies below 5.41 keV. The peak of the sensitivity was expected at about 3 keV on the basis of a Monte Carlo software but an actual measurement in this energy range was missing. The construction of the Bragg source has allowed to overcome this issue.

Another innovative measurement is performed within this thesis work. The facility of calibration is used to accomplish a further step in the characterization of the GPD, studying the correlation between the plane and the measured angle of polarization in search of possible systematic effects. The preliminary results are presented in Chapter 5.

This instrumental work is supported by the definition of the perspectives of measurement of the GPD. That is the third subject of this thesis. Four different proposals have been submitted to space agencies in Italy, Europe and United States and this thesis contributed to the design of these missions, but especially to the definition of their scientific objectives as discussed in Chapter 6.

The forth and last theme analyzed in this thesis is an exploration of new applications of the GPD. The area of the current version of the GPD is 15×15 mm^2, that is too small to collect the large number of photons required to perform an accurate measurement of polarimetry. An X-ray optics is then included in all proposals presented. However in the near future a larger detector could be available and possibly this would open the way for

the construction of an instrument with a large field of view.

This application is indeed very attractive. Many fast transient phenomena occur in the X-ray sky, such as Gamma Ray Bursts, X-ray Flashes and bursts from Soft Gamma Repeaters, and these could be caught with an instrument with a large field of view. The interest around this application is even proved by the independent proposals of competitive polarimeters. However this application could be successful only if the instrument can provide a sufficient sensitivity up to off-axis inclinations of a few tens of degrees. For the first time this problem is discussed in this thesis with a completely original contribution: the photoabsorption of inclined photons is considered for both polarized and unpolarized photons through theory, simulations and measurements as discussed in Chapter 7.

A further possible future application of the GPD is eventually discussed. The energy range of the GPD is basically determined by the mixture filling the gas cell of the instrument and currently it is between 2 and 10 keV. This allows to exploit an interval where astrophysical compact sources are in general very bright and a "traditional" X-ray optics can be easily used. However the development of multilayer optics makes possible the focusing of photons up to energy of several tens of keV and this would make available a sufficient area to perform polarimetry in the hard X-ray range. Thermal emission is often absent in this case and consequently a higher degree of polarization is generally expected. As an example, the study of X-ray pulsar would strongly benefit of observations above 10 keV, since cyclotron lines are easily observed in this energy range. They are expected to be highly polarized and sensitive probes for the study of accretion onto the magnetic poles of the neutron star. The knowledge of obscured sources, such as many AGNs and X-ray binaries, would also be improved by observation which are less affected by low-energy absorption.

The performances of the GPD when the baseline mixture is replaced with ones with a higher atomic number is discussed in Chapter 8. The behavior of the instrument is studied with a Monte Carlo software.

A comprehensive collection of the expectations of X-ray polarimetry, unfortunately not complete, is presented in Chapter 1. It is an original attempt to present in organic manner a subject which is not still organized since the painful lack of observational feedback to scientific expectations. It justifies the importance of X-ray polarimetry and provides the scientific support for all the subsequent work. Then it is rather important part of this thesis.

The Chapter 2, where the GPD is described, is presented with the same purpose. It should be a reference to acquire a first insight of the operation of the instrument as well as the introduction of the arguments presented later on.

Last but not the least, this thesis was carried out at the IASF/INAF of Rome in collaboration with the INFN of Pisa. The author obviously acknowledges the support of a small group, actually only a few people, during all the phases of this thesis. However the arguments presented here always contain a significant and original contribution of the author which is even predominant in many cases.

Chapter 1

The role of polarimetry in the X-ray Sky

The study of the linear polarization has been indicated as a fundamental tool in investigating the geometry and the physics of astrophysical compact sources since the beginning of the X-ray astronomy (Novick, 1975; Rees, 1975; Meszaros et al., 1988; Weisskopf et al., 2006). The degree and the direction of polarization add two parameters to the current observable quantities, namely direction, time and energy of incident photons. This helps in the discrimination between different models which can be otherwise equivalent on the basis of the spectroscopic and timing observations.

More recently, it has been also stressed that X-ray polarimetry could be a powerful probe to study topics of fundamental physics. These include the equation of state of superdense matter, the behavior of the matter in extreme gravitational and magnetic fields and the emergence of effects of quantum gravity.

The expectations in this branch of astronomy have been disappointed so far due to the lack of sensitivity of the X-ray polarimeters which flew. As a matter of fact, it has been possible to register the positive detection of X-ray polarization only in the emission of the Crab nebula (see Sec. 1.3). In this Chapter the role and the importance of the X-ray polarimetry will be presented as it has emerged, despite the lack of experimental feedback, from the 47-years-old history of X-ray astronomy.

1.1 Polarimetry in astronomy

Polarimetry, namely the study of the behavior of the electric field of the electromagnetic waves, has been a fundamental probe to study the Universe at all wavelengths. Partially polarized radiation is expected to emerge in all astrophysical contexts where a "special" direction exists: this includes asymmetries in matter distribution, the presence of an order magnetic field or some peculiar emission processes. Then polarimetry reveals aspects of the astrophysical sources, such as their geometry, that can't be accessible to other observations or are available with difficulties.

There are many examples of the importance of polarimetry in astronomy. Spectro-

polarimetric observations in optical are at the base of the now widely accepted model for AGN emission, which advocates that radiation is scattered (and then polarized) before reaching the observer (Antonucci and Miller, 1985). Polarimetry in optical or IR is used to reveal scattered radiation on clouds or blobs even when the exciting source is obscured. The circular and linear polarization of spectral lines allow to map the magnetic field of the Sun and other stars.

The study of polarization of stellar optical light can also be exploited to investigate the size and the composition of the interstellar dust grains (see for example Whittet, 2003), which are in general elongated and their minor axis is aligned with the interstellar magnetic field. The radiation polarized orthogonally to the minor axis is scattered with more probability and consequently starlight which reaches the observer is partially polarized parallel to the interstellar magnetic field. The detailed investigation of the correlation between the degree of polarization and extinction, which derives from the amount of dust, can unveil the properties of the interstellar grains.

Polarimetry has always been a difficult task from the instrumental point of view (Tinbergen, 1996). Since it is a definite positive measurement, a spurious polarization is always measured and systematic effects must be accurately taken into account to detect real signals. A large amount of data are required to measure the polarization of emission at the level of a few %, which is the signal expected in many interesting cases.

These intrinsic difficulties have delayed or prevented the development of polarimetry for astrophysical applications and the study of polarization in the X-ray range is unfortunately included in the latter class. The meagre current results but the high expectations of this yet unexplored branch of X-ray astronomy are presented in Sec. 1.3 and Sec. 1.4 respectively.

1.1.1 Stokes parameters

The state of polarization of an electromagnetic wave can be described by means of Stokes parameters (see, for example, Rybicki and Lightman, 1979), which completely describe the behavior of the electric field in the plane orthogonal to the direction of propagation. Without loss of generality, an electromagnetic wave can be expressed as sum of two components which are linearly polarized in two orthogonal directions. Examining the electric field $\vec{E}$ in a fixed point along the path of the wave, it can be expressed as:

$$\vec{E} = \vec{E}_x(t) + \vec{E}_y(t) = \hat{x}E_x e^{-(i\omega t - \phi)} + \hat{y}E_y e^{-i\omega t} \tag{1.1}$$

where $\hat{x}$ and $\hat{y}$ identify a frame of reference in the plane orthogonal to the direction of propagation and the phase ϕ takes into account a possible phase difference between the two components. The evolution with time of the two components along x and y is derived taking the real part of $\vec{E}_x$ and $\vec{E}_y$:

$$E_x = \mathcal{E}_x \cos(\omega t - \phi) \qquad E_y = \mathcal{E}_y \cos(\omega t). \tag{1.2}$$

The Eq. 1.2 represents the evolution of the tip of the electric field in the plane xy. In general it traces an ellipse, called polarization ellipse, and then the electromagnetic waves

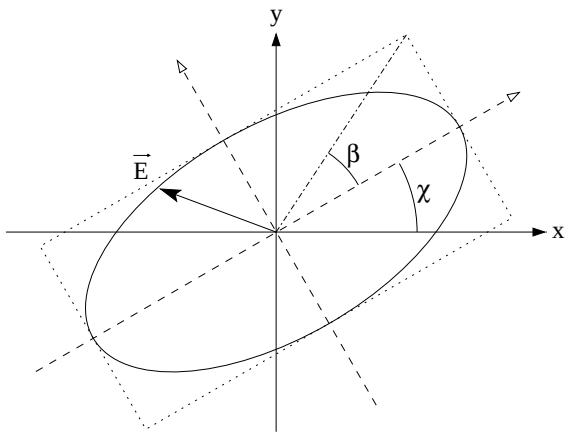

Figure 1.1: Angles which define the polarization ellipse.

is said to be elliptically polarized. The four Stokes parameters are calculated from the characteristics of the polarization ellipse:

$$I \equiv \mathcal{E}_x^2 + \mathcal{E}_y^2 \equiv \mathcal{E}_0^2 \tag{1.3}$$
$$Q \equiv \mathcal{E}_x^2 - \mathcal{E}_y^2 = \mathcal{E}_0^2 \cos\beta\cos\chi \tag{1.4}$$
$$U \equiv 2\mathcal{E}_x\mathcal{E}_y \cos\phi = \mathcal{E}_0^2 \cos 2\beta \sin 2\chi \tag{1.5}$$
$$V \equiv 2\mathcal{E}_x\mathcal{E}_y \sin\phi = \mathcal{E}_0^2 \sin 2\beta \tag{1.6}$$

where the angles β and χ are defined in Fig. 1.1 and $\mathcal{E}_0^2 = \mathcal{E}_x^2 + \mathcal{E}_y^2$. Note that the polarization ellipse for completely polarized radiation is characterized by only three quantities, the fourth Stokes parameter being related by:

$$I^2 = Q^2 + U^2 + V^2. \tag{1.7}$$

This is true only for completely polarized radiation and then Eq. 1.7 holds only in this case: for unpolarized waves $I \neq 0$, $Q = U = V = 0$, while for partially polarized photons $I^2 > Q^2 + U^2 + V^2$.

The interpretation of the Stokes parameters is easier after some manipulations of Eq. 1.6:

$$I = \mathcal{E}_0^2 \tag{1.8}$$
$$V/I = \sin 2\beta \tag{1.9}$$
$$U/Q = \tan 2\chi \tag{1.10}$$

The parameter I is then proportional to the intensity of the wave, while V is the circularity parameter which traces the ratio of the two principal axes of the ellipse. The condition of linear polarization is V=0, V=1 for circularly polarized waves and V >0 or V <0 refers to right- or left-handed polarization. The remaining parameters Q and U are not independent and both measure the orientation of the ellipse with respect to the x-axis.

An important property of the Stokes parameters is that they are additive. Then, for a partially polarized electromagnetic wave, they can be expressed as the sum of a polarized and an unpolarized component:

$$\begin{bmatrix} I \\ Q \\ U \\ V \end{bmatrix} = \begin{bmatrix} \sqrt{Q^2+U^2+V^2} \\ Q \\ U \\ V \end{bmatrix} + \begin{bmatrix} I-\sqrt{Q^2+U^2+V^2} \\ 0 \\ 0 \\ 0 \end{bmatrix}. \tag{1.11}$$

The first term obviously represents a polarized wave and indeed Eq. 1.7 holds, while the latter is the unpolarized one and then the last three Stokes parameters are zero.

1.1.2 Fundamentals

The degree of polarization $\mathcal{P}$ is defined as the ratio of the intensity of the polarized components and the total wave. The intensity is proportional to the first Stokes parameter and then (cf. Eq. 1.11):

$$\mathcal{P} = \frac{I_{pol}}{I_{tot}} = \frac{\sqrt{Q^2+U^2+V^2}}{I}. \tag{1.12}$$

In this thesis only the measurement of the linear polarization will be faced up and then hereafter $V = 0$.

The degree and the angle of polarization in X-rays are typically derived from a $\cos^2$ modulation measured in the angular response of the instruments (modulation curve). The amplitude of this modulation is proportional to the intensity of the component of the incident radiation which is linearly polarized and then it is proportional to the degree of polarization of the incident photons. Instead the angle of polarization corresponds to the maximum (or to the minimum) of the modulation curve.

This procedure of measurement is equivalent to use a filter which transmits only the component of the electric field parallel to a selected direction and absorbs the component orthogonal. By rotating the filter, the intensity measured is modulated as a $\cos^2$ function and the maximum is reached when the direction of polarization is parallel to the axis of the filter. The maximum and the minimum values of the measured intensity are:

$$I_{\max} = I_{pol} + \frac{1}{2} I_{unpol} \tag{1.13}$$

$$I_{\min} = \frac{1}{2} I_{unpol} \tag{1.14}$$

where $I_{pol} = \sqrt{Q^2+U^2}$ and $I_{unpol} = 1 - \sqrt{Q^2+U^2}$ are the intensities of the polarized and unpolarized components in which the incident radiation can be divided (note that V=0 since only the linear polarization is considered). The factor $1/2$ takes into account that unpolarized radiation can be regarded as composed of two waves of equal intensity polarized in two perpendicular directions. From Eq. 1.12 and Eq. 1.14, it follows that:

$$\mathcal{P} = \frac{I_{pol}}{I_{tot}} = \frac{I_{\max} - I_{\min}}{I_{\max} + I_{\min}}. \tag{1.15}$$

The response of the instruments described in this thesis is generally fitted with a $\cos^2$ function:

$$\mathcal{M}(\phi) = A + B\cos^2(\phi - \phi_0), \tag{1.16}$$

and the amplitude of the modulation when completely polarized photons are incident is called modulation factor μ:

$$\mu = \frac{\mathcal{M}_{\max} - \mathcal{M}_{\min}}{\mathcal{M}_{\max} + \mathcal{M}_{\min}} = \frac{B_{100\%}}{B_{100\%} + 2A_{100\%}}. \tag{1.17}$$

The modulation factor for actual instruments is never equal to unity, namely the response to polarization is never complete and the value of μ is then a key parameter for deriving the sensitivity of a polarimeter. The imperfect response to polarization is taken into account in the calculation of the degree of polarization with a factor $1/\mu$:

$$\mathcal{P} = \frac{1}{\mu}\frac{I_{\max} - I_{\min}}{I_{\max} + I_{\min}} = \frac{1}{\mu}\frac{B}{B + 2A}. \tag{1.18}$$

The Eq. 1.18 is the expression used to compute the degree of polarization in X-rays.

1.2 The classical techniques of measurement in X-rays

The "classical" techniques exploited for the measurement of the linear polarization in the X-ray band are Bragg diffraction at 45° and Thomson scattering at 90° (Novick, 1975). They are referred as "classical" as distinct from the polarimeters based on photoelectric effect, that have been developed in the last ten years and will be presented in Chapter 2.

Bragg diffraction relies on "reflection" of photons at nearly 45° on the planes of a crystal. In this case only the component polarized perpendicularly to the plane of diffraction is efficiently reflected and when the incident radiation is polarized, a modulation of the output flux is observed by rotating the instrument around the direction of incidence of photons. The main limitation of this technique is the very narrow energy band: the Bragg law expresses the relation between the incident angle and the energy and the requirement of diffraction at 45° implies that only photons within an energy band of some tens of eV or less are diffracted. Then Bragg diffraction is extremely ineffective when the spectrum of the input photons is continuous, as for the largest part of the astrophysical sources, even if a suitable choice of the crystal allows to analyze photons at energies starting from less than 1 keV. Bragg diffraction is discussed again in Chapter 3 since it is exploited for the construction of a calibration polarized source in the contex of this thesis.

Polarimeters which exploit Thomson scattering at nearly 90° are based on the dependency of its differential cross section on the direction of polarization. For completely polarized photons, the Klein-Nishina cross section is (Heitler, 1954):

$$\frac{d\sigma_{KN}}{d\Omega} = r_0^2\epsilon^2\left(\epsilon - \frac{1}{\epsilon}\sin^2\theta\cos^2\phi\right), \tag{1.19}$$

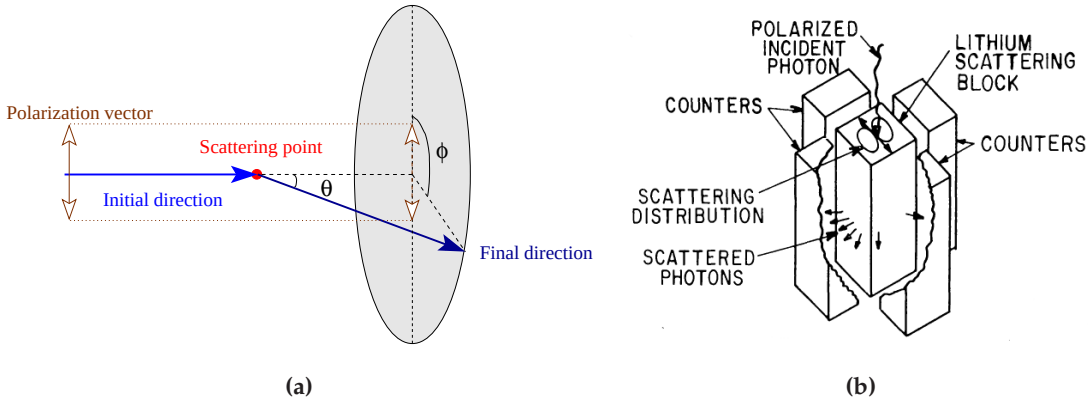

Figure 1.2: (**a**) Geometry of Thomson scattering. (**b**) Concept design of a polarimeter based on Thomson scattering (Novick, 1975).

where ϵ is the ratio between scattered and incident photon energies. If the energy E is much less than the rest mass of electrons, $\epsilon \approx 1$ and then:

$$\frac{d\sigma_T}{d\Omega} = r_0^2 \left(1 - \sin^2\theta \cos^2\phi\right) \qquad r_0 = \frac{1}{4\pi\epsilon_0}\frac{e^2}{mc^2}\,, \quad E \ll m_e c^2 \tag{1.20}$$

where r_0 is the classical electron radius , θ is photon scattering angle and ϕ the angle between the direction of scattering and that of polarization (see Fig. 1.2a). When the scattering is limited in the plane orthogonal to incident direction, i.e. $\theta = \pi/2$, Eq. 1.20 becomes:

$$\frac{d\sigma_T}{d\Omega} = r_0^2 \left(\sin^2\phi\right). \tag{1.21}$$

It results from Eq. 1.21 that the differential cross section, and then the scattered flux, are modulated as a $\sin^2$ function, with a minimum in the direction of polarization and an amplitude proportional to the degree of polarization. Both quantities can then be obtained by measuring the modulation of the flux scattered on a target.

The concept design of polarimeters based on Thomson scattering at 90 degrees is shown in Fig. 1.2b. Due to the competing photoabsorption in the target, this technique can be used only at energies above several keV, where astrophysical sources are fainter, and it has intrinsically a low efficiency. Only the photons scattered in a narrow angular range around $\pi/2$ are accepted and increasing the width of this interval increases the efficiency of detection at the expense of the modulation factor of the instrument. Then a trade-off must be reached.

1.3 The measurement of the polarization of the Crab nebula

The first hint that the emission of the Crab nebula is polarized in X-rays was obtained in the early seventies by means of a rocket launched by the group of Robert Novick at the Columbia University. The two polarimeters on-board the rocket were based on Bragg

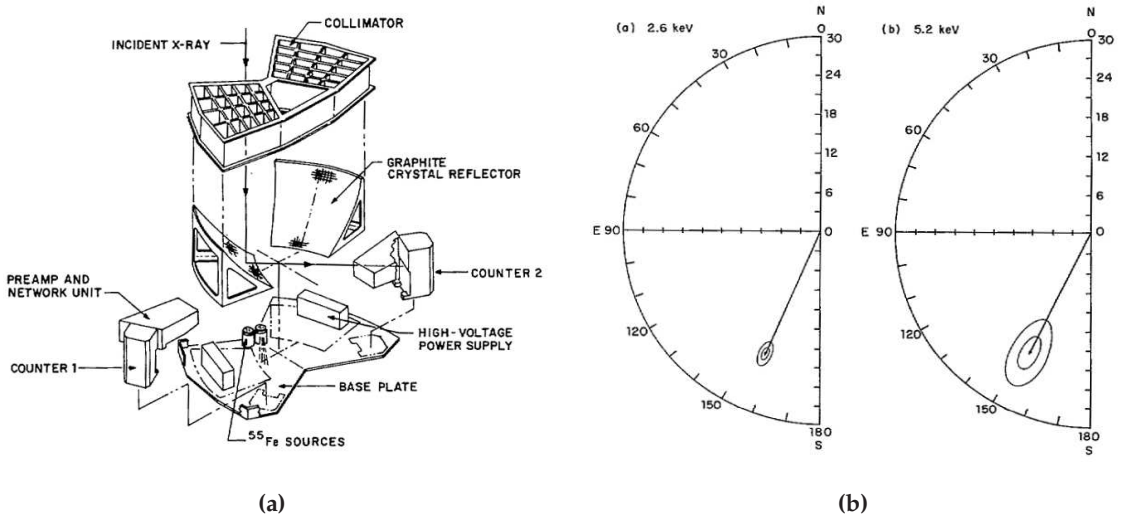

(a) **(b)**

Figure 1.3: (**a**) Polarimeter on-board OSO-8. Two crystals and two detectors are used for redundancy (Weisskopf et al., 1976). (**b**) Polarization of the Crab nebula at 2.6 and 5.2 keV (Weisskopf et al., 1978).

diffraction at 45° and the Thomson scattering at 90°. By combining the results from the former at 2.6 keV, from the latter (5-20 keV) and a previous experiment, Novick et al. (1972) obtained a polarization $\mathcal{P}$=15.4%±5.2%.

A measurement with a higher statistical confidence was obtained by the same group with the polarimeter on-board the OSO-8 satellite (see Fig. 1.3a). Measurements were performed at 2.6 and 5.2 keV, corresponding at the first and the second order of diffraction at 45° from a graphite crystal (Weisskopf et al., 1976, 1978). The high and uniform degree and angle of polarization from radio to X-ray energies allowed to establish the synchrotron origin of the X-ray emission from the nebula and consequently the acceleration of particles up to very high energies by the central pulsar. Indeed the degree and the angle of polarization measured, $\mathcal{P} = 19.2\% \pm 1.0\%$, $\delta = 156.4° \pm 1.4°$ at 2.6 keV and $\mathcal{P} = 19.5\% \pm 2.8\%$, $\delta = 152.6° \pm 4.0°$ at 5.2 keV (see Fig. 1.3b), are consistent with the values measured in optical for the central part of the nebula, where the majority of the X-ray emission originates.

Recently, Dean et al. (2008) measured the polarization of the emission from the Crab nebula at higher energies (between 0.1 and 1.0 MeV) with the SPI instrument on-board the *INTEGRAL* satellite (Winkler et al., 2003). This instrument, despite its design was optimized for high-resolution gamma-ray spectroscopy, can measure the polarization through multiple scattering events in its detectors, since the scattering direction is modulated if photons are linearly polarized (see Eq 1.19). The very high degree of polarization measured in this case, $\mathcal{P} = 46\% \pm 10\%$, and the synchrotron origin of the emission require that the emission region is located near the pulsar, where the magnetic field is rather aligned and hence a higher degree of polarization can be reached. Moreover, the angle of polarization, $\delta = 123° \pm 11°$, is consistent with that measured in the optical for the

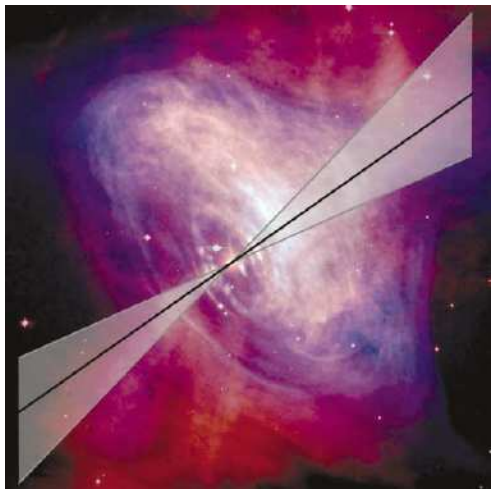

Figure 1.4: The direction of polarization in gamma-rays measured by *INTEGRAL* superimposed on the optical/X-ray image of the Crab nebula from *Chandra* (blue) and the *Hubble Space telescope* (red) (Dean et al., 2008).

unpulsed emission of the pulsar (Kanbach et al., 2005) and it results aligned with the jet seen in the X-ray (see Fig. 1.4). This result has been also confirmed and extended for all the pulsar phases by the measurement above 200 keV of the IBIS instrument, again on-board *INTEGRAL* (Forot et al., 2008).

The discovery of the polarized emission of the Crab nebula has been the only positive result achieved by X-ray polarimetry so far. Silver et al. (1978) analyzed the OSO-8 data to search for a polarized signal in the emission of Crab pulsar, but their search was unsuccessful since no polarization statistically relevant was detected. A tight upper limit of $0.39\% \pm 0.20\%$ was reported for Sco X-1 (Long et al., 1979). Upper limits were also obtained by the OSO-8 satellite for ten strong sources belonging to different classes (Hughes et al., 1984) but, even in this case, they have resulted inconclusive for the comparison between competitive models.

1.4 The expectations of X-ray polarimetry

Theoreticians started to highlight the importance of X-ray polarimetry at the beginning of X-ray astronomy (Novick, 1975; Rees, 1975). Despite the lack of experimental feedback, these works have continued and today it's expected that almost all the classes of astrophysical sources in the X-ray sky emit partially polarized emission. In this Section the main scientific topics that can be tackled with polarimetry are summarized. A particular attention will be dedicated to those, which are related to bright sources or to a higher degree of polarization, that are accessible to the pathfinder missions presented in Chapter 6. The discussion of the observability of some topics presented in this Section is part of this thesis and will be presented in Chapter 6.

1.4.1 Propagation of electromagnetic waves in strongly magnetized plasmas

The propagation of radiation in strongly magnetized plasmas is a central topic for the study of pulsars, isolated neutron stars, magnetars and accreting pulsars. Their emission is typically produced near the surface of the compact object, where a strong magnetic field is present. It's generally described within the cold plasma model, which assumes that all the particles at a given position move with the same velocity and that the perturbations, i.e. the electromagnetic waves in this context, propagate much faster than the typical thermal velocity. In this case the solutions of the Maxwell equations can be represented by means of two normal modes of propagation, called ordinary and extraordinary modes or O- and X-mode respectively. They are characterized by a different dispersion relation when radiation propagates not parallel to the magnetic field (Stix, 1962).

This representation is very useful since the two modes behave in different manners in the presence of a magnetic field. When an electromagnetic wave of angular frequency ω propagates orthogonally to the magnetic field $\vec{B}$ in a homogeneous plasma, the O-mode is linearly polarized parallel to $\vec{B}$, while the X-mode is linearly polarized perpendicularly to the magnetic field. The dispersion relation of the O-mode is unaffected by the magnetic field and it's only modified by the presence of the plasma, but that of the X-mode is characterized by two resonant frequencies, namely there are two frequencies at which the refractive index diverges and the wave is absorbed. These two resonances, in the context of low-density astronomical plasmas, correspond to the ion and electron cyclotron frequencies, $\omega_{ci} = eB_0/m_i$ and $\omega_{ce} = -eB_0/m_e \equiv \omega_B$ respectively.

The modes are elliptically polarized if the electromagnetic wave propagates at an angle ϑ with respect to the magnetic field. In general the electric field would not be orthogonal to the direction of propagation, the longitudinal component being proportional to ω_p^2/ω^2, where $\omega_p = \sqrt{ne^2/\epsilon_0 m_e}$ is the plasma frequency. It can be neglected in the X-ray regime for astronomical plasmas, except near the resonances, thanks to the high frequencies and the low densities considered in this context.

The normal modes are left and right handed circularly polarized in the limit case of propagation parallel to $\vec{B}$. Each mode is characterized by a resonance at the ion or at the electron cyclotron frequency, corresponding to the condition that the electric field of the wave and the gyration of the ions or the electrons are in the same direction.

The polarization of the two normal modes can be described by means of the degree of ellipticity (or ellipticity parameter) $\alpha(\vartheta)$ of the (transverse) polarization ellipse. If the wave propagates along z and the magnetic field is along y, the polarization vectors of the two modes are (Ventura, 1979):

$$\hat{e}_X = c\,(i\alpha, 1, i\lambda_X) \qquad \hat{e}_O = c\,(1, i\alpha, \lambda_O) \tag{1.22}$$

where $\lambda_X, \lambda_O \sim \omega_p^2/\omega^2 \ll 1$ are the longitudinal components of the X- and O-mode respectively and $c = \left(1+\alpha^2\right)^{-1/2}$. The degree of ellipticity can be expressed as:

$$\alpha(\vartheta) = -\frac{b}{1+\sqrt{1+b^2}}, \tag{1.23}$$

with

$$b = 2\frac{\omega}{\omega_B}\left(1 - \frac{\omega_p^2}{\omega^2}\right)\frac{\cos\vartheta}{\sin^2\vartheta} \simeq 2\frac{\omega}{\omega_B}\frac{\cos\vartheta}{\sin^2\vartheta}. \tag{1.24}$$

In Fig. 1.5a the degree of ellipticity for a wave which propagates at an angle ϑ is reported. A value $\alpha \approx 0$ means that the modes are linearly polarized, while a value $\alpha = \pm 1$ corresponds to circular polarization. The normal modes are linearly polarized when $\vartheta = \pi/2$, as highlighted before, and are almost linearly polarized when $\omega \ll \omega_B$ and $\theta \neq \pi/2$. Moreover, only the extraordinary mode results resonant at the cyclotron frequency (see Fig. 1.5b).

The propagation of the two normal modes in a strongly magnetized plasma is deeply affected by the direction of the magnetic field. Indeed, the latter constrains the movement of the electrons along the field lines and quantizes that orthogonally to the magnetic field. This in turn reduces the cross section of the interactions of the electromagnetic waves when the electric field of the wave is orthogonal to $\vec{B}$ (Canuto, 1970). Considering the interesting case of X-ray emission from accreting pulsars $\left(B \sim 10^{12}\ \mathrm{G}\right)$, the angular frequency of the wave is $\omega \gg \omega_p, \omega_{ci}$ but $\omega < \omega_B \simeq 10\ B_{12}$ keV. In this context, the scattering cross section of the X-mode is reduced by a factor $\sim \omega^2/\omega_B^2$ with respect to that of the O-mode (Canuto et al., 1971):

$$\vartheta \approx 0 \Rightarrow \begin{cases} \sigma_X(\vartheta) \simeq \sigma_T\left[\frac{\omega^2}{(\omega_B-\omega)^2} + \frac{1}{2}\sin^2\vartheta\right] & \simeq \sigma_T\left[\frac{\omega^2}{(\omega_B-\omega)^2}\right] \\ \sigma_O(\vartheta) \simeq \sigma_T\left[\frac{\omega^2}{(\omega_B+\omega)^2} + \frac{1}{2}\sin^2\vartheta\right] & \simeq \sigma_T\left[\frac{\omega^2}{(\omega_B+\omega)^2}\right] \end{cases} \tag{1.25}$$

$$\vartheta \approx \frac{\pi}{2} \Rightarrow \begin{cases} \sigma_X(\vartheta) \simeq \sigma_T\left[\frac{\omega^2}{(\omega_B-\omega)^2} + \frac{1}{2}\cos^2\vartheta\right] & \simeq \sigma_T\left[\frac{\omega^2}{(\omega_B-\omega)^2}\right] \\ \sigma_O(\vartheta) \simeq \sigma_T\sin^2\vartheta & \simeq \sigma_T \end{cases} \tag{1.26}$$

In Fig. 1.6 the cross sections for the extraordinary and ordinary modes are reported for two values of the ratio ω/ω_B. The lower cross section (and consequently opacity) of the X-mode can give rise to a high polarization, since X-mode photons can escape more freely. Moreover it can collimate the emission, since the photons can emerge more easily orthogonally to the magnetic field lines.

The magnetic field typical of accreting pulsars and magnetars are not too far and even greater than the critical field $B_c = m_e^2c^3/e\hbar \approx 4.413 \times 10^{13}$ G. In this case the classical cyclotron energy of an electron becomes equal to its rest mass energy and a quantum mechanical treatment of the plasma and radiation is required (Meszaros, 1992). In particular the strong magnetic field changes the polarization properties of the vacuum and, in turn, affects the propagation of electromagnetic waves (Meszaros and Ventura, 1978, 1979). In a plasma even magnetic fields of the order of one tenth of B_c can deeply affect the propagation of the waves by modifying the degree of ellipticity of the normal modes. This effect is expressed by means of an addition term, which is proportional to

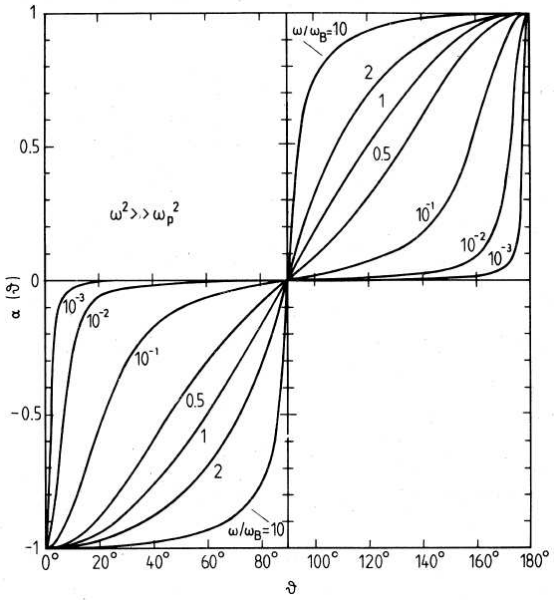

(a)

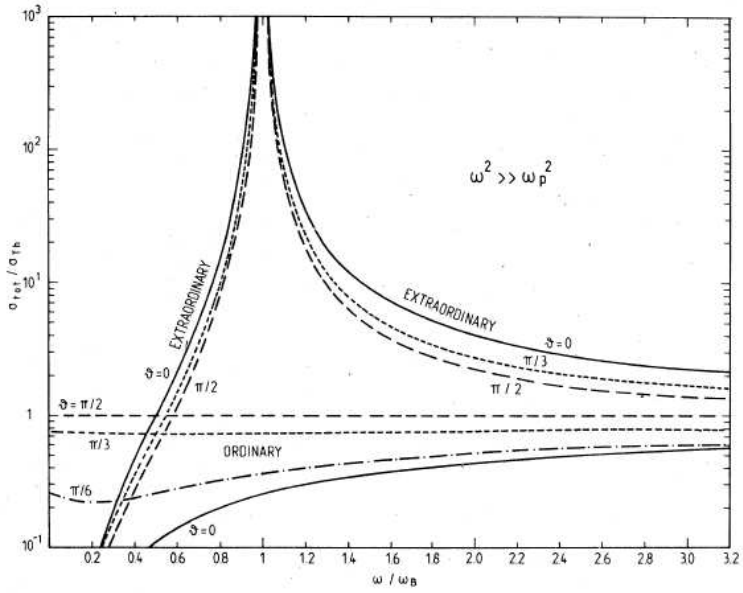

(b)

Figure 1.5: (**a**) The ellipticity parameter of the normal modes for propagation at an angle ϑ and various energies in the hypothesis $\omega \gg \omega_p$. (**b**) Ratio between the scattering Thomson cross section near the cyclotron frequency for the extraordinary and ordinary modes. Note that only the X-mode is resonant (Ventura, 1979).

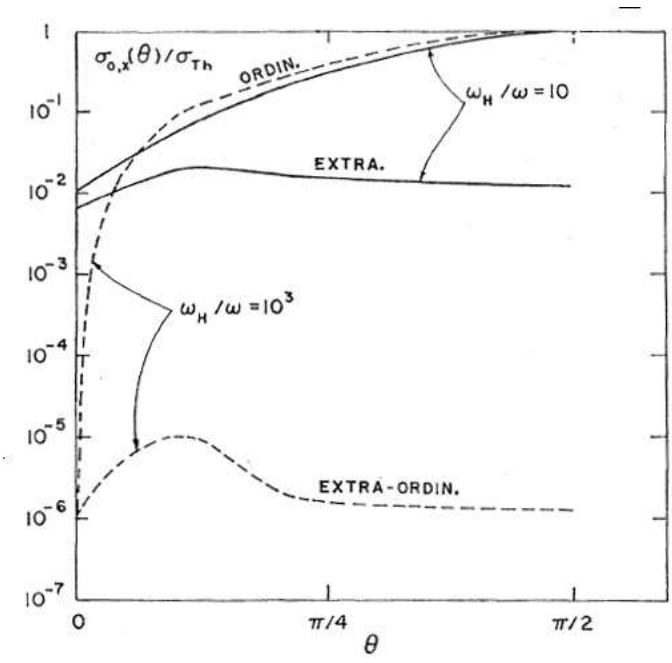

Figure 1.6: Cross section of the extraordinary and ordinary normal modes in magnetized plasma for two values of ω/ω_B (Canuto et al., 1971).

$\delta = \left(e^2/45\pi\hbar c\right)\left(B^2/B_c^2\right) \simeq 0.5 \times 10^{-4} B^2/B_c^2 \ll 1$, in the definition of b (cf. Eq. 1.24)[1]:

$$b_V = 2\frac{\omega}{\omega_B}\left(1 - \frac{\omega_p^2}{\omega^2}\right)\frac{\cos\vartheta}{\sin^2\vartheta}\left[1 + 3\delta\frac{\omega^2}{\omega_p^2}\frac{\omega - \omega_B}{\omega_B}\right]^{-1}. \tag{1.27}$$

Note that the transition from plasma-dominated to vacuum-dominated behavior occurs when the term in square brackets is null, b_V vanishes and the description of electromagnetic waves with X- and O-mode becomes ambiguous. This takes place at a frequency which depends on the density by means of the plasma frequency ω_p and induces a resonance in the spectrum (Ventura et al., 1979). The effect of this resonance on the polarization of the electromagnetic waves and how it affects the observed emission is discussed in Sec. 1.4.4.

The degree of ellipticity for $\omega = 0.5\,\omega_B$ and an increasing contribution of the vacuum polarization with respect to that of plasma, expressed by a decreasing factor ω_p^2/ω^2, is shown in Fig. 1.7a. The value of the ellipticity parameter is modified even for relatively high plasma density, $\omega_p^2/\omega^2 \lesssim 10^{-5}$, and changes dramatically for $\omega_p^2/\omega^2 \approx 3 \times 10^{-7}$. The value of the degree of ellipticity without the vacuum effects and for various values of ω/ω_B is reported in Fig. 1.7b for comparison. The inclusion of the vacuum polarization basically forces a more linearly polarized behavior on the normal modes of propagation.

[1]This definition of b_V is the inverse of that used by Meszaros and Ventura (1978, 1979) but preserves the consistency with the definition given by Ventura (1979) and used in Eq. 1.24.

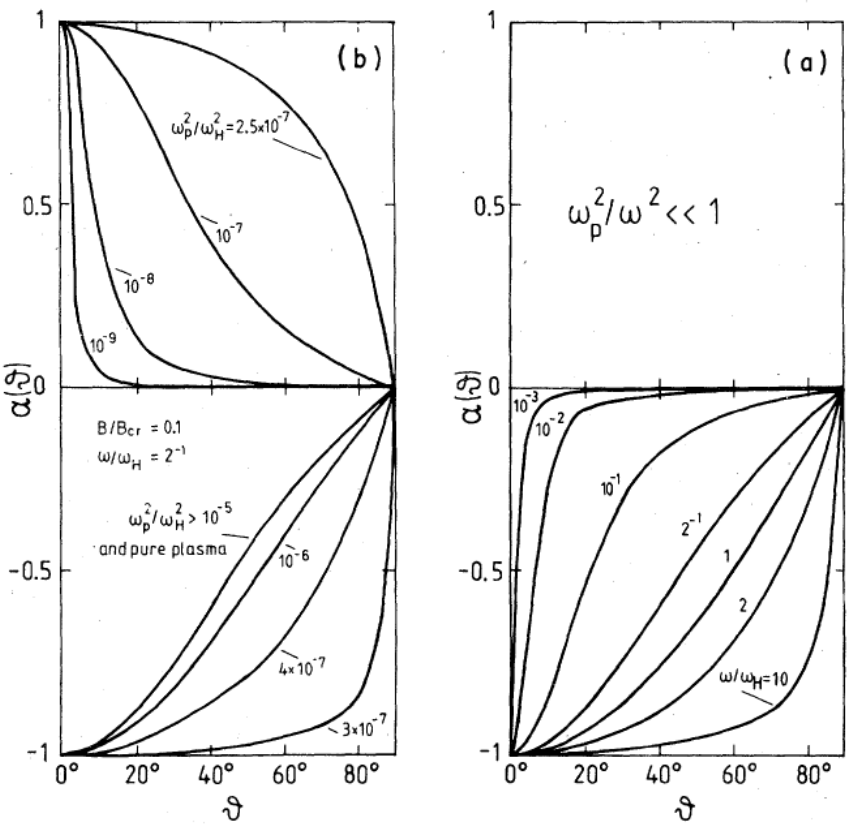

Figure 1.7: (**a**) Effect of an increasing contribution of the vacuum polarization on the degree of ellipticity for $\omega = 0.5\,\omega_B$. (**b**) Ellipticity parameter without vacuum effects for various values of the angular frequency ω reported for comparison (Meszaros and Ventura, 1979).

The change of the degree of ellipticity modifies the polarization vectors of the normal modes. This in turn influences the cross sections of the electromagnetic interactions (Lodenquai et al., 1974), since their dependency on the polarization vectors is generally of the form:

$$\frac{d\sigma_{\alpha\beta}}{d\Omega} = |\hat{e}^*_\beta \cdot S \cdot \hat{e}_\alpha|^2, \tag{1.28}$$

where α and β are the normal-wave-mode indices ($\alpha, \beta = 1$ for X-mode, $\alpha, \beta = 2$ for O-mode), S is the scattering amplitude matrix and $\hat{e}_\alpha$ and $\hat{e}_\beta$ are the polarization vectors of the incident and output wave respectively.

The integrated Thomson scattering cross section of X- and O-mode, $\sigma_\alpha = \Sigma_\beta \sigma_{\alpha\beta}$, calculated by means of Eq. 1.28 when vacuum effects are neglected or included, is reported in Fig. 1.8a as a function of the propagation angle ϑ. Vacuum polarization also affects the cross section at the cyclotron resonance and, including its effect, also the ordinary mode is resonant for $\vartheta \neq 0$ or $\pi/2$ (see Fig. 1.8b).

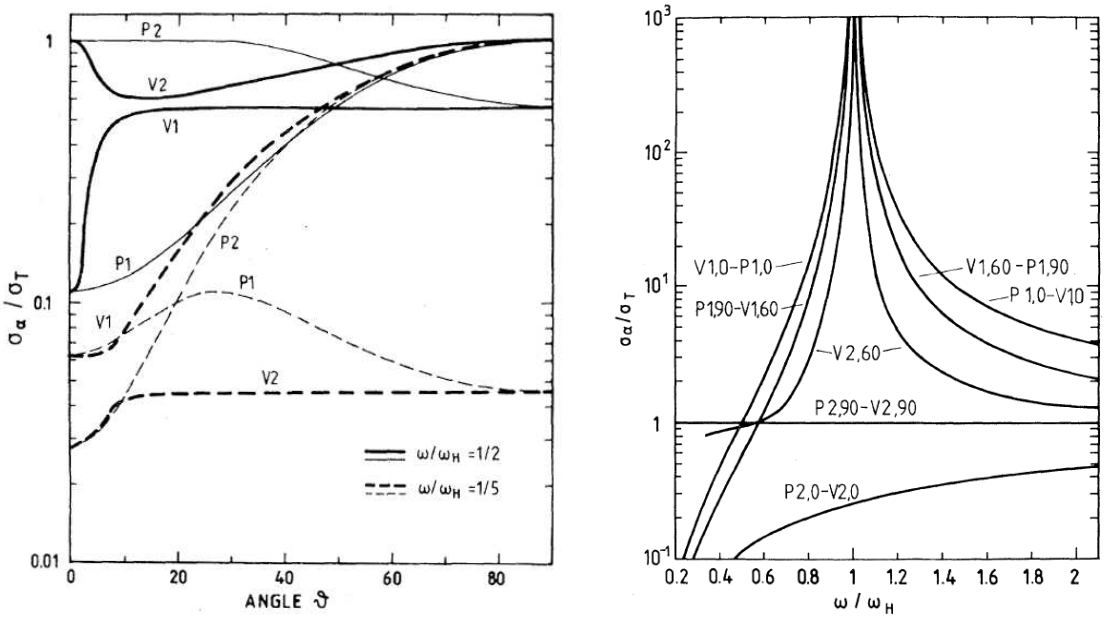

(a) **(b)**

Figure 1.8: (**a**) Integrated total cross section including (curves labelled with "V") and neglecting (curves labelled with "P") vacuum polarization effects as a function of the angle of propagation ϑ. $B/B_c = 0.1$, $\omega/\omega_B = 0.5$ and 0.2. Extraordinary and ordinary modes are labelled with "1" and "2" respectively. (**b**) Integrated cross section near cyclotron resonance. The 0, 60 and 90 after the comma are the values of ϑ (Meszaros and Ventura, 1978).

Another effect of a strong magnetic field is that it makes the vacuum birefringent, namely the velocity of the electromagnetic waves depends on their polarization (Euler and Kockel, 1935; Toll, 1952; Adler, 1971). The different velocity of the components polarized parallel and perpendicularly to the magnetic field can be expressed by means of different indices of diffraction (Tsai and Erber, 1975):

$$n_{\parallel}(B,\vartheta) \simeq 1 + \frac{\alpha}{4\pi}\sin^2\theta\left[\frac{14}{15}\left(\frac{B}{B_c}\right)^2 - \frac{13}{315}\left(\frac{B}{B_c}\right)^4\right] \tag{1.29}$$

$$n_{\perp}(B,\vartheta) \simeq 1 + \frac{\alpha}{4\pi}\sin^2\theta\left[\frac{8}{45}\left(\frac{B}{B_c}\right)^2 - \frac{379}{5040}\left(\frac{B}{B_c}\right)^4\right] \tag{1.30}$$

where α is fine structure constant.

The difference between the velocities of the two components polarized parallel and orthogonally to the magnetic field produces a rotation of the plane of polarization. As an example, for $B = 3 \times 10^{12}$ G, $n_{\parallel} - n_{\perp} \approx 4 \times 10^{-7}$ for propagation transverse to the field and in this case the path length for one wave retardation is only 3 mm for a wavelength $\lambda = 10$ Å ($E \approx 1.2$ keV). Novick et al. (1977) proposed that the large retardation that is

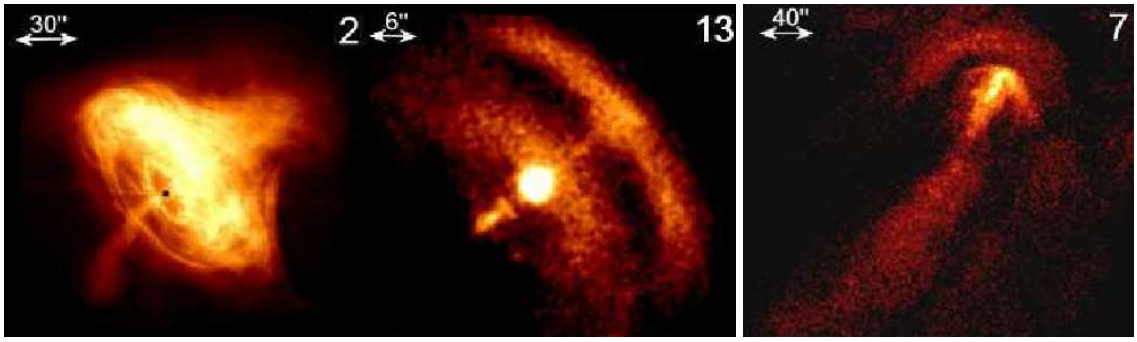

(a) (b)

Figure 1.9: Pulsar Wind Nebulae detected by *Chandra*. (**a**) Two examples of a "typical" PWN with the jets and the toroidal component. The Crab and Vela nebula are on the left and right respectively. (**b**) The Jellyfish nebula, powered by the PSR B1509-58, as an example of the bow-shock nebulae (Kargaltsev and Pavlov, 2008).

accumulated because of even small differences in the path and energy of photons could completely depolarized the radiation produced in strong magnetic fields. In subsequent papers (Gnedin et al., 1978; Chanan et al., 1979) it was instead recognized that generally only circular polarization is removed since only two of the four Stokes parameters vary so rapidly with wavelength to vanish. The degree of (linear) polarization is however reduced of a factor $|\cos\phi|$, where ϕ is angle between the direction of polarization and the projection of the magnetic field on the plane orthogonal to the direction of propagation (Chanan et al., 1979).

As highlighted above the vacuum effects can deeply affect the polarization of the X-ray radiation produced in the strong magnetic field found near compact objects. In the next Sections the consequences of these effects on the emission of astrophysical sources will be discussed.

1.4.2 Pulsar wind nebulae

Pulsar Wind Nebulae (PWNe) are a class of diffuse sources which shine because of the confinement of the magnetized wind produced by a pulsar in its surrounding environment (for a recent review, see for example Gaensler and Slane, 2006). They can manifest themself with a "typical" structure formed by a torus and two jets (see Fig. 1.9a) or have a cometary-like morphology (bow-shock nebulae) due to the high motion of the pulsar in the surrounding medium (see Fig. 1.9b).

The "typical" PWNe are so-called since the Crab nebula is the prototype of this class and hence they are the most studied. The basic model for explaining their emission was presented by Kennel and Coroniti (1984a,b): in their picture, a central pulsar emits the large part of its rotational energy as a spherically symmetric magnetized and relativistic wind. Its energy flux is characterized by a particle and a Poynting component, the latter due to the magnetic field in the wind. The magnetization parameter σ is the ratio of the

energy flux of these two components:

$$\sigma \equiv \frac{F_{E\times B}}{F_{particle}} = \frac{B^2}{4\pi\rho\gamma c^2}, \tag{1.31}$$

where ρ and γ are the mass density and the Lorentz factor of the particles respectively. The relativistic wind is terminated by a strong shock which decelerates the flux and increases the pressure to match the conditions in the nebula. The particles, which are randomized by the shock, emit synchrotron radiation in the magnetic field of the nebula which is of the order of one mGauss.

Kennel and Coroniti, and even before Rees and Gunn (1974), derived for the Crab pulsar a value of $\sigma \approx 0.03$. This small value emerges independently from both the confinement of the wind in the boundary conditions of the nebula and its total synchrotron luminosity. However in virtually all models of pulsar wind, the wind is strongly dominated by the Poynting flux, i.e. $\sigma \gg 1$. The mechanism which converts the Poynting-dominated wind at the light cylinder to a particle-dominated one at the termination shock is still unclear and is referred as the σ-problem.

The discovery by *Chandra* (Weisskopf et al., 2002) of the jet-torus structure of the Crab nebula (Weisskopf et al., 2000) challenged the spherically symmetric model proposed by Kennel and Coroniti. The torus component can be obtained in the framework of their model by assuming that the wind is anisotropic (Bogovalov and Khangoulian, 2002; Shibata et al., 2003), but the jet is more puzzling. It seems to originate from the pulsar and its formation could be possible thanks to the predominant toroidal magnetic field (collimation by magnetic hoop stress) in the nebula, but this mechanism is extremely ineffective in the relativistic wind before the termination shock, namely near the pulsar.

The formation of the jet could be explained if its collimation occurs downstream of a strongly asymmetric shock, induced by the anisotropic wind (Lyubarsky, 2002; Komissarov and Lyubarsky, 2003). In this case the wind is no more relativistic and the collimation by magnetic hoop stress is much more effective. Moreover, if the shock is close to the pulsar near the rotation axis, the jet looks as if it originates from the pulsar itself (see Fig. 1.10).

Recent axially symmetric, magnetohydrodynamics relativistic simulations support this scenario (Del Zanna et al., 2004). Moreover they highlight the role of X-ray polarimetry for the study of the PWNe (Bucciantini et al., 2005; Del Zanna et al., 2006). Since the particles emit synchrotron radiation, a high degree of polarization is expected (up to $\sim$70%). Space-resolved measurements of the direction and degree of polarization could probe the velocity of the wind and the magnetic field in the nebula (see Fig 1.11).

Within the model of Kennel and Coroniti, Nakamura and Shibata (2007) infer the presence in the Crab nebula of a disordered component of the magnetic field, contributing 60% to the total magnetic energy. This is derived from the integrated degree of polarization measured by OSO-8. Moreover they concluded that space-resolved measurements of polarization of the emission of the torus should reveal a maximum degree of polarization of $\sim$40% and probe the flow in the nebula.

It's worth noting that, at least in principle, this kind of studies could be performed also at lower energies, i.e. in optical, where polarimeters are readily available. However

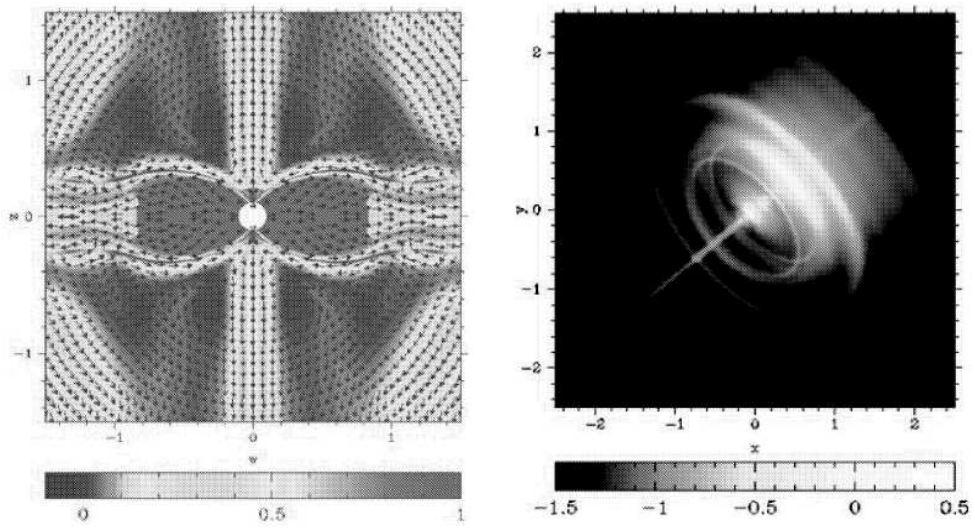

(a) (b)

Figure 1.10: (**a**) Flow direction and velocity of the wind in a PWN assuming a strong asymmetric shock. Note the backflow above the equatorial outflow. (**b**) Simulated X-ray image of the nebula assuming synchrotron emission. The presence of the torus and the jets emerge clearly (Komissarov and Lyubarsky, 2003).

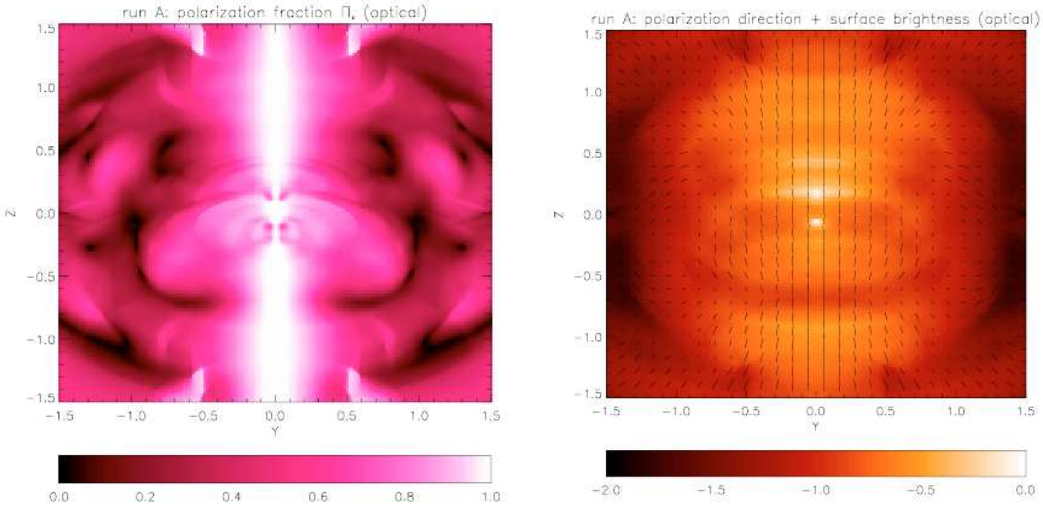

(a) (b)

Figure 1.11: Expected degree and angle of polarization for PWNe in optical calculated by means of MHD simulations. The results for the X-ray energy range were not published by the authors because of the lack of X-ray polarimeters. (**a**) Polarization fraction normalized to the maximum value of ∼70%. (**b**) Direction of polarization superimposed on the surface brightness (Del Zanna et al., 2006).

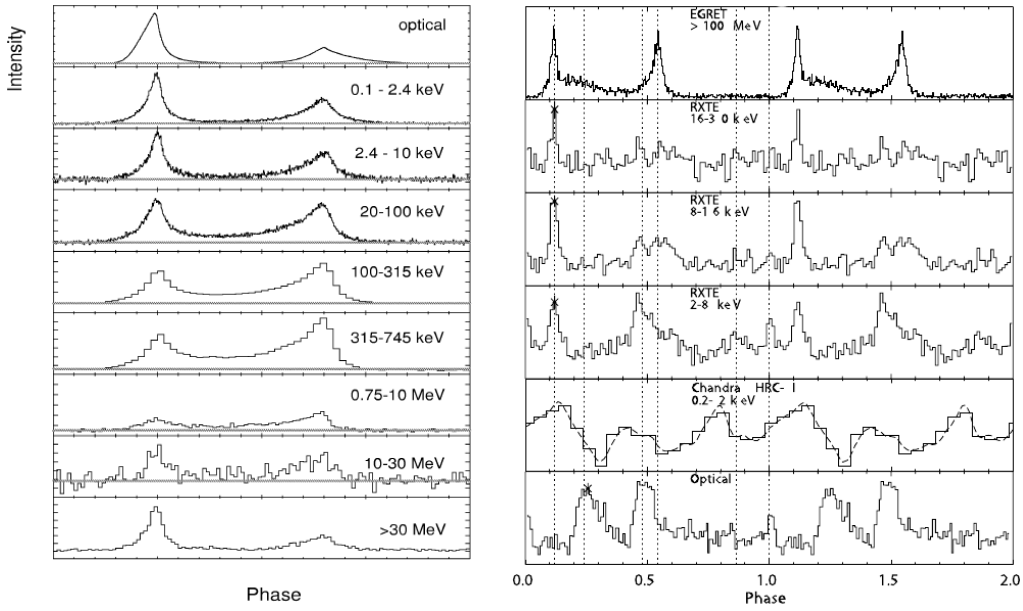

(a) **(b)**

Figure 1.12: Emission from the Crab (**a**) and the Vela (**b**) pulsars, as example of the pulse profiles of young and middle-age objects (Kanbach, 2002; Harding et al., 2002).

the torus/jet structure is clearly visible only in the X-rays. Moreover the particles which emit in this energy range have a shorter life time and so radiate closer to the acceleration site, probing better the mechanism of production of high energy particles.

1.4.3 Pulsars

Despite the 40-years-old discovery of pulsars, many fundamental questions about the processes which produce their emission remain open. In particular the geometry and the mechanism that generate the very regular pulses, which are the signature of this kind of sources at all wavelengths, are poorly understood. For example, young pulsars have a similar pulse profile from radio to gamma-rays (see Fig. 1.12a). Instead that of middle-age objects is very different, suggesting that the emission at different energies occurs in different regions (see Fig. 1.12b).

It is universally accepted that the pulsed emission is produced by electron-positron cascades developed along the magnetic field lines of the pulsar. However there is no consensus on the place where the acceleration of the primary particles which produce the cascades occurs. Two classes of models have been proposed, both starting from the fundamental electrodynamics to obtain the observed radiation. The polar cap models (Ruderman and Sutherland, 1975; Harding, 1981; Daugherty and Harding, 1982) advocate the acceleration of the primary particles near the surface of the pulsars (see Fig. 1.13). In this case the emission occurs in a hollow and narrow cone and hence these models re-

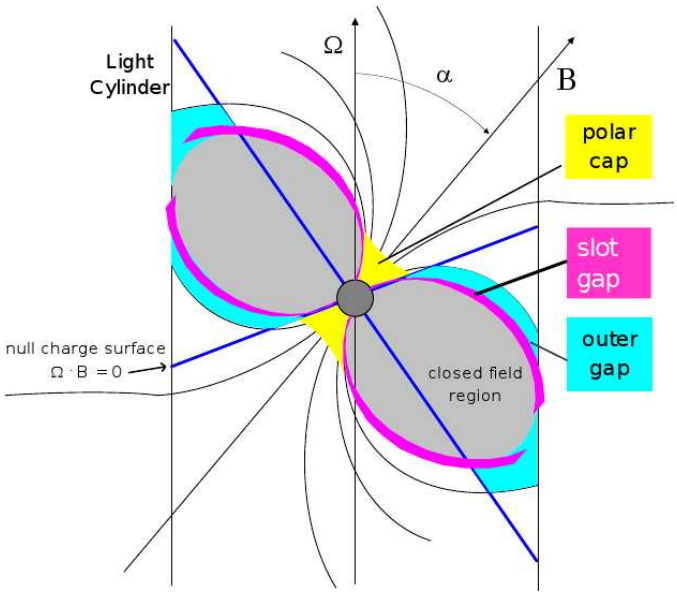

Figure 1.13: Acceleration region for the polar cap, outer gap and two-pole caustic models (Kaspi et al., 2006).

quire that the magnetic and the rotational axes are nearly co-aligned to reproduce the typical pulse profiles of pulsars composed of two wide peaks. Outer gap models (Cheng et al., 1986a,b) instead assume that the acceleration occurs near the light cylinder of the pulsar along/above the last open magnetic field line. These models correctly reproduce the spacing between the peaks of the pulse profiles but not its trailing and off-pulse emission. Indeed the emission quickly goes to zero when the line of sight cross the last open magnetic field line.

A way to overcome the difficulties of these two "classical" approaches was proposed by Dyks and Rudak (2003) with the two-pole caustic model. This advocates that the emission occurs along the last open magnetic field line from the surface of the pulsar to the light cylinder. Although this model has not a complete physical justification, it can reproduce the pulse profile quite well, suggesting that the classical models are missing something in the description of the basic processes at work in pulsars.

Phase-resolved polarimetry from radio to optical has been a powerful diagnostic tool to investigate the processes which act in pulsars. The pulsed non-thermal emission, basically produced by curvature emission or inverse Compton scattering, is expected to be highly polarized either parallel or orthogonally to the magnetic field. The phase-resolved measurement of the angle of polarization then traces the evolution of the magnetic field as the pulsar rotates. This can provide important hints on the region of acceleration of the primary particles since each model has a different signature. For example, an S-shape swing of the angle of polarization is the signature of acceleration near the poles of a dipolar magnetic field (Radhakrishnan and Cooke, 1969). Comparisons between observations from radio to optical and models have been performed (see Fig. 1.14), even if conclusive

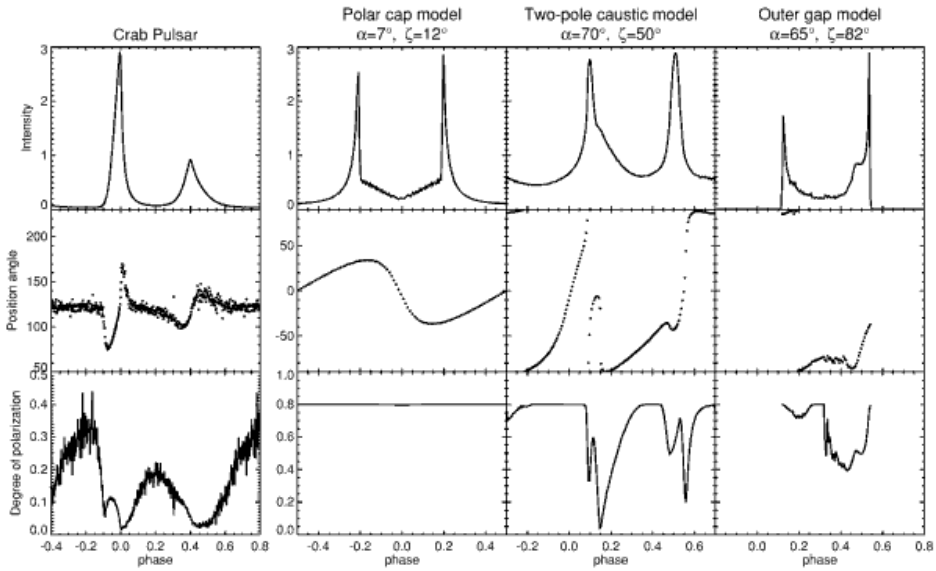

Figure 1.14: From top to bottom, pulse profile, angle and degree of polarization of the Crab pulsar measured in optical. It is compared with the signature of the polar cap, two pole caustic and outer gap models (Dyks et al., 2004).

results have not been achieved yet. X-ray polarimetry could be more appropriate since in this energy band the emission can be easier separated from that of the nebula. Moreover the pulsed emission in this energy band is a much more significant fraction of the spin-down energy ($\sim 10^{-3}$ for the Crab, up to 0.1 for other pulsars with respect to the 10^{-6} in radio) and then traces more directly the phenomena which accelerate particles.

The strong magnetic field near pulsars makes the vacuum birefringent (see Sec. 1.4.1). This effect is too small to affect the spectrum or the light curves of a normal pulsar with $B \lesssim 10^{14}$ G, but it can be observable with polarimetry. The difference between the velocities of the components polarized orthogonally to the magnetic field produces in the unit of time a small lag between them. It is to be compared with a very sensitive probe, namely the wavelength of the radiation which is of the order of 1Å for X-rays.

Heyl and Shaviv (2000) proposed that the vacuum birefringence may decouple the polarization modes for photons with energy $E > 1.49 \times 10^{-3}$ eV $B_{12}^{-2} R_6^{-1}$, where R_6 is the radius of the pulsar in unit of 10^6 cm. The two modes would propagate independently and the plane of polarization relative to an external observer would "follow" the magnetic field lines until the modes are coupled again. This occurs at a distance which depends on the energy of radiation but it's of order of several stellar radii. Since higher energy photons couple after travelling a larger distance, the rotation of the magnetic field before the coupling could drag the direction of polarization: the net effect is a lag between the plane of polarization of higher and lower energy radiation (see Fig. 1.15). This could be exploited to distinguish between different emission processes, since they occur in regions with different magnetic field intensity and structure. Moreover it would probe

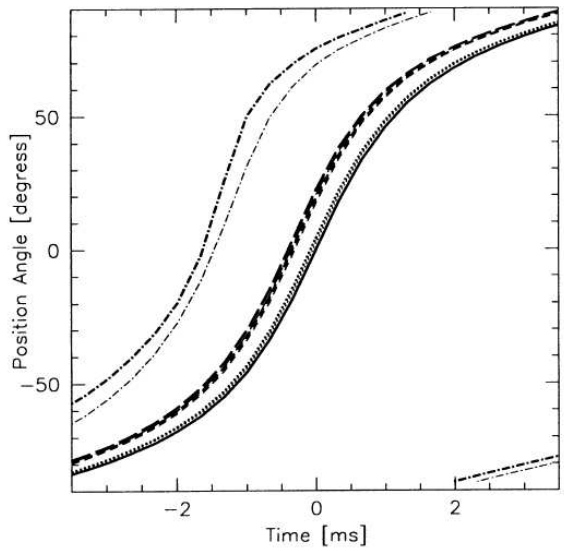

Figure 1.15: Lag of the angle of polarization as a function of time and photon energy for a model of the Crab pulsar. The energy are 5.2 MeV (dot-dashed), 5.2 keV (long-dashed), 2.6 keV (short-dashed) 4.48 eV(dotted) and zero (solid) (Heyl and Shaviv, 2000).

the magnetosphere in the region between the surface of the pulsar and the light cylinder where the coupling occurs.

1.4.4 Isolated neutron stars and magnetars

Magnetized neutron stars reveal themself not only as pulsar but also by means of thermal emission, which derives from cooling or as a by-product of non-thermal processes. Isolated neutron stars (Haberl, 2007; van Kerkwijk and Kaplan, 2007) and central compact objects (Pavlov et al., 2002) belong to the first class: the former appear as isolated soft thermal sources, while the latter are found as non-pulsating (except in one case) sources in supernova remnants. Pulsars and magnetars, neutron stars with $B \sim 10^{15}$ G (Duncan and Thompson, 1992; Thompson and Duncan, 1995), instead emit thermal emission which derives from non-thermal process occurring in their magnetosphere.

It's expected that the X-ray emission from the surface of a cooling neutron star is significantly polarized because the opacity of radiation in a strongly magnetized plasma depends on its direction of polarization with respect to the magnetic field $\vec{B}$ (see Sec. 1.4.1). Photons which propagate as an X-mode electromagnetic wave, which is almost linearly polarized perpendicularly to $\vec{B}$, has a reduced opacity. They can escape from deeper and hotter layers of the atmosphere, while O-mode radiation, polarized parallel to the magnetic field, emerges from superficial layers. Then the observed emission is expected to be dominated by X-mode photons which are produced in a higher temperature environment.

Pavlov and Zavlin (2000) highlighted that the degree of polarization of the emission (instead of its spectrum) is very sensitive to the magnetic field and to the ratio between the mass M and the radius R of the neutron star. The radiation emerges from the surface locally polarized orthogonally to the magnetic field because of the different opacity of the two normal modes. As photons escape from the neutron star, they are bent by the strong gravitational field which sums incoherently photons produced in different points on the surface and then polarized in different directions. A partial depolarization occurs but the emission brings memory of the intensity of the gravitational field encountered. The visible fraction of the surface, and consequently the amount of the depolarization, increases with it and this eventually allows to probe the mass-to-radius ratio of the neutron star and consequently the equation of state of superdense matter.

The dependence on B instead allows to derive an estimate of the magnetic field. In case of isolated neutron stars, it seems to be somehow higher than that of pulsars: for at least a few objects the putative detection of an ion cyclotron absorption line at energy of some hundreds of eV suggests $B \gtrsim 10^{13}$ G (Haberl et al., 2003; Bignami et al., 2003; van Kerkwijk et al., 2004). The expected degree of polarization as a function of mass-to-radius ratio, expressed with the gravitational redshift $g_r = \sqrt{1 - 2GM/c^2R}$, is reported in Fig. 1.16a (Pavlov and Zavlin, 2000), while the dependence on the magnetic field is in Fig. 1.16b. Both are as a function of the inclination of the magnetic moment with respect to the direction of observation Θ.

The depolarization effect of the gravitational bending was criticized by Heyl and Shaviv (2002). These authors proposed that the birefringence induced by the strong magnetic field (see Sec. 1.4.1) decouples the modes of propagation in the magnetosphere. The net effect is that the direction of polarization is correlated to that of $\vec{B}$ up to the polarization-limiting radius:

$$r_l = \left(\frac{\alpha}{45}\frac{\nu}{c}\right)^{\frac{1}{5}} \left(\frac{\mu}{B_c}\sin\beta\right)^{\frac{2}{5}} \simeq 1.2 \times 10^2 \left(\frac{\nu}{10^{17}\ \mathrm{Hz}}\right)^{\frac{1}{5}} \left(\frac{\mu}{10^{30}\ \mathrm{G\ cm^3}}\right)^{\frac{2}{5}} \sin^{\frac{2}{5}}\beta\ \mathrm{km}, \quad (1.32)$$

where α is the fine structure constant, ν the frequency of the electromagnetic wave and β the angle between the magnetic axis and the line of sight.

For typical values, $r_l \gg R$. Hence the radiation couples far from the surface of the neutron star, where the magnetic field is almost uniform with respect to the small bundle of rays which eventually arrives to the detector. Consequently when modes are coupled the direction of polarization of photons escaping from different regions of the surface are almost summed in phase (see Fig. 1.17). The alignment of the planes of polarization increases the degree of polarization of the emission of a factor five to seven (Heyl et al., 2003). Even including the birefringence of the vacuum, the degree of polarization retains memory of the ratio between the mass and the radius of the neutron star, thus confirming the polarimetry as a primary diagnostic tool for its investigation.

Another effect due to the vacuum polarization can affect the polarization from isolated neutron stars. The standard way of classifying electromagnetic waves in a magnetized plasma in X- and O-mode becomes ambiguous when the value of the degree of ellipticity is zero (see Sec. 1.4.1 and in particular Eq. 1.27 and the subsequent discussion). This occurs at the cyclotron frequency but also when the wave encounters a resonant

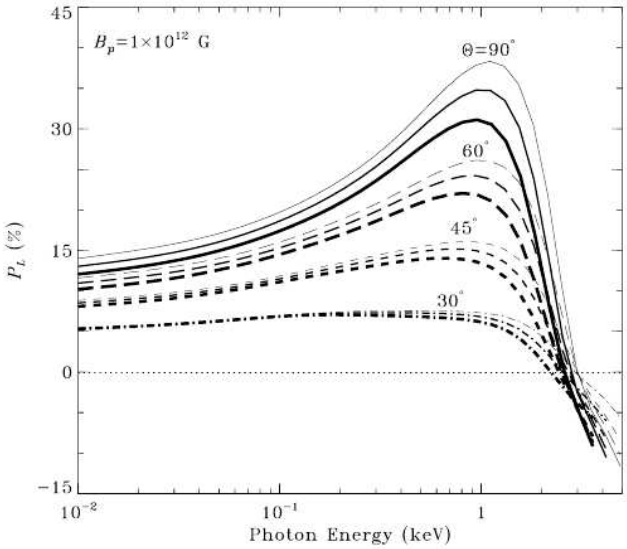

(a)

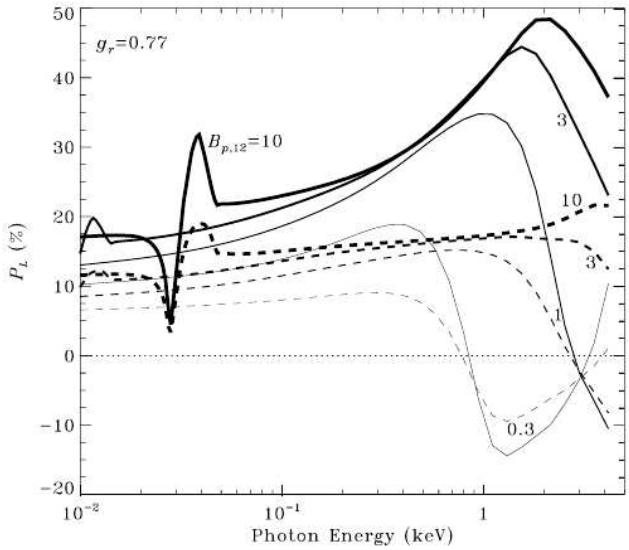

(b)

Figure 1.16: (**a**) Dependence of the degree of polarization on M/R for $B = 10^{12}$ G. Thin, medium and thick lines are for redshift parameters $g_r = 0.90, 0.77, 0.66$, while solid, long dashed, short-dashed and dot-dashed lines refer to $\Theta = 90°, 60°, 45°, 30°$ respectively. (**b**) Effect of the magnetic field for $g_r = 0.77$. The curves are for $B_{12} = 0.3, 1.0, 3.0, 10.$, while solid and dashed lines refer to $\theta = 90°, 45°$ respectively (Pavlov and Zavlin, 2000).

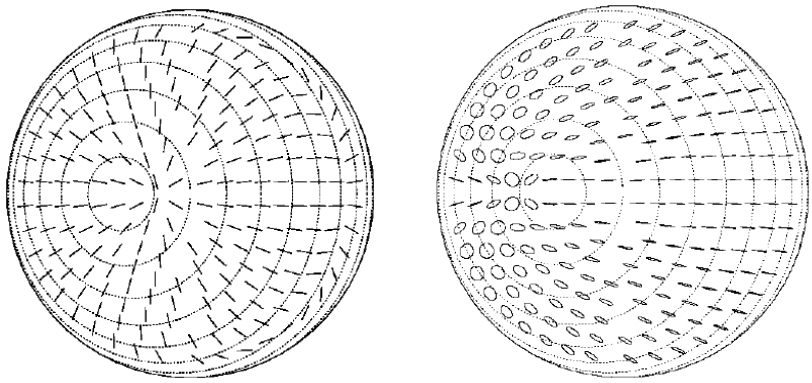

(a) **(b)**

Figure 1.17: Observed ellipse of polarization of photons escaping from different regions of the surface of the neutron star neglecting (**a**) and including (**b**) vacuum polarization effects. The observed radiation is the sum of the photons emitted from the whole surface. It's assumed that only O-mode photons are emitted. The circular curves are lines of constant latitude on the surface of the neutron star (Heyl and Shaviv, 2002).

density (Lai and Ho, 2002):

$$\rho_{res} \simeq 0.964\, Y_e^{-1}\, (B_{14} E_{keV})^2\, \eta^{-2}\ \mathrm{g\ cm^{-3}}, \tag{1.33}$$

where Y_e is the electron fraction Z/A, E_{keV} is the energy in keV and $\eta \sim 1$ is a slowly-varying function of the magnetic field. While many authors analyzed the emergence of a resonant line in the spectra (Ventura et al., 1979), Lai and Ho (2002, 2003) studied the behavior of the polarization across this resonance. The mode of the electromagnetic wave is adiabatically converted from a mode to the other with a probability (Lai and Ho, 2002):

$$P_{conv} = 1 - P_{jump} = 1 - e^{-\frac{\pi}{2}\gamma_{res}}, \tag{1.34}$$

where P_{jump} is the probability that the state is preserved "jumping" the adiabatic conversion and $\gamma_{res} = (E/E_{ad})^3$. The resonant energy E_{ad} is:

$$E_{ad} = 2.52\, (\eta \tan\vartheta)^{\frac{2}{3}} \left|1 - \frac{\omega_{ci}}{\omega}\right|^{\frac{1}{3}} \left(\frac{1\ \mathrm{cm}}{H_\rho}\right)^{\frac{1}{3}}\ \mathrm{keV}, \tag{1.35}$$

where ϑ is the angle between the direction of propagation and the magnetic field and $H_\rho = |dz/d\ln\rho|$ is the density scale height evaluated at the resonant density along the wave. From the large dependency of γ_{res} on the energy, it results that for $E \gtrsim 2\ E_{ad}$ the conversion is almost complete, while for $E \lesssim 0.5\ E_{ad}$ the mode is conserved.

The conversion of normal modes in an inhomogeneous plasma for $E = 5$ keV is graphically represented in Fig. 1.18a. The evolution of the degree of ellipticity across the resonant density follows the dotted or the dashed line according to its initial mode, while for $E \ll E_{ad}$ the evolution would be represented by a horizontal line.

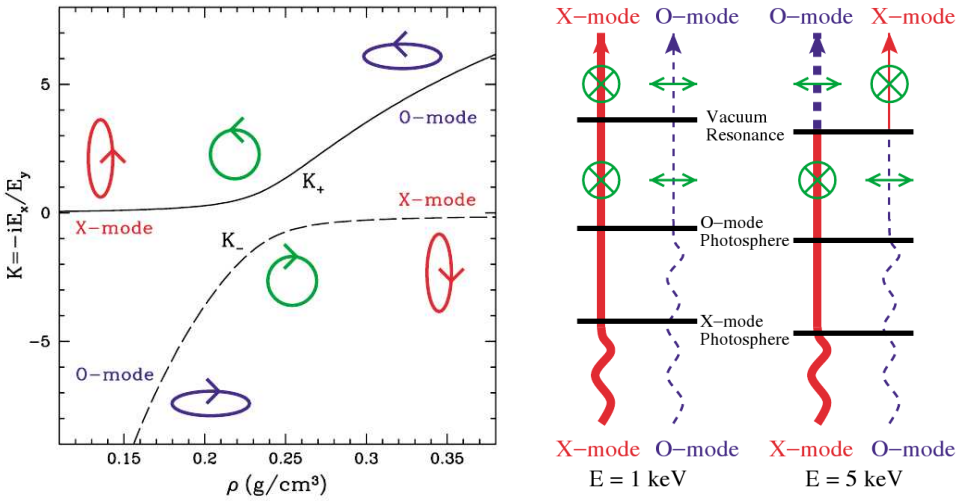

Figure 1.18: (**a**) Degree of ellipticity of normal modes across the resonant density for $E = 5$ keV and $B = 10^{13}$ G. (**b**) Schematic view of how radiation emerges from the atmosphere of an isolated neutron star in the case $B < B_l$ (Lai and Ho, 2003).

This behavior is both a signature of an interesting quantum electrodynamic effect and a probe to investigate the magnetic field of the neutron star. It can be experimentally observed with measurements of polarization of X-ray emission from isolated neutron stars and magnetars, since Lai and Ho (2003) pointed out that these two classes of sources belong to two different regimes. If the magnetic field is of "normal" intensity, i.e.:

$$B < B_l \simeq 6.6 \times 10^{13} T_6^{-1/8} E_{keV}^{-1/4} \left(1 - e^{-\frac{E}{kT}}\right)^{-1/4} \text{G}, \tag{1.36}$$

the vacuum resonance is outside both the X- and O-mode photospheres ($\rho_{res} < \rho_X, \rho_O$), whereas in magnetars $B > B_l$ and $\rho_O < \rho_{res} < \rho_X$.

As described at the beginning of this Section, the X-mode is expected to dominate the emission from the surface of isolated neutron stars or magnetars, $I_X^{(0)} \gg I_O^{(0)}$. The dominance of X-mode (solid red line) over the O-mode (dashed blue line) is represented in Fig. 1.18b by the thicker line. The straight lines in the same Figure indicate that modes after crossing their own photosphere can escape (almost) freely.

If $B < B_l$, the vacuum resonance is encountered after the photosphere of both modes and hence the emitted radiation is:

$$I_X = (1 - P_{conv})\, I_X^{(0)} + P_{conv} I_O^{(0)} \tag{1.37}$$

$$I_O = (1 - P_{conv})\, I_O^{(0)} + P_{conv} I_X^{(0)} \tag{1.38}$$

For $E < E_{ad}$, $P_{conv} \approx 0$, $I_X \approx I_X^{(0)}$, $I_O \approx I_O^{(0)}$ and the emission remains dominated by the X-mode, polarized orthogonally to the magnetic field. Instead, for $E > E_{ad}$, $P_{conv} \approx$

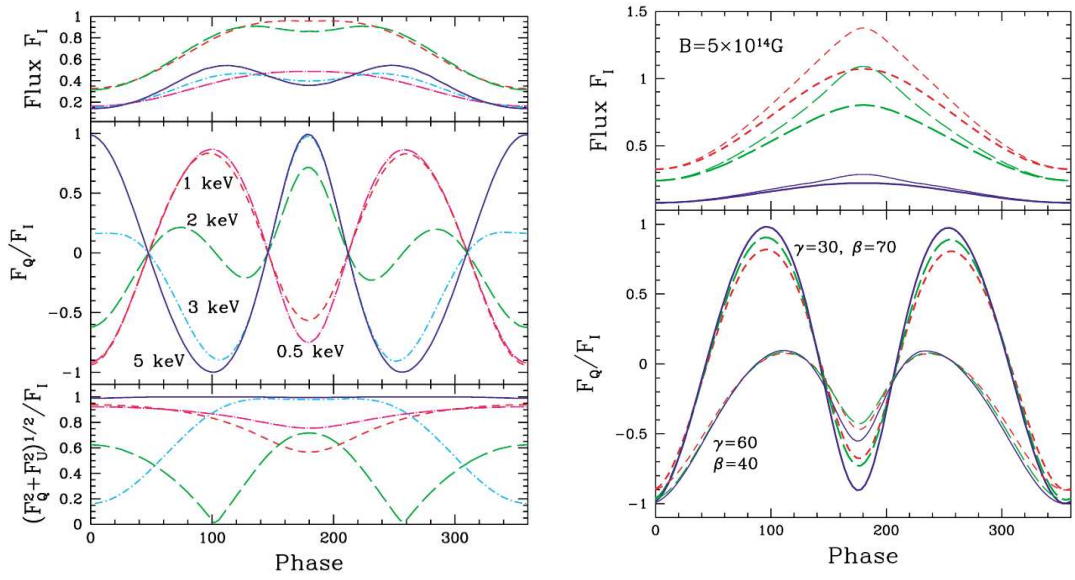

Figure 1.19: (**a**) Light curve (upper panel) and phase evolution of the linear and the degree of polarization for an isolated neutron star ($B = 10^{13}$ G). (**b**) The same as (**a**) for a magnetar ($B = 5 \times 10^{14}$), but without the degree of polarization (Lai and Ho, 2003).

1, $I_X \approx I_O^{(0)}$, $I_O \approx I_X^{(0)}$ and then the resonant conversion makes the radiation dominated by the O-mode which is parallel polarized to the magnetic field (see Fig. 1.18b).

For magnetars the vacuum resonance is encountered below the photosphere of the O-mode. Then the conversion occurs as well but in this case the O-mode radiation can't escape freely and is reconverted into X-mode. The signature of a "normal" magnetic field is then the orthogonality of the direction of polarization at low and high energy, while such effect is not expected for the stronger magnetic field of the magnetars (see Fig. 1.19).

1.4.5 Accretion powered neutron stars

The transfer of matter in a binary system from a donor star to a compact object, either a neutron star or a black hole, is the most important process which powers the X-ray sources in the sky. Two classes of galactic systems have been identified, the High and the Low Mass X-ray Binaries, HMXBs and LMXBs respectively (White et al., 1995; Tauris and van den Heuvel, 2006). The former is associated to young early-type massive stars and the transfer of matter occurs via the strong wind of the donor star. When the binary system harbors a neutron star, the typical signature of these sources is a periodic modulated emission at the spin frequency of the compact object. Since the HMXBs are, in general, young systems, the young neutron star has a sufficient strong magnetic field to funnel the accreting matter on the magnetic poles, which are not aligned with the rotation axis. Despite the amplitude of the modulation is generally only a small fraction of the total

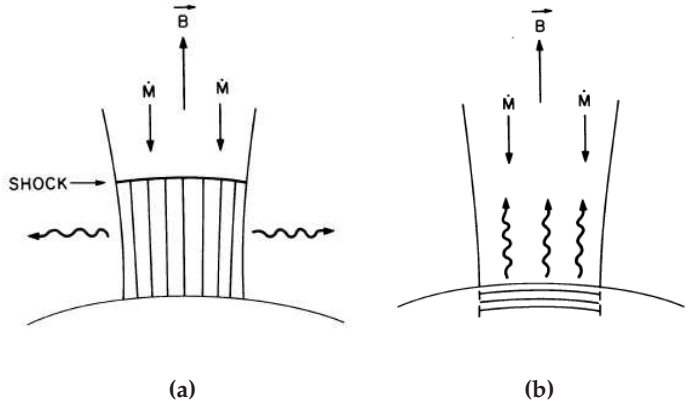

Figure 1.20: Schematic view of the fan (**a**) and pencil (**b**) beam models. The emission occurs orthogonally and parallel to the magnetic field respectively (Meszaros, 1984).

emission, these sources are often called X-ray pulsars or pulsators.

The LMXBs are instead associated to evolved late-type stars, with a mass $\lesssim 2M_{\odot}$. The accretion in this case occurs via Roche lobe overflow and the formation of an accretion disk, with the emergence of quasi-periodic oscillations as the matter is accreted on the compact object. The neutron star harbored in these systems have in general a relatively low magnetic field ($B \sim 10^9 - 10^{11}$ G) and this makes X-ray pulsations rather uncommon. However this class is characterized by thermonuclear bursts (Strohmayer and Bildsten, 2006). They consists in the sudden nuclear fusion of accreted matter on the surface of the neutron star and are not present in HMXBs since they are inhibited in magnetic field strength $> 10^{11}$ G.

LMXBs should emit partially polarized radiation, at least the subclass known as millisecond X-ray pulsars. It is formed by several binary systems where the accretion has spun-up the neutron star up to a period of some milliseconds. The emission in this case is modulated and the scattering of photons on the accretion disk or on the infalling column of matter should produced polarized radiation (Sazonov and Sunyaev, 2001; Viironen and Poutanen, 2004). The most interesting objects are however the binary systems which harbor neutron stars or black holes (tackled in the next Section). The formers are attractive since they have magnetic fields of the order of 10^{12} G and hence it's expected that the propagation of the photons in their vicinity is influenced by the wealth of effects described in Sec. 1.4.1.

Two models have been developed to explain the emission from X-ray pulsars, the fan and the pencil beam models. The former advocates the presence of a radiative or a collisionless shock, the value of the luminosity being $>$ or $<$ 10^{37} erg/s, which decelerates the infalling matter. In this case the emission produces a fan beam which is emitted perpendicularly to the magnetic field lines (see Fig. 1.20a). The Pencil beam model instead assumes that for low luminosity sources the infalling matter is stopped directly on the surface of the neutron star by Coulomb and nuclear collisions. The radiation in this case is emitted in the direction of the magnetic field lines (see Fig. 1.20b).

The polarization signature of the these two models was calculated by Meszaros et al. (1988) and allows to distinguish them. When the flux is maximum, the degree of polarization is maximum for the fan beam model and minimum for the pencil one (see the curves at low energy in the Fig 1.21). This effect has a physical justification: in the fan case, the peak emission occurs when photons are emitted perpendicularly to the magnetic field. Below the cyclotron energy, the opacity of the X-mode is strongly reduced with respect to that of the O-mode and so the emission is dominated by the former. On the contrary the radiation is produced along the field lines in the pencil beam model. Then both modes have a reduced opacity during the maximum, since the polarization is orthogonal to the magnetic field in any case. The lack of a dominant mode depolarizes the emergent radiation.

The dominance of a specific mode can also be traced by the angle of polarization. When one of the two modes dominates the emission for the whole rotation of the neutron star, the angle of polarization oscillates continuously, while the change of the predominant mode produce a jump of 90° (see the last panels in Fig. 1.21).

1.4.6 Black hole binaries

The transfer of matter in galactic binaries with black holes (McClintock and Remillard, 2006) occurs via the formation of a geometrically thin but optically thick accretion disk, at least in the thermal high soft state. In this case Thomson scattering dominates the opacity in the inner part of the disk where X-ray emission is produced (Shakura and Syunyaev, 1973).

Unpolarized radiation scattered by an anisotropic distribution of matter becomes linearly polarized parallel to the major axis of the projection of the distribution in the sky (Chandrasekhar, 1946, 1950). This result was derived for optically thick clouds, but it also holds for accretion disks as long as the opacity is dominated by Thomson scattering. The degree of polarization depends on the angle θ between the normal to the major axis and the line of sight and reaches a maximum value of 11.7% for edge-on disks.

The polarization of Comptonized photons scattered by a distribution of matter with finite opacities was calculated by Sunyaev and Titarchuk (1985) and it is reported in Fig. 1.22a in function of $\mu = \cos\theta$. The positive or negative sign of the polarization refers to its direction, i.e. parallel or perpendicular to the accretion disk respectively. Note that only these two directions are possible in the Newtonian theory of gravity. The emergence of polarization is related to the breaking of a geometrical symmetry and this occurs only along a preferred direction of the system, such as the axis of symmetry of the disk or its orthogonal direction.

The expected degree of polarization of the emission, integrated on all wavelengths, from a geometrically thin but optically thick accretion disk is reported in Fig. 1.22b (Sunyaev and Titarchuk, 1985). The degree of polarization depends on the disk inclination with respect to the line of sight and its opacity, reaching a maximum value of 11.7% in the case of edge-on disks. For symmetry reasons, the degree of polarization vanishes for face-on disks, for which there aren't any preferred directions. The angle of polarization is aligned to the disk for $\tau > 2$, while it is parallel to its axis of symmetry in the case of

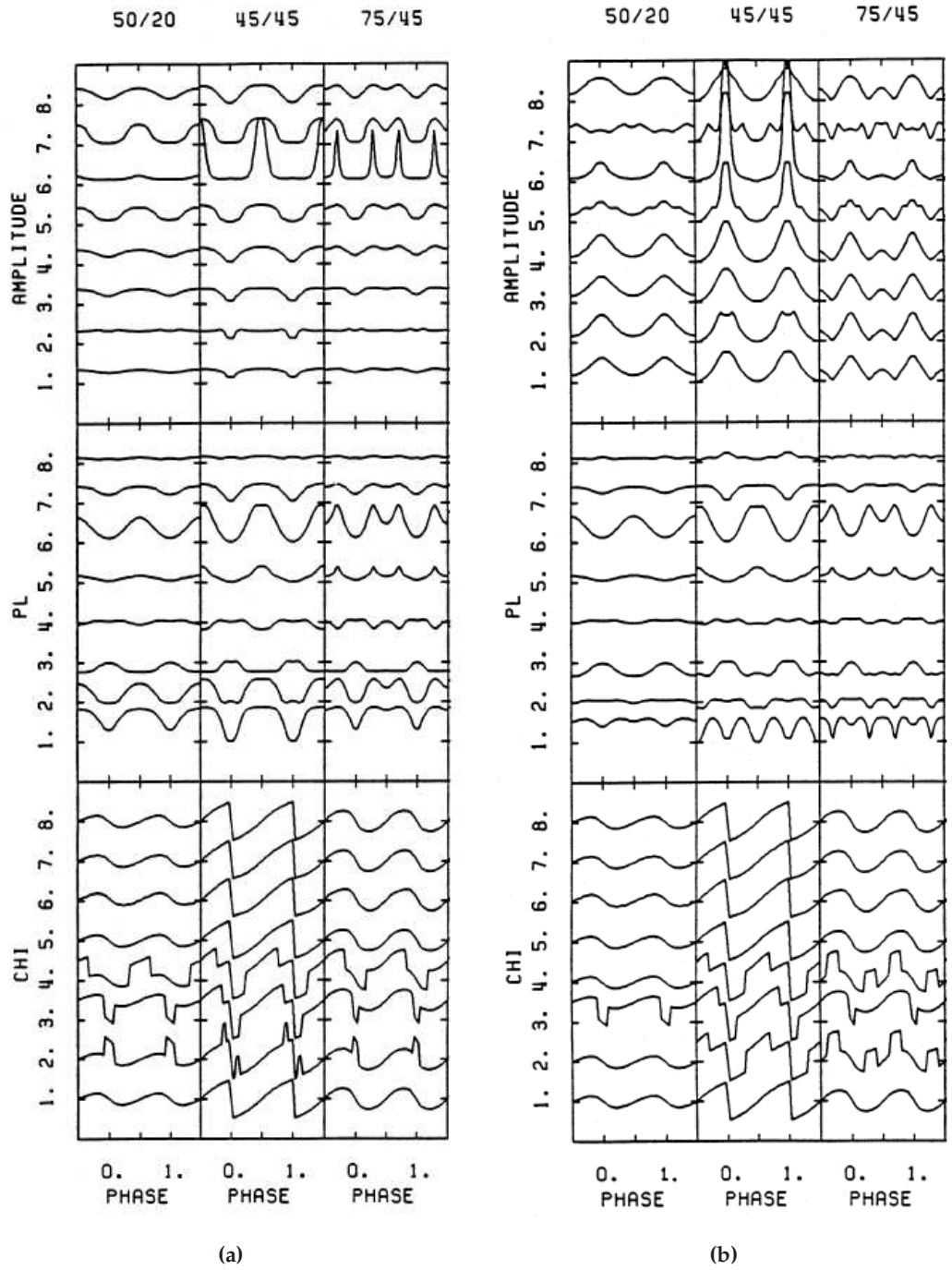

Figure 1.21: Intensity, polarization degree and plane of polarization for fan (**a**) and pencil (**b**) beam models. The different curves refer to different energies which, from bottom to the top, are 1.6, 3.8, 9.0, 18.4, 29.1, 38.4, 51.7 and 84.7 keV. The cyclotron energy is 38 keV, while the numbers on the top refer to the angles that the axis of rotation form with the line of sight and the magnetic moment respectively (Meszaros et al., 1988).

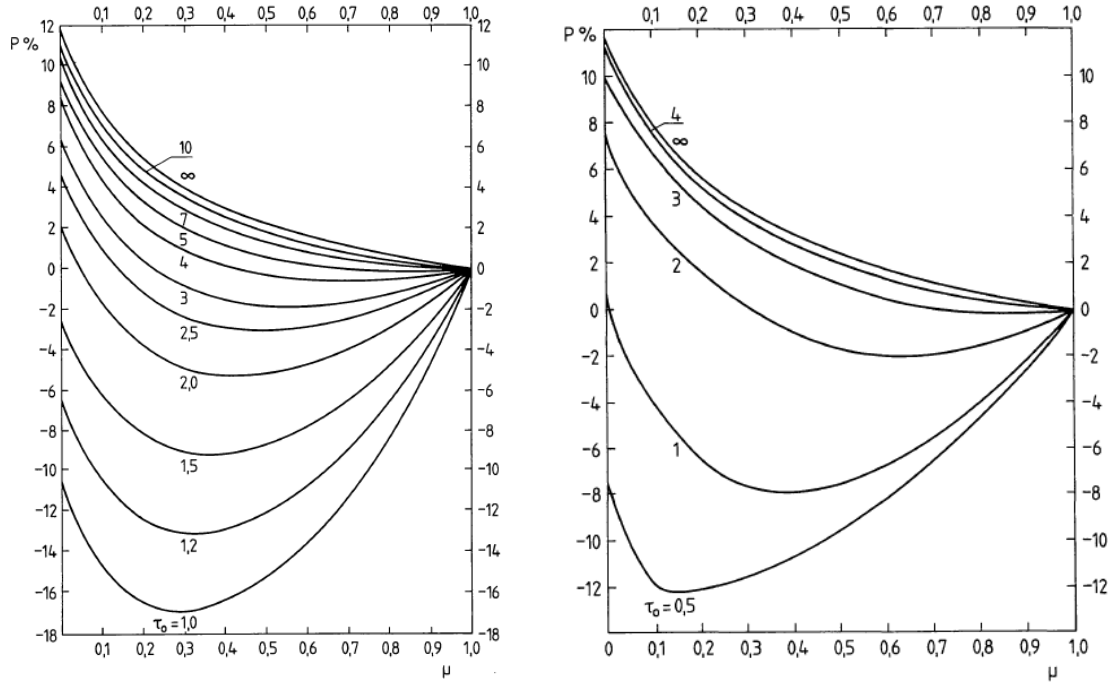

(a) **(b)**

Figure 1.22: (**a**) Degree of polarization of the radiation which emerges from a plane parallel atmosphere whose opacity is due only to the electron scattering. (**b**) Degree of polarization of thermal radiation produced in a thin accretion disk and Comptonized in a plane parallel atmosphere whose opacity is dominated by Thomson scattering (Sunyaev and Titarchuk, 1985).

optically thin atmospheres.

The detection of X-ray polarized emission from accretion disks could reveal the geometry of the binary system exploiting the energy range where these systems are brighter. It's expected that at low energy the degree of polarization is aligned to the axis of symmetry of the disk, while at higher energy the emission produced by the disk but reflected from the donor star could emerge at least during some orbital phases (Rees, 1975). Since even this component should be highly polarized, the direction of polarization could reveal both the plane of the orbit and that of the disk.

But X-ray polarimetry is also a powerful probe to investigate the black hole harbored in the binary system. The inner edge of the accretion disk, at least in the thermal high state, is very close to the black hole and, since X-ray emission is produced in this region where an extreme gravitational field is present, it strongly affects the polarization characteristics of the emergent radiation (Stark and Connors, 1977; Connors et al., 1980).

Photons which emerge from the disk are expected to be partially polarized parallel to it, as discussed above. However gravitational bending due to the intense field curves the light geodesics and the net effect is a mixing of photons coming from different regions.

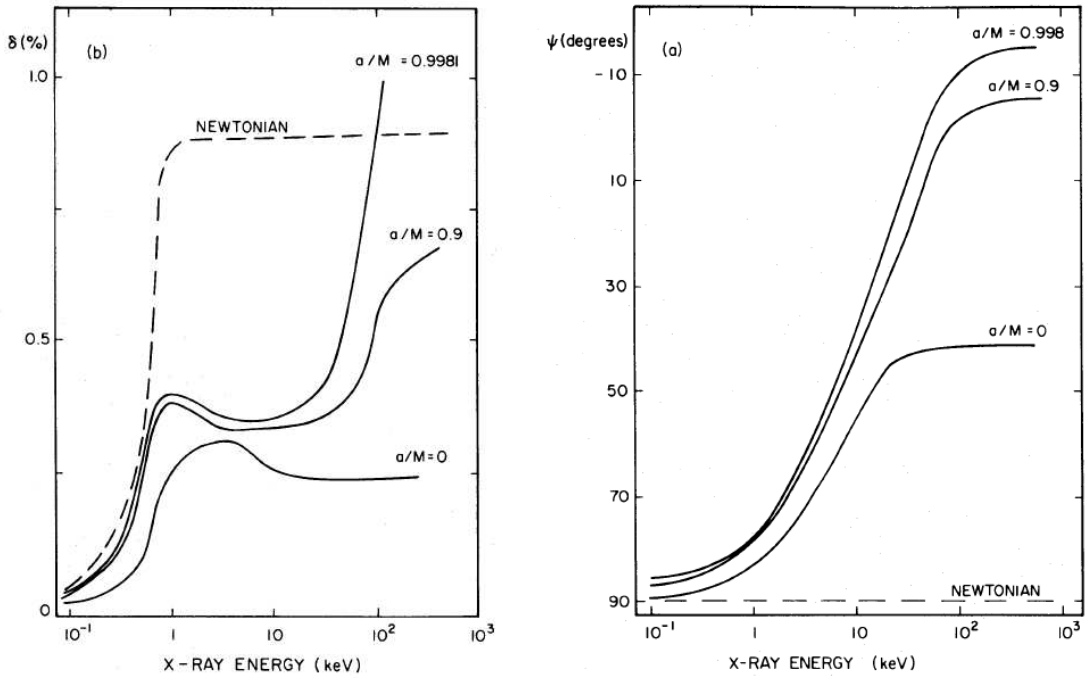

(a) **(b)**

Figure 1.23: Dependence of the degree (**a**) and angle (**b**) of polarization with energy including general relativistic effects in the case of thermal emission from accretion disks (Connors et al., 1980).

Consequently a depolarization of the emission with respect to the Newtonian case occurs (see Fig. 1.23a). A further effect is the continuous rotation of the plane of polarization with energy. In the general relativistic case, it is not forced parallel or perpendicularly to the disk by symmetry, the amplitude of the rotation depending on the intensity of the gravitational field. Higher energy radiation, produced closer to the black hole, is expected to be more affected by the stronger gravitational field and the total effect, reported in Fig. 1.23b, is a continuous rotation of the plane of polarization with energy.

A larger rotation is expected for a rotating black hole (Kerr case). The difference with a non-rotating black hole (Schwarzschild case) arises because in the former case the disk is truncated much closer to the black hole. The innermost stable circular orbit (ISCO) is $R_{ISCO}^{Schw} = 6GM/c^2$ for a Schwarzschild black hole, while in the case of a Kerr one $R_{ISCO}^{Schw} = GM/c^2$ (for a co-rotating disk). Hence in the latter case the high energy radiation is produced where a much stronger field is present.

The measurement of the rotation of the direction of polarization with energy could reveal if a rotating black hole is harbored in the system. This would confirm the indications currently coming from the study of the relativistic Fe K line profile (see for a review Miller, 2007). The observability of these effects in the context of the forthcoming missions will be discussed as part of this thesis in Chapter 6.

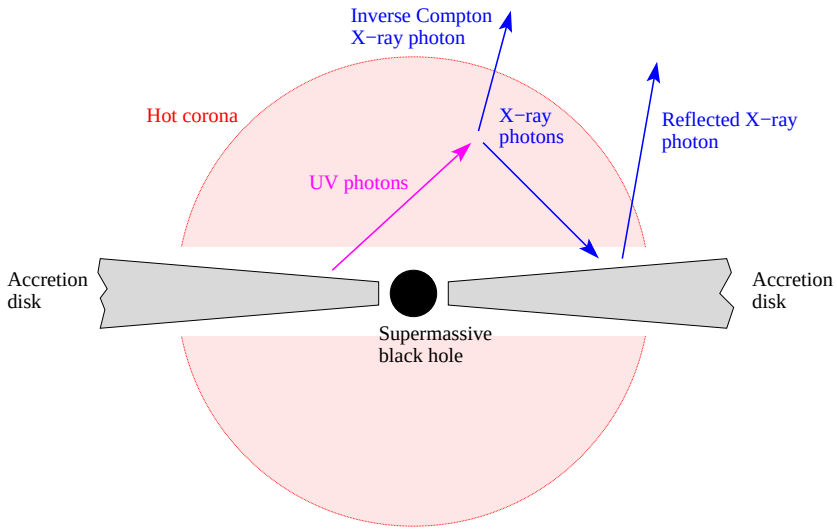

Figure 1.24: Geometry of the standard model of X-ray emission from AGNs.

1.4.7 Active galactic nuclei

Active galactic nuclei (AGNs) are galaxies in which the central core emits a large part of the total luminosity. The standard model (Urry and Padovani, 1995) advocates that these sources are powered by a supermassive black hole ($M \sim 10^6 - 10^{10}\ M_\odot$) surrounded by an accretion disk, which emits predominantly in UV. X-ray emission should be obtained by inverse Compton scattering of UV photons produced by the disk on a hot corona (Haardt and Maraschi, 1991). This in turn illuminates the accretion disk giving rise to fluorescence emission lines and Compton-reflected X-rays (see Fig. 1.24): at least the latter component should be highly polarized and detectable at energy above some keV, where the reflected emission typically dominates (Matt et al., 1993).

This standard picture is today challenged by the discovery that the temporal variation of the continuum component of MGC-6-30-15 is not correlated with that of the iron fluorescence line (Fabian et al., 2002; Vaughan and Fabian, 2004). To explain this puzzling result, Miniutti et al. (2003) proposed that the source which illuminates the accretion disk is moving along the spin axis of the black hole. The apparent luminosity of the continuum component will be strongly affected by the bending of light in the strong gravitational field of the black hole and its variation will be then increased by gravitational effects with respect to that of the iron line.

In the context of the lamp-post model, which assumes that the illuminating source is located at a height h above the disk (Martocchia and Matt, 1996), Dovčiak et al. (2004) calculated the polarization signature of the total emission, composed of the primary and reflected components, as a function of h and the viewing angle θ. These authors found that it is rather sensitive to the geometry of the model (see Fig. 1.25): consequently it could provide additional and invaluable informations to discriminate among the different models.

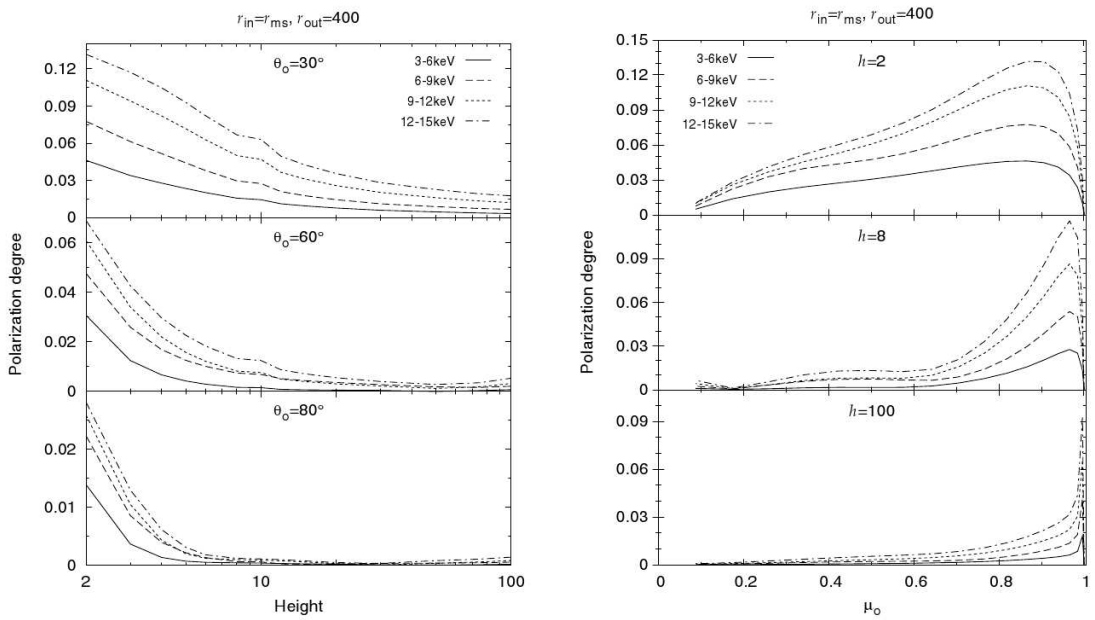

(a) **(b)**

Figure 1.25: Polarization expected in the lamp-post model as a function of the height of the illuminating source (**a**) and viewing angle, $\mu_0 = \cos\theta$ (**b**) at different energies.

1.4.8 Jets and blazars

Jets are collimated outflows of highly relativistic plasma which are commonly observed from Active Galactic Nuclei and a number of X-ray binaries (for a review, see Fender, 2006). They have been traditionally studied in the radio band, even if jets from AGNs have been also observed in X-rays since the advent of the *Einstein* observatory (Schreier et al., 1979). Instead X-ray emission from galactic jets is emerging only recently from both black hole (e.g. XTE J1550-564, Corbel et al., 2002) and neutron star binaries (e.g. Cir X-1, Heinz et al., 2007). The jets are characterized by bright spots, known as knots, with X-ray and radio emission well correlated (see Fig. 1.26).

Extragalactic jets are the most studied, since are generally brigher. Their emission from optical to radio is well described with synchrotron production, explaining their non-thermal spectra and the high degree of polarization which is often measured. In the case of the jet of the AGN M87, it reaches 65% (see Fig. 1.27a) and actually optical polarimetry has been successfully exploited to derive the magnetic field structure in the jet (see Fig. 1.27b).

Instead the origin of X-ray emission remains debated. Synchrotron scenario requires ultrarelativistic electrons ($\gamma > 10^7$), while inverse Compton on external radiation, such as the Cosmic Microwave Background, or synchrotron self Compton (SSC) may play a role. In the latter case low energy synchrotron photons are scattered by the same electrons which produced them.

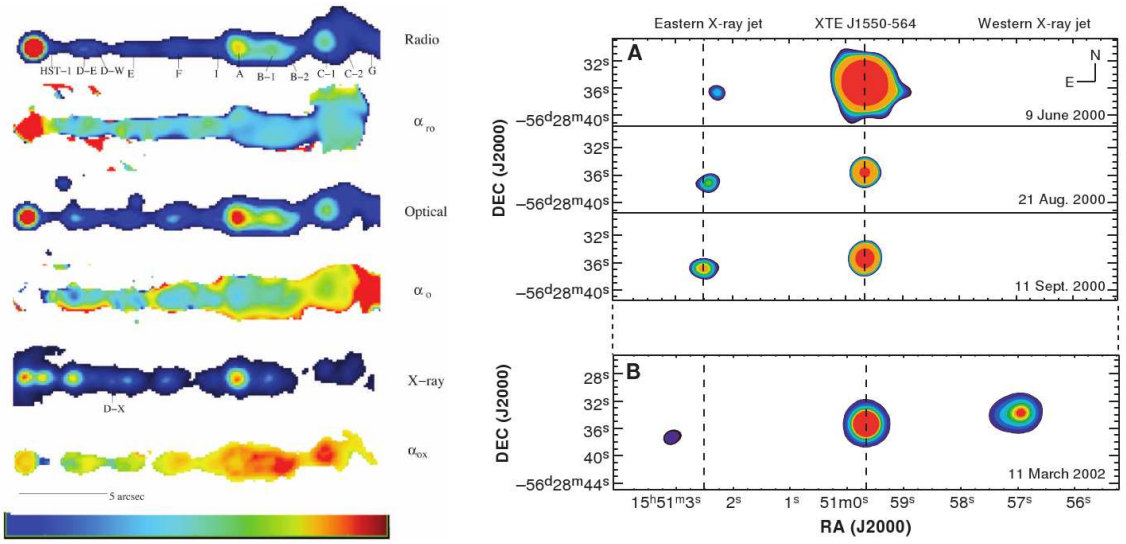

(a) **(b)**

Figure 1.26: (**a**) Jets of M87 and spectral index of the emission α at different energies (Perlman and Wilson, 2005). (**b**) Plasma ejection from the black hole binary XTE J1550-564 in X-rays (Corbel et al., 2002).

The knots could instead trace regions where electrons are accelerated (Wilson and Yang, 2002; Perlman and Wilson, 2005). Their radiative cooling time is much shorter than the time required to cover the distance at which the emission occurs and then in situ acceleration of electrons is required. A certain anticorrelation between X-ray emission and degree of polarization in optical suggests that the magnetic field in knots could be less uniform, possibly caused by a shock wave which accelerates electrons and reorders the magnetic field. X-ray polarimetry could test this hypothesis; moreover a certain degree of polarization is expected, at least in the SSC scenario, for jet emission (Celotti and Matt, 1994).

Blazars are a peculiar class of AGNs thought to be those sources in which the jet points toward the observer. Their luminosity and temporal variability (on time-scales down to a few hours, see Fig. 1.28) are amplified by special relativistic effects caused by the bulk motion of particles in the jets. The emission, observed from radio to γ rays, is characterized by a non-thermal and featureless spectrum.

At low energy, from radio to optical, the synchrotron emission should dominate and indeed large degrees of polarization are measured (Jannuzi et al., 1994). At higher energy two possible processes have been proposed, inverse Compton or SSC: in X-rays the emission is dominated by synchrotron or inverse Compton/SSC on the basis of the parameters of the jet. X-ray polarimetry could be exploited to distinguish between different processes, since a significant degree of polarization is expected in the case of SSC emission (Poutanen, 1994). Moreover it would be an important tool to select blazars among AGNs.

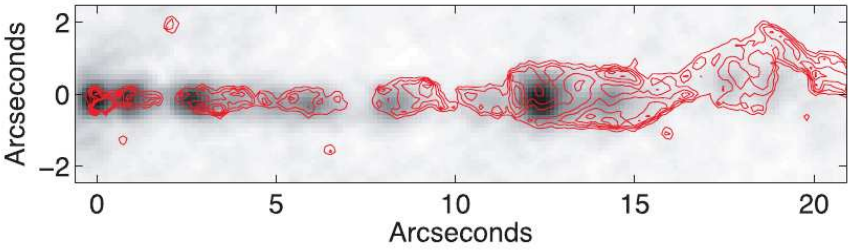

(a)

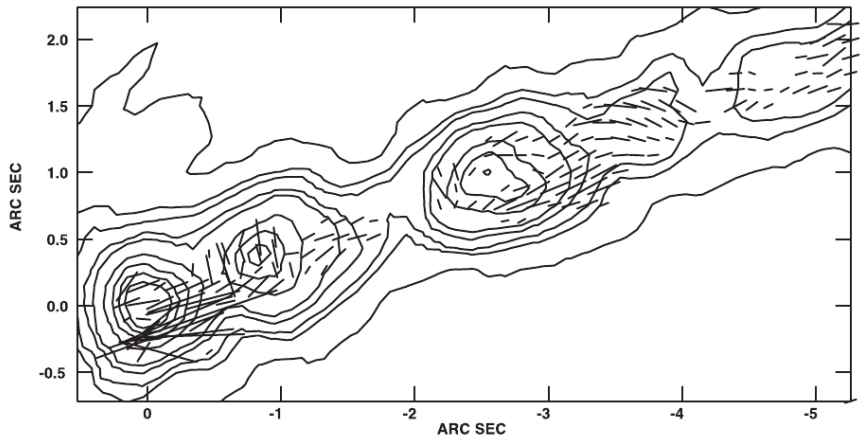

(b)

Figure 1.27: (**a**) X-ray flux (grey scale) and optical polarization (red contours) of the jet of M87. (**b**) Direction of the magnetic field as derived by the angle of polarization in optical light for the inner part of the jet of M87 (Perlman and Wilson, 2005).

1.4.9 The case of the molecular cloud Sgr B2

Sgr B2 is a giant molecular cloud located near our Galactic center, at projected distance of about 100 pc from Sgr A*. Since many years it has been proposed that Sgr B2, and other fainter molecular clouds near the galactic center (Murakami et al., 2001b), is actually reflecting X-ray radiation produced by a source external to the cloud (Sunyaev et al., 1993; Koyama et al., 1996). Its hard spectrum and prominent iron fluorescence line at 6.4 keV (see Fig. 1.29) support this hypothesis and the recent detection of a temporal variation of the morphology of the iron line from the cloud complex M0.11-0.11 also suggests this scenario (Muno et al., 2007).

A flare of an X-ray binary seems excluded by the high flux required. Murakami et al. (2001a) estimated a luminosity of the external source of $\sim 10^{39}\,(D/100\,\mathrm{pc})^2$, where D is its distance from the cloud center. The straightforward conclusion is that the flare which illuminated Sgr B2 in the past came from the supermassive black hole hosted in the center of the Galaxy, currently in a puzzling underluminous state. The flare faded

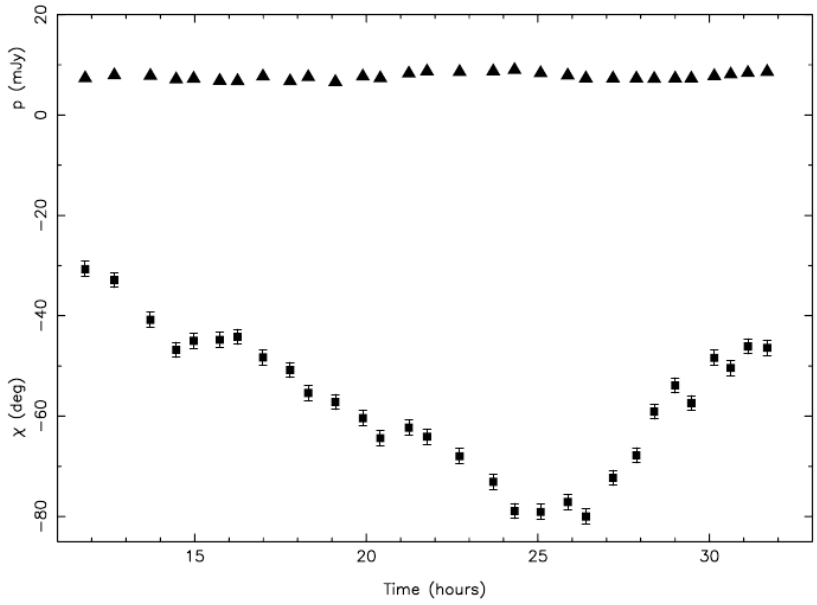

Figure 1.28: Temporal variability of the integrated polarized flux (top) and angle of polarization (bottom) of the blazar 0716+714 at cm wavelengths (Gabuzda et al., 2000).

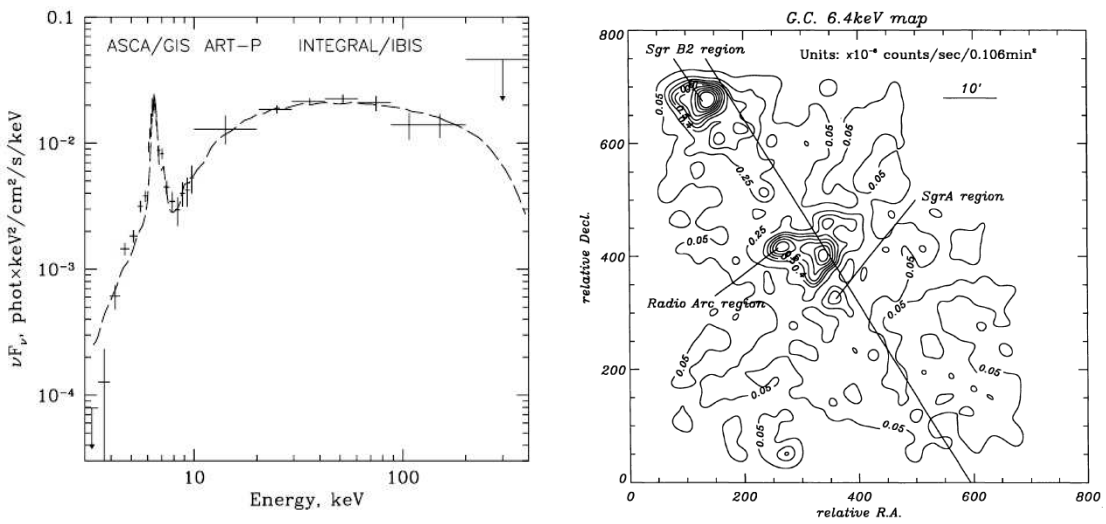

(a) **(b)**

Figure 1.29: (**a**) Spectrum of the Sgr B2 cloud obtained by combining data from *ASCA* (3-10 keV), *GRANAT* (10-20 keV) and *INTEGRAL* (20-400 keV) (Revnivtsev et al., 2004). (**b**) Brightness distribution of the 6.4 keV iron line measured by ASCA (Koyama et al., 1996).

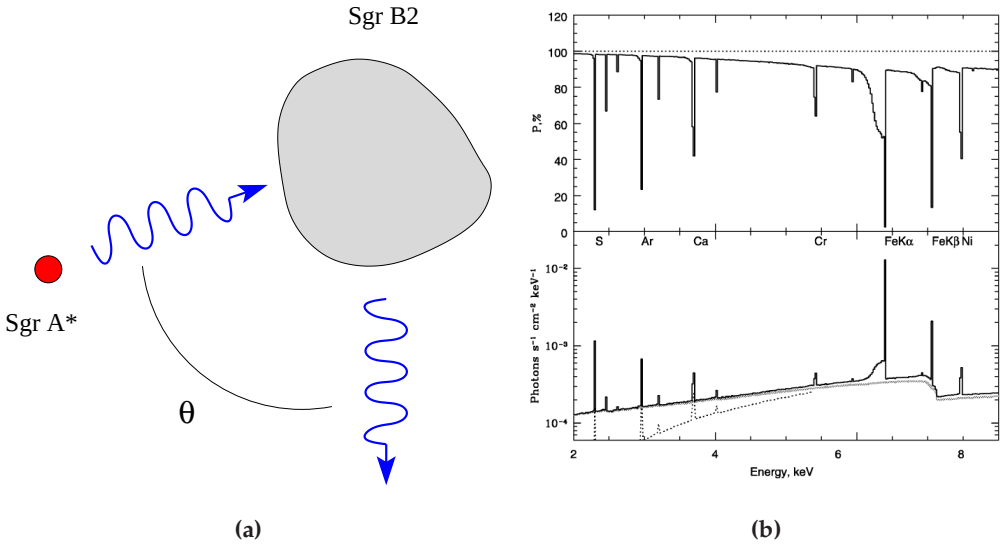

Figure 1.30: (**a**) Geometry of the reflection of the flare from Sgr A* on Sgr B2. (**b**) Expected degree of polarization (top panel) and flux (bottom panel) of the emission from Sgr B2. It's assumed $\theta \approx \pi/2$ (Churazov et al., 2002).

about 300 years ago, namely the projected light distance between Sgr A* and Sgr B2, and lasted a few years. It reached a 2-10 keV luminosity of $5{\times}10^{38}$erg s^{-1}, about 10^5 times the current value and similar to that of the low luminosity AGNs (Revnivtsev et al., 2004).

X-ray polarimetry will definitely answer to the question about the external source illuminating Sgr B2 in the past. Scattered photons acquire a high degree of polarization in the direction orthogonal to the scattering plane. If θ is the scattering angle (see Fig. 1.30a), the degree of polarization is:

$$\mathcal{P} = \frac{1-\cos^2\theta}{1+\cos^2\theta}. \tag{1.39}$$

In the case of Sgr B2, $\theta \approx \pi/2$ and the radiation should be almost completely polarized. Numerical simulations (Churazov et al., 2002) confirm that unpolarized fluorescence lines should be superimposed on a almost completely polarized continuum (see Fig. 1.30b). The measurement of the degree of polarization allows to derive the scattering angle θ and then the three dimensional position of Sgr B2 with respect to the illuminating source. This constrains their actual distance and then the time of the flare. Instead the direction of polarization is orthogonal to the scattering plane and then locates the angular position of the illuminating source.

1.4.10 Gamma ray bursts

Gamma ray bursts (GRBs) are short and intense transient sources which emit the large part of their energy in the hard X and γ rays (for a recent introduction, see Rosswog and Bruggen, 2007, cap. 7). Since their origin is extragalactic, they appear uniformly distributed in the sky and involve very high isotropic luminosities of the order

of $\sim 10^{51} \div 10^{54}$ erg, even if collimation (and hence lower luminosities) is suspected to occur. After the initial burst in γ rays (prompt emission), GRBs are often associated with rapidly fading sources (afterglow emission) which emit from X-rays to radio (Costa et al., 1997). They allow the fine positioning of the GRBs and the discovery of their parental galaxies.

Two populations of GRBs have emerged. The former is composed of bursts lasting more than a few seconds (long GRBs) and is associated with star forming galaxies and often to supernova explosions. The latter is instead characterized by short γ ray emission (less than a few seconds), harder spectra, closer galaxies of all types and involves luminosities smaller by several orders of magnitude. These two classes of GRBs reflect two different progenitors: the long ones should derive from the explosion of massive stars (Woosley, 1993; Paczynski, 1998), while the short GRBs are thought to be the result of the merging of binary systems with compact components like neutron stars and black holes (Gehrels et al., 2005),

Despite the different central engine, the mechanism for the production of a GRB should be similar for both classes. It should be based on fireballs, namely shells of electron-positron pairs which expand at ultra-relativistic velocities ($\Gamma > 100$) in a collimated outflow (jet). The prompt and afterglow emissions should be generated by the dissipation of the kinetic energy of the fireballs in shocks. In particular, the former emission should be the result of the interaction of faster and slower fireballs within the jet itself (internal shocks), while the latter should be produced by the deceleration of the fireball in the external environment (external shocks).

X-ray polarimetry will be a powerful probe to clarify the emission processes at work in GRBs (Lazzati, 2006). Afterglow emission may be dominated by synchrotron emission and then should be highly polarized, even if this picture is challenged by the small degree of polarization ($1 \div 3\%$) measured in optical afterglows (Covino et al., 1999; Wijers et al., 1999). Time variability of the degree and angle of polarization has been also reported (see Fig. 1.31, Greiner et al., 2003).

The study of the polarization of prompt emission will be an even better diagnostic tool (Granot, 2003). A strong magnetic field generated by the central engine could be essential to produce the relativistic jet which forms the fireballs: the common presence of a high polarization ($\mathcal{P} \sim 70\%$) could be the signature of synchrotron emission in a rather uniform magnetic field ("intrinsic" models, Granot and Königl, 2003; Lyutikov et al., 2003). A high degree of polarization (some tens of %) could be also obtained within "geometrical" models which instead advocate a random distribution of the magnetic field. Polarized radiation can derive from synchrotron emission in the (low) magnetic field generated by the shock or inverse Compton scattering: however this occurs only under favorable conditions, namely narrow fireballs and an appropriate line of sight near the edge of the jet (see Fig. 1.32). A null degree of polarization is instead expected when the observer is along the axis of the jet. A statistical study of the polarization of GRBs prompt emission could then discriminate between intrinsic and geometrical models.

Putative detections of a high degree of polarization in the GRBs prompt emission have been reported, even if not confirmed (Coburn and Boggs, 2003; Willis et al., 2005) or with low statistical significance (Kalemci et al., 2007; McGlynn et al., 2007).

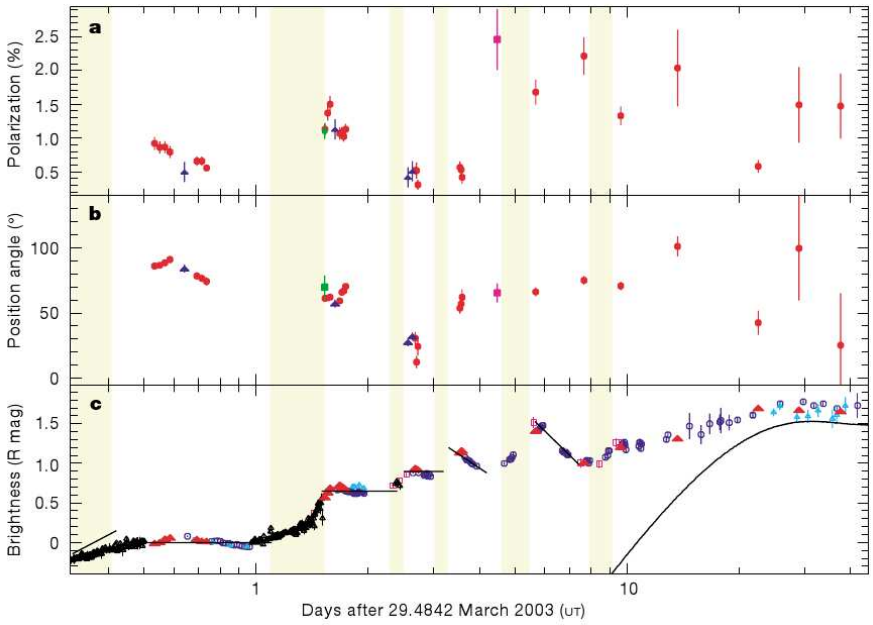

Figure 1.31: Optical afterglow of GRB030329. Temporal evolution of the degree (top panel) and plane of polarization (middle panel), together with the flux (bottom panel). The polarization reached ∼2.5% and did not correlate with the flux. The solid line in the bottom panel indicates the contribution of the supernova that accompanied the GRB which was negligible for the large part of the measurement (Greiner et al., 2003).

Since the large interest in this subject, the possibility to develop a photoelectric polarimeter with a large field of view to detect polarization of transient source like GRBs will be analyzed as a part of this thesis in Chapter 7.

1.4.11 Quantum gravity theories

The unification of the quantum mechanics with gravity is one of the most debated topic in theoretical physics. Unfortunately, even if a number of theories are under development, experimental feedback is still lacking. A possibility of testing these theories has emerged when it was realized that the vacuum would be dispersive in some approaches to quantum gravity (Amelino-Camelia et al., 1998). The difference between the velocity of photons at different energies causes a small delay in their arrival time and hence this effects should be observable as a lag between the emission of distant sources like gamma ray bursts at different energies. Even if this approach is promising, the timing capabilities of current experiments are not able to set constrains on different theories.

In the particular case of the Loop Quantum Gravity, high energy polarimetry is a much more sensitive probe. Gambini and Pullin (1999) found that in this theory vacuum results dispersive and birefringent. The latter property implies that the plane of polarization of linearly polarized radiation rotates as the photons propagate in vacuum. This

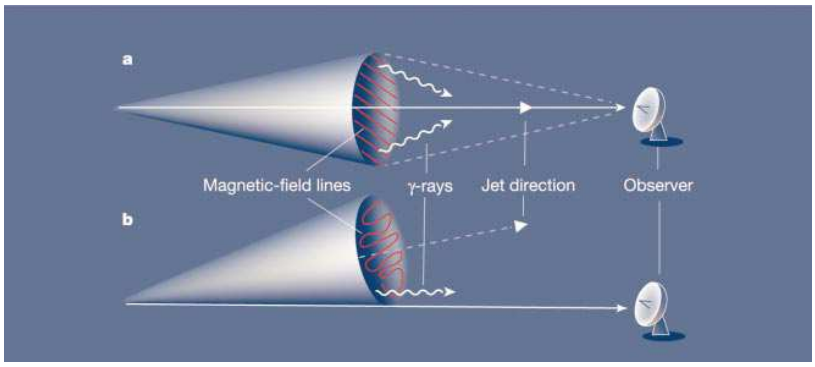

Figure 1.32: Models for the GRBs prompt emission. If synchrotron emission in an order magnetic field is involved, a high degree of polarization is expected for all viewing angles (**a**). Instead in the geometrical models (**b**) a high degree of polarization is expected only with particular favorable conditions because of the random magnetic field (Waxman, 2003).

effect is particularly sensitive because the even small wave retardation accumulated is to be compared with the wavelength of the radiation, which can be extremely small (λ a few Å for X-rays). In the case of dispersive theories the probe is much less sensitive since it is the path of photons during the expected retardation.

The rotation of the plane of polarization for linearly polarized photons propagating in vacuum can be easily calculated. The group velocity depends on the elicity, i.e. on the verse of the circular polarization of the radiation (Mitrofanov, 2003):

$$v_{\pm} = c\left[1 \pm \chi\left(\frac{E}{E_{QG}}\right)^{n}\right], \tag{1.40}$$

where χ is of the order of unity, $E_{QG} = \sqrt{\hbar c^5/G} \approx 10^{19}$ GeV is the Planck energy and n is the order of the theory, $n = 1$ for the simplest case of a linear dependence. The rotation of the angle of polarization is then:

$$\Delta\phi(E) \simeq \chi \frac{D_{ly}}{hc}\frac{E^2}{E_{QG}} \simeq \chi E_{keV}^2 D_{ly}, \tag{1.41}$$

where D_{ly} is the distance in light years.

Severe estimates on the parameter χ was derived by exploiting polarization of distance sources at high energy. Kaaret (2004) derived $\chi < 10^{-4}$ by the lack of rotation of polarization between optical and 2.6 keV in the emission of the Crab nebula ($\Delta\phi < 0.3°$). Maccione et al. (2008) obtained $\chi < 9 \times 10^{-9}$ from the measurement of the polarization of the Crab nebula in γ rays (Dean et al., 2008). Eventually Mitrofanov (2003) derived $\chi < 10^{-14}$ on the basis of the polarization of the GRB021206 (Coburn and Boggs, 2003), which was however not confirmed. These estimates can be even improved and the quadratic case can be tested by polarimetric observations of distant and highly polarized sources, like AGNs and blazars.

Chapter 2

The Gas Pixel Detector

Polarimeters based on Bragg diffraction or Thomson/Compton scattering have not been successful to measure the wealth of effects presented in Chapter 1. Even if refined experiments based on these techniques have been proposed (Weisskopf et al., 2006), the technological development today makes possible the construction of new devices based on photoelectric effect, the major advantages of using the latter technique being the larger efficiency and band pass. Photoelectric effect is the most probable interaction between X-rays and matter up to tens of keV and then can be effectively used where X-ray optics works better and fluxes of astrophysical sources are higher.

In this Chapter polarimeters based on photoelectric effect are described with a particular emphasis on the *Gas Pixel Detector* (GPD hereafter). It is one of the most advanced project in the field of X-ray polarimetry and its development is the overall aim of this thesis. Its design will be compared to alternative ones used in competitive instruments in Sec. 2.5

2.1 The photoelectric effect

Photoelectric effect consists in the absorption of a photon by an atomic electron with the subsequent ejection of the electron which is then called photoelectron. The energy E of the absorbed photon must be greater than the binding energy I to extract the electron, the latter being emitted with an energy $E_e = E - I$.

Photoelectric absorption strongly depends on the atomic number of the element Z. For the K-shell (Heitler, 1954):

$$\sigma_{ph}^{K} = 4\sqrt{2}\frac{8\pi r_0^2}{3} Z^5 \alpha \left(\frac{E}{mc^2}\right)^{7/2}, \tag{2.1}$$

where α is fine structure constant and r_0 is the classical electron radius. Even for low Z elements, photoelectric absorption is the most probable interaction between X-ray radiation and matter up to tens of keV. Actually the energy dependence of the interaction cross section of each shell and orbital can be described with better details (Yeh, 1993). However the Eq. 2.1 is suitable to drive the discussion to follow.

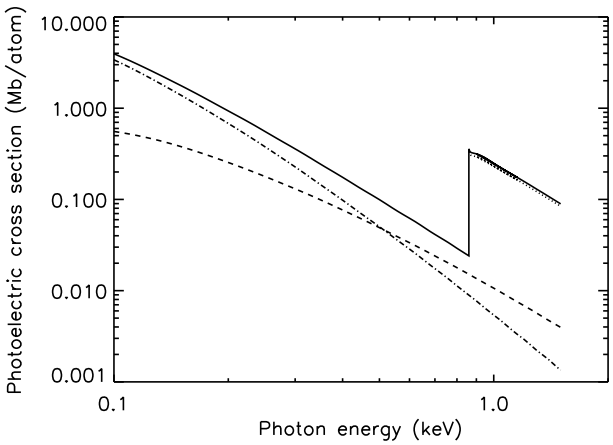

Figure 2.1: Dependence of total photoelectric cross section (solid line) with energy for neon. Contributions of 1s, 2s and 2p orbitals are dotted, dashed and dot-dashed respectively. Note the steep increase of the total cross section when the energy becomes higher than the binding energy of the orbital 1s (0.87 keV) (data from Yeh, 1993).

The cross section of the process is obtained by summing the contributions of each electron shell. When the energy is sufficient to extract electrons from inner shells, their contribution become predominant with respect to that of outer shells. Indeed above the binding energy the photoabsorption cross section of each orbital quickly decreases with energy, $\sigma_{ph}^{K} \sim E^{-7/2}$ (see Eq. 2.1). As a matter of fact in the X-rays only the inner shells are involved.

The emission of the photoelectron leaves a vacancy in an inner shell of the atom which is filled by an electron from an outer shell. The energy of the transition, which is almost equal to the binding energy of the emitted photoelectron since the binding energy of the external electron is negligible with respect to that of the inner shell, is released with the production of an X-ray photon (fluorescence emission) or the emission of a further electron, called Auger electron (Bambynek et al., 1972).

Fluorescence emission is less probable for low-Z elements (see Fig. 2.2). Photoabsorption is followed by the isotropic emission of an Auger electron at least in half the cases for $Z \lesssim 30$. An empirical fit to the fluorescence yield for the K-shell ω_K provides (Byrne and Howarth, 1970):

$$\omega_K = (1 + \alpha_K Z^{-m})^{-1}, \tag{2.2}$$

where $\alpha = (1.16 \pm 0.07) \times 10^5$ and $m = 3.36 \pm 0.02$. The values of ω_K for some elements are reported in Table 2.1. Values for L-shell are generally lower (Bambynek et al., 1972).

2.1.1 Dependence on the polarization

The direction of emission of the photoelectron brings memory of the linear polarization of the absorbed radiation since there is indeed a higher probability that it is emitted along the electric field of the photon. In the non-relativistic case ($E \ll m_e c^2$) and for

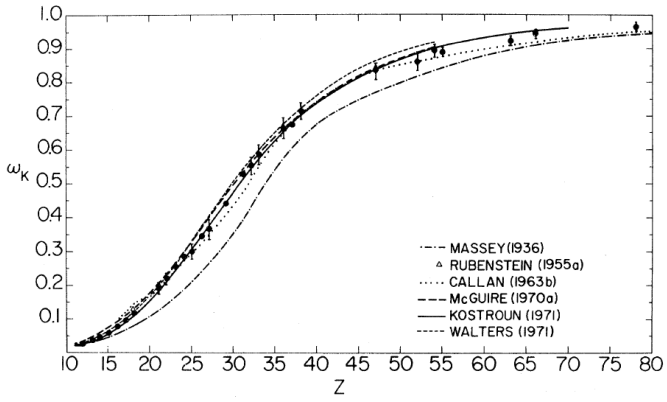

Figure 2.2: Theoretical and experimental K-shell fluorescence yield as a function of the atomic number Z (Bambynek et al., 1972).

Element	ω_K (%)	Element	ω_K (%)
Aluminum	3.8	Titanium	22.1
Silicon	4.3	Chromium	28.3
Chlorine	9.6	Iron	34.2
Argon	12.2	Krypton	66.0

Table 2.1: Fluorescence probability of K-shell for some elements (Bambynek et al., 1972).

energies far from the edge of the orbital the differential cross section of the K-shell can be written as (Heitler, 1954):

$$\frac{d\sigma_{ph}^{K}}{d\Omega} = r_0^2 \alpha^4 Z^5 \left(\frac{m_e c^2}{E}\right)^{\frac{7}{2}} \frac{4\sqrt{2}\sin^2\theta\cos^2\phi}{(1+\beta\cos\theta)^4}, \tag{2.3}$$

where β is the photoelectron velocity in unit of c, r_0 the classical electron radius, θ and ϕ are the angles that the direction of emission makes with the direction of the absorbed photon and its electric field[1] (see Fig. 2.3).

If incident photons are linearly polarized, the number of photoelectrons emitted per azimuthal angle is modulated as a $\cos^2$ function. The amplitude of this modulation is proportional to the degree of polarization and the maximum is in the direction of polarization. If photons are 100% polarized, the directions of emission are completely modulated and then photoabsorption from K-shell is a perfect analyzer for the polarization.

At low energy, $\beta \ll 1$, photoelectrons are emitted preferentially in the plane orthogonal to the incident direction of photons ($\theta = \pi/2$). However when $\beta \gtrsim 0.1$ (or $E \gtrsim 2.6$ keV) the most probable angle of emission can differ significantly from $\pi/2$ .The effect of this forward folding is of primary importance for the development of X-ray polarimeters with large field of view and will be investigated in detail in Chapter 7.

[1]Note that in Heitler (1954) the denominator of Eq. 2.3 is $(1-\beta\cos\theta)^4$ because of a different definition of the angle θ.

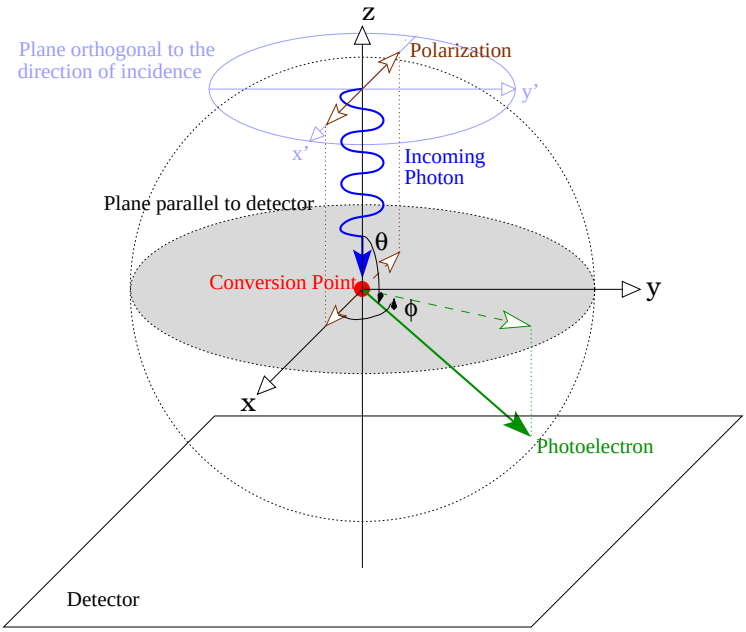

Figure 2.3: Definition of the angles of emission of the photoelectron.

When the photon is absorbed by an orbital which is not spherical, the modulation of the directions of emission of photoelectrons is no more complete. The angular dependence becomes (cf. Eq. 2.3, Ghosh, 1983):

$$\frac{d\sigma_{ph}}{d\Omega} = \frac{\sigma_{ph}^{tot}}{4\pi}\left[1 + \frac{b}{2}\left(\frac{3\sin^2\theta\cos^2\phi}{(1+\beta\cos\theta)^4} - 1\right)\right], \tag{2.4}$$

where σ_{ph}^{tot} is the total photoionization cross section and b is the asymmetry factor, which is less than 2 in general but equals 2 for spherical symmetric orbitals, 1s, 2s, etc. (see Fig. 2.4). In this case Eq. 2.3 is obtained.

The contribution of the photoelectrons extracted from not spherical orbitals is then not completely modulated even for 100% polarized photons. However in the X-ray range only the inner shells contribute to the absorption and when the energy of photons is higher than the binding energy of the K-shell, the contribution of the orbital 2p is in general negligible with respect to that of 1s and 2s (see Fig. 2.1). In the working configuration of current X-ray polarimeters this condition is always satisfied.

2.2 The GPD as an X-ray photoelectric polarimeter

The polarimeters based on the photoelectric effect basically reconstruct the direction of emission of photoelectrons, deriving the degree and the angle of polarization from the amplitude of the modulation and the peak of the histogram of the angles of emission

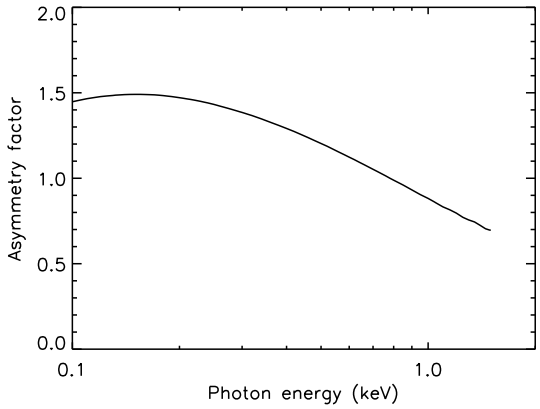

Figure 2.4: Asymmetry factor for the 2p orbital of neon (data from Yeh, 1993).

respectively. Current devices measure the path of photoelectrons in a gas since their range in semiconductors is too small to be resolved.

The Gas Pixel Detector (GPD hereafter) has been developed by INFN of Pisa and INAF/IASF of Rome. Its operation is sketched in Fig. 2.5 (Costa et al., 2001). An X-ray photon is absorbed in a gas cell and a photoelectron is emitted with more probability in the direction of its electric field. As the electron propagates in the gas, it loses energy by ionization and produces electron-ion pairs (primary pairs). They drift and are amplified in an electric field generated by a Gas Electron Multiplier (GEM, Sauli, 1997) which produces the secondary pairs eventually collected by a fine sub-divided pixel detector. In the case of the low-Z atoms used in these devices, the emission of a photoelectron is very likely followed by the ejection of an Auger electron. The latter must be distinguished because its direction of emission doesn't contain any information about the initial polarization.

The instrument basically measures the projection of the photoelectron track on the plane of the detector and it is of fundamental importance that it is finely resolved. The initial direction of emission is indeed confused by scatterings on atomic nuclei which isotropize the propagation of photoelectrons. Moreover the diffusion of primary and secondary pairs in the drift electric field smears the track.

The information about polarization is codified only in the first part of the path, which must be distinguished from the end of the track to retrieve the direction of emission of the photoelectron correctly. This can be done on the basis of the density of the charge collected. The energy loss by ionization of photoelectrons in the gas cell is indeed inversely proportional to their energy (Longair, 1992):

$$-\frac{dE_e}{dx} = \frac{e^4 nZ}{8\pi\epsilon_0^2 mc^2\beta^2}\left[\ln\frac{m\gamma^2c^2\beta^2E_{\max}}{2I^2} - \left(\frac{2}{\gamma}-\frac{1}{\gamma^2}\right)\ln 2 + \frac{1}{\gamma^2} + \right.$$
$$\left. + \frac{1}{8}\left(1-\frac{1}{\gamma}\right)^2\right] \propto \frac{1}{\beta^2} \propto \frac{1}{E_e}, \qquad (2.5)$$

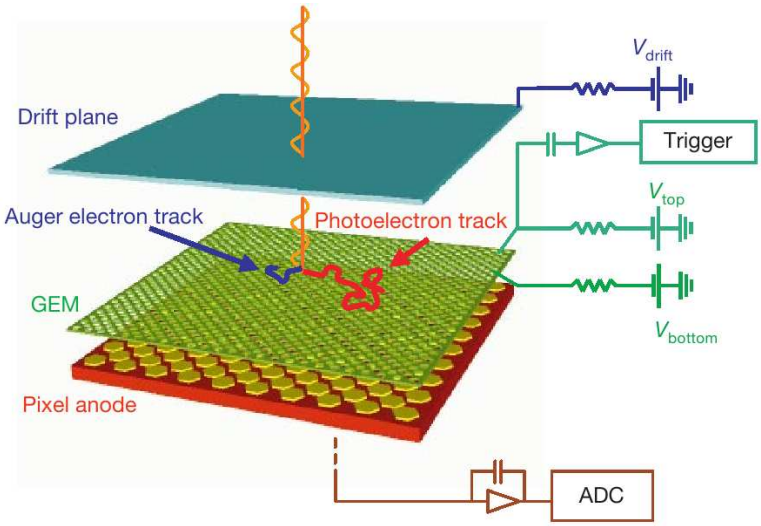

Figure 2.5: Principle of operation of the Gas Pixel Detector. The direction of emission of the photoelectron carries a significant memory of the polarization of the absorbed photon. It is reconstructed by collecting the charges produced by the propagation of the photoelectron in a gas (Costa et al., 2001).

where n is the number density of atoms in the gas and Z their atomic number, γ the Lorentz factor of the photoelectron, $E_{\max}$ the maximum energy which can be transferred to an atomic electron and I the ionization potential of the atoms. Photoelectrons are more energetic in the initial part of the path in the gas and consequently energy losses are smaller. Instead a peak in the charge distribution (Bragg peak) is present in the final part of the tracks and corresponds to the point where photoelectrons are eventually stopped and absorbed.

An example of measured photoelectron tracks is reported in Fig. 2.6. The reconstructed direction of emission and the estimated absorption point of the photon is derived with an automatic algorithm (see Sec. 2.2.1). The high spatial resolution reached with the current detector allows to clearly resolve the tracks despite they are heavily affected by nuclear scatterings. The peak in the charge distribution at the end of the track corresponds to the point where the photoelectron is absorbed. Note however that another smaller peak is present at the beginning of the track, near the estimated absorption point of the photon. This corresponds to the absorption of the Auger electron which must be distinguished since its direction of emission doesn't contain any information about the polarization.

In the working condition of photoelectric polarimeters the photoelectron must have an energy higher than Auger electron so that the former has a longer track and can be easily distinguished. Moreover in this case the peak associated to the absorption point of the Auger electron is less significant with respect to the Bragg peak, allowing to recognize the final and the initial part of the track. The condition that the energy of the photoelectron must be higher than that of the Auger electron corresponds to a low energy limit

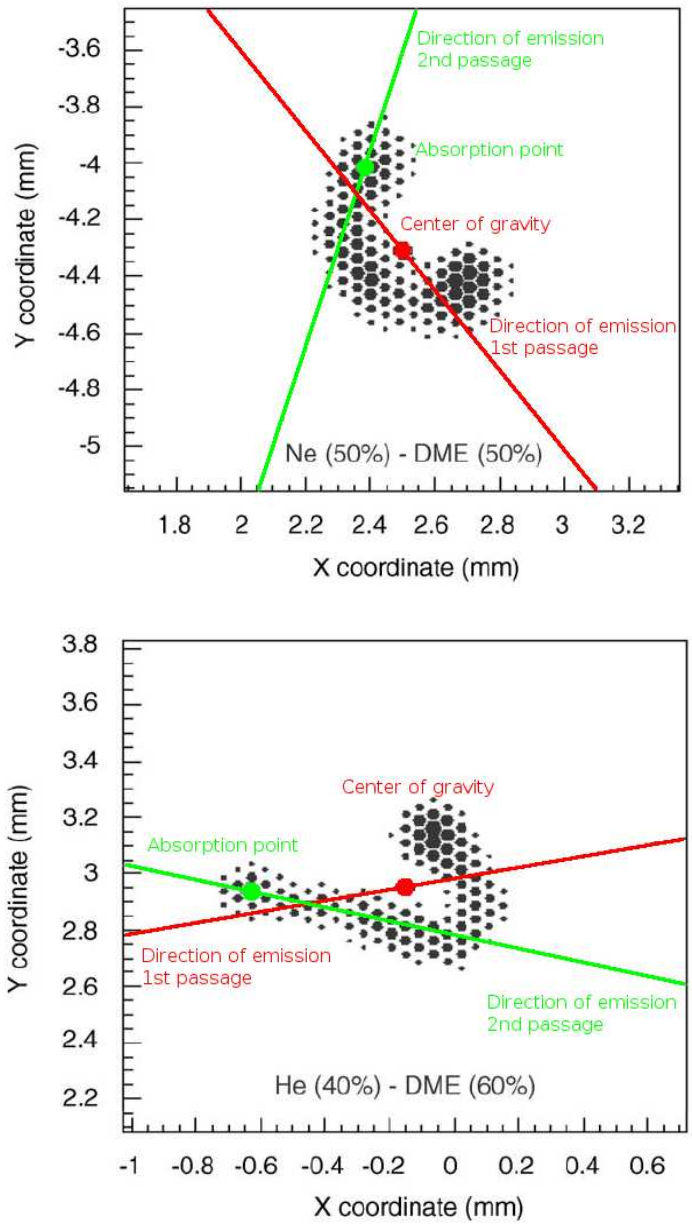

Figure 2.6: Example of measured photoelectron tracks at 5.41 keV in a He-DME mixture. Red line indicates the direction of emission reconstructed by the first part of the algorithm, while the green one indicates the refined direction of emission together with the estimated absorption point(see Sec. 2.2.1). The area of the pixels is proportional to the charge collected (Bellazzini et al., 2006b).

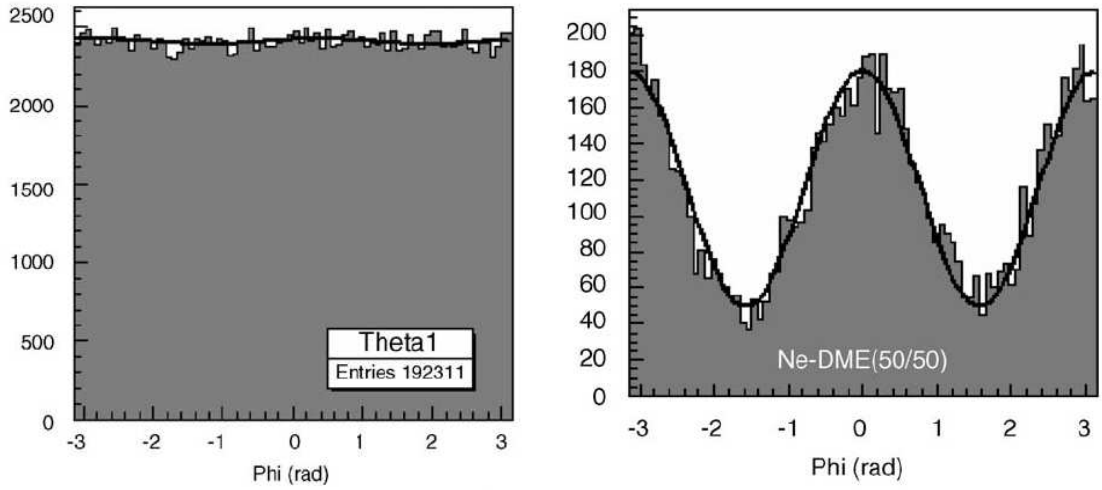

(a) **(b)**

Figure 2.7: (**a**) Histogram of directions of emission of photoelectrons measured at 5.9 keV with a radioactive Fe^{55} source. (**a**) Modulation measured for 6.4 keV polarized photons (Bellazzini et al., 2006b).

which is equal to about twice the binding energy of the photoelectron which is expected to be emitted.

Two examples of the response of the GPD for unpolarized and polarized radiation are reported in Fig. 2.7. The histogram of the directions of emission of photoelectrons is unmodulated for unpolarized radiation (see Fig. 2.7a); instead a large modulation appears when polarized photons are absorbed (see Fig. 2.7b). Note that a small modulated component is measured even in former case, since the presence of a $\cos^2$ modulation is a definite positive quantity, i.e. a modulated signal is always measured for statistical reasons. A large number of photons (several tens of thousands) is then required to perform an accurate polarimetric measurement (see Sec. 2.4).

The capability to reconstruct the absorption point with a resolution of the order of 100 μm makes the GPD a good imaging device (see Fig. 2.8). Moreover it is basically a proportional counter and hence can provide even spectroscopic and temporal informations. The GPD is then sensitive to all properties of photons, i.e. polarization, direction, arrival time and energy. With respect to the classical techniques, the GPD doesn't need to be rotated to measure the polarization or to reduce systematic effects and this is a great advantage for the use on-board space satellite (see Sec. 5.2).

2.2.1 The reconstruction algorithm

The GPD provides the projection of the track on the plane of the detector which is analyzed by an automatic algorithm to derive the projected direction of emission of the photoelectron and the absorption point of the photon. The algorithm is divided into two

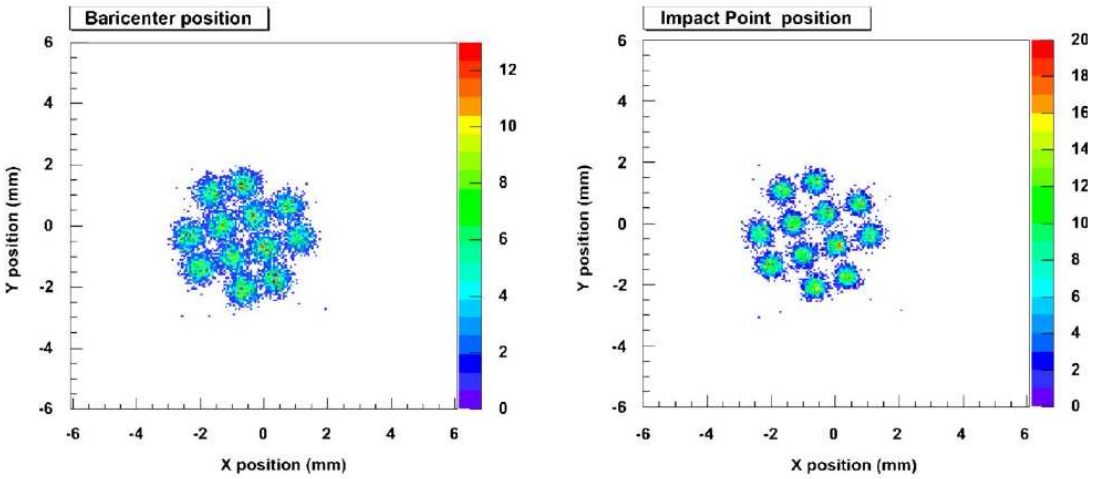

(a) (b)

Figure 2.8: Imaging capabilities of the GPD. In (**a**) the image is reconstructed with the center of mass of each track, while in (**b**) the absorption point derived by the algorithm of analysis is used. The holes have a diameter of 0.6 mm and a spacing of 2 mm (Bellazzini et al., 2006b).

main steps. The first analyzes the entire track to derive a first estimate, while the second one is repeated only in the first part which is more sensitive to polarization since is less affected from scatterings (Bellazzini et al., 2003).

The point of interaction is initially calculated as the center of gravity of the charge distribution:

$$x_c = \frac{\sum_i Q_i \, x_i}{\sum_i Q_i} \tag{2.6}$$

$$y_c = \frac{\sum_i Q_i \, y_i}{\sum_i Q_i} \tag{2.7}$$

where x_i and y_i are the coordinates of the hit pixels and Q_i the charge collected.

The linear development of the track in a certain direction ℓ characterized by an angle Φ with respect to the x-axis can be described by the second moment of the charge distribution, $M_2(\Phi)$. It is the (quadratic) sum of the distance of the pixels from the center of mass, projected on the direction ℓ and weighted with the charge collected in each pixel. Its definition is then:

$$M_2(\Phi) = \frac{\sum_i Q_i \, x_i'^2}{\sum_i Q_i} = \frac{\sum_i Q_i \left[(x_i - x_c)\cos\Phi + (y_i - y_c)\sin\Phi\right]^2}{\sum_i Q_i}, \tag{2.8}$$

where x_i' are the abscissas of the pixels in the $x'y'$ frame of reference, rotated with respect to xy of the angle Φ (see Fig. 2.9). Hence in this case x' corresponds to the ℓ direction.

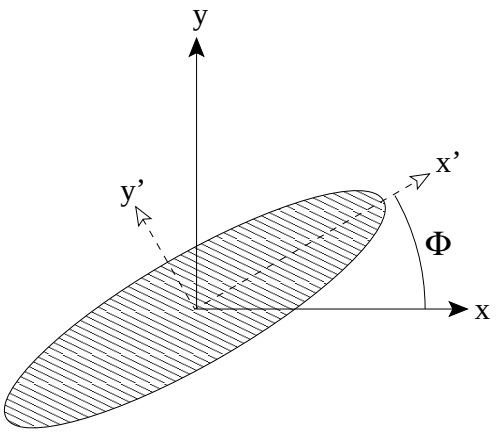

Figure 2.9: Frames of reference for the calculation of the second moment of the photoelectron tracks. Note that they are assimilated to elliptical distributions. Frames are centered in the center of gravity of the tracks.

The angle $\Phi_{\max}$ which maximizes the second moment provides the first estimate of the direction of emission of the photoelectron. Its value can be found within the critical points of the function $M_2(\Phi)$ and one of these points is Φ_0:

$$\frac{dM_2(\Phi)}{d\Phi} = 0 \implies \Phi_0 = -\frac{1}{2}\arctan\frac{2\sum_i Q_i\ (x_i - x_b)\,(y_i - y_b)}{\sum_i Q_i\left[(y_i - y_b)^2 - (x_i - x_b)^2\right]}. \tag{2.9}$$

The angle Φ_0 spans between $-\pi/4$ and $\pi/4$ and corresponds to the maximum or to the minimum value of the second moment which falls in this angular range. The value of $M_2(\Phi_0)$ is then compared to that in the orthogonal direction $M_2(\Phi_0 - \pi/2)$ to distinguish if Φ_0 corresponds to the maximum or to the minimum of $M_2(\Phi)$:

$$M_2(\Phi_0) = \frac{\sum_i Q_i\left[(x_i - x_b)\cos\Phi_0 + (y_i - y_b)\sin\Phi_0\right]^2}{\sum_i Q_i} \tag{2.10}$$

$$M_2(\Phi_0 - \frac{\pi}{2}) = \frac{\sum_i Q_i\left[-(x_i - x_b)\sin\Phi_0 + (y_i - y_b)\cos\Phi_0\right]^2}{\sum_i Q_i} \tag{2.11}$$

Note that if Φ_0 corresponds to the minimum value of the second moment, $\Phi_0 - \pi/2$ is the angle which maximizes $M_2(\Phi)$ and vice versa. Indeed the use of the second moment assimilates the track of the photoelectron to an ellipsoid and the maximum and minimum second moments, $M_2^{\max}$ and $M_2^{\min}$ respectively, brings memory of its major and minor axes.

The ratio between $M_2^{\max}$ and $M_2^{\min}$ provides the degree of asymmetry ϵ of the charge distribution. A higher value of ϵ means that the track is more developed in a certain direction. Since tracks are easier reconstructed when the asymmetry is higher, ϵ is used as a quality parameter for the possible selection of the data. On the contrary photoelectrons emitted nearly orthogonally to the detector or a very low energy produce round tracks.

These don't contain any asymmetry and then polarimetric information at this stage of the analysis.

The absorption of the photoelectron causes a peak in the charge distribution since the energy loss is inversely proportional to the energy (see Eq. 2.5). The initial part is then distinguished on the basis of the asymmetry of the charge density, which is expressed with the third moment of the distribution calculated in the direction $\Phi_{\max}$:

$$M_3 = \frac{\sum_i Q_i \, x_i'^3}{\sum_i Q_i} = \frac{\sum_i Q_i \left[(x_i - x_b)\cos\Phi_{\max} + (y_i - y_b)\sin\Phi_{\max}\right]^3}{\sum_i Q_i}. \tag{2.12}$$

The sign of the third moment is positive if the Bragg peak is on the right with respect of the center of mass, while is negative if it is on the left. The initial part of the track is then on the left or on the right of the center of mass if $M_3 > 0$ or $M_3 < 0$ respectively.

The refined estimate of the absorption point is calculated as the center of mass of a subset of the hit pixels which fulfil the two following conditions. The pixels must be on the other side with respect to the Bragg peak and then:

$$\frac{x_i'}{M_3} < 0 \implies \frac{(x_i - x_c)\cos\Phi_{\max} + (y_i - y_c)\sin\Phi_{\max}}{M_3} < 0. \tag{2.13}$$

The second condition is that the distance d_{cm} from the center of mass, normalized to the maximum second moment, must be between a small and a large radius. Then $r_{\min} < d_{cm} < r_{\max}$ where:

$$d_{cm} = \sqrt{\frac{(x_i - x_c)^2 + (y_i - y_c)^2}{M_2^{\max}}}. \tag{2.14}$$

This cut allows to select only the initial part of the track since it excludes its central part and the Auger electron when it is not emitted parallel to photoelectron. Note that the distance between the absorption point and the center of mass depends on the linear development of the track which is related to the maximum second moment. The normalization with $M_2^{\max}$ allows to remove the effect of the length of the track (and so of the energy of the absorbed photon) on d_{cm}. In this case the values of $r_{\min}$ and $r_{\max}$ can be derived from Monte Carlo simulations (see Sec. 2.2.2) for each mixture and they don't depend on the energy.

The center of mass of the pixels which fulfil these two conditions provides the impact point, namely the refined estimate of the absorption point of the photon. The direction of emission is re-calculated by means of the same procedure described above based on the second moment but in this case the significance of the first part of the track is increased. The charge collected in each hit pixel is weighted on the basis of the distance d_{pi} from the impact point, the weight $\mathcal{W}(d_{ip})$ being:

$$\mathcal{W}(d_{ip}) = \exp\left(-d_{pi}/w\right), \tag{2.15}$$

where w is a constat for each mixture as derived from Monte Carlo simulations.

The reconstruction algorithm allows to derive the direction of emission and the absorption point with good effectiveness until the tracks are well resolved (see Fig. 2.6 and

Fig. 2.8). Its complexity is not a problem for on-ground data analysis but it requires some resources if track reconstruction must be performed in real-time on-board space satellites. This problem will be faced up in Chapter 6.

2.2.2 The Monte Carlo software

An important role in the development of the GPD has been held by a Monte Carlo software. Simulations have driven the optimization of the reconstruction algorithm and the choice of the mixture filling the gas cell, allowing to readily study different configurations so that only the most interesting ones are eventually tested with measurements.

The Monte Carlo software is basically exploited in two contexts in this thesis. The former is the calculation of the high energy response of the GPD (see Chapter 8) and hence in this case the Monte Carlo software is used as a tool for investigating the behavior of the GPD with new mixtures. The Monte Carlo results are also exploited to derive the sensitivity of GPD for astrophysical contexts which drives the design and the scientific objectives of the missions presented in Chapter 6 and eventually proposed to Space Agencies.

The validation of the Monte Carlo results with measurements is then of primary importance but it has been traditionally verified only at relatively high energy, namely above 5.41 keV. The recent availability of Bragg calibration sources (see Chapter 3 and Chapter 4) allows the measurement of the GPD sensitivity in the range of maximum sensitivity, i.e. at a few keV. The comparison between measurements and expected results ultimately validates the Monte Carlo simulations as a reliable tool for the study of the GPD (see Chapter 5).

The Monte Carlo software accurately describes the operation of the GPD. The depth in the gas cell where photons are absorbed is calculated from the photoabsorption cross section of the specific mixture, allowing for the study of the effect of diffusion in the drift field. Photoelectrons are emitted with an angle θ and ϕ according to the distribution (cf. Eq. 2.4):

$$f(\theta,\phi) \propto \sin\theta \cdot \frac{d\sigma_{ph}}{d\Omega}. \tag{2.16}$$

The factor $\sin\theta$ takes into account that the element of solid angle must be expressed in function of $d\theta$ and $d\phi$, $d\Omega = \sin\theta d\theta d\phi$. Only the angular dependence is taken from Eq. 2.16 and then:

$$f(\theta,\phi) = \sin\theta\left[1+\frac{b}{2}\left(\frac{3\sin^2\theta\cos^2\phi}{(1+\beta\cos\theta)^4}-1\right)\right]. \tag{2.17}$$

The direction of incidence of photons and the polarization can be freely changed (Muleri, 2005) and then the effects of inclined penetration in the gas cell can be studied (see Chapter 7).

The absorption from the shells K (1s) and L (2s and 2p) is considered and the relative probability of interaction of each shell is reported in Table 2.2 for some elements. Note that the contribution of the orbital 1s, which is completely modulated for polarized

Element	E_{1s} (keV)	P_{1s} (%)	P_{2s} (%)	P_{2p} (%)	b
Carbon	0.284	95.2	4.2	0.6	0.958
Oxygen	0.543	94.1	4.3	1.6	0.955
Neon	0.870	93.3	4.2	2.5	0.955
Argon	3.206	92.0	5.1	2.9	0.820

Table 2.2: Relative probability of photoabsorption among inner atomic orbitals for some elements. b is the asymmetry parameter of the orbital 2p. Data are evaluated at the energy of the edge of the K-shell from the fit of data presented by Yeh and Lindau (1985) and Yeh (1993).

photons, is always predominant. The asymmetry parameter b of the orbital 2p is also reported in the Table. Both b and the probabilities of absorption are calculated at the energy of the K-shell E_{1s} of each element. These values are assumed also at energies above E_{1s} since actual data are not available in the literature.

The propagation of photoelectrons and Auger electrons is computed on the basis of the algorithm developed by Joy (1995). It assumes that the path of electrons is scattered only by elastic coulombic collisions on atoms, while inelastic scatterings are neglected. Their probability is inversely proportional to the energy loss ΔE_e and produce deflections of the order of $\Delta E_e/E_e$ (Egerton, 1986). Hence only small energy losses with consequently small deflections are probable.

The distance between two subsequent collisions is computed from the mean free path in the gas, λ:

$$\lambda = \frac{A}{N_A\ \rho\ \sigma_{scat}}, \tag{2.18}$$

where A is the atomic weight of atoms, ρ the density of the gas and N_A the Avogadro constant. The cross section for scattering σ_{scat} is evaluated from the expression:

$$\sigma_{scat} = 4.7 \cdot 10^{-18} \frac{Z^{1.33} + 0.032Z^2}{E_e + 0.0155Z^{1.33}\ E_e^{0.5}} \frac{1}{1 - 0.02Z^{0.5}e^{-u^2}}, \tag{2.19}$$

where $u = \log_{10}(8E_eZ^{-1.33})$. The Eq. 2.19 is a parameterization of the Mott cross section (Browning, 1991) and is preferred with respect to the Rutherford expression since the former provide a better approximation for $Z \gtrsim 30$ and $E_e \lesssim 20$ keV.

Photoelectrons propagate in a mixture in the case of GPD and then its composition is used to calculate an average mean free path $\bar{\lambda}$, the probability of a collision after a distance d being $P = \exp\left(-d/\bar{\lambda}\right)$. A value of d with this distribution is derived from:

$$d = -\bar{\lambda}\ln(\text{RND}), \tag{2.20}$$

where RND is a random number between 0 and 1. Eventually the element of the mixture which actually interacts with the electron is selected on the basis of the relative values of the cross section.

The direction of emission after the collision is characterized with respect to the incident one with the angle of scattering ψ and the azimuthal angle ω (see Fig. 2.10). The

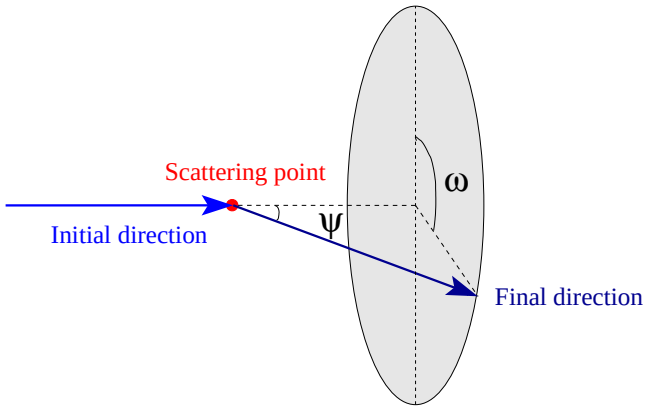

Figure 2.10: Geometry of the elastic scatterings.

latter is uniformly distributed between 0 and 2π while the angle ψ is obtained from the expression (Joy, 1995):

$$\cos\psi = 1 - \frac{2\,\alpha_{screen}\,(\mathrm{RND})^2}{1+\alpha_{screen}-\mathrm{RND}}, \tag{2.21}$$

where RND is a random number and $\alpha_{screen} = 3.4\times10^{-3}E^{0.67}/E$ is the Rutherford screening factor. The Eq. 2.21 provides a good approximation for the angular distribution of scattered electrons except for very low energy ($E_e \lesssim 1$ keV). Below this threshold the full tabulated Mott cross-section should be used but this is neglected in our code. The path of an electron below 1 keV is very short ($< 10\ \mu m$) and it would not be resolved by the instrument in a standard mixture.

Electrons are assumed to lose continuously their energy between a collision and the subsequent one. Energy losses are uniformly distributed along the path between interactions and include ionization and inelastic scatterings, expressed with a semi-empirical modified Bethe formula (Joy and Luo, 1989):

$$\frac{dE_e}{d\xi} = -78500\frac{Z}{A\,E_e}\ln\left(\frac{1.166\,(E_e+0.85\,J)}{J}\right), \tag{2.22}$$

where ξ is the product of path of electron and the density of the mixture. The second term in the logarithm corrects the behavior of Bethe formula below a few keV. The value of the mean ionization potential J represents the effective energy loss per interaction and its dependence with Z is parameterized as (Berger and Seltzer, 1964):

$$J = \left[9.76\,Z + \frac{58.5}{Z^{0.19}}\right]\ 10^{-3}\ \mathrm{keV}. \tag{2.23}$$

Energy losses along the path are divided by the average ionization potential, providing the mean number of primary electron-ion pairs generated along the path. Their number is eventually Poisson-distributed.

The position of arrival on the GEM is smeared by diffusion of primary pairs during the drift. The linear blurring is gaussian-distributed with a standard deviation (Sauli, 1977):

$$\sigma_{diff} = \sqrt{Dt}, \tag{2.24}$$

where D is the diffusion coefficient, which for electrons depend on the electric field $\vec{E}$, and t is the time of diffusion. This formula is parameterized as:

$$\sigma_{diff} = \frac{D(|\vec{E}|)\sqrt{L}}{\sqrt{p}}, \tag{2.25}$$

where $D(|\vec{E}|)$ is the diffusion coefficient and L the distance between the point where pairs are generated and the GEM. The diffusion coefficient is of the order of $100\mu\text{m}/\sqrt{1\text{cm}}$, depending on the gas mixture. The pressure of the mixture p is made explicit to scale the diffusion for mixtures at different pressures.

As electrons from the primary pairs arrive to GEM, they are multiplied and collected by the hexagonal pixels of the chip, their number being Poisson-distributed. The diffusion from the GEM to the collecting plane of the detector is neglected as well as a possible loss of the charges which hit the GEM. In practice it is assumed that the multiplication by the GEM, the loss of a fraction of the charges and the drift from the GEM to the metal pads of the chip don't modify the shape of the track.

2.2.3 The role of the gas mixture and the energy range of the GPD

Even if the GPD can resolve the track of photoelectrons, it is basically a very sophisticated version of a conventional proportional counters which have a long history of successful use in space satellites. The gas mixture filling the detector is however of fundamental importance to maximize the polarimetric performances and to avoid its long term pollution in space.

The overall sensitivity of the GPD to polarization depends both on its efficiency and on the capability to reconstruct correctly the directions of emission of photoelectrons (see Sec. 2.4). The former depends on the probability of photoelectric absorption and strongly varies with the mean atomic number of the mixture, $\sigma_{ph}^{K} \sim Z^5$ (cf. Eq. 2.1). The efficiency increases with Z but also with the pressure and the depth of the gas cell since they increase the effective thickness of the mixture.

At the contrary the reconstruction of the initial direction of photoelectrons works worse if these parameters are increased. The thickness of the cell should be minimized to reduce the diffusion of primary pairs as they drift toward the detector in the electric field of the GEM. The diffusion can be reduced by increasing the pressure of the mixture as $D \sim 1/\sqrt{p}$ but this also decreases the range of photoelectrons, the tracks being consequently shorter and correctly reconstructed with more difficulty. Eventually a higher mean atomic number of the mixture increases the scattering cross section of photoelectrons. Indeed for the elastic scattering on atoms with atomic number Z (Rutherford

scattering, see for example Povh et al., 2008):

$$\frac{d\sigma_{Ruth}}{d\Omega} = \frac{\left(Ze^2\right)^2}{\left(4\pi\epsilon_0\right)^2 \left(4E_e\right)^2 \sin^4\left(\psi/2\right)}, \tag{2.26}$$

where ψ is the scattering angle (see Fig. 2.10).

A trade-off among the composition, the pressure and the thickness of the gas cell must then be reached to obtain the best polarimetric performances.

The gas mixture is generally composed of a noble gas and a quenching. The latter component absorbs the UV photons produced by the propagation of charges in the gas and decreases the diffusion of the primary pairs. In the case of GPD DME (dimethyl ether, C_2H_6O) is typically used to this aim because of its low diffusion coefficient.

Noble gases are used since they prevent the recombination of electrons as they drift in the electric field and the choice of the noble gas, except for helium, selects the energy range of the instrument. The necessity of distinguishing the Auger electron from the photoelectron requires that the latter has a higher energy. This set a low energy threshold of about twice the binding energy of the electron which absorbs the photon. An additional low energy limit is due to the requirement that the tracks are well resolved by the pixels of the chip to maintain the capability to reconstruct correctly the directions of emission of photoelectrons even at low energy.

The high energy limit generally depends on the efficiency of the mixture. This decreases quickly with energy, $\sigma_{ph}^K \sim E^{-7/2}$ (see Eq. 2.1), and hence a sufficient number of photons can't be collected above a certain energy. A further constrain generally less tight is that tracks of photoelectrons must be completely absorbed in the gas cell. When charges are collected by one of the pixels at the edge of the detector, the event is automatically not acquired and this condition sets a limit in the maximum energy of photons. Indeed the range R_e of photoelectrons depends on its energy (Iskef et al., 1983):

$$\ln\left(\frac{Z}{A}R_e\right) = -4.5467 + 0.31104\ln E_e + 0.07773\left(\ln E\right)^2, \tag{2.27}$$

where R_e is in μg/cm^2 and E_e in eV (E<10 keV).

The current development of the GPD is focused in the energy range between ∼2 and ∼10 keV and this depends on several considerations. Even if there are many exceptions, spectra from astrophysical sources in the X-ray range are often bounded between a low and a high energy limit. The former depends on the photoabsorption of X-rays by gas present around the source or along its path toward the observer. The latter instead depends from the common observation that spectra decrease quickly with energy: above a few keV generally the fluxes scale as a power law $\sim E^{-\Gamma}$ with index $\Gamma \sim 1 \div 3$. The energy range ∼2 and ∼10 keV is often between these two limits and then fluxes are generally higher. Moreover it has been traditionally studied by many instruments.

The choice of the 2-10 keV range is even suggested by instrumental and programmatic considerations. The GPD will be placed in orbit with an X-ray optics whose typical energy range of operation is below ∼10 keV (see Sec. 6.2). At higher energy grazing

Element	E_{1s} (keV)	E_{2s} (keV)	E_{2p} (keV)
Hydrogen	0.014		
Helium	0.025		
Carbon	0.284	0.018	0.009
Nitrogen	0.410	0.037	0.012
Oxygen	0.543	0.042	0.014
Neon	0.870	0.049	0.028
Argon	3.206	0.326	0.251
Krypton	14.326	1.921	1.731

Table 2.3: Binding energies for inner orbitals of some elements.

incidence reflection occurs only for very small angles and hence "classical" (namely, one-layer) X-ray optics work better and are less expensive at low energy. Moreover the extension at higher energy requires long focal lengths and this in turn implies higher costs also in term of weight, bus performances and launcher.

The X-ray sky is currently nearly unexplored with X-ray polarimetry. A pathfinder mission which operates in the energy range where astrophysical sources are brighter and telescopes are easier and cheaper to build appears the right compromise (see Chapter 6). Both these conditions contribute to the definition of the energy range between $\sim$2 and $\sim$10 keV. A certain degree of polarization is expected in this energy range on the basis of the expectations presented in Chapter 1 and the higher flux should then favor positive detections. Subsequent missions could afterwards probe the emission at higher energy with more confidence of the scientific results but with an inevitably higher cost. The fluxes of astrophysical sources would be lower and consequently the requirements on the collecting area would be more stringent. However above 10 keV non-thermal processes should completely dominate over thermal emission and a higher degree of polarization is expected in this condition. The asymmetry and the role of intrinsically polarized mechanisms of emission is indeed emphasized.

In the 2-10 keV energy range the GPD works at best with mixtures based on neon or helium. The K-shell binding energy of the neon is 0.870 keV (see Table 2.3) and hence the mixtures based on this element can work only above $\sim$ 2 keV with a peak sensitivity at a few keV. Instead the binding energy of helium is 25 eV and then mixtures of this element plus organic components can provide optimal capabilities of track reconstruction even at lower energy. Note that helium is almost transparent to X-rays above a few hundreds of eV and consequently photons are absorbed by the quencher, mainly from carbon and oxygen atoms which compose the DME. In this case the binding energy of the elements which absorb photons is of the order of 280 and 540 eV respectively (see Table 2.3). Measurements above $\sim$1 keV should then be accessible, even if low pressure mixtures may be required to sufficiently resolve the tracks, penalizing the efficiency above a few keV. A discussion on the sensitivity and the comparison among different mixtures with the current detector is presented in Sec. 2.4.

Currently the baseline for future instruments is a mixture composed by 20% of helium and 80% of DME at 1 atm and 1 cm thick. The use of a baseline He-DME mixture doesn't

preclude the use of different mixtures to extend the energy range of the GPD. A possible future application in the hard X-ray range of the GPD can be planned with mixtures of neon, argon or even krypton (see Table 2.3), studied as a part of this thesis in Chapter 8.

2.3 The current detector

The current detector (Bellazzini et al., 2006b) is based on the third generation of an Application Specific Integrated Circuit (ASIC) chip (see Fig. 2.11a). Its active area is 15×15 mm^2 and is composed of 105600 pixels organized in a hexagonal pattern (see Fig. 2.11b). This shape reduces possible azimuthal systematic effects: square pixels would introduce a strong asymmetry every 90° while hexagon ones provide a more uniform response. If any residual effect is present, it should have a periodicity of 60°.

The small size of the pixels (50 μm) is essential for the optimal polarimetric performances of the GPD, allowing for the accurate sampling of the track of photoelectrons even at low energy in 1 atm mixtures. Each pixel is directly connected to an independent analog electronic chain which processes the charge collected (see Fig. 2.11b). The electronic noise of each pixel is only 50 electrons (r.m.s.) and then the device is sensitive to the single electron produced in the gas cell even when the gain of the GEM is low, i.e. a few hundreds.

The chip has self-triggering capabilities. It can discriminate the region where the secondary pairs are collected and only the pixels in a rectangular region around those which have triggered are read-out. This allows to convert only a few hundreds of pixels against the 105k of the whole detector, thus significantly reducing the read-out and dead time.

During the use in space the information about the track will be further reduced after the digital conversion of the signal. The pixels which are in the read-out reactangular area but didn't collect charge are removed (zeros-suppression). This procedure is performed by the Back-End Electronic which controls and powers the detector. The mean number of hit pixels after the zero-suppression depends on the energy but it is less than a hundred for a 3 keV photon. Note that each electron is multiplied by a factor $\sim$500 by the GEM and the electronic noise is very low, 50 electrons (r.m.s.). Then the separation of pixels that collected a charge and those that didn't is very sharp even from a single primary electron.

The chip is mounted very close (400 μm) to a GEM which amplifies the charge produced by the photoelectron of a factor $\lesssim 1000$. The GEM is a 50 μm thin foil of kapton perforated with 50 μm pitch holes in a triangular pattern. Each hole has a diameter of 30 and 15 μm on the top and in the middle of the kapton layer respectively. The top and the bottom faces of the GEM are metal-coated so that an electric field is generated by applying a different voltage to them. The electric field is uniform in the gas cell to collect the pairs produced but it is much more intense in the holes to generate secondary pairs.

The gas cell is delimited by the GEM and a thin 50 μm beryllium window which is almost transparent above 2 keV. In the current version of the detector, the cell containing the mixture is sealed (see Fig. 2.12a) however it can be refilled to test different mixtures. Thanks to the use of low-outgassing materials no degradation of the performance has

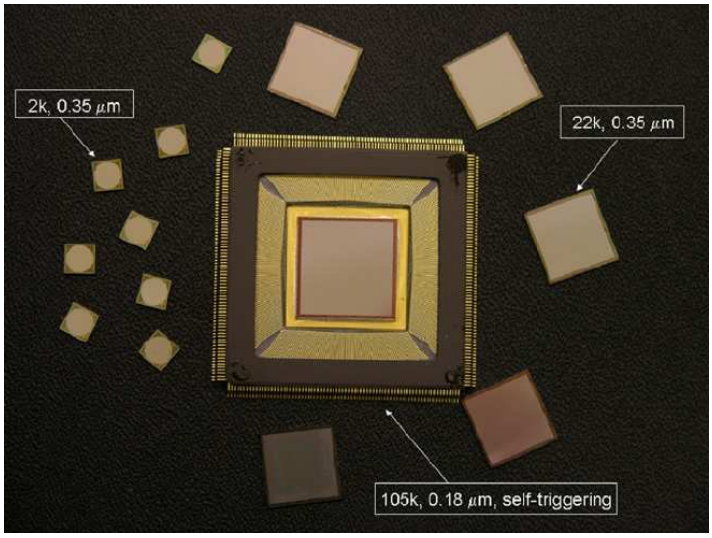

(a)

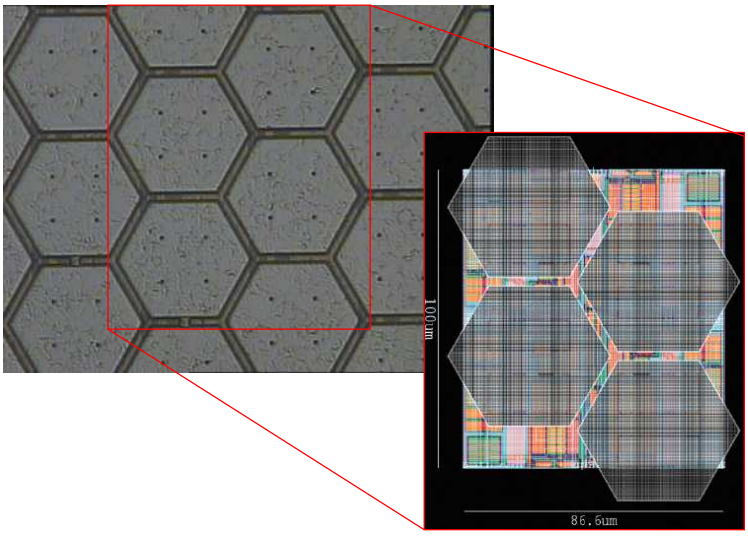

(b)

Figure 2.11: (**a**) The three generations of chips with an increasing number of pixels and area. They are the essential part of the GPD. (**b**) A picture of the hexagonal pixels (Bellazzini et al., 2007b).

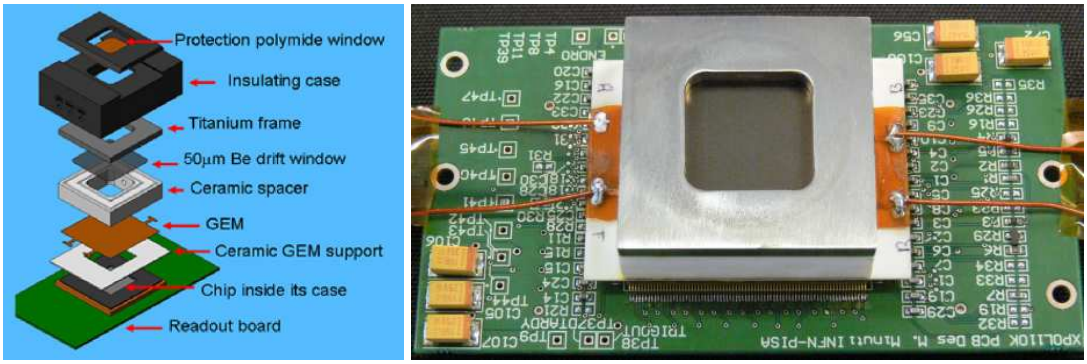

(a) **(b)**

Figure 2.12: (**a**) Exploded view of the sealed GPD. (**b**) A picture of the detector. The frame is made of titanium (Bellazzini et al., 2007b).

been measured during a period > 1 year, that is comparable to that of a small satellite mission (Bellazzini et al., 2007b). The lack of a refilling system is obviously a great advantage for space use in terms of weight and simplicity: the device is very small and weights only 50 g (see Fig. 2.12b).

The whole prototype used in the laboratory weights 1.6 kg and it is contained in a box $140\times190\times70$ mm^3 (see Fig. 2.13). This includes the detector and the Back-End Electronic which controls the instrument and acquires the data. Data are download via an USB connection to a standard personal computer and are analyzed by a software which applies the reconstruction of the track described in Sec. 2.2.1. It also allows to perform cuts on the data on the basis of the shape of the track, length and position of the absorbed photon.

The main characteristics of the current version of the GPD are summarized in Table 2.4.

2.4 The sensitivity to polarization

X-ray polarimeters measure the polarization of the incident radiation by means of the modulation of their azimuthal response: the phase and the amplitude of this modulation is then exploited to derive the degree and the direction of polarization respectively.

In the case of photoelectric polarimeters, the response of the instrument is the histogram of the direction of emission of photoelectrons. Even if the incident radiation is completely unpolarized the number of photoelectrons emitted per bin of angle is Poisson-distributed around the mean value. This results in a certain spurious modulation which mimics a polarized signal: the amplitude of the modulation for incident unpolarized photons only due to statistical fluctuations is called Minimum Detectable Polarization (MDP). Only a detection of a modulation greater than MDP is then statistically significant.

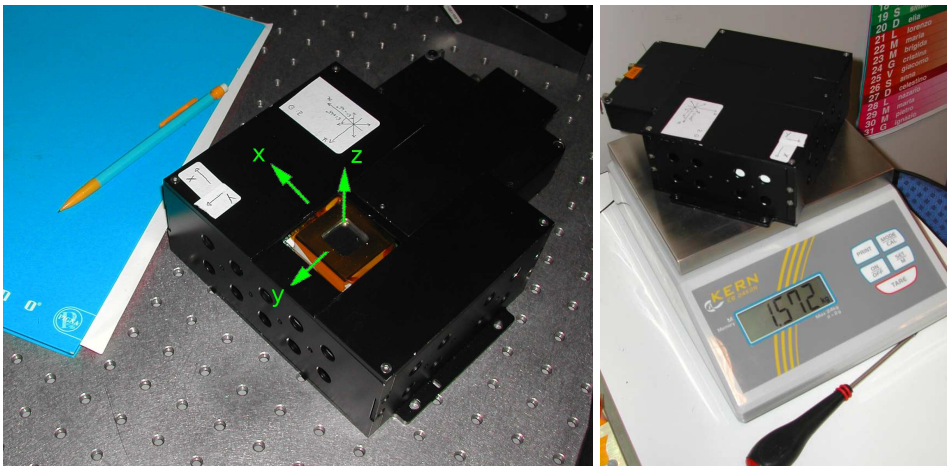

(a) **(b)**

Figure 2.13: The box which contains the GPD and the electronic for the acquisition of data (**a**). Note the frame of reference of the instrument. The whole weights only 1.6 kg (**b**).

Area:	15×15 mm^2
Active area fill fraction:	92%
Window:	50 μm, beryllium
Mixture:	He 20% + DME 80%, 1 atm
Cell thickness:	1 cm
GEM material:	gold-coated kapton
GEM pitch:	50 μm
GEM holes diameters:	30 μm
GEM thickness	50 μm
Gain:	∼500
Pixels:	300×352, hexagonal pattern
Pixel noise:	50 electrons ENC
Full-scale linear range:	30000 electrons
Peaking time:	3-10 μs, externally adjustable
Trigger mode:	internal, external or self-trigger
Self-trigger threshold:	3000 electrons (10% FS)
Pixel trigger mask:	individual
Read-out mode:	asynchronous or synchronous
Read-out clock:	up to 10 MHz
Frame rate:	up to 10 kHz in self-trigger mode
Parallel analog output buffers:	1, 8 or 16
Access to pixel content:	direct (single pixel) or serial (8-16 clusters, full matrix, region of interest)

Table 2.4: Characteristics of the current version of the GPD.

A key-parameter for the calculation of the MDP and then for the sensitivity of a polarimeter is the modulation factor μ, which is defined as the amplitude of the modulation of the response when completely polarized photons are incident on the instrument (see Sec. 1.1.2). A higher value means that the instrument responds to polarized radiation with a larger modulation and the effect of statistical fluctuations is in proportion lower. Being the total number of absorbed photons equal, lower polarized signals can be detected when μ is larger.

The modulation factor of actual instruments is measured from the histogram of directions of emission when completely polarized radiation is absorbed. The curve of modulation is fitted with the function (cf. Eq. 1.16):

$$\mathcal{M}(\phi) = A_{100\%} + B_{100\%} \cos^2(\phi - \phi_0). \tag{2.28}$$

The constat $A_{100\%}$ takes into account that the instrument has not a perfect response to polarization, since the response will not be completely modulated for any actual instrument. In the case of GPD, this is caused by tracks not correctly reconstructed. The modulation factor is then defined as:

$$\mu = \frac{\mathcal{M}_{\max} - \mathcal{M}_{\min}}{\mathcal{M}_{\max} + \mathcal{M}_{\min}} = \frac{B_{100\%}}{B_{100\%} + 2A_{100\%}}. \tag{2.29}$$

The modulation factor and the efficiency for some mixtures are reported in Fig. 2.14. The baseline mixture 20% helium and 80% DME at 1 atm and a gas cell 1 cm thick is represented by the solid line[2]. Its behavior is compared with a lighter mixture (30% He and 70% DME, 0.25 atm, 1 cm, dotted line), a medium (80% Ne and 20% DME, 2 atm, 2 cm, dashed line) and a heavy (60% Ar and 40% DME, 2 atm, 2 cm, dot-dashed line) mixture. In general μ increases with energy, since longer tracks are better reconstructed, but it reaches a constant value at high energy less the unity. Even when tracks are very long, in some cases the initial direction of emission is intrinsically not properly reconstructed. This can happen for example when photoelectrons are scattered near the absorption point or when they are emitted almost orthogonally to the detector. Note that lighter mixtures are characterized by higher values of μ since, as discussed in Sec. 2.2.3, higher is the efficiency and lower is the modulation factor.

The values of the modulation factor plotted in Fig. 2.14a are derived from Monte Carlo simulations. These fully take into account the physics of absorption of X-rays, the emission and the propagation of photoelectrons in the gas, the drift of primary pairs in the electric field of the GEM and eventually their amplification (see Sec. 2.2.2). The Monte Carlo results have been validated on the whole energy range of the GPD within this thesis work (see Chapter 5).

The MDP can be derived from the modulation factor and the total number of collected photons. Assuming Poisson statistics and 99% confidence level (Novick, 1975):

$$\text{MDP} = \frac{4.29}{\epsilon \mu F} \sqrt{\frac{B + \epsilon F}{ST}}, \tag{2.30}$$

[2]Numerical values of the modulation factor and the efficiency for the baseline mixture are reported in the Appendix A.

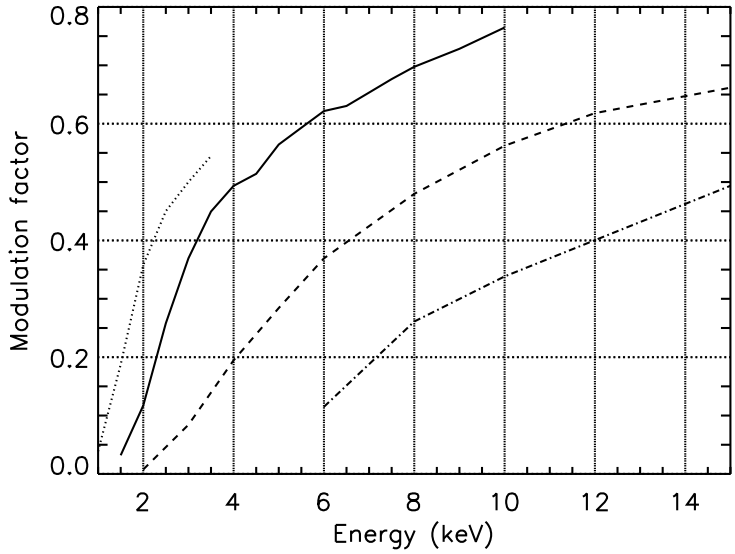

(a)

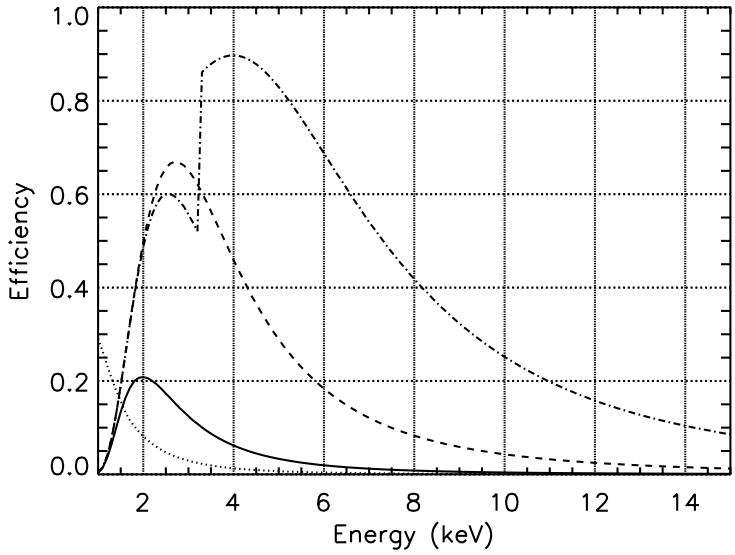

(b)

Figure 2.14: Modulation factor (**a**) and efficiency (**b**) for different mixtures. Solid line refers to the baseline mixture composed of 20% He and 80% DME at 1 atm and a gas cell 1 cm thick. Dotted, dashed and dot-dashed lines refer to 30% He and 70% DME (0.25 atm, 1 cm), 80% Ne and 20% DME (2 atm, 2 cm) and 60% Ar and 40% DME (2 atm, 2 cm) respectively. The efficiency includes a beryllium 50 μm window. In the case of 30% He and 70% DME (0.25 atm, 1 cm) mixture a Kapton window 900 nm thick is assumed.

where F and B are the source and the background fluxes in the selected energy range, ϵ the detector efficiency, S the collecting area and T the observation time.

The background will be negligible in all practical situations for the GPD. Even the fainter sources accessible to X-ray polarimetry will have a relatively high flux to collect the large number of photons required to perform an accurate measurement in a reasonable observation time. Moreover the GPD will be placed in the focus of an X-ray optics and since it is an imaging device the flux of the source must be compared only with the background inside the point spread function of the telescope. This argument will be quantitatively discussed in Sec. 6.2.1 but an example can be useful. In the context of the PolariX mission (see Sec. 6.3.1) the fainter sources observable will have a flux of the order of 0.1 mCrab. This corresponds to a flux of $\sim 1.7\times10^{-2}$ counts/s between 2 and 10 keV which allows to collect 17×10^4 counts in 1 Ms, sufficient to measure a degree of polarization $\gtrsim$10%. The expected internal background is 2.7×10^{-5} counts/s and that diffuse is 1.6×10^{-8} counts/s.

If the background can be neglected the MDP is inversely proportional to the so-called quality factor $\mu\sqrt{\epsilon}$. This differs from the typical dependence of the sensitivity in X-ray astronomy because, even if the background is negligible, the polarized fraction is to be compared with the fluctuations of the total counts from the source. Both increase with the efficiency and this explains the dependence of the MDP with the square root of ϵ.

The quality factor is not convolved with the area of the optics. However it can be used to represent the sensitivity of the instrument to polarized radiation at different energies. The choice of the parameters of the GPD (mixture, pressure, cell thickness) should then maximized the quality factor within a selected energy range in tune with the band-pass of the optics and the spectra of astrophysical sources.

The quality factor of the GPD filled with different mixtures is reported in Fig. 2.15, for the same ones in Fig. 2.14. The increase of the modulation factor and the decrease of the efficiency with energy produce a peak in the quality factor which varies from $\sim$ 2 keV for the lightest mixture to $\sim$ 10 keV of the mixture based on argon. Then different mixtures can provide an optimal energy coverage from $\sim$1 keV to a few tens of keV.

Note that the value of the quality factor for heavy mixtures is higher than that of light mixtures. However it doesn't include neither the optics area nor the spectra of astrophysical sources. Since both these quantities are rapidly decreasing with energy, the total maximum sensitivity is reached with the He-DME mixture which are more effective at low energy.

2.5 Comparison with different designs

The GPD images the track of photoelectrons by means of a pixel detector. This design is not the only possible for a photoelectric polarimeter: an alternative approach is that of the Time Projection Chamber (TPC, Black et al., 2007). In this case the plane of the detector is parallel to the direction of photons (see Fig. 2.16a) and the pairs generated drift orthogonally. Eventually they are amplified by an electric field produced with a GEM and read-out by vertical strips. The two dimensional image of the track is reconstructed from the hit strip, which provides the y coordinate (see Fig. 2.16b), and on the basis of the

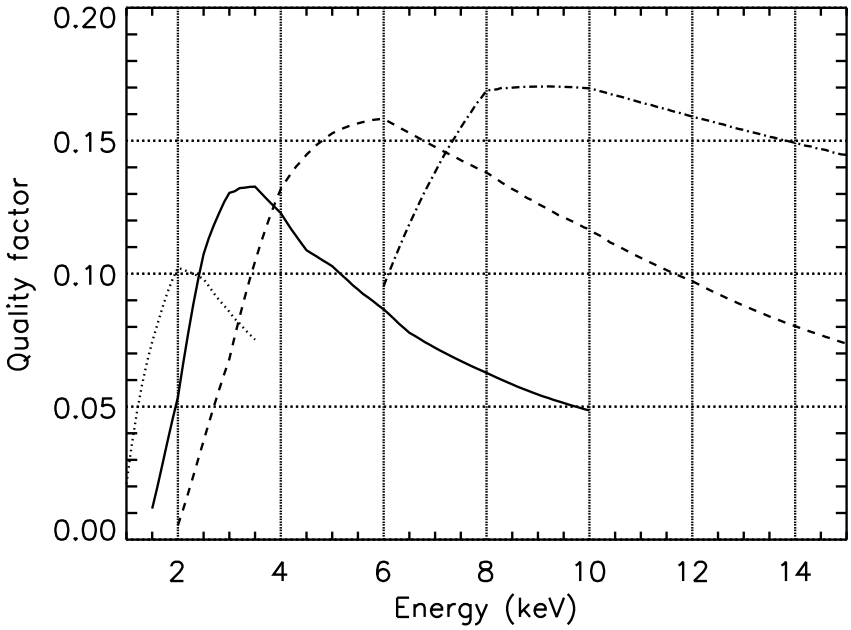

Figure 2.15: Quality factor of the GPD for different mixtures. The curves refer to the same mixtures as in Fig. 2.14 with the same conventions.

temporal delays among signals. Pairs created closer to the detector are detected before those generated far from it and hence their relative x position can be derived from the delays among signals reaching the same strip.

The reconstruction performed by the TPC is physically equivalent to that the GPD, at least for the current prototypes. Both devices image the projection of the track on the plane orthogonal to the incident direction of photons and can't establish neither the depth at which the photon is absorbed nor the angle θ between the direction of emission of the photoelectron and that of incident photon. The great advantage of the approach of the TPC is that the depth of the gas cell is not correlated with the drift path of primary pairs. The efficiency can then be increased by increasing the thickness of the cell and the length of the strips, without affecting the modulation factor. Indeed the average drift path of the pairs remains constant, at least for collimated incident photons.

There are however both intrinsic and "hardware" limitations in the approach of the TPC. In the former class, a disavantage is the loss of the bidimensional imaging capabilities of the device. It is well known that the Drift Chambers have found a limited application for X-ray imaging because of the ignorance of the time when the interaction occurred. Even if the drift velocity in the gas is known, the acquisition is triggered by the passage of the pairs across the GEM. Then only the relative position of the pairs, not their absolute x coordinate, can be derived from the temporal delays. The imaging capabilities are retained only in the y direction thanks to the knowledge of the position of the hit strip.

This is a problem which involves not only those sources, like PWNe, which could be

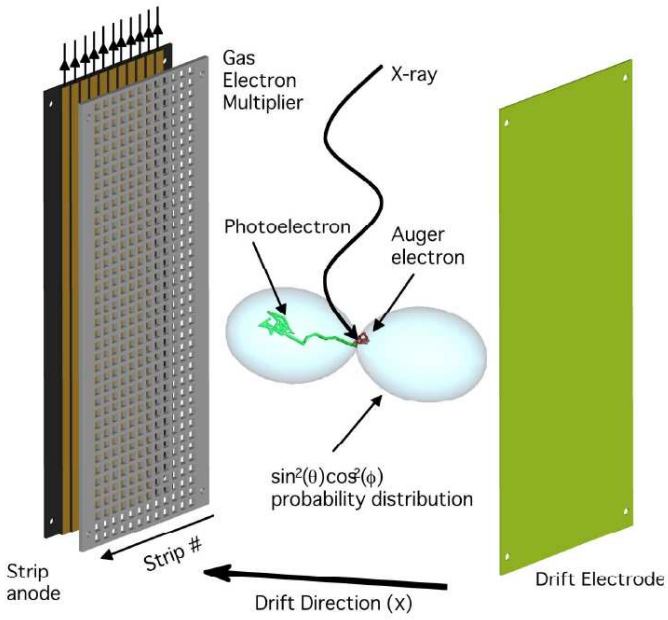

(a)

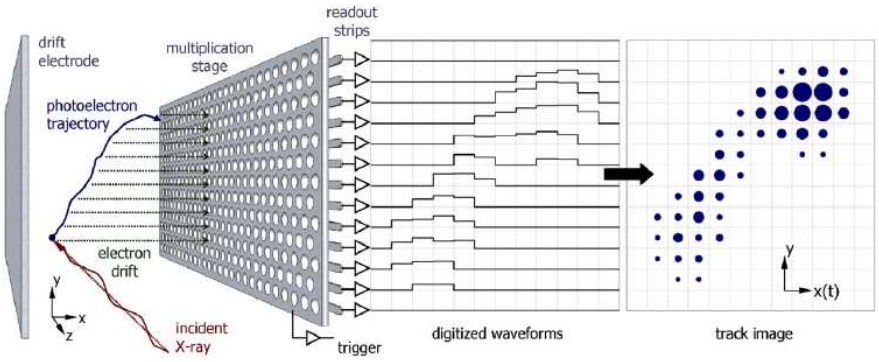

(b)

Figure 2.16: (**a**) Concept of the Time Projection Chamber (Hill et al., 2007). (**b**) Reconstruction of a track of a photoelectron when a 6.4 keV photons is absorbed. The gas mixture is composed of 50% of neon and 50% of DME at a pressure 0.6 atm (Black et al., 2007).

resolved. The main effect of the loss of imaging capabilities is that the background which affects each strip is higher since it corresponds to that collected in a slice of the gas cell. By increasing the volume of the gas cell to increase the efficiency the background may be no more negligible for fainter sources.

Another intrinsic limitation is that the response of the TPC is not symmetric. A photoelectron can be emitted equivalently toward the detector or in the opposite direction: however the drift path is different in these two cases and hence tracks are differently affected by diffusion. This front-back asymmetry produces a systematic effect in the reconstruction of the initial direction of emission which has to be removed, since it would appear as an asymmetry between the two peaks of the $\cos^2$ modulation. For unpolarized radiation this would produce a spurious modulation higher than that expected from statistical fluctuations only.

These systematic effects are removed by rotating the detector around the incident beam so that no preferred direction is present in average. However the requirement to rotate the instrument complicates its use in space: the construction of spinning satellite is no more a standard task and probably it would be simpler to put the instrument on a platform which is slowly rotated with respect to a 3-axis stabilized spacecraft. This however makes the connections to the instrument more difficult and less reliable in space.

The operation of the TPC is also less straightforward from the hardware point of view. The reconstruction of the track requires to resolve small temporal delays of the order of a few tens of ns and the sampling of the signal of the strips in such a small temporal intervals makes difficult the measurement of the charge collected. Indeed the read-out had to be performed within a time interval which doesn't allow the complete shaping of the analog signal and this may result in a distorted measurement of the charge collected.

A precise adjustment of the drift field is also required to sample the track on square pixels, which currently are 130 μm in size (Black et al., 2007). While in the y direction they correspond to the strips, in the x axis the dimension of the pixels depends on the drift velocity: indeed they are determined by the drift distance covered during the sampling period. Smaller pixels then require smaller strips and higher sampling frequencies or lower drift velocities. The correct sampling of the track on square pixels is of fundamental importance to avoid systematic effects on the direction of emission of photoelectrons. Rectangular pixels would mimic a polarized signal since they would have the same periodicity as a $\cos^2$ function.

Another difficulty related to the geometry of TPCs is that strips have intrinsically a higher background than pixels since they have a larger size. Higher gain of the GEM, a few thousands, must then be used to be sensitive to the single primary electron. This may be a risk in the space environment since the passage of charged particles may initialize destructive discharges of the GEM when a high electric field is used.

The TPC design is of great interest despite the limitations of its approach, mainly the lack of bidimensional imaging capabilities and the requirement to rotate the instrument. The gain in efficiency is indeed very important to perform accurate polarimetric measurements. The hardware limitations, which reflect the youth of the project, could be overcome in the near future but currently they may prevent the use of TPC on space-satellite missions in place of the GPD. The development of the latter is actually in a more

advanced phase: a version which could flight in a few years and would achieve breakthrough results has been working in laboratory for a few years. The use of this device in space has been studied within the PolariX project (see Chapter 6) and all critical problems has been already faced. Nevertheless a mission based on the TPC has been approved for a phase A study for a NASA small mission competition and it was preferred to the an analogous proposal which included the GPD, described in Sec. 6.3.3.

The TPC has been also proposed as an X-ray polarimeter with a large field of view for the study of GRBs (Hill et al., 2007). Even if a detailed analysis will be performed in Chapter 7, this use is not a simple extension of that as a focal plane instrument. Severe systematic effects arise when photons are absorbed at large angles and they may eventually question the use of photoelectric polarimeters with large field of view.

Chapter 3

The calibration source based on Bragg diffraction

The calibration of an X-ray polarimeter is not a trivial task. X-ray polarimeters for astrophysical applications have not been developed for many years and then even their calibration with polarized radiation is not a standard procedure. In the case of GPD this issue has been at first tackled with a source based on Thomson scattering (Costa et al., 1990), whose operation is "reverse" to that of polarimeters quickly described in Sec. 1.2. Unpolarized photons are scattered at 90° on a target and result completely polarized in the direction orthogonal to the scattering plane. Incident (unpolarized) X-rays are produced with an X-ray tube and a lithium target, enclosed in beryllium to prevent its oxidation and nitridation, is chosen to reduced the photoelectric absorption with respect to the scattering. Since the geometry of the source constrains the scattering, output radiation is almost completely polarized.

The main issue behind this technique is that its use is limited at low energy by the photoelectric absorption in the lithium target which is more probable than scattering below ∼10 keV. Nevertheless the Thomson-scattering source has been successfully exploited to measure the modulation factor of the GPD with chromium (5.41 keV), iron (6.4 keV) and copper (8.04 keV) X-ray tubes (Bellazzini et al., 2007a). The Monte Carlo software (see Sec. 2.2.2) has been instead used to extend the measured performances at lower energies. As a matter of fact the modulation factor in the energy where maximum sensitivity is expected, i.e. at about ∼3 keV, was never measured.

Another issue is that the scattered radiation is not monochromatic but resembles the spectrum of incident radiation produced by the X-ray tube. This prevents the precise measurement of the dependence of the modulation factor with energy, which is expected to be rather variable at a few keV on the basis of Monte Carlo results. Many authors have stressed the importance of spectro-polarimetry in the study of astrophysical sources (Rees, 1975; Connors et al., 1980; Mitrofanov, 2003) and then the precise measurement of the response of the instruments at different energies is particularly important.

Synchrotron facilities can easily produce polarized radiation at energies of a few keV. However they can hardly be used for the continuous and time-consuming development of a new generation detector as the GPD. This is why a dedicated calibration source based

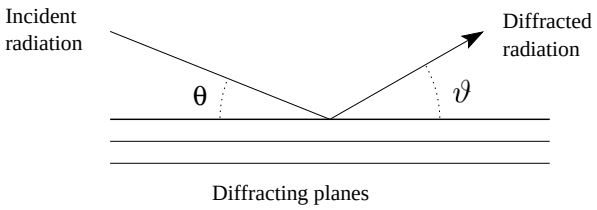

Figure 3.1: Definition of the glancing angles of incidence and diffraction. In general $\vartheta \neq \theta$ even if the rocking curve is strongly peaked when $\vartheta = \theta$.

on Bragg diffraction at nearly 45° has been developed within this thesis work. The design and the construction of a first prototype is presented in this Chapter but a much more powerful source will be described in Chapter 4. The prototype source was used for the first measurement of the modulation factor of the GPD at low energy, presented in Chapter 5.

The work presented below was published by Muleri et al. (2007).

3.1 Bragg diffraction

The diffraction of photons on the planes of a crystal lattice is called Bragg diffraction. When continuum radiation is incident at a glancing angle θ to the planes of a flat crystal, only photons whose energy E is equal to the Bragg energy for that angle are diffracted (Guinier, 1994). The Bragg energy $E_B(\theta)$ is:

$$E_B(\theta) = \frac{nhc}{2d \sin \theta}, \tag{3.1}$$

where h and c are respectively Planck's constant and the speed of light, d the crystal lattice spacing and n an integer which specifies the diffraction order. The Eq. 3.1 relates the angle of diffraction and the energy of diffracted photons and is called Bragg's Law. Since many orders are diffracted for any specific value of θ, the spectrum is composed of equally spaced lines, each corresponding to different orders of diffractions. Their relative intensities depend on the incident flux and the decreasing efficiency of diffraction as the diffraction order increases (see Sec. 3.3).

Consider monochromatic radiation of energy E incident on a crystal with a glancing angle θ. The ratio between the diffracted and incident intensity is function of the diffraction angle ϑ and it is called rocking curve $P_E(\vartheta)$ (see Fig. 3.1). The rocking curve is strongly peaked at the angle $\vartheta = \theta$ and is very narrow, a few arcseconds for flat crystals. For this reason hereafter it will be implicitly assumed that the angle of diffraction is equal to the one of incidence.

The efficiency of diffraction, i.e. the total intensity of diffracted radiation, is a characteristic of the crystal. It is commonly expressed with the integrated reflectivity R_E:

$$R_E = \int_0^{\frac{\pi}{2}} P_E(\vartheta)\, d\vartheta, \tag{3.2}$$

Crystal	Bragg Energy ($\theta = 45°$) (keV)	$R_E \times 10^4$ (radians)
WS_2	1.40	15.0
MoS_2	1.43	8.3
PET	2.01	4.3
Graphite (mosaic)	2.61	15.9
Calcite	2.89	3.5
LiH	4.3	35.0
LiF	4.35	5.2

Table 3.1: Theoretical integrated reflectivity for some crystals for $\theta = 45°$. The Bragg energy is also reported. The value obtained in practice is close to that listed only for graphite and molybdenum disulfide (data from Silver et al., 1989).

where ϑ is the angle of diffraction. A higher integrated reflectivity means that the intensity of diffracted radiation is higher.

The theoretical integrated reflectivity for some crystals is reported in Table 3.1 for diffraction at 45°. In practice the best integrated reflectivity is obtained with graphite crystal and it is close to the theoretical value listed in the Table. Note the small numerical values of integrated reflectivities which express the intrinsic inefficiency of Bragg diffraction. The peak of the rocking curve reaches a value near 0.5 or higher only in a very narrow interval, centered on the incident angle and extending over a few arcseconds for a perfect crystal. This corresponds to less than one eV and consequently only a tiny fraction of the spectrum of the incident radiation is diffracted with high efficiency, while the large part is not diffracted at all. Unfortunately this is the major limitations of polarimeters based on this technique, since spectra from astrophysical sources are typically continuous. Moreover narrow lines, when present, are in general unpolarized.

A substantial flux can be produced by means of X-ray tubes or strong radioactive sources and then the inefficiency of the diffraction is not a critical issue for the construction of a calibration source. Even more important the diffraction can be exploited much more effectively with monochromatic radiation. If photons with energy E equal to the Bragg one at an angle $\hat{\theta}$ are incident exactly at the angle $\hat{\theta}$, the diffraction of all photons occurs at the peak of the rocking curve. In this case a substantial part of the incident intensity, about a half, is diffracted and high fluxes can be then easily obtained.

Note that monochromatic emission can be easily produced by means of fluorescence emission extracted from X-ray tubes. The use of diffracted line photons is then particularly convenient (see Sec. 3.3).

3.1.1 Sensitivity to polarization

The integrated reflectivity of crystals depends on the direction of polarization of the incident radiation. Without loss of generality, electromagnetic waves can be considered as the superimposition of two orthogonally polarized waves. The radiation incident on the crystal can be decomposed in two components, parallel (π-component) and perpen-

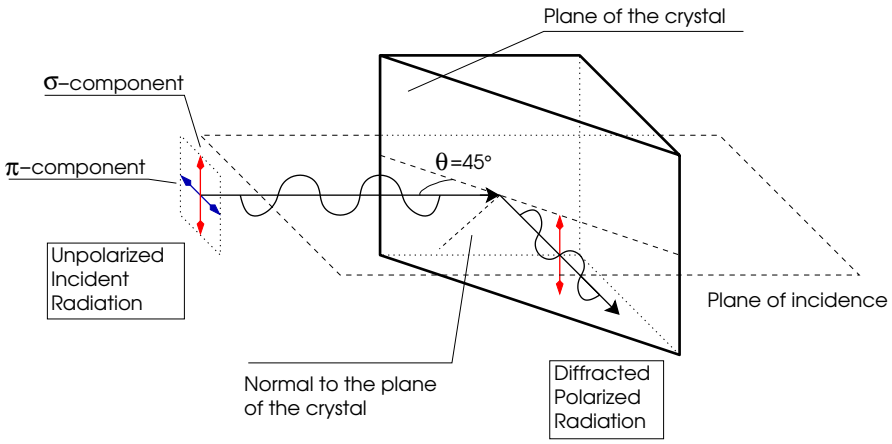

Figure 3.2: Geometry of Bragg diffraction at 45°. Only the σ-component, orthogonally polarized to the plane of incidence, is efficiently diffracted. Then the output radiation is linearly polarized.

dicularly (σ-component) polarized to the plane of incidence, that is the plane where the direction of the incident radiation and the normal of diffraction planes lie (see Fig. 3.2).

The ratio $k = R_E^\pi / R_E^\sigma$ of the integrated reflectivity of the π and σ components depends on the diffraction angle but it is generally lower than 1. Then the diffracted radiation is partially polarized perpendicularly to the plane of incidence, the degree of polarization being (Evans et al., 1977):

$$\mathcal{P} = \frac{1-k}{1+k}. \tag{3.3}$$

In Fig. 3.3a and Fig. 3.3b the value of k and the expected polarization are reported as a function of the incident angle θ for a graphite crystal. The former is calculated by Henke et al. (1993), while the latter is derived from Eq. 3.3. The same is reported in Fig. 3.4 for an aluminum crystal.

When the diffraction angle is 45°, $k = 0$ and the radiation is completely polarized orthogonally to the plane of incidence. Hence constraining the diffraction angle to nearly 45° the radiation is almost completely polarized. Note also that photons which are diffracted must satisfy the Bragg condition within less than one eV for flat crystals (see Eq. 3.1). The spectrum is then composed of equally spaced and nearly monochromatic lines corresponding to the Bragg energies with $\theta = 45°$.

The large dependence of the value of k with respect to θ requires that the constrain on the diffraction angle must be very tight. If the spectrum of the incident radiation is continuous, there are photons which can be diffracted at angles different from 45° since they can be incident at the right angle and have the right energy to be diffracted. On the one hand they increase the diffracted flux but on the other hand diffraction occurs with $k \neq 0$ and hence the mean polarization of the output radiation is reduced.

The integrated reflectivity and consequently the diffracted flux from continuum can be increased with the use of mosaic crystals. In this case the crystal is not flat, i.e. formed

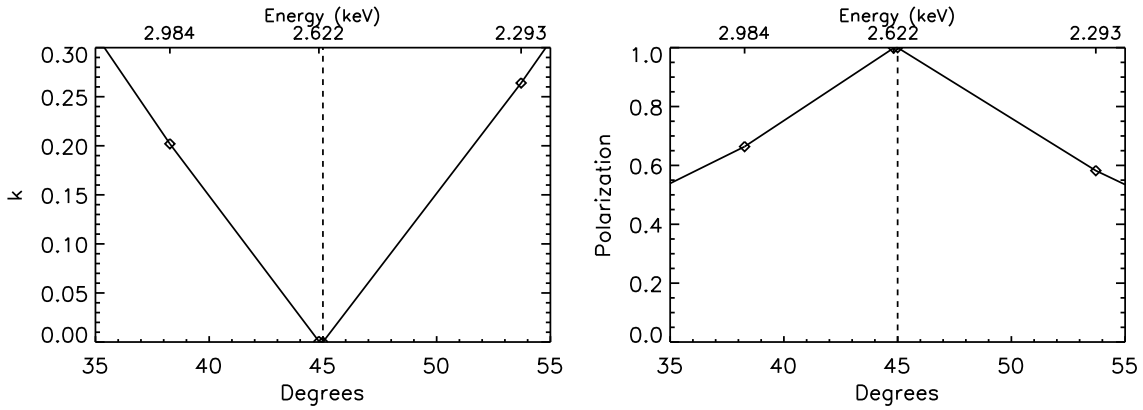

Figure 3.3: Production of polarized radiation by means of diffraction on graphite crystals. Note that the diffraction angle and energy are related by Bragg's Law (see Eq. 3.1). The energies correspond to K or L fluorescence lines of elements. (**a**) Dependence of the ratio of integrated reflectivity for incident radiation completely polarized parallel and perpendicular to the plane of incidence with diffraction angle. (**b**) Expected degree of polarization, derived from Eq. 3.3. The value of k was calculated by Henke et al. (1993).

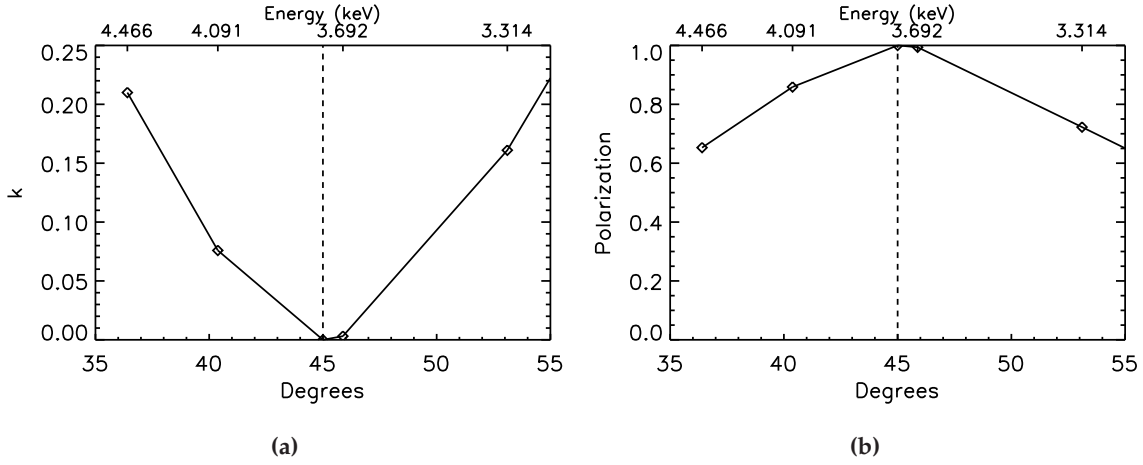

Figure 3.4: The same as in Fig. 3.3 for aluminum crystals (data from Henke et al., 1993).

Fluorescence line	E (keV)	Crystal	θ	$\mathcal{P}$
Lα Molybdenum	2.293	Rhodium (001)	45.36°	0.9994
Kα Chlorine	2.622	Graphite (002)	44.82°	0.9986
Lα Rhodium	2.691	Germanium (111)	44.86°	0.9926
Kα Calcium	3.692	Aluminum (111)	45.88°	0.9938
Kα Titanium	4.511	Fluorite CaF_2 (220)	45.37°	0.9994
Kα Manganese	5.899	Lithium Floride (220)	47.56°	0.8822
Kα Copper	8.048	Germanium (333)	45.06°	0.9849

Table 3.2: Tuning between fluorescence lines and diffraction at 45 degrees on different crystals. θ is the incident angle and $\mathcal{P}$ is the polarization of diffracted photons. Data from calculation performed by Henke et al. (1993).

by a plane parallel lattice, but it is composed of small domains each acting as an independent crystal. Domains are slightly and regularly misaligned with a FWHM gaussian misalignment which usually is between some tenths and $\sim 1°$. Since the domains are smaller than the absorption length of X-ray photons, radiation crosses many domains and can be diffracted if one of them is properly aligned. Hence diffraction occurs at angles slightly different from the average one and consequently at energies slightly different. This increases the energy band-pass up to some tens of eV but at the same time it reduces the mean degree of polarization of diffracted radiation. The energy width of the diffracted lines can be eventually used to estimate the mean degree of polarization of the output radiation.

The mere diffraction of monochromatic incident photons is a sufficient condition for establishing the angle of incidence and then their polarization. Indeed diffraction can occur only at the angle corresponding to their energy and a match of the energy of incident radiation with the Bragg energy at 45° of crystals allows the production of highly polarized photons. In Table 3.2 is reported a list of fluorescence lines and crystal pairs which can be used for the production of polarized photons at a few keV. The diffraction angle and the polarization calculated from the well known fluorescence energy and Eq. 3.3 are also reported. Since the former is always near to 45°, an high and precisely known degree of polarization is reached.

3.2 Design and construction

The properties of Bragg diffraction can be exploited to build a polarized calibration source at a few keV. Different crystals allow to produced radiation at different energies; collimators are used to constrain the direction of incidence (and diffraction) of photons on the crystal at about 45°. The choice of the degree of collimation allows to reach a reasonable trade-off between the degree of polarization and the flux (see Sec. 3.1.1). A modular source was then designed to allow for easily changing each component and fine tune the characteristics of the source to specific needs.

Important requirements for the design of the Bragg source we needed included lim-

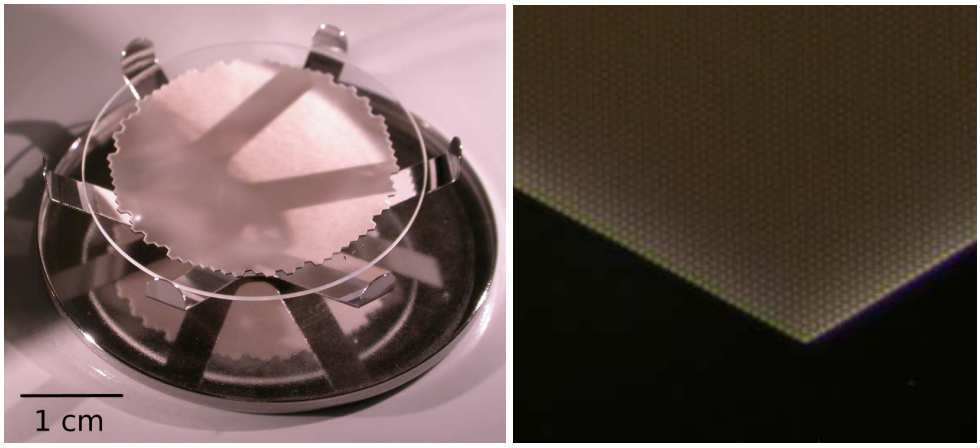

(a) **(b)**

Figure 3.5: (**a**) A capillary plate built by Hamamatsu Photonics used as a collimator. (**b**) An enlargement view showing the hexagonal pattern and the 10 μm holes.

ited size, portability, reliability and simple operation. The first two requirements are achieved by means of the use of capillary plates as collimators. They are plates made of lead-glass, which is completely opaque to X-rays below ∼20 keV, with small holes of 10 μm diameter (see Fig. 3.5). Their hexagonal pattern allows an on-axis transparency of 57%. The thickness is 0.4 or 1 mm and then, thanks to the small diameter of the holes, they can narrow the beam with a semi-aperture of $1/40 = 1.4°$ and $1/100 = 0.6°$ respectively despite the very limited size. The diameter of the broad and the narrow capillary plate is 25 and 33 mm respectively while the effective diameter of the pattern of the holes is about 20 and 27 mm.

The choice of the crystals derives from the requirement on the energy range of the diffracted photons. They should cover the interval of maximum sensitivity of the Gas Pixel Detector, namely from ∼2 to ∼4 keV (see Sec. 2.4). A mosaic graphite and a perfect (flat) aluminum crystals were selected from Table 3.2: the graphite is the crystal with the higher intergrated reflectivity (see Table 3.1); the choice of the aluminum is instead due to the convenient match with a small and low power X-ray tube already present in our laboratory. Other crystals in the Table 3.1 are used for the improved version of the Bragg source presented in Chapter 4.

X-ray tubes are strong sources of X-rays produced by means of collisions of electrons on a target (anode). The output spectrum is composed of unpolarized lines and a continuum bremsstrahlung emission: the former correspond to electronic transitions (fluorescence) of atoms in the target, the latter is due to the breaking of electrons. This component may be partially polarized (see, for example, Eberhard and Werner, 2004).

In Fig. 3.6 the spectrum of the X-ray tube with calcium anode is reported. The energy of the emission depends on the energy of the incident electrons which corresponds to the high voltage which is supplied to the tube. In this case high voltage was 7 kV and consequently the spectrum of X-ray photons reaches to 7 keV. The lines correspond to Kα

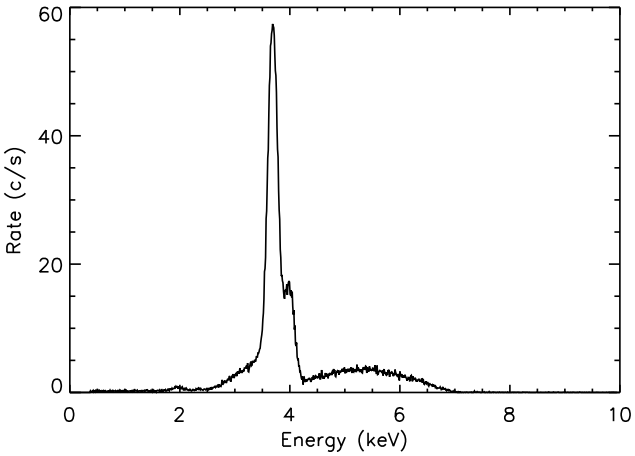

Figure 3.6: Spectrum of the X-ray tube with calcium anode. Kα and Kβ lines at 3.692 and 4.013 keV are not completely resolved by the detector used. Continuum emission at higher energy is due to bremsstrahlung.

and Kβ transitions of calcium at 3.692 and 4.013 keV.

The choice of the calcium tube and the aluminum crystal allows to exploit the diffraction of Kα line emission at nearly 45° (see Table 3.2). The contribution of the diffracted continuum can be safely neglected with respect to the much more intense line emission. This assumption allows for the precise determination of the degree of polarization from Eq. 3.3, which results in this case equal to 99.38%.

Continuum bremsstrahlung emission is used for the diffraction on the graphite crystal. Line emission from chlorine would be diffracted at about 45°, but X-ray tubes with anodes made of this element (or some material where it is contained) are not commercially available (but see Sec. 3.4). Diffraction on graphite was exploited for the production of polarized photons at 2.61 keV (I order) and 5.22 keV (II order) and to this aim a small and low power X-ray tube with copper anode is used. Since the bremsstrahlung radiation increases with the square of the atomic number of the target, the use of the copper anode is preferable with respect to the calcium one. Mosaic crystals with a misalignment FWHM of 0.8 and 1.2 degrees, grade B and D respectively, are used to increase the diffracted flux.

In Fig. 3.7 the aluminum and the grade B and D mosaic crystals are shown. The first is 20 mm in diameter, while the graphite crystals are 20×20 mm^2. Both graphite crystals have unpolished surfaces and care is attended to avoid that edge imperfections destroy the right alignment with the incident radiation.

Each crystal and each capillary plate is mounted in an aluminum holder so that any component of the source is easily interchangeable. The capillary plates are protected with 4 μm thin polypropylene film to avoid dust deposition and assures 96% transparency at 2.61 keV. The holders are locked to a central body which constrains the diffraction angle at 45° and is half-cube shaped with 46.5 mm side (see Fig. 3.8a).

For simplicity the holders are mounted without allowing for tilt regulation. This

(a) **(b)**

Figure 3.7: (**a**) From left to right: aluminum and graphite crystals built by Matek. Graphite crystals differ from the amplitude of domains misalignment. (**b**) Enlargement view of the grade B graphite crystal, illuminated with grazing incidence light to highlight the roughness of its surface.

choice has been revised in the design of the improved Bragg source (see Chapter 4). The polarizer, i.e. the block formed by the central body, the crystal and the capillary plates is shown in Fig. 3.8b.

Air absorption heavily affects low energy photons and then the distance between input and output capillary plate was minimized to only 5 cm . Two standard gas feedthroughs were also added to allow helium flowing in the polarizer and typically it is used below $\sim$3 keV (air transparency at 2.6 keV is 23% for a 5 cm path).

Numerically controlled instruments were used to build every part of the source. Nevertheless the alignment of the capillary plates and the crystal was checked by means of optical measurements (see Fig. 3.9). The polarizer is locked on a manual rotational stage and a laser is reflected alternatively by the capillary plates and the aluminum crystal as the polarizer is rotated at 45° steps. The laser hits a reference plane placed at 95.6 cm from the polarizer and the misalignment of each component is derived from the movement of the spot on the reference plane. The measurement has an estimated sensitivity of 5′ (about $0.1°$).

The capillary plates resulted aligned within errors. Instead the crystal holder was aligned within about $0.2°$ by means of a thin wedge. The alignment was also verified by measuring the energy of diffracted photons (see Sec. 3.3).

The design of the source was performed at the IASF/INAF of Rome (a drawing is reported in Fig. 3.10a) but the realization of the mechanical parts was outsourced. A picture of the complete polarized source is shown in Fig. 3.10b. It is contained in a box $262\times98\times69$ mm^3. The small X-ray tube is locked with a Teflon grab to an aluminum flange and the polarizer is independently screwed to the flange. The replacement of capillary plates or crystal doesn't require the disassembling of the X-ray tube. An aluminum case completely covers the source during operation to avoid leakage of radiation or the damage of the X-ray tube.

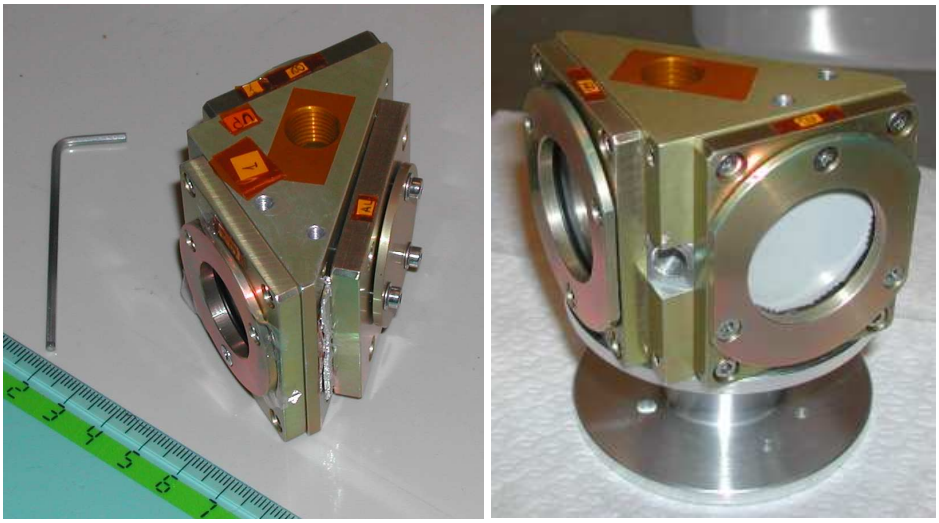

(a) **(b)**

Figure 3.8: The assembled polarizer. (**a**) Top view, showing the central half-cube shaped body and the holders of the crystal and the capillary plates. The threaded hole is for helium flowing. (**b**) Side view, with the capillary plates in the foreground and the crystal in the opposite side, hidden from the view. The hole in the middle was made in order to check the alignment between capillary plates and crystal.

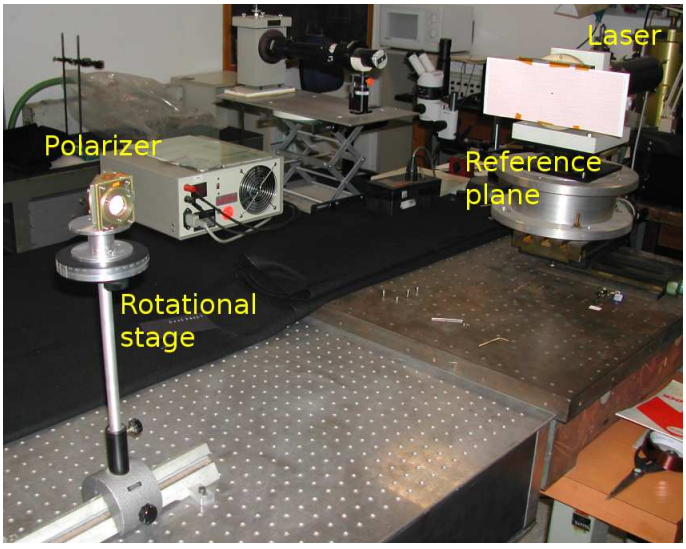

Figure 3.9: Setup used for the alignment of the components of the polarizer.

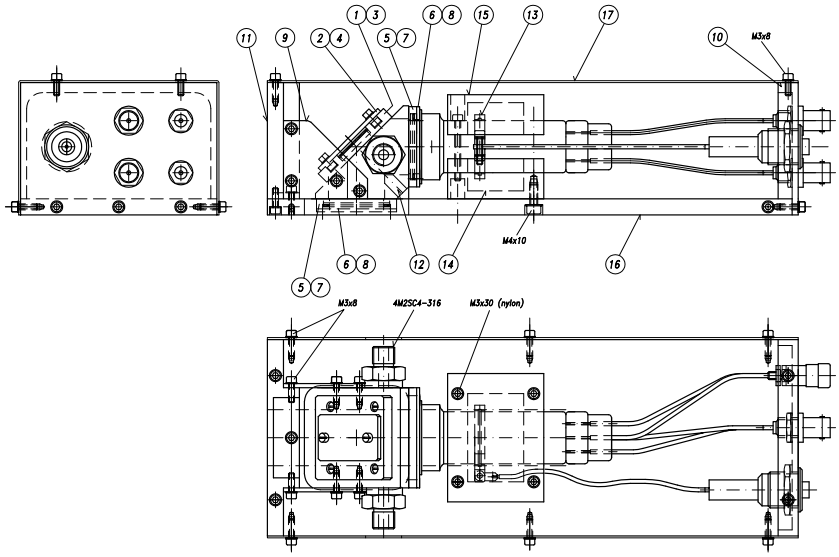

(a)

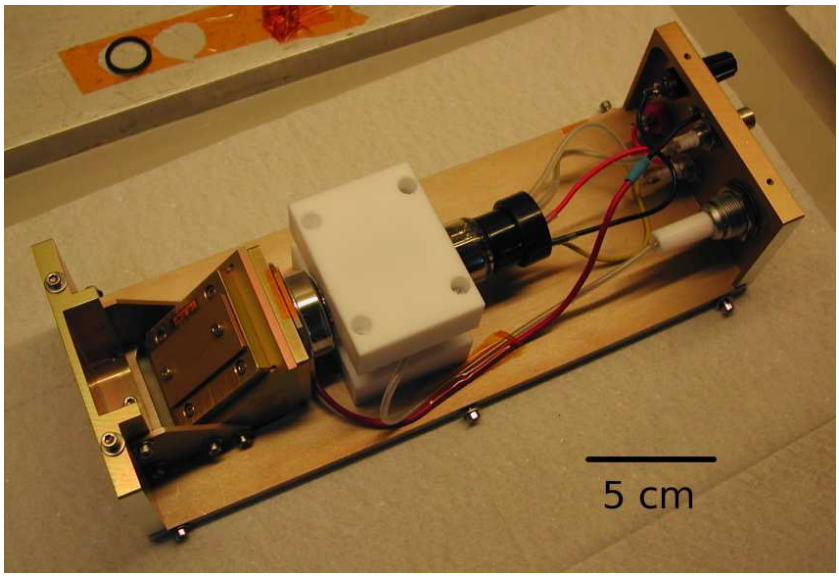

(b)

Figure 3.10: The drawing (**a**) and a picture (**b**) of the complete source of polarized photons. The polarizer is on the left while the small X-ray tube is on the right.

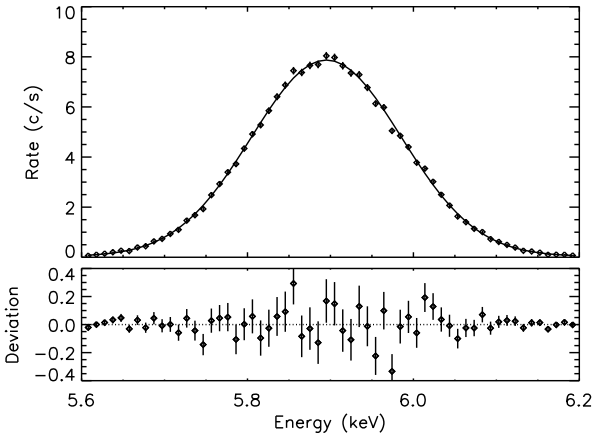

(a)

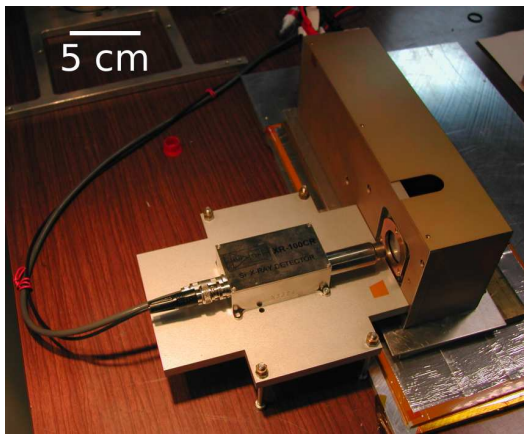

(b)

Figure 3.11: (**a**) The spectrum of 5.899 keV line from Fe^{55} radioactive source measured with the Amptek detector. A gaussian fit provides 213 eV FWHM. (**b**) Measurement setup for the spectrum of diffracted radiation.

3.3 Spectrum and estimated polarization

The spectrum of diffracted photons is measured with a commercial Amptek XR100CR Si-PIN spectrometer, with an energy resolution of 213 eV at 5.899 keV (see Fig. 3.11a). The energy and the width of the lines are exploited to derive an estimate of the degree of polarization, since the energy is related to the diffraction angle (and consequently to the degree of polarization) with the Bragg's Law. The detector is placed as close as possible to the output capillary plate to reduced air absorption (see Fig.3.11b).

Many configurations of the polarizer with different crystals and collimators have been tested. Two examples are reported in Fig. 3.12: the spectra between 1 and 10 keV in the case of the grade B graphite and aluminum crystal are shown in Fig. 3.12a and in Fig. 3.12b respectively. Incident radiation is continuous in both cases but two broad capillary plates are used with the graphite mosaic crystal, while only a narrow collimator is used for diffraction on aluminum, being the crystal flat.

The X-ray tube high voltage selects the maximum energy of incident photons and then the number of diffracted orders. It is 8 and 10 kV in the case of graphite and aluminum and then only photons with energy below 8 and 10 keV are incident on the crystals. The first three orders of diffraction (2.61, 5.22 and 7.83 keV) are visible in the case of graphite. Instead only the diffraction at 3.74 and 7.48 keV can occur with the aluminum crystal. The different fluxes of the different orders depend on the spectrum of the unpolarized incident radiation, the air absorption and the decreasing efficiency of Bragg diffraction when the order increases.

Note that the background is low and mainly due to the incomplete charge collection in the spectrometer. The line at about 3 keV in Fig. 3.12b is an artefact of the instrument since it is the fluorescence of the silver collimator of the detector.

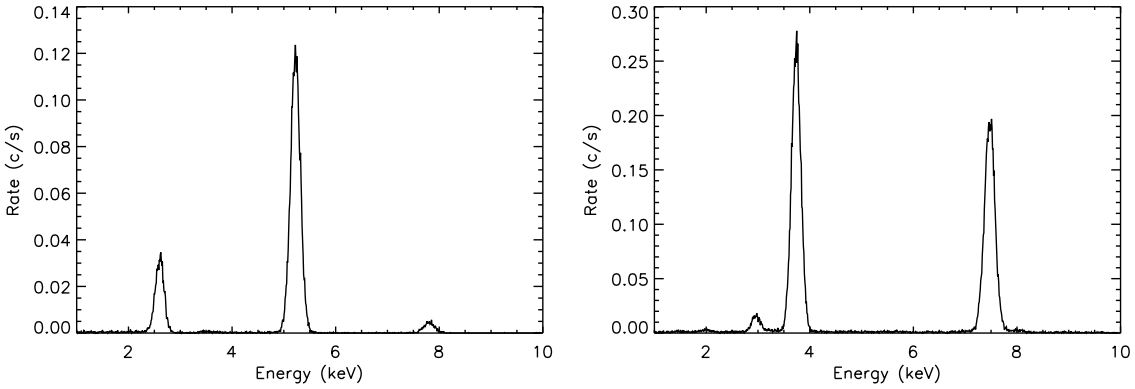

(a) **(b)**

Figure 3.12: Spectrum of radiation diffracted on graphite (**a**) and aluminum (**b**) crystals. In both measurements continuum radiation is used. Three order of diffraction (2.61, 5.22 and 7.83 keV) are visible in (**a**), while only the first two orders are present in the spectrum diffracted on the aluminum. The line at about 3 keV in (**b**) is an instrumental artefact.

3.3.1 Diffraction on graphite

The lines corresponding to the different orders of diffraction are fitted with gaussian profiles. Two examples obtained with the graphite crystal at the first and second order are reported in Fig. 3.13 and correspond to the lines in Fig.3.12a. The parameters of the fits are reported in Table 3.3.

The measured energy of the line allows to derive the angle of diffraction from Bragg's Law. Its value for the different configurations and different orders is reported in Table 3.3 and is in general consistent with 45° within mechanical tolerance.

The degree of polarization can be estimated from the diffraction angle and Eq. 3.3. This procedure can be strictly applied only if the line width is very narrow with respect to the variation of k. However if the line is unresolved from the detector its width is less than ∼200 eV and an approximate estimate of the degree of polarization can be calculated anyway. Otherwise a lower limit to the polarization is provided by the measured line width since it gives a hint of the energy of the photons which are diffracted at angles different from 45°. It varies in a range approximately as large as the FWHM and centered at the line peak. Thanks to the Bragg's Law this interval translates to an angular one which typically includes the angle θ=45°. Then the boundaries of the interval correspond to the higher values of k within it (see Fig. 3.3a). The lower limit of the polarization is derived from the higher value of k between those at the boundary.

Comparing the line width when two broad collimators are used with the detector resolution, measured by means of fluorescence lines, it results that the first order line is unresolved. The degree of polarization is then about 98%; the second order is instead resolved and the 10 eV line width set a 96% lower limit to the degree of polarization (see Table 3.3).

A similar analysis is repeated when a single broad collimator is used. The results,

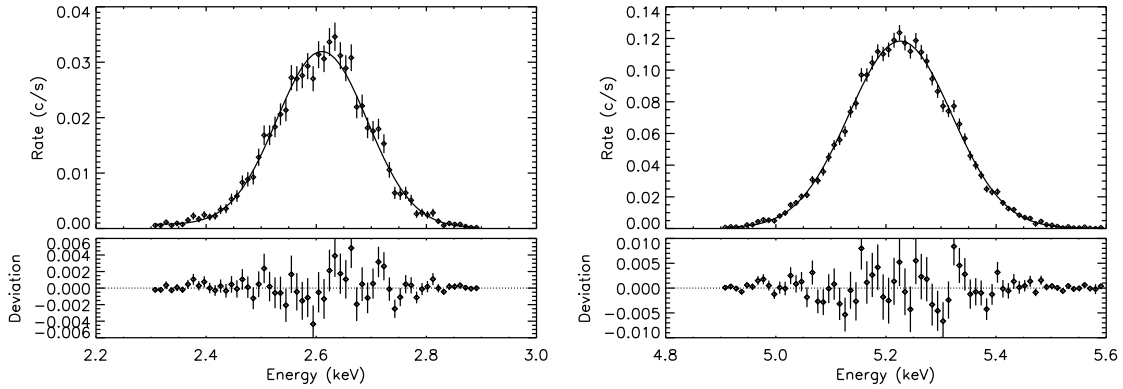

Figure 3.13: Gaussian fit of the lines corresponding to the first (**a**) and second (**b**) order of diffraction on the graphite grade B crystal. Two broad collimators were used.

reported in the bottom part of Table 3.3, show that the flux is increased by a factor 5 with a modest decrease of the polarization degree lower limit.

3.3.2 Diffraction on aluminum

The gaussian fit is also applied to the spectrum produced with the aluminum crystal as shown in Fig. 3.14. The results of the fits when continuum photons are produced by the copper X-ray tube are reported in the top part of Table 3.4. Since the aluminum crystal is flat, the spectrum is composed of lines which are very narrow and both orders are indeed unresolved. Despite the FWHM of the second order is ∼235 eV, it is still lower than the resolution of the Amptek detector at that energy.

In the bottom part of Table 3.4 is reported the analysis performed for the diffraction of line emission produced with calcium X-ray tube (see Fig. 3.15). The energy of the line, consistent with the weighted average of the Kα1 and Kα2 calcium lines, and the very narrow width support the lack of any contamination from continuous photons. Then it can be assumed that radiation is diffracted at 45.88° and is 99.38% polarized (cf. Table 3.2). Note that the use of the line emission of the calcium results in an increase of the counting rate by over a factor 20 respect to the intensity obtained with the diffraction of continuum photons.

3.4 The feasibility of an on-board calibration source

The very compact design of the Bragg source suggests the feasibility of a device for the calibration of X-ray polarimeters on-board satellite missions. It should be based on a radioactive source rather than on an X-ray tube, since only the former can be easily inserted together with the instrument in the focal plane.

Diffraction	Incident radiation	E (keV)	FWHM (eV)	χ^2	θ_{Bragg}	$\mathcal{P}$	Rate (c/s)
Incoming and output $1/40$ collimators							
Graphite, I or.	Continuum	2.6105±0.0020	193.6±3.2	0.849	45.07°	~ 0.98	0.66
Graphite, II or.	Continuum	5.2261±0.0018	220.1±1.6	1.101	45.02°	> 0.96	2.8
Output $1/40$ collimator							
Graphite, I or.	Continuum	2.6109±0.0036	198.6±4.7	1.096	45.07°	> 0.95	3.5
Graphite, II or.	Continuum	5.2269±0.0037	248.2±2.6	0.926	45.01°	> 0.94	16.8

Table 3.3: Gaussian fit parameters, diffraction angle and estimated polarization for the lines obtained with the grade B graphite crystal and different configurations of capillary plates. Incident radiation is continuous. The increase of the FWHM with energy is partially due to the decreasing resolution of the detector. Air absorption is not taken into account in the calculation of the rate.

Diffraction	Incident radiation	E (keV)	FWHM (eV)	χ^2	θ_{Bragg}	$\mathcal{P}$	Rate (c/s)
Output $1/100$ collimator							
Aluminum, I or.	Continuum	3.7388±0.0016	210.2±2.2	1.268	45.14°	> 0.97	5.9
Aluminum, II or.	Continuum	7.4733±0.0021	234.7±1.5	1.044	45.18°	~ 0.98	4.9
Output $1/40$ collimator							
Aluminum, I or.	Calcium Kα line	3.6889±0.0024	200.1±0.2	1.396	45.93°	0.9938	140.1

Table 3.4: Gaussian fit parameters, diffraction angle and estimated polarization for the lines obtained with the aluminum crystal and different configurations of capillary plates. In the top part, continuum emission and a single narrow output collimator is used. The parameters for diffraction of Kα calcium line with a single output broad collimator is reported in the lower part of the Table.

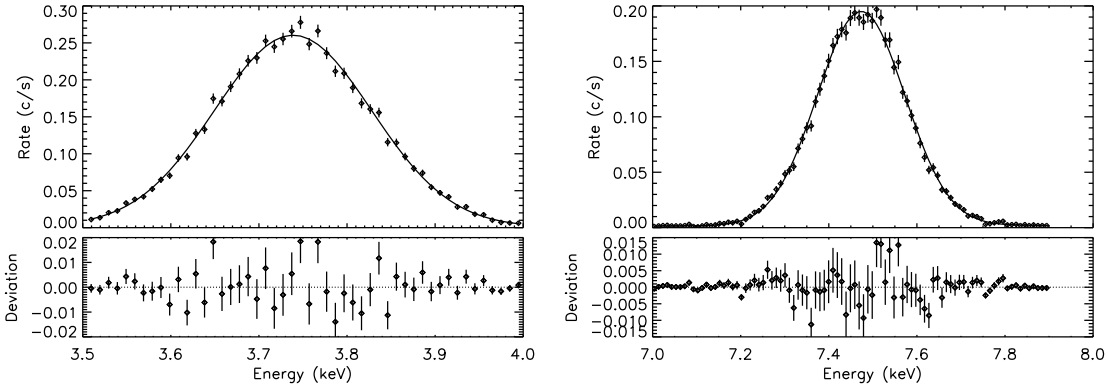

Figure 3.14: Gaussian fit to the lines corresponding to the first (**a**) and second (**b**) order of diffraction on aluminum flat crystals when continuum photons are incident. Only a narrow output collimator is used.

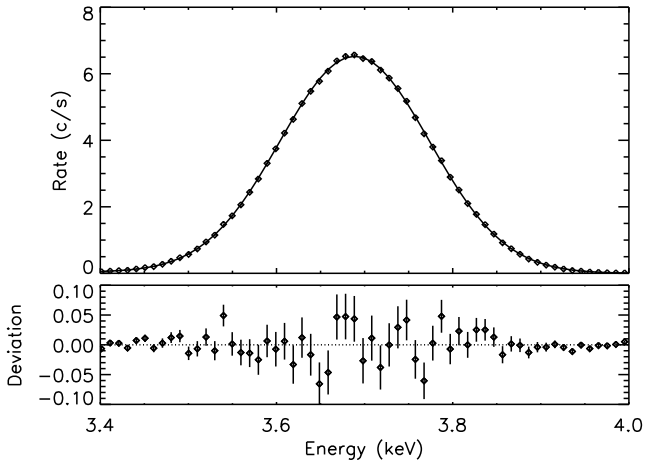

Figure 3.15: Gaussian fit to the calcium Kα line diffracted on the aluminum flat crystal.

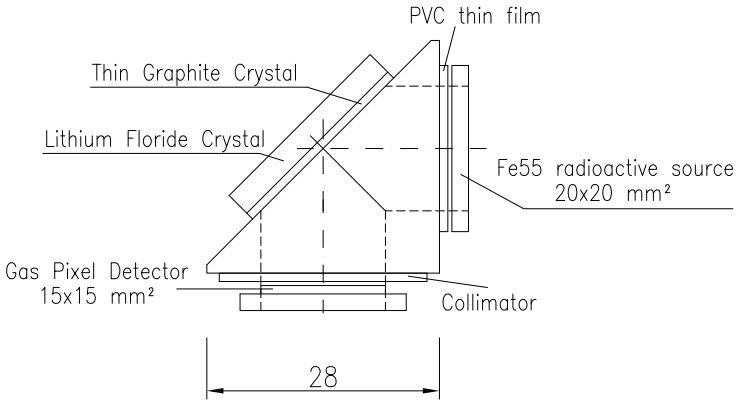

Figure 3.16: Sketch of the on-board polarized source.

From Table 3.2 it results that 5.899 keV Kα manganese emission, readily produced from Fe^{55} decay, is well in agreement with the diffraction at 45° on a lithium floride crystal. However the sensitivity of photoelectric polarimeters such as the Gas Pixel Detector peaks at about 3 keV and then manganese emission doesn't cover the energy range of major interest.

This issue can be overcome by means of diffraction on a mosaic graphite crystal. Its Bragg energy at 45° is about 2.61 keV and hence near the peak of sensitivity of the GPD; moreover graphite is the crystal with the higher integrated reflectivity. The Kα line at 2.622 keV of chlorine is well in accordance with the diffraction on graphite but unfortunately this line can't be directly produced by means of a radioactive source. However it could be extracted from a thin PVC film (C_2H_3Cl) irradiated by the Fe^{55} source. Since the 2.622 and 5.899 keV lines are spectrally well resolved by the Gas Pixel Detector, they can provide simultaneously an effective instrumental calibration on a wide energy range.

In Fig. 3.16 a sketch of the calibration source is shown. A single radioactive Fe^{55} nuclide produces unpolarized photons at 5.899 keV which are diffracted on a lithium floride crystal. A thin PVC film is mounted between the radioactive source and the crystal and partially absorbs X-ray photons produced by Fe^{55}. Chlorine is the atoms with the highest atomic number within those composing the PVC and hence photons are mainly absorbed by this element. Eventually they are re-emitted isotropically as 2.622 keV fluorescence emission and a fraction of photons which are incident at the right angle on a thin graphite crystal, placed in front of the lithium floride, is eventually diffracted. If the graphite crystal thickness is 22 μm, i.e. such that the photon path is equal to the absorption length of 2.622 keV radiation, it results 85% transparent to 5.899 keV photons.

The expected degree of polarization is 99.86% and 88.22% for the 2.622 and 5.899 keV lines respectively (see Table 3.2). The entire 15×15 mm^2 surface of the GPD could be calibrated at the same time with a single Fe^{55} radioactive source with the same effective surface. Since the incident photons are monochromatic, no collimators are required to constrain the diffraction angle at nearly 45°. Photons at 2.622 and 5.899 keV can be diffracted only if they are incident with a grazing angle equal to 44.82° and 47.56° on the

	Graphite crystal	Lithium Floride crystal
2.622 keV Kα Chlorine	44.8°	—
2.816 keV Kβ Chlorine	41.1°	—
5.899 keV Kα Manganese	18.3	47.6
6.490 keV Kβ Manganese	16.6	42.1

Table 3.5: Diffraction angle for monochromatic photons produced by Fe^{55} decay and chlorine fluorescence on graphite and lithium floride crystals. The diffraction of chlorine lines on the lithium floride crystal is not possible. The production of Kβ chlorine emission is strongly suppressed respect to the Kα and hence it is reported only for completeness.

graphite and lithium fluorite crystal respectively.

A broad collimator could be anyhow needed to exclude stray radiation. Neglecting the scattered photons, monochromatic radiation at 2.622, 5.899 and 6.490 keV is isotropically distributed, where the radiation at 6.490 keV is produced as Kβ manganese emission obtained from Fe^{55} decay. A collimator may be required to stop diffraction on lithium floride of 6.490 keV photons, which occurs at an angle close to 45° (see Table 3.5). A custom capillary plates could be used to provide such a collimation with very limited size.

This calibration source has a very limited volume (of the order of 28×28×28 mm^3) and hence it could be easily placed on the top of the GPD in the focal plane of future satellite missions (see Chapter 6).

3.4.1 The PVC thickness

The thickness of the PVC film should be chosen to assure a good transparency for the 5.899 keV photons to perform the high energy calibration but it should also maximize the production of chlorine fluorescence emission. The optimal thickness can be derived by balancing the absorption of 5.899 and 6.490 keV photons in the PVC and the self-transparency to 2.622 keV radiation.

For a monochromatic parallel beam of radiation orthogonally incident to the PVC film, the transfer equation at energy E can be written as (Rybicki and Lightman, 1979):

$$I_E(L) = I_E(0)e^{-\rho\mu_E L} + \int_0^L e^{-\rho\mu_E(L-x)} j_E(x)dx, \tag{3.4}$$

where $I(L)$ is the beam intensity at a depth L, $\rho = 1.5$ g/cm^3 is the PVC density, μ_E is the absorption coefficient at the energy E and $j_E(x)$ is the emission coefficient at the depth x. Considering only the chlorine line at 2.622 keV, $I_E(0) = 0$ and then:

$$I_{2.6}(L) = \int_0^L e^{-\rho\mu_{2.6}(L-x)} j_{2.6}(x)dx. \tag{3.5}$$

The emission coefficient depends on the fluorescence production and is directly proportional to the absorbed photons. Assuming that incident photons have energy equal to

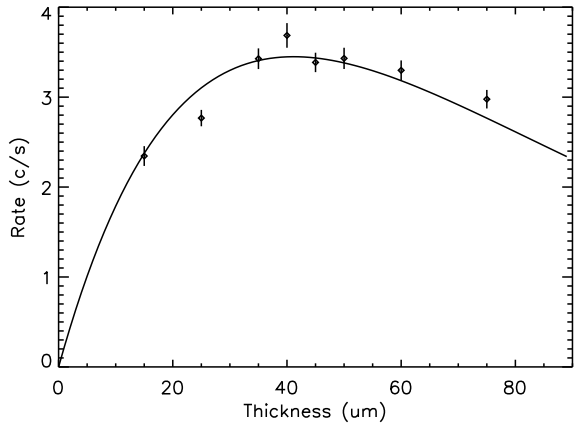

Figure 3.17: Measured counting rate of the Kα line of chlorine with respect to the PVC thickness. Only the normalization of the fitting function (Eq. 3.9) is a free parameter. A 40 μCi Fe^{55} source is used to extract the fluorescence emission.

5.899 keV[1], the dependence of the emissivity on x can be expressed with:

$$j_{2.6}(x) \propto e^{-\rho\mu_{5.9}x}. \tag{3.6}$$

Replacing Eq. 3.6 in Eq. 3.5, it is obtained:

$$I_{2.6}(L) \propto \frac{e^{-\rho\mu_{5.9}L} - e^{-\rho\mu_{2.6}L}}{\rho\left(\mu_{2.6} - \mu_{5.9}\right)}, \tag{3.7}$$

where the function $I_{2.6}(L)$ peaks at:

$$L_w = \frac{1}{\rho\left(\mu_{2.6} - \mu_{5.9}\right)} \ln\left(\frac{\mu_{2.6}}{\mu_{5.9}}\right) \approx 41\mu m. \tag{3.8}$$

In Fig. 3.17 the measured counting rate of the chlorine 2.622 fluorescence line extracted with a 40 μCi Fe^{55} source is reported as a function of the PVC thickness. The curve is fitted with the function:

$$I_{2.6}(x) = K\left[e^{-\rho\mu_{5.9}L} - e^{-\rho\mu_{2.6}L}\right], \tag{3.9}$$

where only the normalization constant K is a free parameter. The good agreement between expected and measured counting rate confirms that the fluorescence from chlorine is maximized with a $\sim 40\mu m$ thick PVC film. Such a thin film is 93% transparent to 5.899 keV radiation, hence allowing also an efficient high energy calibration.

[1]The contribution of 6.490 keV photons to the fluorescence emission is about a factor 10 lower.

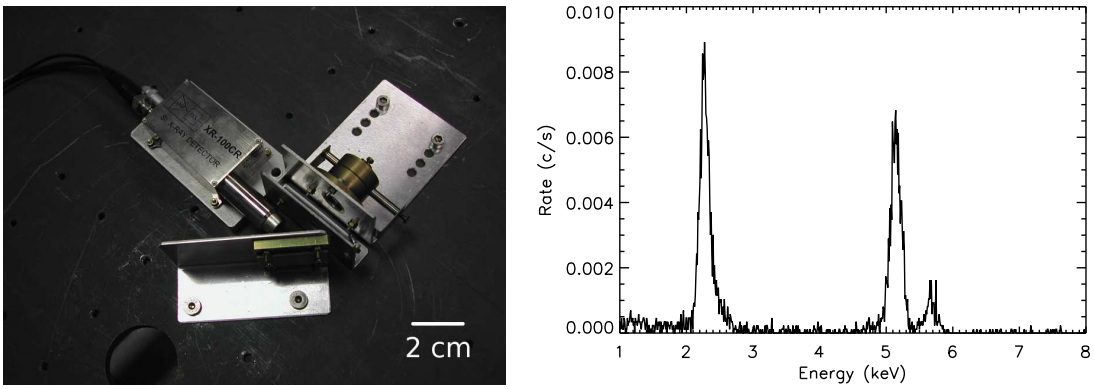

(a) **(b)**

Figure 3.18: (**a**) Setup for the study of diffraction of chlorine Kα line on the graphite crystal. The Fe^{55} source is on the top right in a brass holder, while the graphite crystal is on the bottom. (**b**) Spectrum of the diffracted emission when a 40 μCi Fe^{55} is used. The fluorescence of manganese at 5.899 keV and 6.490 keV is scattered and not diffracted, even if a high polarization is expected in any case.

3.4.2 Intensity of the Fe^{55} radioactive source

The intensity of the Fe^{55} source required to achieve a reasonable flux on the GPD is estimated by means of a weak 40 μCi Fe^{55} source. The latter is placed in a brass holder on a optical table and extracts chlorine fluorescence emission from a 45 μm PVC film. Eventually it is diffracted on a grade B graphite crystal (see Fig. 3.18a). Collimators are not used.

The spectrum (see Fig. 3.18b) is measured with the Si-PIN Amptek detector. It is composed of the diffracted radiation at 2.622 keV and scattered photons produced by the Fe^{55} source. The latter component is only slightly less intense with respect to the diffracted one but it should be negligible in the actual calibration source. Indeed graphite thickness would be reduced to some tens of micron and hence it would be almost transparent to the 5.899 and 6.490 keV photons.

A gaussian fit to the line at 2.622 keV returns a counting rate of about 0.13 counts/s. Taking into account for the air absorption, the Amptek detector 5×5 mm^2 area and the efficiency of the Gas Pixel Detector filled with the standard He 20% DME 80% mixture, a rate of about 110 counts/s is expected for a 5 mCi source. Since the decay time of the Fe^{55} is about 2.7 years, a moderately strong source is sufficient for the calibration of the Gas Pixel Detector for the whole operational life of a dedicated small space borne mission.

Chapter 4

A facility for the calibration of X-ray polarimeters

In this Chapter a facility for the systematic calibration of the GPD is presented. It has been built in the laboratory of IASF/INAF of Rome and can produce both polarized and unpolarized monochromatic radiation. The former is produced by means of an improved version of the calibration source based on Bragg diffraction: radiation in the energy range from 1.65 to more than 10 keV is available. Instead unpolarized photons are obtained with radioactive sources or X-ray tubes. The beam can be collimated by means of capillary plates, narrow collimators and diaphragms, allowing a trade-off between collimation and high fluxes at different energies. The position and the inclination of the beam is accurately arranged by means of high precision motorized stages, whose movements are controlled via computer so that long and automatic sequences of measurements can be done.

This facility allows a great step forward in the development of the GPD, since it is designed to completely characterize the instrument in its whole energy range. Possible systematic effects in the measurement of degree and angle of polarization can be investigated and in particular it allows to study the reconstruction of the angle of polarization and to map the response of the detector (see Chapter 5). A further innovative application, extensively described in Chapter 7, is the study of the systematic effects which arise when photons are not incident orthogonally to the detector.

Despite this facility is designed for the use with the GPD, it was (and will be) effectively used even for the calibration of other devices. Imaging detectors can exploit the fine positioning of the beam and spectrometers can be calibrated thanks to the monochromatic beams produced by means of Bragg diffraction (Feroci et al., 2009).

The work presented in this Chapter was partially published by Muleri et al. (2008c).

4.1 X-ray sources

The calibration of the GPD must be performed with both polarized and unpolarized photons. The latter are easily obtained with radioactive sources or X-ray tubes (see

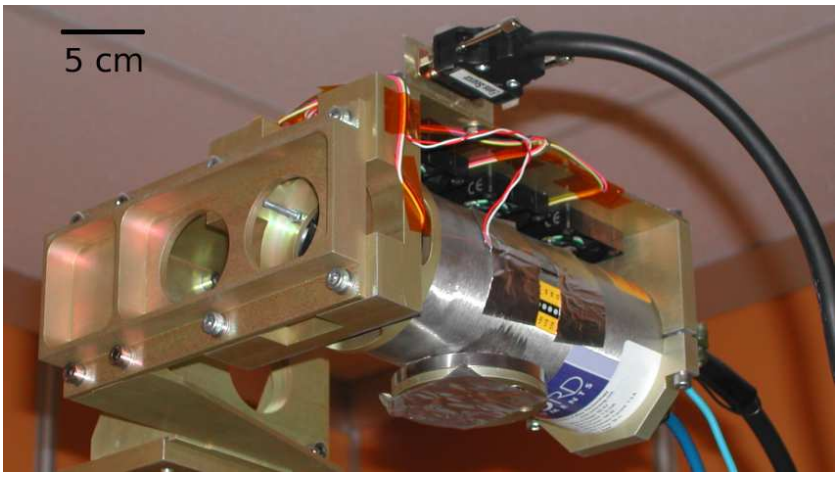

Figure 4.1: One of the new X-ray tubes with its cooling system. It is mounted on the mechanical assembly described in Sec. 4.2. X-rays are emitted downwards.

Sec. 4.1.2). Polarized radiation is instead produced with a more powerful version of the source based on Bragg diffraction. That first prototype (see Chapter 3) is based on a small power X-ray tube (200 mW) and the flux produced is insufficient to obtained beams collimated and diaphragmed. For example the measurement of the space resolution of the GPD requires a beam with a diameter smaller than 50 μm, which corresponds to the size of the pixels. The maximum flux obtained from the prototype Bragg source is reached with the diffraction of the calcium line (see Table 3.4) and is ∼140 counts/s on a diameter about 5 mm. Hence a flux of the order of $\sim 140 \times (50/5000)^2 \approx 0.01$ is expected when a diaphragm of 50 μm is used.

Both polarized and unpolarized sources described in this Section are eventually interfaced with the mechanical assembly presented in Sec. 4.2.

4.1.1 The improved Bragg source

A source based on Bragg diffraction was already presented in Chapter 3; in this Section an improved version of that first prototype is described. It shares the same base-design as the prototype. The same lead-glass capillary plates are used to collimate X-rays, since they assure good collimation with limited size. Unpolarized X-rays are produced by means of much more powerful commercial tubes, manufactured by Oxford Instrument. They can absorb a maximum power of 50 W and hence a factor 250 higher than those used in the prototype source and a maximum current of 1 mA and high voltages between 4 and 50 kV can be applied.

A picture of one of this new medium-power tubes is reported in Fig. 4.1. X-rays are emitted orthogonally to the tube through a thin beryllium window. Four fans cool the case and a temperature sensor is used to check that its temperature is always well below 55° C at which the manufacturer declares that the anode may be irremediable damaged.

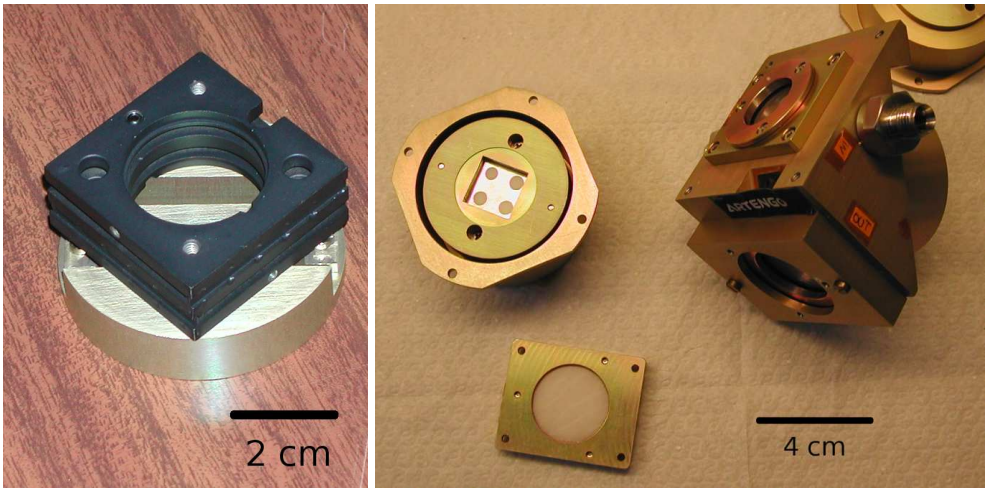

(a) **(b)**

Figure 4.2: (**a**) The manual stage on which each crystal is mounted. It allows two axes tilt regulation in the range $\pm 3°$ and then an optimum alignment to the Bragg condition. The aluminum case of the crystal is below the stage. (**b**) The mounted polarizer (right), the case of a crystal (left) and a capillary plate (bottom).

Three different tubes with anode of molybdenum, rhodium and titanium are used to produce line emission at 2.293, 2.691 and 4.511 keV respectively. These energies are in accordance with Bragg diffraction at about 45° from rhodium (001), germanium (111) and fluorite (CaF_2, 220) crystals (see Table 3.2). An ADP (101) and a PET (002) crystals are used to produce polarized emission at 1.65 and 2.04 keV by means of diffraction of continuum radiation.

An important difference between the prototype and the improved version of the source is that in the latter each crystal case is mounted on a manual stage which allows two axes tilt regulation in the range $\pm 3°$ (see Fig. 4.2a). It is regulated to achieve the best alignment to the Bragg condition by means of laser reflection and X-ray measurements. A mirror mounted on the case of the crystal is used to reach the optimum angle between the crystal and the collimators, which are partially reflective. The inclination is eventually refined with X-ray measurements to reach the highest flux in the case of monochromatic incident emission, or the right energy when continuum photons are used. The crystal and the capillary plates are mounted on a central body, called polarizer (see Fig. 4.2b). The complete source, consisting of the polarizer and the X-ray tube, is shown in Fig. 4.3.

The role of capillary plates is more critical in the case of the improved source since much higher fluxes are produced by medium-power tubes. Even a small fraction of the incident photons which are not diffracted on the crystal can significantly affect the output spectrum. Two issues can detach the output radiation from the ideal condition of monochromatic and highly polarized photons. The first one is that radiation can be scattered at nearly 90° on the crystal or on its case and then photons are polarized but not monochromatic. The second issue is that the input radiation is partially absorbed

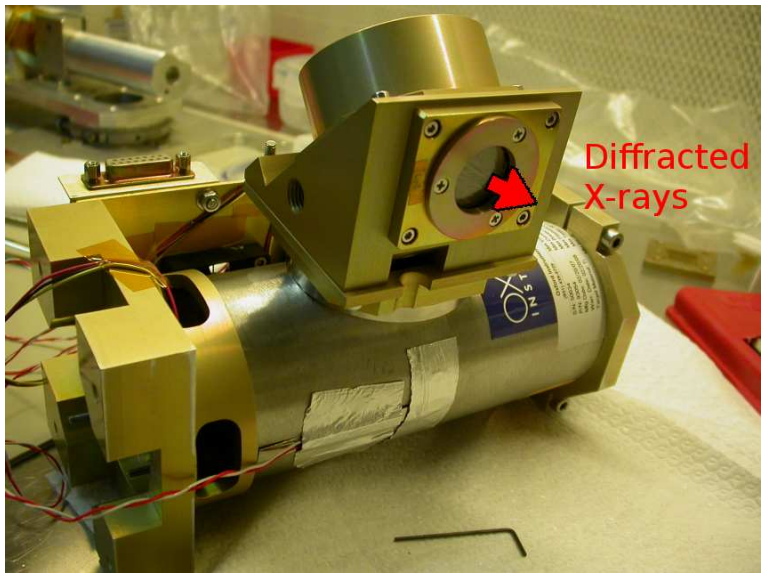

(a)

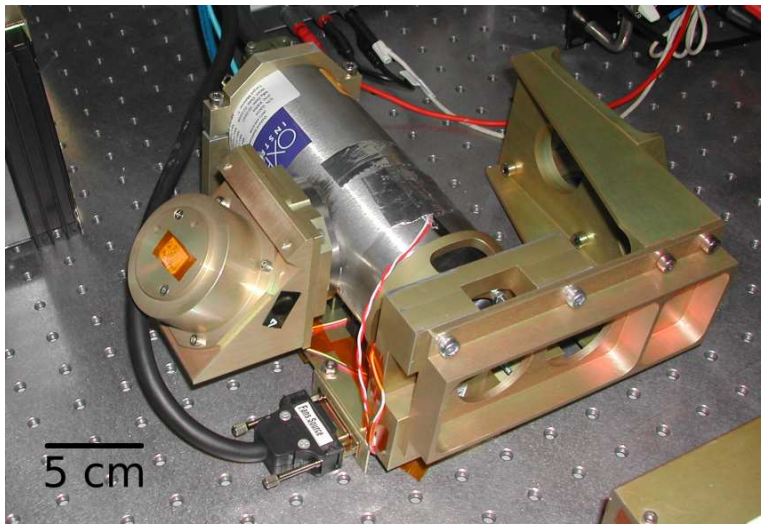

(b)

Figure 4.3: The polarized source composed of the polarizer and the X-ray tube. In (**b**) the interface with the assembly described in Sec. 4.2 is also visible.

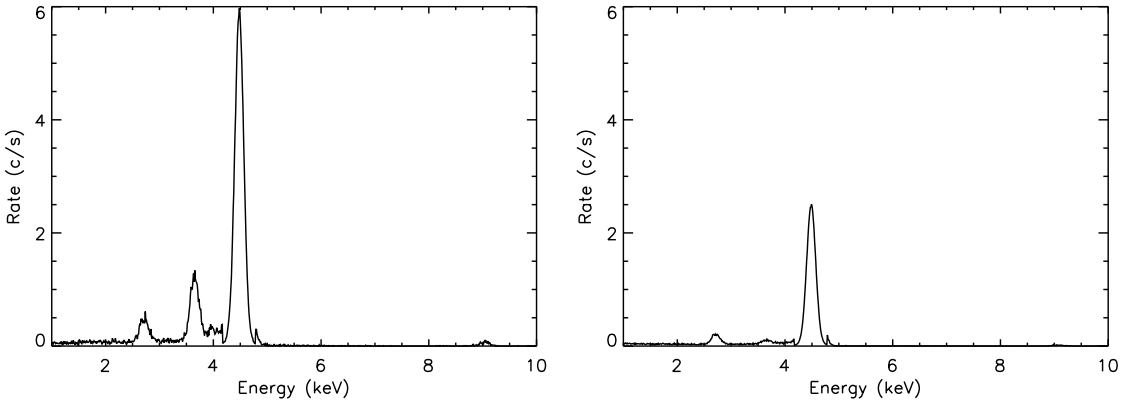

(a) **(b)**

Figure 4.4: Spectrum of the source when the X-ray tube with titanium anode and the fluorite crystal are used, measured with the Amptek XR100CR detector. Note that the flux of the line at 4.511 keV was multiplied by 0.1 to make it comparable with other features of the spectrum. The peak in the middle is the fluorescence of the calcium, while the peak on the left is the escape peak of the line at 4.511 keV from the silicon detector. (**a**) One collimator with $\frac{1}{40}$ is used to constrain the direction of diffracted photons. (**b**) The same as (**a**), but when $\frac{1}{40}$ and $\frac{1}{100}$ collimators are used to constrain the direction of input and output radiation respectively.

in the crystal and aluminum case and consequently unpolarized fluorescence emission is isotropically produced. This problem is especially important when fluorescence lines can be confused with those produced with diffraction. As an example this occurs when 1.65 keV polarized photons are produced with the ADP crystal, since the aluminum Kα fluorescence is at 1.486 keV. However it occurs even when the fluorite crystal is used: this crystal contains calcium and the 3.692 Kα fluorescence of this element has a comparable energy (and hence absorption) with respect to the polarized photons at 4.511 keV produced with 45° diffraction on that crystal.

The contribution to the spectrum of fluorescence and scattered radiation can be decreased with respect to that of polarized photons by means of narrower collimators. The first two components are approximately proportional to the total incident radiation; on the contrary the intensity of diffracted photons depends only on the flux of the line incident at 45° on the crystal, which is basically not modified by the presence of narrower collimators.

An example of the effect of narrower collimators is reported in Fig. 4.4. The spectra obtained from diffraction on the fluorite crystal is shown in Fig. 4.4a and in Fig. 4.4b when one or two collimators are used. The ratio between the fluxes of the polarized line at 4.511 keV and that of the fluorescence of calcium at 3.692 keV is reported in Table 4.1 and changes from $\sim$60 to $\sim$440, with a reduction of the flux of the polarized line of a factor ~ 2.

Each crystal was chosen so that the first order of diffraction occurs in the energy range between $\sim$1.5 and $\sim$5 keV. This covers the range of maximum sensitivity of the current

Collimators	Flux^{polarized} (c/s)	Flux^{fluorescence} (c/s)	Ratio
Input: $\frac{1}{40}$	1073.7±3.0	18.04±0.47	∼60
Input: $\frac{1}{40}$, output $\frac{1}{100}$	458.38±0.79	1.046±0.072	∼440

Table 4.1: Ratio between the fluxes of the polarized line at 4.511 keV and that of the fluorescence at 3.692 keV. The same fluorite crystal and X-ray tube with titanium anode are used, however with different configurations of collimators.

version of the GPD and for the same reason X-ray tubes with lines in accordance with crystals in this energy range was selected. However the continuum radiation produced with X-ray tubes by bremsstrahlung can be used to produce also high energy and polarized radiation exploiting higher orders of diffraction, occurring at energies which are integer multiples of first order. The medium-power X-ray tubes can be very efficiently used to this aim since the high voltage which accelerate the electrons can be controlled independently from their current. This allows to select the maximum energy of the photons and the flux separately.

For example polarized photons at 9.07 keV can be produced exploiting the second order of diffraction from fluorite at exactly 45°. In this case the high voltage can be set at 13.5 kV, namely just below the energy of the third order of diffraction, to increase the flux which scales as the square of the high voltage. At the same time the current can be independently varied up to 1 mA to linearly increase the flux. If it is still not sufficient, the high voltage can be further increased but in this case the third order of diffraction at 13.61 keV is also produced.

Continuum emission for diffraction on ADP or PET is typically produced with the tube with titanium anode, since it has the thinner window (75 μm) among new medium-power tubes. Rhodium and molybdenum tubes have windows 125 μm thick which then absorb more efficiently low energy photons. However, when higher orders are produced, anode made of elements with high atomic number Z are preferred because above a few keV the window is transparent to X-rays in any case but the production of bremsstrahlung increases as Z^2.

In Fig. 4.5 the spectrum between 1 and 11 keV obtained with diffraction of continuum radiation on the PET crystal is reported. The first five orders are visible: their fluxes depend mainly on the different efficiency of the diffraction for each order and the spectrum of the unpolarized incident radiation. The fluxes of the lines, fitted with a gaussian profile, are reported in Table 4.2. Note that helium flowing was used to avoid that the large part of the flux is absorbed by air.

4.1.2 Unpolarized X-rays sources

The improved and the prototype versions of the Bragg source are used to produce polarized radiation. However the direct emission of the medium-power X-ray tubes can also be used to obtain unpolarized photons. In this case the spectrum is composed of both fluorescence lines of the anode and continuum bremsstrahlung (see Fig. 3.6).

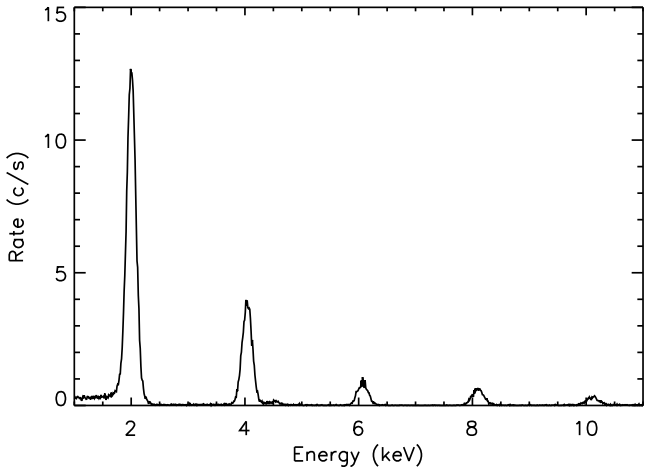

Figure 4.5: Spectrum between 1 and 11 keV of radiation diffracted on the PET crystal. Input radiation is obtained with the X-ray tube with titanium anode (15 kV, 0.5 mA). The first five orders of diffraction are visible.

	Flux (c/s)		Flux (c/s)
2.04 keV - I order	224.0±1.5	8.16 keV - IV order	13.44±0.43
4.08 keV - II order	73.5±1.0	10.20 keV - V order	7.41±0.27
6.12 keV - III order	17.10±0.39		

Table 4.2: Flux of the lines corresponding to different orders of diffraction on PET crystal. The incident radiation is produced with the titanium tube (15 kV, 0.5 mA).

The fluorescence lines exploited for diffraction on crystals have energy 2.293, 2.691 and 4.511 keV. The first and the second correspond to the Lα emission from molybdenum and rhodium and the third is the Kα line of titanium. There are however many other fluorescence lines from these elements and the most intense and useful for calibration of X-ray instruments are listed in Table 4.3.

The presence of continuum emission can be a disadvantage for calibrations, however the flux without the polarizer is obviously higher. Note that if an unpolarized beam is required, the continuum bremsstrahlung emission must be used with care since a low degree of polarization could be present in this component, depending on the accurate geometry of the breaking of electrons in the target (see, for example, Eberhard and Werner, 2004). The polarization, if present, could be completely removed with the continuous rotation of the detector with respect to the beam during the measurement. This operation is easily performed with the mechanical assembly described below.

Monochromatic and completely unpolarized emission can be produced by means of radioactive sources. A moderately intense Fe^{55} nuclide which emits at 5.899 and 6.490 keV and whose intensity was 5 mCi in January 2008 is available in the facility.

Radiation produced in the facility can be obtained directly with X-ray tubes, the Fe^{55}

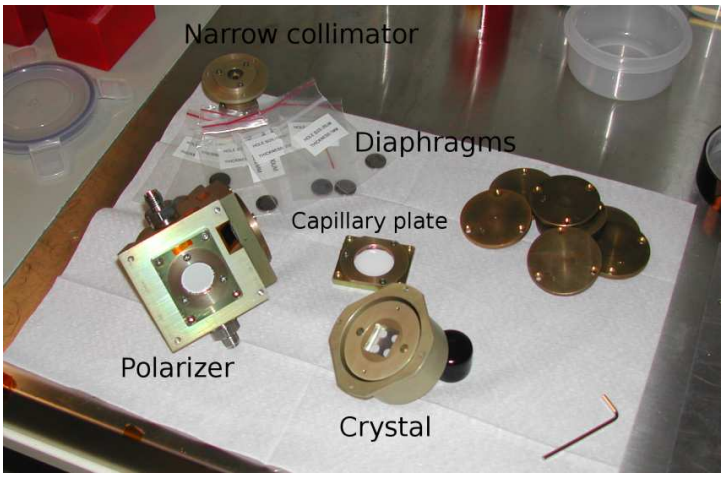

Figure 4.6: Diaphragms used to control the size of the beam. Their diameter varies from 25 μm and 2 mm. The very narrow collimator which is obtained with the use of two diaphragms is on the top left.

radioactive source and the prototype and the improved polarizers. A set of diaphragms from 25 μm to 2 mm can be used to control the size of the beam and a very narrow collimator can be constructed by means of two diaphragms separated by a distance of 40 mm (see Fig. 4.6). It can produce a beam collimated up to a semiaperture $\sim 1/1000 \sim 3'$ with a size of some tens of μm, but obviously in this case fluxes are rather small.

In Table 4.3 the properties of the X-ray sources available in our facility are summarized including both the prototype and the improved polarized sources. Radiation from 1.65 keV to more than 10 keV can be produced with first or higher orders of diffraction, with three strong lines in the energy range of GPD maximum sensitivity. In this case highly collimated and diaphragmed polarized beams can be obtained. In the Table are also reported the unpolarized emission which can be produced with medium-power X-ray tubes and radioactive sources.

4.2 Mechanical design and construction

The source based on Bragg diffraction has allowed to overcome the age-old problem of the measurement of the low energy performances of the GPD which will be presented in Chapter 5. The next step in the calibration of the instrument is the systematic study of its sensitivity and uniformity with space-controlled beams. The sources of polarized and unpolarized radiation have been presented in Sec 4.1: in this Section the mechanical assembly and the movements exploited to move the beam are described.

The design of the facility has been driven by three classes of systematic measurements. The first is the sampling of the relation between the incident and the reconstructed angle of polarization: the lack of systematic effects proves the lack of azimuthal asymmetries in the reconstruction of the tracks, allowing to design polarimeters which don't

Incident radiation (X-ray tube)	E (keV)	Crystal	θ	$\mathcal{P}$
Polarized radiation				
Continuum	1.65	ADP ($NH_4H_2PO_4$, 101)	45°	∼1.0
Continuum	2.04	PET ($C(CH_2OH)_4$, 002)	45°	∼1.0
Lα Molybdenum (50 W)	2.293	Rhodium (001)	45.36°	0.9994
Continuum	2.61	Graphite (002)	45°	∼1.0
Lα Rhodium (50 W)	2.691	Germanium (111)	44.86°	0.9926
Kα Calcium (200 mW)	3.692	Aluminum (111)	45.88°	0.9938
Kα Titanium (50 W)	4.511	Fluorite CaF_2 (220)	45.37°	0.9994
Kα Manganese (Fe^{55} radioactive source, 5mCi in 2008-01)	5.899	Lithium Floride (220)	47.56°	0.8822
Kα Copper (200 mV)	8.048	Germanium (333)	45.06°	0.9849
Unpolarized radiation				
Lα Molybdenum (50 W)	2.293	—	—	∼0
Lα Rhodium (50 W)	2.691	—	—	∼0
Kα Titanium (50 W)	4.511	—	—	∼0
Kα Manganese (Fe^{55} radioactive source, 5mCi in 2008-01)	5.899	—	—	0
Kβ Manganese (Fe^{55} radioactive source, 5mCi in 2008-01)	6.490	—	—	0
Kα Molybdenum (50 W)	17.479	—	—	∼0
Kα Rhodium (50 W)	20.216	—	—	∼0

Table 4.3: X-ray sources available in our facility. Polarized sources are in the first part of the Table. The prototype source is reported because it can be mounted on the mechanical assembly described in Sec. 4.2. Continuum radiation is used for diffraction on ADP, PET and graphite crystals. It can be produced by any tube since no line emission in accordance with the Bragg energy at 45° is available. In this case the energy and the polarization in the Table are referred to the photons diffracted at exactly 45°. Only the energies corresponding to the first order of diffraction are reported but note that each crystal can produce polarized radiation even at energies which are integer multiples of those reported. The degree of polarization is calculated from results by Henke et al. (1993). Unpolarized sources include medium-power X-ray tubes and radioactive sources.

need to be rotated. This is very important for at least two reasons: the first is that the instrument has a lower cost and the second that it is more reliable. The lack of systematic effects which must be averaged allows a higher confidence in the results and this is particularly true in X-ray astronomy since most of the sources are variable. The rotation of the instrument will produce a situation in which the flux will not be the same at different angles and the collected flux should be normalized to the actual rate. However an independent monitoring of the source flux (and spectrum) could be required.

Physically systematic effects in the response of the GPD may be caused by the hexagonal pattern of the chip pixels and in this case a periodicity of 60° should emerge; moreover incorrect angular reconstruction could be also caused by differences in the response of the GPD in different regions of its surface. A preliminary study of the correlation between the incident and reconstructed angle of polarization is presented in Chapter 5.

The GPD is an imaging device and the non-uniformity of the response could prevent polarimetry of extended sources. The XY-mapping of the response of the GPD with polarized and unpolarized narrow beams is then the second class of systematic studies that should be performed.

The small area of the current version of the GPD requires the presence of an X-ray optics to collect enough photons to perform polarimetry at a few % level as needed by astrophysical expectations. The behavior of X-ray optics with respect to the polarization of focused radiation will be faced up in Appendix B on the basis of the even meagre literature currently available. Here it should be noted that another problem could affect the operation of the GPD: the absorption of photons occurs in a cell gas 1 cm thick and then the focal plane is not infinitely thin with respect to the focal length. Since photons are incident not orthogonally to the detector, their inclined penetration in the gas causes a blurring which degrades the angular resolution.

This effect can be explored by means of measurements with beams inclined of a few degrees, which is the inclination expected for photons focused by a grazing incidence optics. However the facility is designed to perform also measurements with beams inclined up to $\sim$60°, since there is an increasing interest in the development of X-ray polarimeters with large field of view. A discussion of the use of the GPD in this field will be presented in Chapter 7 as a part of this thesis.

Note that the use of the facility is not limited to the measurements presented above. There is the maximum freedom both in the radiation which can be produced and the movements of the beam. Both the instrument and the source can be easily changed and adapted to specific needs.

4.2.1 Movements

The detector is mounted on a platform which can be rotated, inclined and moved with respect to the beam (see Fig. 4.7). The choice to move the detector instead of the sources is due to its lower weight. The improved Bragg source weights about 4.3 kg against the 1.6 kg of the GPD.

Two "towers" support the detector and the source and eight motorized stages and two manual ones are used to control their reciprocal position. Moreover the source is

mounted on a rail with a graduated scale which allows a quick movement when maintenance operations are performed on the tower supporting the detector.

Both the detector and the sources are mounted on an optical table in a dedicated room which shields X-ray radiation with a 1 mm of lead. All the motorized stages are connected to a controller, which in turn is connected with a PC by means of an ethernet cable. The motorized stages can be manually moved with a remote control or a web interface of the controller, the latter being accessible to personal computers placed outside of the shielded room.

The mechanical design of the facility (see Fig. 4.7a) was performed at the IASF/INAF of Rome while the realization of the single mechanical parts was outsourced. A picture of the complete facility is reported in Fig. 4.7b.

The stages are divided into two groups. The first includes five motorized stages which actually change the direction of the detector with respect to the beam; the second one is used to align the beam with the detector. In the former group there are (see fig. 4.8):

1. δ (*inclination angle*, resolution 1″): The main purpose of this stage is to allow the inclination of the detector at large angles, typically between +60 and -60°. Moreover it is used with η to automatically adjust the tilt angle of the detector, i.e. to align the detector orthogonally to the incident beam (see Sec. 4.3.2).

2. ϵ (*polarization angle*, resolution 0.2″): This stage rotates the tower supporting the detector, then changing the direction of polarization of the beam. The range is between 0 and 360°.

3. x: (resolution 0.5 μm) This stage allows the XY mapping together with y and it is used to center the detector with the beam. Its range is $\pm$25 mm.

4. y: (resolution 0.5 μm) The role of this stage is complementary to x.

5. z: This stage is used to adjust the distance between the detector and the source. X-rays at energy of a few keV are heavily affected by air absorption and then the distance from the source and the detector must be reduced. However, when the measurements at large angles of inclination are performed, the rotation axis of δ should cross the center of the gas cell of the GPD to prevent the movement of the beam on the detector with the increase of the inclination angle (see Sec. 4.3.2). This stage for all practical purposes has two positions, UP when the distance from the source is reduced, and DOWN when measurements at large inclination are performed.

The stages which instead are used only to align the detector with the beam are:

6. η: This motorized stage allows to tilt the plane of the detector to align it orthogonally to the incident beam. It is composed of a motorized linear actuator which drives the rotation of the upper plane of a goniometer. The linear range of the actuator is 12.5 mm and it can tilt the plane of the detector in the range $\pm$10°.

7. xso (resolution 0.1 μm): The purpose of this motorized stage is to center, together with yso, the beam with the axis of rotation of the stage ϵ. They must be aligned

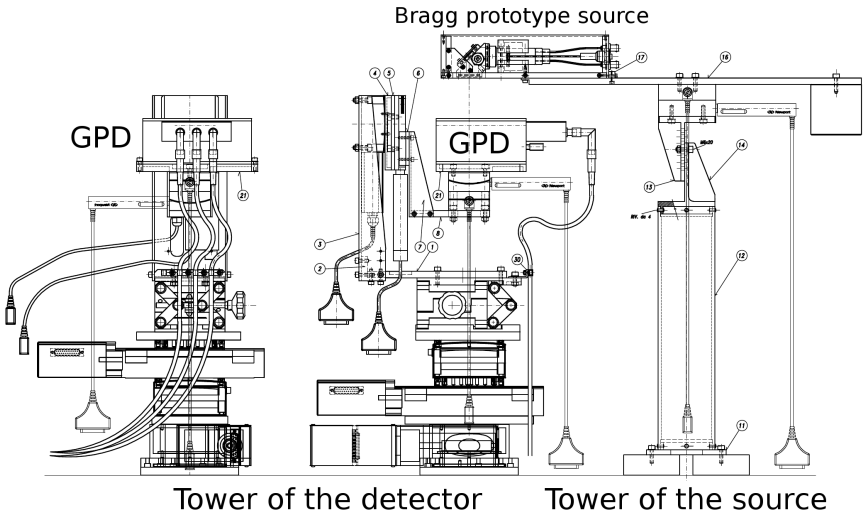

(a)

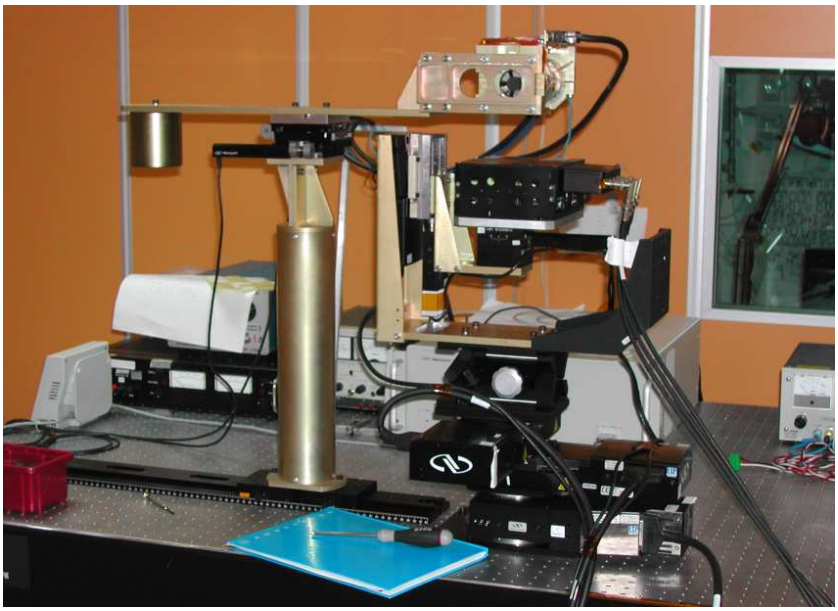

(b)

Figure 4.7: The mechanical drawing of the facility (**a**) and its picture (**b**). In (**b**) the source is on the left and the tower supporting the detector on the right. In this case the unpolarized direct radiation of the titanium anode X-ray tube is used. In the background a wall of the shielded room is visible. The window on the left is made of lead glass.

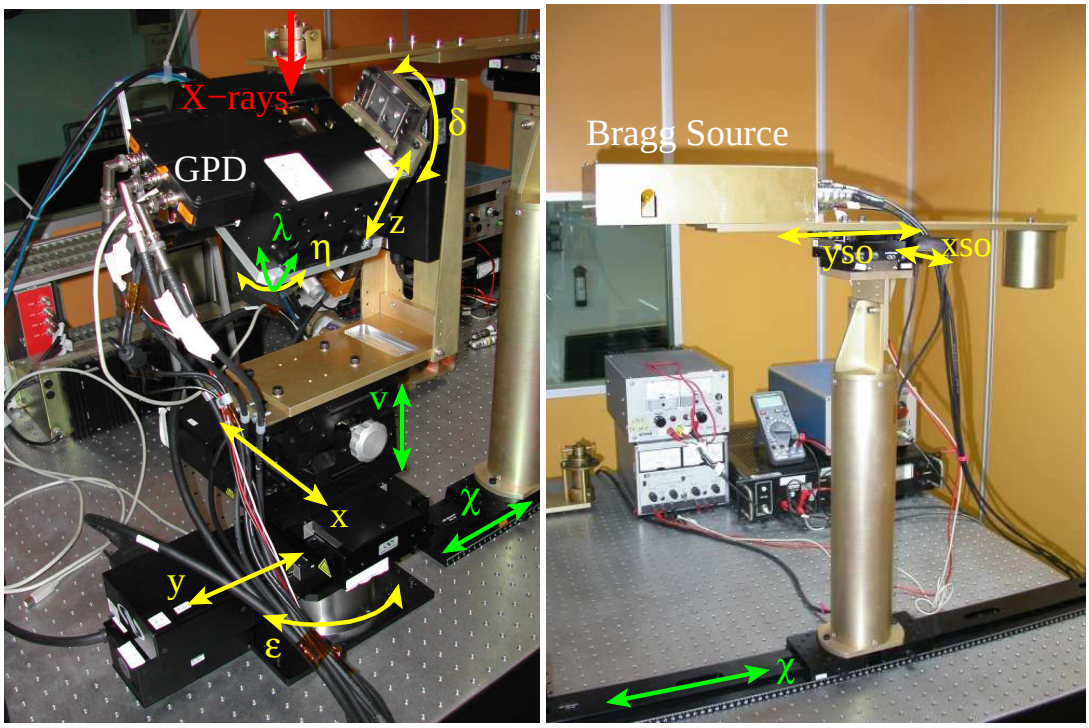

(a) **(b)**

Figure 4.8: The definition of the name of the stages for the towers supporting the detector (**a**) and the source (**b**). In yellow are the motorized stages, while in green are the manual ones.

to study the reconstruction of the angle of polarization. Indeed when the detector is rotated with ϵ, the beam should remain in the same point of the detector. This occurs only if the beam and the axis of rotation of ϵ are aligned (see Fig. 4.9).

8. yso (resolution 0.1 μm): The role of this motorized stage is complementary to xso.

9. λ: This stage allows a manual tilt regulation of the plane of the detector. For all practical purposes this stage is redundant with respect to δ.

10. χ: The rail which allows the quick movement of the source when maintenance operation are performed on the tower. The rail is provided with a graduated scale with 1 mm pitch.

—. ν: A further stage allows a vertical adjustment with a range of 44 mm with a different purpose with respect to z. The latter moves only the "basket" which supports the detector and which can be inclined with δ. Instead ν moves all the upper part of the tower, namely both the basket and its mechanical support. This stage has not a graduate scale and then it will not be considered as an independent stage in the following.

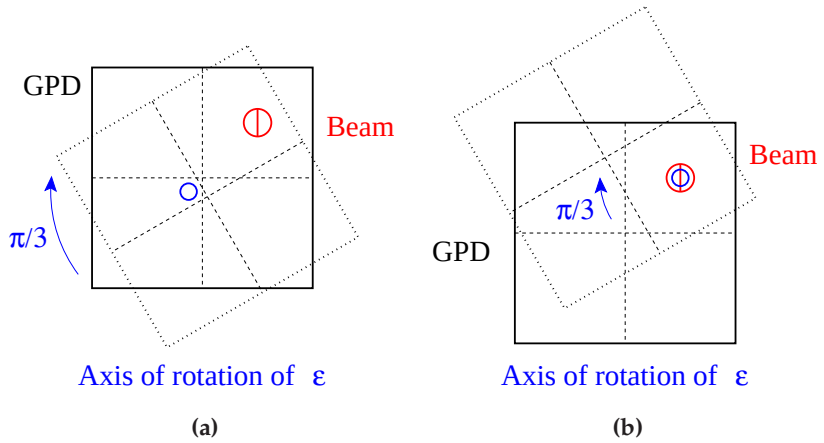

Figure 4.9: Effect of the misalignment of the beam with the axis of rotation of ϵ (**a**). The beam doesn't move with respect of the position on the detector only if they are aligned (**b**).

In Table 4.4 the characteristics of the motorized movements are summarized. The stages are manufactured by Newport and their weights, on-axis maximum load and range are also reported in the Table. Note that for the stages δ and ϵ not all the accessible positions to each stage are allowed because of mechanical obstacles or constrains. These for example include the twisting of the cables of the detector and the stages when the angle of polarization is changed with ϵ. Despite this may seem a minor issue, it's a actual problem when long and automatic measurements are performed without the intervention of the user, since cables may be damaged and in any case the measurements are not correctly performed. Then all the cables are accurately organized. Moreover angles ϵ less or equal to 180° are conventionally reached clockwise, while positions greater than 180° are reached anticlockwise. For example the stage would by default rotate clockwise and anticlockwise to reach $\epsilon = 150°$ or $\epsilon = 230°$ from the position $\epsilon = 0°$ to minimize the angle of rotation; however the stage would also rotate clockwise to pass from 150° to 230°. In this case, the right sequence is to pass from $\epsilon = 150°$ to $\epsilon = 0°$ and eventually to $\epsilon = 230°$.

4.3 The control software

The movements of the stages and the acquisition of the data are controlled by means of a LabView software which can manage both the GPD and the Amptek XR100CR spectrometer. Long-lasting sessions of sequentially measurements can be performed without any involvement of the user and are organized in two subsequent steps. The first is the alignment of the detector with the beam in the so-called "home position", pinpointed with a procedure described in Sec. 4.3.2 which involves all eight motorized stages. The second step is to perform the actual measurements: while η, xso and yso are dedicated only to the alignment, in this phase δ, ϵ, x, y and z can be changed with reference to the

Name	Range	Resolution	Load (kg)	Allowed positions
δ	$0 \Leftrightarrow 360°$	$1''$	20.4	$0° \Leftrightarrow 60°, 300° \Leftrightarrow 0°$
ϵ	$0 \Leftrightarrow 360°$	$0.2''$	183.7	$0° \Leftrightarrow 180°, 180° \Leftrightarrow 0°$
x	$-25 \Leftrightarrow +25$ mm	0.5 μm	25.5	-25 mm $\Leftrightarrow$ 25 mm
y	$-25 \Leftrightarrow +25$ mm	0.5 μm	25.5	-25 mm $\Leftrightarrow$ 25 mm
z	$0 \Leftrightarrow 50$ mm	—	10.	0 mm $\Leftrightarrow$ 50mm
η	$0 \Leftrightarrow 25$ mm	0.1 μm	9.2	0 mm $\Leftrightarrow$ 25 mm
xso	$0 \Leftrightarrow 25$ mm	0.1 μm	9.2	0 mm $\Leftrightarrow$ 25 mm
yso	$0 \Leftrightarrow 25$ mm	0.1 μm	9.2	0 mm $\Leftrightarrow$ 25 mm

Table 4.4: Main characteristics of the motorized stages. The load is the maximum allowed on-axis.

home position. Each measurement is then characterized by six parameters, namely the position of these five stages (δ, ϵ, x, y and z) and the number of photons to acquire.

The position of each stage in the home postion and the parameters of each measurement are written in text files. An example of the former is:

```
All the lines before "BEGIN" are ignored.

Home position for motorized stages.

Delta    Epsilon x       y       z       Eta     xso     yso
BEGIN:
0        0       3.15    6.6     0       12.5    10.2    2.3
```

The latter has a similar format but list only the six parameters required for each measurement:

```
Delta    Epsilon x      y        z       N
BEGIN:
0,000    0,000   7,500   7,500   0,000   30000,000
0,000    0,000   7,500   0,000   0,000   30000,000
0,000    0,000   7,500  -7,500   0,000   30000,000
0,000    0,000   0,000   7,500   0,000   30000,000
0,000    0,000   0,000   0,000   0,000   30000,000
0,000    0,000   0,000  -7,500   0,000   30000,000
0,000    0,000  -7,500   7,500   0,000   30000,000
0,000    0,000   7,500   0,000   0,000   30000,000
0,000    0,000  -7,500  -7,500   0,000   30000,000
```

The text file which lists the measurements can be very long and difficult to write correctly: the above example represents a "simple" matrix of 3×3 positions. At this aim a graphical interface was developed (see Fig. 4.10) which can also "show" the session of measurements. The graph on the bottom right in Fig. 4.10 represents the surface of the GPD: each blue circle, red or black line is a different measure. The blue circles represent the positions of the beam and its diameter, which can be changed thanks to diaphragms. Red lines represent the direction of polarization in each position and eventually black lines show the inclination that is zero when they cross the center of the beam. In the

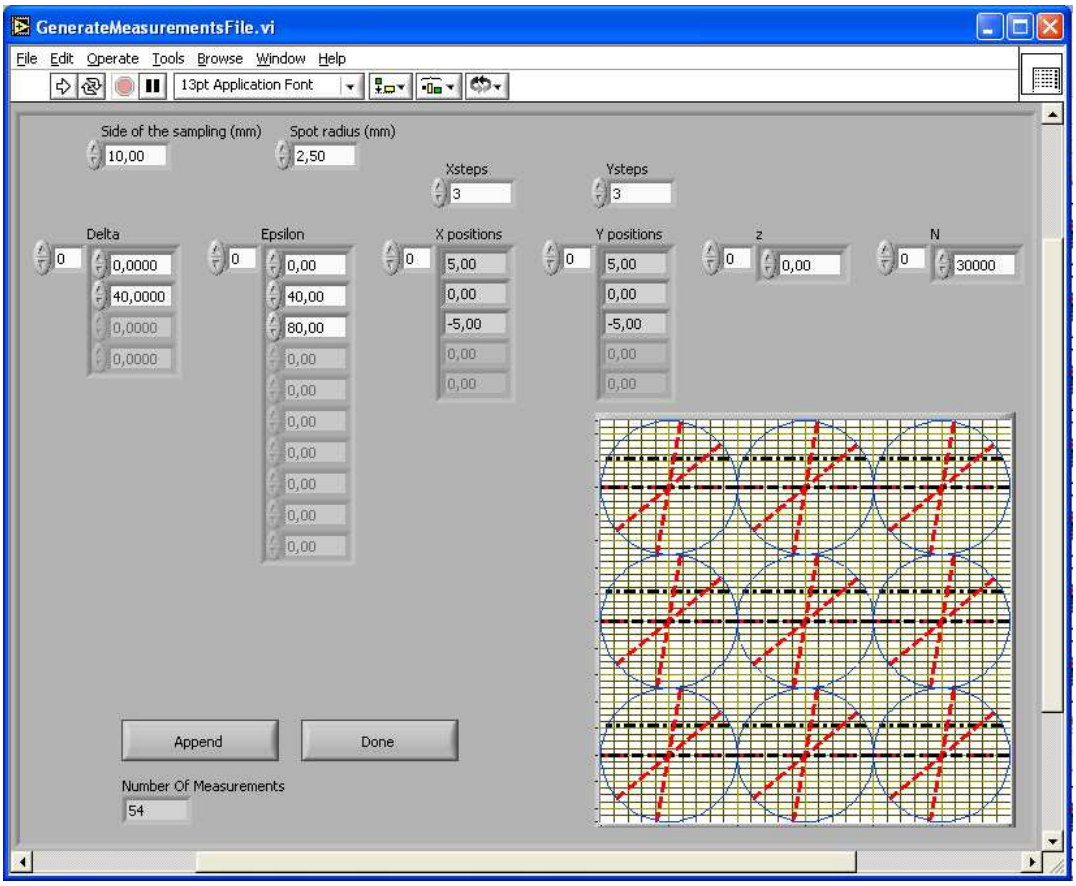

Figure 4.10: Graphical interface of the program which writes to a text file the parameters of the measurements.

example reported in Fig. 4.10, 54 measurements are shown. A 3×3 mapping is repeated for ϵ=0°, 40° and 80° and for δ=0° and 40°.

The control program is managed with graphical interfaces. When it is executed, the interface reported in Fig. 4.11a requests the text files where the home position and the parameters of the measurements are written. It allows to insert some informations about the setup which are saved in log files. When all the informations are provided, the program automatically moves the stages to the home position and eventually to the positions of the first measurement. Subsequent positions are reached soon after the first measurement was done. A second panel (see Fig. 4.11b) reports the current measurement and the progress of the session. It calculates the estimated time at which the measurements should end on the basis of the mean rate and shows the current measurement with the same representation described above.

The positions of all stages are saved in a log and data file for subsequent automatic analyzes (see Sec. 4.3.3). When all the measurements are finished, the stages are moved to the "zero position" that corresponds to the position zero of all stages (see Sec. 4.3.1).

The automatic movement of the motorized stage is performed with care. At the beginning of the sessions it is verified that all the positions are within the allowed range of each stage. The position of the stages is read-out and written in logs files after each movements to record possible misalignments. These may be caused for example by mechanical obstacles which prevent to arrive to the correct position. The rotation of ϵ is performed in clockwise direction between 0 and 180°, while angles between 180° and 360° are reached anticlockwise to prevent the twisting of the cables.

The block diagram of the control software which illustrate the main components of the program is reported in Fig. 4.12.

4.3.1 Frames of reference

Two different frames of reference are defined in the control software. The first is the one defined by the motorized stages, the Stage frame of reference or SR hereafter. Its origin is the position zero of all the motorized stages ("zero position") and their movements define also the axes and the direction of this frame of reference.

The GPD is an imaging device and then it has also a characteristic frame of reference. Its origin is chosen in the center of the detector and the directions of the x and y axes are defined as in Fig. 2.13. This is the Detector frame of reference, DR hereafter.

The roles of SR and the DR are complementary in the control software since in general they don't share neither the origin nor the direction of their axes. The positions of the beam are provided by the user in the DR and then a beam in $x_{\text{DR}} = 7.5$ mm and $y_{\text{DR}} = 7.5$ mm means that it is the top right angle of the square 15×15 mm^2 surface of the GPD. However the actual movement of the stages requires the position of the detector in the SR, which must be derived from that in the DR and the knowledge of the position in which the beam is centered with the instrument ("home position"). This must be characterized with an alignment procedure presented in the next Section: in general in the zero position the beam will not be neither incident exactly in the center of the detector nor aligned with the rotation axis of ϵ.

Note that only the five stages δ, ϵ, x, y and z are defined in the DR, since these are the only ones involved in the measurements. The stages η, xso and yso are dedicated only to the definition of the home position and then they are defined only in the SR.

The transformation from the DR to the SR depends on the detailed position and direction of each stage, from the mechanical assembly and the definition of the frame of reference. In the current configuration they are:

$$\begin{aligned}
\delta_{\text{SR}} &= -\delta_{\text{DR}} + \delta_{\text{HP}} \\
\epsilon_{\text{SR}} &= \epsilon_{\text{DR}} + \epsilon_{\text{HP}} \\
x_{\text{SR}} &= -x_{\text{DR}} + x_{\text{HP}} \\
y_{\text{SR}} &= -y_{\text{DR}} + y_{\text{HP}} \\
z_{\text{SR}} &= z_{\text{DR}} + z_{\text{HP}}
\end{aligned}$$

where HP refers to the home position.

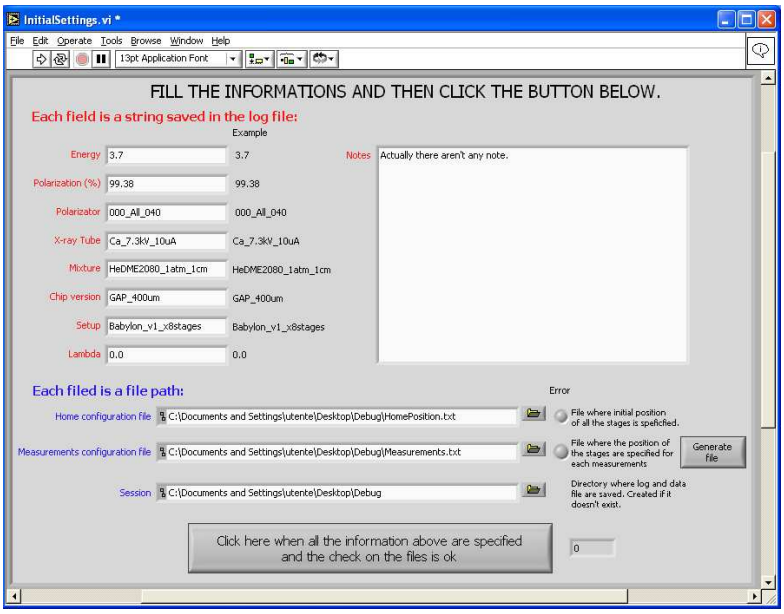

(a)

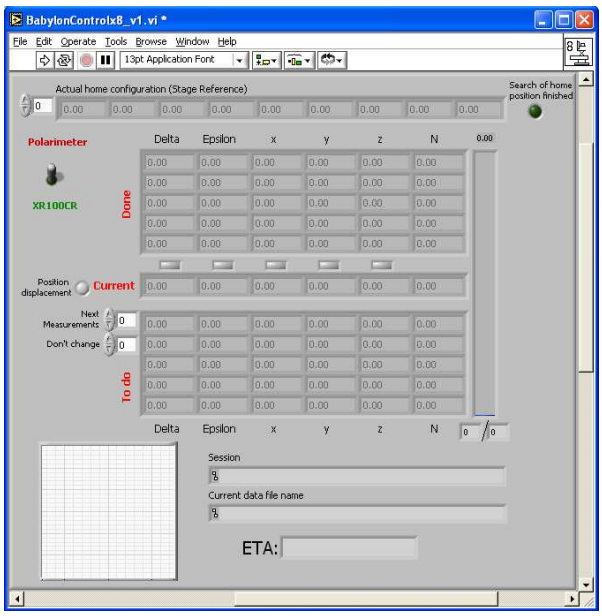

(b)

Figure 4.11: User interface of the program which controls the motorized stages. (**a**) Interface in which all the informations are at first collected. (**b**) The panel which allows to control the state of the measurements.

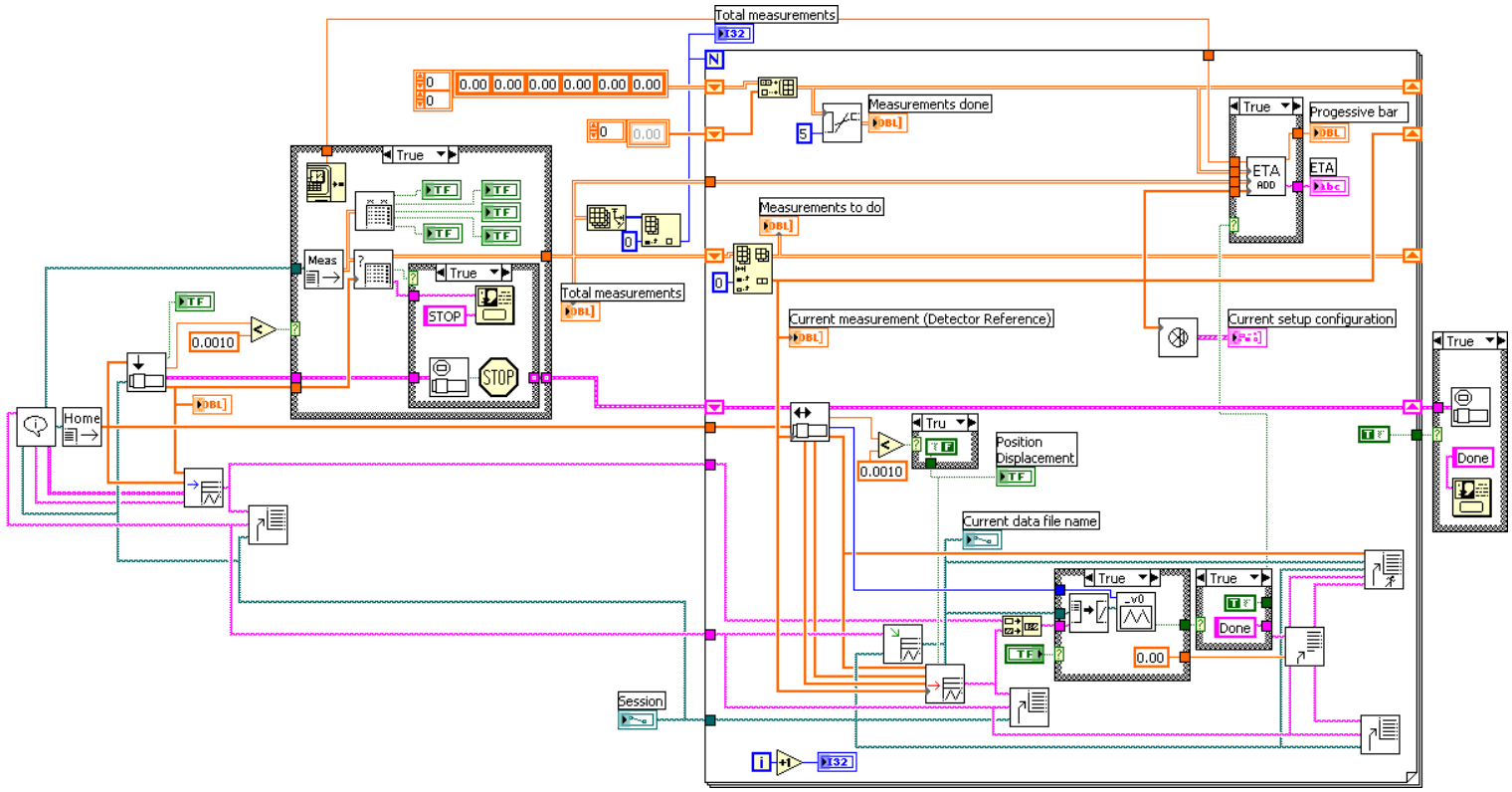

Figure 4.12: Block diagram of the control software. Each box is a subroutine.

4.3.2 Procedure of alignment

The alignment procedure is designed to find the home position in which the beam is centered with the detector. All the eight motorized stages must be used to reach a complete alignment and then this procedure can be quite complex. It consists of five independent steps which can be in case neglected when only some particular measurements are performed. For example the XY-mapping of the detector with unpolarized radiation doesn't require the movement of ϵ and the alignment of the beam with its axis of rotation is not necessary.

The five steps are:

1. *The alignment of the center of the detector to the beam*, required to perform XY-mapping. The alignment is found exploiting the imaging capabilities of the GPD: a small diaphragm is mounted in front of the source and the stages x and y are moved so that the spot is in the center of the instrument.

2. *The alignment of the rotation axis of ϵ to the beam*. This is required to study the relation between the incident and reconstructed angle of polarization in the same region of the detector and is performed with a diaphragmed beam: the XY position of the spot is measured for $\epsilon = 0, 90°, 180°$ and $270°$. The alignment is reached when xso and yso are moved so that the beam is in the center of these four points. Only the stages xso and yso are involved in this step.

3. *The alignment of the detector to the rotation axis of δ*, which is required when measurements at high inclinations are performed. When the detector is not aligned, a rotation of δ causes a movement of the spot on the detector. The displacement is $\Delta = d \tan\delta$, where d is the distance between the surface of the detector and the axis of rotation (see Fig. 4.13). Δ is measured exploiting the imaging capabilities of the GPD and the aligned position of z is found increasing its value of $d = \Delta / \tan\delta$. Note that this an approximation since this procedure is valid only if the detector is initially orthogonal to the beam. However a small displacement is not critical for the GPD because photons are absorbed in a gas cell 1 cm thick and consequently their inclined penetration smears the absorption points in a strip of length $= \tan\delta$ cm. In this step only the stage z is aligned.

4. *The alignment of the beam with the perpendicular to the detector*. This procedure is based on the assumption that the external titanium frame of the detector is parallel to the chip (see Fig. 2.12). A raw alignment is reached with a bubble level while a better result can be obtained placing a capillary plate above the frame. If the incident beam is highly collimated, the maximum flux beyond the capillary plate is reached when its axis is aligned with the beam. Then δ and η are moved and the alignment is reached in the position which maximizes the flux. In this phase a diaphragms is not required.

5. *The alignment of the direction of polarization with the x axis*. A possible misalignment is measured as an offset in the linear relation between the incident and the reconstructed angle of polarization.

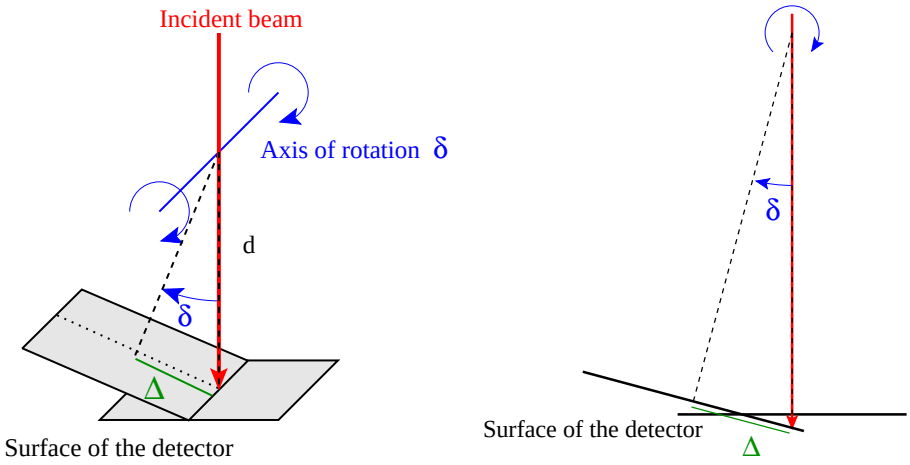

Figure 4.13: Displacement of the beam caused by the inclination of the detector.

The mechanical assembly is designed to retain the alignment. The change of the X-ray source or its movement with χ however can destroy the alignment below a few hundreds of μm. The procedure must then be repeated if very high precision is needed.

4.3.3 Data and log files hierarchy

The data files are identified by two parameters, a *RunID*, e.g. `20080301` and a *ScanID*, e.g. `00001`. The former is a reference date while the latter is a progressive number. The name of the data files is *RunID_ScandID*, e.g. `20080301_00001.dat` and they are saved in a directory named as the RunID.

A session of measurements starts when the control program is executed. The current date is used to derive the RunID and is used for all the session. If it lasts more than a day the RunID of all measurements is the same, namely the day of the first measurement. If two sessions are started during the same day they share the same RunID but the ScanID starts automatically from the last one of the previous session.

A log file named RunID`_Log.txt` is saved after each measurement in the same directory as data. It contains all the information about the setup, the home position and the positions of the stages in both the Stage and Detector frame of reference. These information are divided into two parts:

1. a static header, e.g.:

```
************************
*** Setup:
Energy(keV)=3.7 Polarization(%)=99.38 Polarizator=000_All_040
X-rayTube=Ca_6.0kV_19uA Mixture=XR100CR ChipVersion=XR100CR
Setup=Babylon_v1_x10stages Lambda(mm)=15
*** Requested home position (Stage Reference):
DeltaHome(deg)= 0.000000  EpsilonHome(deg)= 0.000000
```

```
xHome(mm)= 3.150000  yHome(mm)= 6.600000
zHome(mm)= 0.000000  EtaHome(deg)= 12.500000
xsoHome(mm) = 0.000000  ysoHome(mm) = 0.000000
*** Actual home position (Stage Reference):
DeltaHome(deg)= 0.000000  EpsilonHome(deg)= 0.000000
xHome(mm)= 3.150000  yHome(mm)= 6.600000
zHome(mm)= 0.000000  EtaHome(deg)= 12.500017
xsoHome(mm) = 0.000000  ysoHome(mm) = 0.000000
*** Notes: Actually there aren't any note.
*** Start date: 19/02/2008 18.04
************************
```

which contains the informations about the setup, requested when the session starts, and the home position in the SR. This header is printed in the log file only at the beginning of each session. While the notes on the setup can have a variable size, the positions of the stages are saved with a constant number of digits after the decimal point to simplify the subsequent automatic analyzes.

2. a dynamical header, e.g.:

```
BEGIN: C:\data\20080220_CampAl\20080219_00001.root
Actual position (Stage Reference):
Delta(deg)= 0.000000  Epsilon(deg)= 180.000000  x(mm)= 1.650000
  y(mm)= 5.100000  z(mm)= 0.000000 Counts= 30000
Actual position (Detector Reference):
Delta(deg)= 0.000000  Epsilon(deg)= 180.000000  x(mm)= 1.500000
  y(mm)= 1.500000  z(mm)= 0.000000 Counts= 30000
Actual position (Stage Reference):
Delta(deg)= 0.000000  Epsilon(deg)= 180.000000  x(mm)= 1.650000
  y(mm)= 5.100000  z(mm)= 0.000000 Counts= 30000
Actual position (Detector Reference):
Delta(deg)= 0.000000  Epsilon(deg)= 180.000000  x(mm)= 1.650000
  y(mm)= 5.100000  z(mm)= 0.000000 Counts= 30000
Start date: 19/02/2008 18.04
Done
```

It contains for each measurement the requested and the actual position of the stages. The former is the position requested by the user while the latter is that actually measured after the movement: if they are different, a problem prevented the stages from reaching the required position. All these fields have a constant format, i.e. a constant number of digits after the decimal point. The dynamical header is written in the log file before performing the measurement and only the last string "Done" is written when it is finished.

A second log file called *RunID*_`LogQuick.txt` is saved in the same directory as data. This file provides an easy and "human readable" format which contains only the approximate actual positions of the stages δ, ϵ, x, y and z in the DR. This log file is intended only for quickly retrieving a particular measurement and it's not used for the automatic analysis of the data.

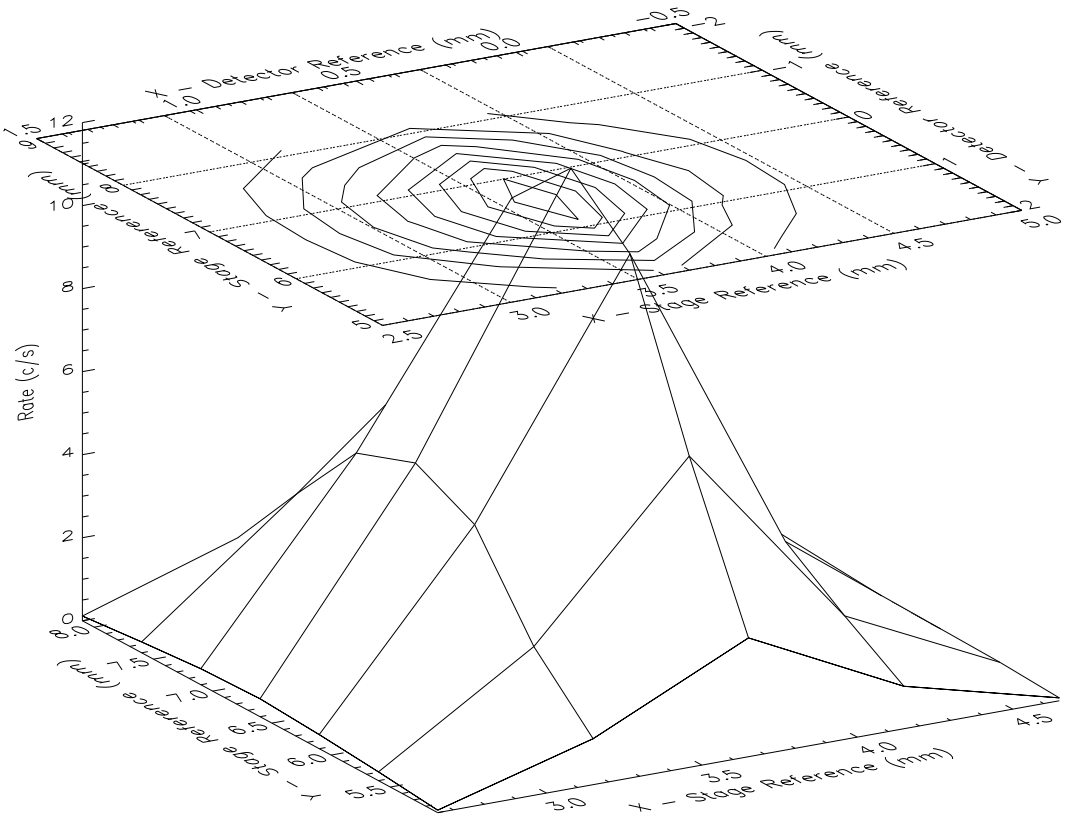

Figure 4.14: Map (7×5 points) of the line rate produced with the prototype Bragg source at 3.692 keV. The beam is elliptical, with a major axis in the direction of polarization of about 4 mm FWHM.

4.4 Test results

A test of the mechanical assembly and the control software is performed by using the Amptek XR100CR Si-PIN detector. The spectrum of the prototype Bragg source with the calcium tube and the aluminum crystal is mapped with a diaphragm of 1 mm in front of the detector.

The map of the diffracted line rate is shown in Fig. 4.14. It is sampled on a grid of 7×5 points at steps of 0.5 mm. The beam is elliptical, with a major axis of about 4 mm FWHM and aligned with the plane of polarization. In the perpendicular direction the extension of the beam is 2 mm FWHM. The diffraction should not change the section of the beam and then the elliptical shape of the beam should reflect the shape of anode of the X-ray tube.

The properties of the line in all the central 7×3 points are reported in Fig. 4.15. The central part of the beam is selected to analyze a sufficient number of counts and to obtain a reliable fit. The FWHM of the line is reported in Fig. 4.15a, while its energy is shown in Fig. 4.15b. The former is clearly consistent within errors during all the measurements. An

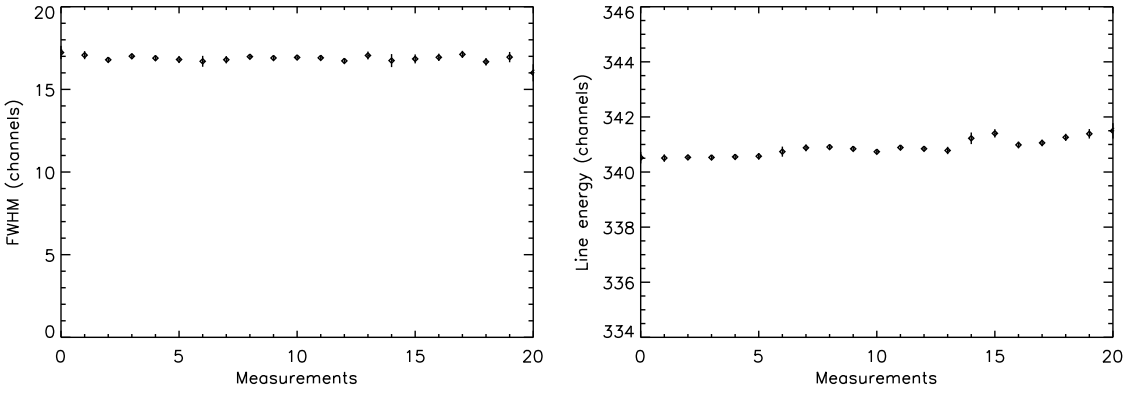

(a) **(b)**

Figure 4.15: FWHM (**a**) and energy (**b**) of the 3.692 keV Kα calcium line diffracted by the aluminum crystal. In the x-axis the index of the 7×3=21 measurements is reported. Note that both the FWHM and the energy of the line are expressed as a function of the channels of the spectrometer.

increasing trend is instead measured in the energy of the line. This can be attributed to a drift of the gain in the silicon detector since the increase follows the temporal sequence as the measurements are performed.

Chapter 5

First systematic calibrations of the GPD

This Chapter is devoted to describe the first applications of the calibration sources and the facility already presented. In particular two different measurements are reported: the first is performed with the prototype Bragg source and it is dedicated to the measurement of the modulation factor of the GPD at low energy, namely in the range of maximum sensitivity. The results were published by Muleri et al. (2008a).

The second measurement is the study of the correlation between the plane and the reconstructed angle of polarization. It was performed only very recently and the results obtained, being only preliminary, have not been published yet. Nevertheless they are included in this thesis because this was the first application of the facility described in Chapter 4. The attention should be focused more on the method than on the results which have not been confirmed yet. A brief discussion of them is anyway reported in Sec. 5.2.

5.1 The modulation factor of the GPD at low energy

The calibration of the GPD requires both unpolarized and polarized radiation. The former allows to study possible systematic effects in the response of the detector: the presence of a residual modulation for unpolarized radiation can be the actual limit of the sensitivity of a polarimeter. The spurious modulation measured for the GPD is very low and consistent with statistical fluctuations alone. Bellazzini et al. (2006b) reported a value of 0.70%$\pm$0.32% measured with a Fe^{55} radioactive source (lines at 5.899 and 6.490 keV spectrally not resolved by the detector) in a mixture 50% neon and 50% DME.

Measurements with completely polarized photons are important as well. They allow to measure the modulation factor μ of the instrument (see Sec. 1.1.2): the minimum polarization statistically measurable depends on μ when the systematic effects are negligible (see Sec. 2.4).

The modulation factor of the GPD was measured at 5.41, 6.40 and 8.04 keV with a polarized source based on Thomson scattering (Bellazzini et al., 2007a), these energies cor-

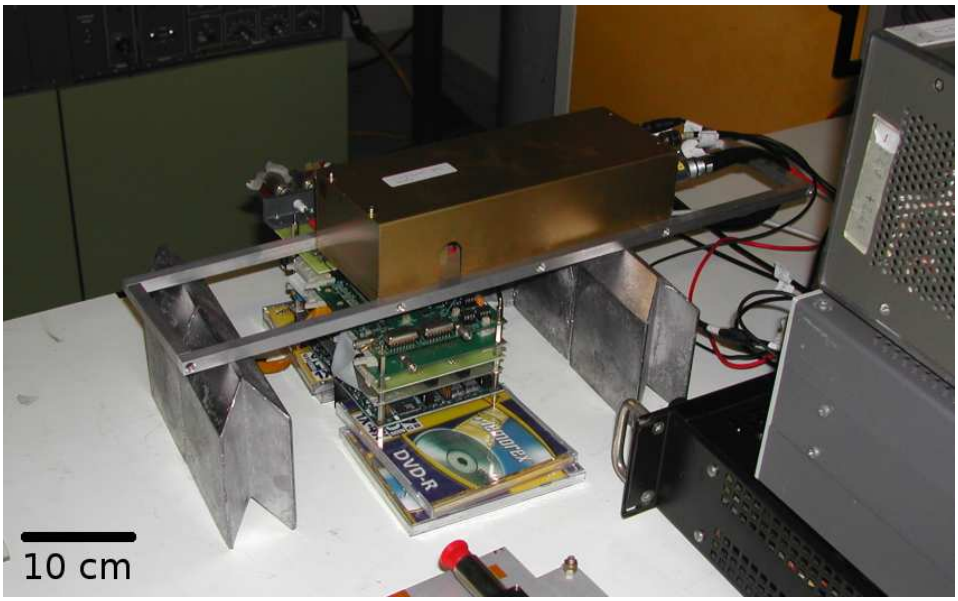

Figure 5.1: Setup of the measurements performed at the INFN of Pisa. The GPD is below the prototype Bragg source.

responding to chromium, iron and copper Kα fluorescence emission obtained by means of X-ray tubes. The modulation factor at lower energies has been derived extending these measurements with Monte Carlo simulations (see Sec. 2.2.2).

The maximum sensitivity of the GPD should be reached in the energy range between $\sim$2 and $\sim$5 keV (see Sec. 2.4), but an actual measurement of the modulation factor in this energy range has been possible only after the construction of the Bragg source presented in Chapter 3.

5.1.1 Setup

The prototype Bragg source was designed to be small and portable and this allowed to perform the measurements at the INFN of Pisa in March 2007, where the GPD was already working. A picture of the setup is reported in Fig. 5.1: the 105k pixels, 50 μm pitch, sealed version of the GPD filled with 20% helium and 80% DME mixture was used (Bellazzini et al., 2007b). Data are analyzed in the standard way, without any optimization for the reconstruction of low energy photoelectrons tracks.

The graphite and the aluminum crystals are used, the former with continuum incident photons to produce polarized radiation at 2.61 and 5.22 keV in correspondence to the first two orders of diffraction. The aluminum crystal is instead coupled with the low-power calcium X-ray tube which is exploited for the diffraction of the line at 3.692 keV.

The measurements at 2.61 and 3.692 keV are performed setting the X-ray tube high voltage below the energy of the second order to avoid the contamination of the spectrum with photons diffracted at higher orders. In the analysis at 5.22 keV photons at 2.61 keV

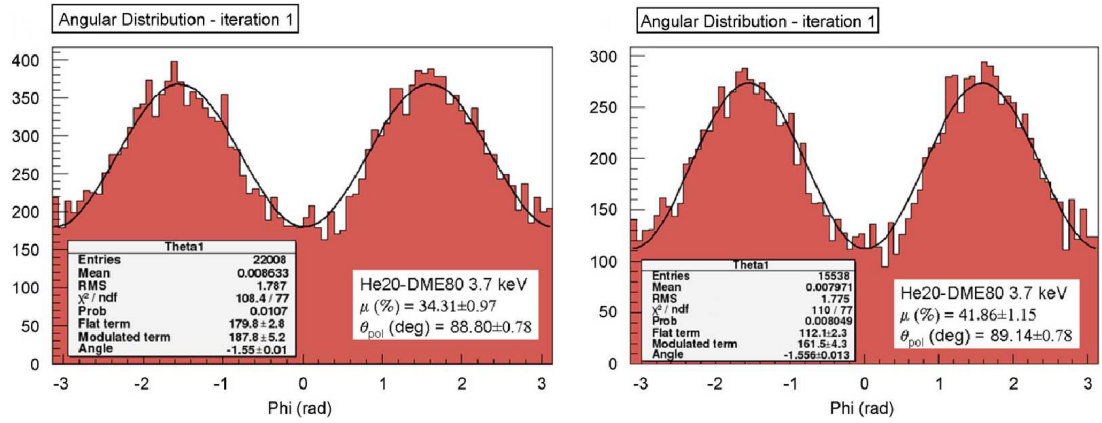

(a) **(b)**

Figure 5.2: Increase of the modulation factor with cuts. Modulation of reconstructed angles at 3.692 keV without any cuts (**a**) and with cuts implying a reduction of the efficiency of 29% (**b**).

are removed from off-line selection of the energy of the event.

All the measurements are performed with the output collimator only. This increases the flux of the source at the expense of a slight reduction of the estimated degree of polarization; nevertheless it is very high (see Table 3.3 and Table 3.4). The detector is placed as close as possible to the output capillary plate to reduce air absorption.

The spot of diffracted photons on the imaging GPD is limited by the diameter of the incident beam to about 5 mm and then only events in this region are analyzed. Cuts are applied to the third momentum to discard the less asymmetric tracks since they would be hardly reconstructed correctly. Selective cuts increase the modulation factor but reduce the effective efficiency ϵ of the detector. The minimum detectable polarization is inversely correlated with the quality parameter $\mu\sqrt{\epsilon}$ and hence a careful data selection is required to minimize the MDP.

5.1.2 Results

An example of the histogram of the directions of emission of photoelectrons obtained at 3.692 keV is shown in Fig. 5.2. The selection of data with cuts improves the modulation factor from ∼34% without any cuts (see Fig. 5.2a) to ∼42% (see Fig. 5.2b), implying a reduction of the efficiency of 29%.

The modulation factor measured at 2.61, 3.692 and 5.22 keV with and without cuts is reported in Table 5.1. The values at 2.61 and 5.22 keV are corrected assuming that incident radiation is 0.95 polarized (see Table 3.3). The reduction of the efficiency ϵ_R due to the cuts is also reported; cuts are varied to find the best value of the quality factor, which is reported in the last column.

The comparison between the expected modulation factor and the measured values is reported in Fig. 5.3. Cuts are applied on data, with an efficiency reduction of 23%, 29%

E (keV)	Efficiency	μ	ϵ_R (%)	$\mu\sqrt{\epsilon}$
2.61	0.1623	0.2106 ± 0.0119	0	0.0848
		0.2205 ± 0.0122	4	0.0870
		0.2614 ± 0.0138	23	0.0924
		0.2762 ± 0.0143	31	0.0924
3.692	0.0764	0.3431 ± 0.0097	0	0.0948
		0.4186 ± 0.0115	29	0.0975
		0.4310 ± 0.0118	33	0.0975
5.22	0.0293	0.4653 ± 0.0095	0	0.0796
		0.5447 ± 0.0104	22	0.0823

Table 5.1: Measured modulation factor of the GPD at different energies. ϵ_R is the reduction of the efficiency caused by data selection. The quality factor $\mu\sqrt{\epsilon}$ is reported in the last column. The values of the modulation factor at 2.61 and 5.22 keV assume that incident polarization is 0.95 polarized.

and 22% at 2.61, 3.692 and 5.22 keV respectively.

There is a good agreement between expected and measured modulation factor and this is important among other things for two main reasons. Firstly it ultimately proves the feasibility of X-ray photoelectric polarimetry with the GPD, since its operation is verified in the energy range where the maximum sensitivity was expected. The consistency between expected and measured performances gives also much more confidence with the Monte Carlo results. Their correctness basically depends on the assumptions made and algorithms used to describe the instrument and these are overall confirmed if the results of simulations are consistent with the measured values of the modulation factor, even if the comparison is performed only for the He-DME gas mixture. This is of particular importance for the development of the instrument since the Monte Carlo software is intensely used for the optimization of the reconstruction algorithm (see Sec. 2.2.1) and the choice of the best mixtures in a selected energy range, a subset of which are eventually tested in laboratory.

Despite this good agreement, the measured modulation factor results slightly lower than that predicted. Even if a further investigation is needed, this could be due to the 1.2 mm gap between the Gas Electron Multiplier and the collection plane which may introduce a little additional blurring on tracks caused by diffusion. This has not yet fully implemented in the Monte Carlo software but a new version of the detector with this distance reduced to 400 μm has been already built and will soon be tested.

Nevertheless the results are rather encouraging. The GPD currently reaches the $\sim$80% of the polarimetric sensitivity, i.e. the quality factor, expected from the Monte Carlo estimates. Moreover for the first time an effective low energy polarized source can be exploited to achieve a further improvement of the performance of the detector in the region of maximum interest.

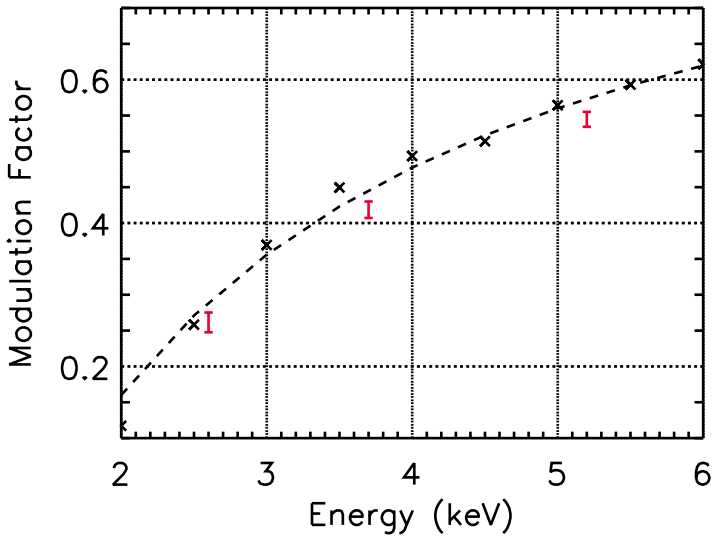

Figure 5.3: Comparison between modulation factor expected from the Monte Carlo simulations (crosses) and the measured values at 2.61, 3.692 and 5.22 keV (red). It is assumed that the degree of polarization at 2.61 and 5.22 keV is 0.95. Data selection, with a reduction of efficiency of 23%, 29% and 22% are applied to 2.61, 3.692 and 5.22 keV data. The dashed line is the fit to Monte Carlo values.

5.2 Angle reconstruction

Photoelectric polarimeters derive the angle and the degree of polarization from the reconstruction of the angle of emission of photoelectrons. However this procedure can be affected by systematic effects: in this case the response of the instrument is not uniform in the azimuthal plane. The existence of some special direction implies that the response deviates from the ideal $\cos^2$ dependence and consequently the angle of polarization may be not properly reconstructed.

A non-uniform response of the instrument may be intrinsic or instrumental. The former class includes those instruments which exploit a geometry which is azimuthally asymmetric as for example the Time Projection Chamber (see Sec. 2.5). In this case photoelectrons are emitted in the gas toward the plane of the detector or in the opposite direction and charges must drift longer distances in the latter case. Then they are more affected by diffusion and this implies a lower probability of correctly reconstructing the initial direction of emission. This front-back asymmetry causes a systematic effect with periodicity of 180° which must be removed to achieve a reliable measurement of the polarization.

The response of the GPD is intrinsically uniform if the photons are incident orthogonally to the detector. However it may be affected by instrumental asymmetries which could be caused for example from the hexagonal pattern of the pixels. Indeed their shape characterizes a special direction with a periodicity of 60° (see Fig. 5.4).

The presence of systematic effects is an evident limit of the instrument since they can

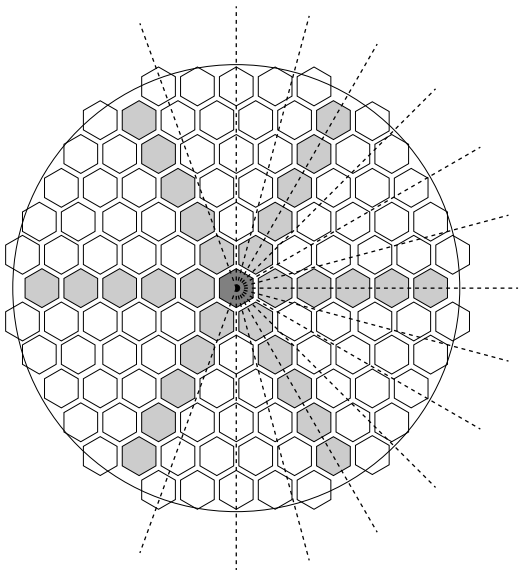

Figure 5.4: Special directions in an array of hexagonal pixels. Dashed lines are the direction sampled with the measurements presented in this Section.

strongly affect the measurement of signals at the few % level. As in the case of TPC, they could be removed by continuously rotating the instrument around the incident beam so that the presence of special directions is averaged. This procedure is effective to cancel all azimuthal asymmetries if the photons are incident orthogonally to the instrument but it introduces significant difficulties in the use of the instrument in space. This in turn implies a higher cost of the mission and a lower confidence in the scientific results.

The study of the angular reconstruction of the GPD is one of the measurements which has driven the design of the facility presented in Chapter 4. Intrinsic systematic effects should not be present and the further lack of instrumental ones would allow to use the GPD without rotation. This would be of primary importance for the small missions which will be discussed in Chapter 6.

5.2.1 Setup

The measurements of angular reconstruction were performed at the IASF/INAF of Rome in November 2008. The GPD is filled with a mixture composed of 30% helium and 70% DME at 1 atm, the gas cell is 1 cm thick and the GEM is 400 μm far from the chip. The diffraction of titanium line at 4.511 keV on the fluorite crystal is used (see Fig. 5.5), the high voltage of the X-ray tube being set to 10 kV. A narrow and a broad collimators are used to constrain the direction of incidence and diffraction respectively so that the output radiation is dominated by the 4.511 keV line which is polarized at 99.94% level (see Table 4.3).

Only a raw alignment between the beam and the axis of rotation of ϵ is performed

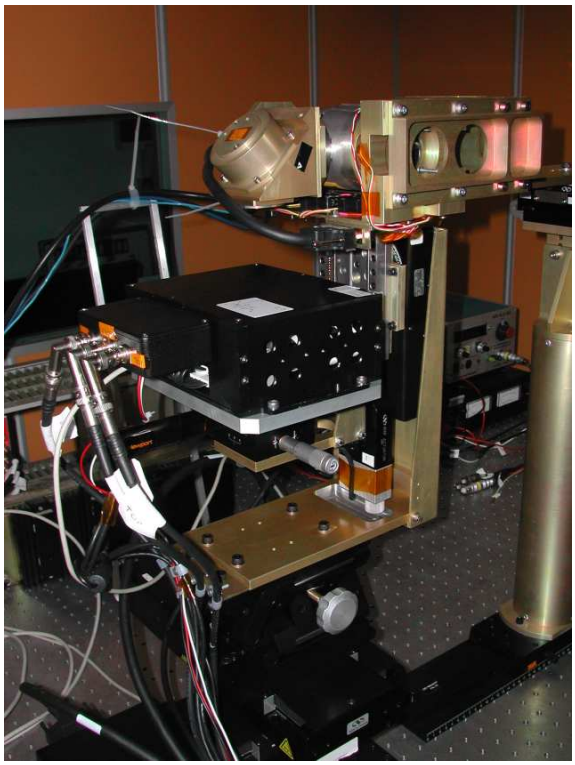

Figure 5.5: Setup of the facility for the measurement of possible systematic effects on the angle of polarization reconstruction. The 4.511 keV line of titanium is diffracted on the fluorite crystal.

(see Sec. 4.3.2) and indeed as the polarization plane is changed the spot moves of ∼3 mm but remains well within the active area of the GPD. The angle of polarization is measured for ϵ=250°, 270°, 285°, 300°, 315°, 330°, 345°, 0°, 15°, 30°, 45°, 60°, 75°, 90° and 110° (see Fig. 5.4).

Data are selected on the basis of the third momentum of the track. Only that with $M_3 > 1.3$ are analyzed and this implies a reduction of the efficiency of a about 18%. About 106×10^3 counts are analyzed for each measurement after the cuts.

The background is 0.092 c/(s cm^2) while the flux of the polarized source after the cuts is 359.4 c/(s cm^2) on a spot 5.5×4 mm^2.

5.2.2 Preliminary results

The modulation curves obtained at different angles ϵ are fitted with a $\cos^2$ function and the results are in Table 5.2. The relation between the plane and the reconstructed angle of polarization is reported in Fig. 5.6a: it is fitted with a line of equation $y = mx + q$ which provides m=0.9969±0.0011 and q=2.087°±0.068°. Then the relation is consistent at 3σ with a linear dependency with unitary slope as expected but there are significant

ϵ (°)	ϵ_{recon} (°)	μ	χ^2_{red}
-110	-108.72 $\pm$ 0.27	44.72 $\pm$ 0.30	1.22
-90	-87.82 $\pm$ 0.27	43.83 $\pm$ 0.30	1.19
-75	-72.50 $\pm$ 0.27	45.14 $\pm$ 0.30	1.12
-60	-56.93 $\pm$ 0.27	44.68 $\pm$ 0.30	1.27
-45	-41.96 $\pm$ 0.27	45.30 $\pm$ 0.30	1.58
-30	-26.68 $\pm$ 0.26	46.23 $\pm$ 0.30	1.36
-15	-12.24 $\pm$ 0.25	47.28 $\pm$ 0.30	1.07
0	1.96 $\pm$ 0.25	47.52 $\pm$ 0.30	0.98
15	16.39 $\pm$ 0.26	47.03 $\pm$ 0.30	1.41
30	31.06 $\pm$ 0.26	46.27 $\pm$ 0.30	1.60
45	45.86 $\pm$ 0.27	45.38 $\pm$ 0.30	1.38
60	61.02 $\pm$ 0.27	45.04 $\pm$ 0.30	1.44
75	77.07 $\pm$ 0.28	43.68 $\pm$ 0.31	1.49
90	92.06 $\pm$ 0.27	44.07 $\pm$ 0.31	1.64
110	112.70 $\pm$ 0.27	44.76 $\pm$ 0.30	1.51

Table 5.2: Results of the fits to the modulation curve at different angles ϵ.

deviations (up to $\sim$1°) around the average curve having a very well defined periodicity of 180°.

A similar result is obtained with the fit of the modulation factor with a linear function (see Fig. 5.6b). In this case m=-0.0007$\pm$0.0012 and q=0.45408$\pm$0.00078 and then it is constant in average as expected but again a clear modulation appears in the deviations from the linear dependence. This puzzling result is also related to a bad $\cos^2$ fit, whose χ^2 is reported as a function of the direction of polarization in Fig. 5.7.

The emergence of this systematic effect, whose periodicity of 180° is particularly unexpected, is still to be confirmed but it could emerge in basically three contexts. The first is the detector but systematic effects with periodicity of 180° could be hardly imputed to the hexagonal shape of the pixels. It also difficult to explain these effects with hot pixels or inhomogeneities in their response since the angle of emission is reconstructed from the analysis of a track which is sampled on many pixels and moreover the spot on the detector is about 2 mm large. Hence each local effect should be averaged.

The periodicity of 180° could be caused by the imperfect alignment of the GPD to the beam, even if it's not clear how it could produce the deviation observed. However any misalignment has the right periodicity, i.e. 180°. Eventually the systematic effect could emerge from the algorithm used to derive the angle of emission of photoelectrons.

The presence of these systematic effects will be soon verified with new measurements and a complete alignment of the detector with the beam; a diaphragms will be used to hit only a small region of the GPD. Note that, even if confirmed, the rotation of the GPD will not be anyhow required during its use in space, since the deviation for the angle reconstruction and the modulation factor is quite small, $\sim$1° and $\sim$2% respectively. Moreover the deviation from the average behavior could be easily corrected by the knowledge of

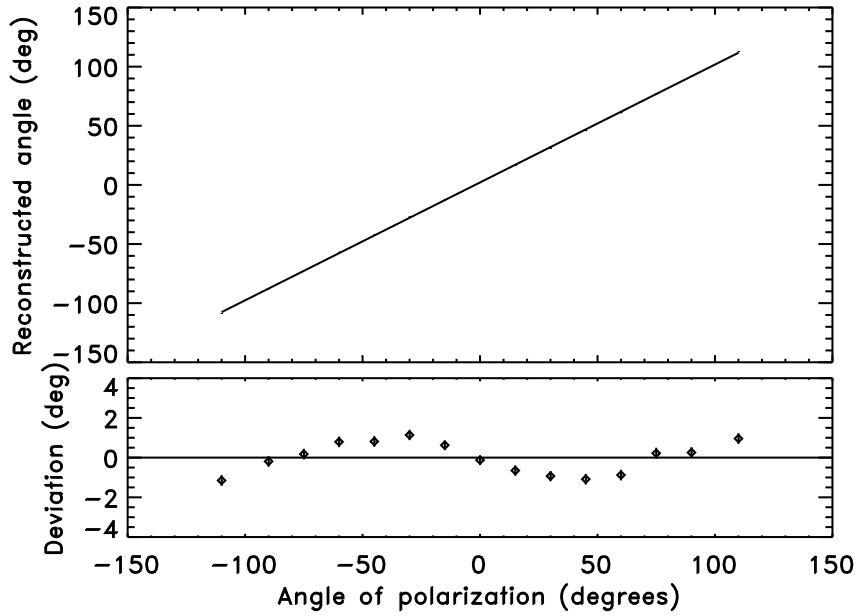

(a)

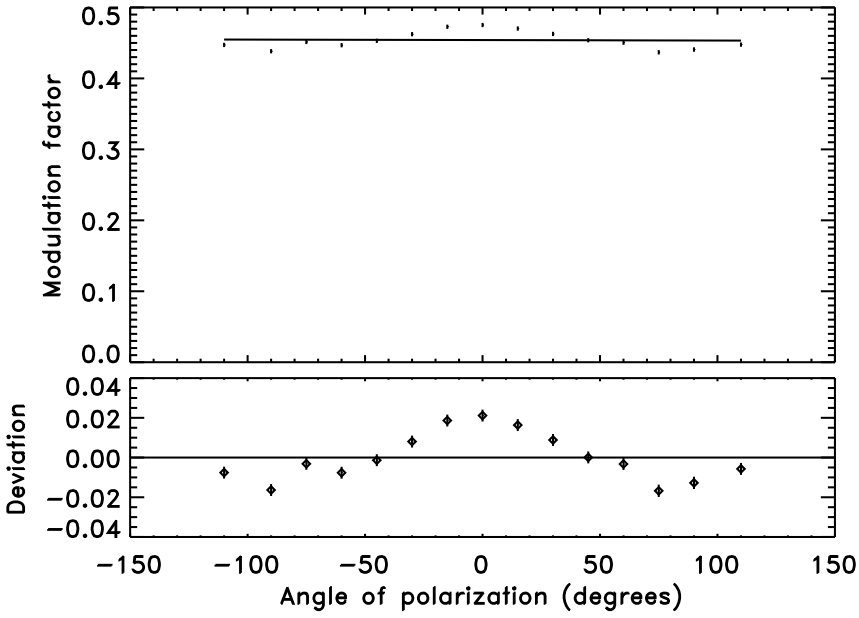

(b)

Figure 5.6: Angle of polarization (**a**) and modulation factor (**b**) measured when the plane of polarization is changed. Note that the average dependence is a line with slope ≈1 and ≈0 respectively, as expected. However a significant and periodic deviation from this dependence is measured.

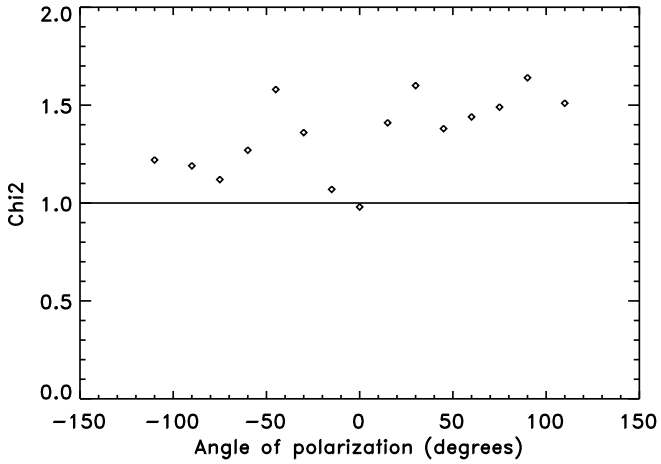

Figure 5.7: Values of the reduced χ^2 of the fit to the histograms of the emission directions. A certain deviation from the expected $\cos^2$ dependence is measured.

the pointing of the satellite. Its roll angle doesn't vary during an observation and then the measurements are performed at a constant angle of polarization (in the hypothesis that the polarization of the emission doesn't intrinsically change). A tabulated correction to the modulation factor and the angle of polarization could then be applied after the analysis of data.

Chapter 6

The GPD on-board the next satellite missions

The advanced status of development of the GPD allows to plan its use in the near future space missions. Many proposals have been submitted to space agencies in Italy, Europe and United States and two scenarios have emerged. The first is a small mission, intended as a low-cost pathfinder to unveil for the first time the polarimetry in the X-ray sky. It would be able to measure the polarization of galactic and bright extragalactic sources in a few days of observation with a low-cost X-ray telescope.

The results of the pathfinder(s) will be exploited to drive the optimization of a subsequent large throughput mission and in fact the GPD is inserted in the focal plane of the International X-ray Observatory. The international collaboration would make available resources to build an optics of much larger area and longer focal length and, despite the telescope should be shared with the other instruments in the focal plane, the time dedicated to X-ray polarimetry could be used to study the most interesting sources emerged from the results achieved by pathfinder missions. Thanks to the longer focal length, a large mission would unveil the polarimetry of sources which require a high angular resolution, e.g. galactic and extragalactic jets; moreover even the faint extragalactic sources would be accessible with observations of $\sim$1 day and this would make possible a survey of these objects.

In this Chapter the use in space and the perspectives of measurement of the GPD are discussed in both scenarios. The former argument is accurately defined within the Phase A study of the PolariX mission which ended in December 2008.

This thesis has contributed to these themes in different aspects. It has directly taken part into the definition of the requirements, the layout and the operation of the instrument in space (see Sec. 6.1) but it also contributed to the design of the missions and the preparation of the proposals submitted to space agencies (see Sec. 6.3 and Sec. 6.4). The scientific objectives of each mission have been for the most part defined within this thesis (see Sec. 6.5).

The most part of the work presented in this Chapter is still unpublished since it is inserted in the different proposals to space agencies. Nevertheless references will be provided where available.

6.1 Space use of the GPD

The current version of the GPD could be used in space within a few years since all the critical issues have been already tackled. Actually it is 105×10^3 independent proportional counters with a common gas volume and the most critical issue is the pollution of the gas mixture. However there is a long history of successful use of these devices in space: for example, the *Proportional Counter Array* has been working steadily since 1996 on board the *Rossi X-ray Timing Explorer* (Jahoda et al., 1996). A sealed version of the GPD has been working in laboratory for more than 15 months without showing any degradation of the performances.

The VLSI (Very Large Scale of Integration) technology has been used to build the ASIC chip of the GPD and it is expected to withstand the radiation levels forseen in orbit. Moreover test has been performed in the Heavy Ion Medical Accelerator in Chiba (HIMAC) and the performances of the GPD remained nominal after the irradiation of iron ions corresponding to several years in orbit.

The detector survived to vibrations and thermo-vacuum tests between -15 and 45°C and both the GEM and the 50 μm thin beryllium window are compatible with the use in space. The former in particular works with a quite low gain and then the probability of destructive discharges is very low. Extensive qualification tests will be performed to assure the mechanical resistance of the beryllium window to vibrations and stresses occurring during the launch but in case a grid will be used for its support.

6.1.1 On-board data handling

The management of the ASIC chip and the acquisition of the event in orbit follows the same chain which is already working in laboratory. The ASIC chip is divided into 16 clusters which are further divided into mini-clusters, each composed of 4 pixels. The charge collected by mini-clusters is compared with a threshold fixed for each cluster and a trigger is produced when is collected a sufficient amount of charge, corresponding to a few electrons before the amplification of the GEM. A region of 10 or 20 pixels around those which triggered, called Region Of Interest (ROI), is fetched so that the address and the charge collected in the ROI are read-out by the Back-End Electronics (BEE hereafter). BEE tags each event with the time of the trigger with an absolute precision is a few μs.

The self-triggering capabilities of the chip allow to read-out only the ROI, which is composed of only several hundreds of pixels, and this procedure strongly reduces the dead time of the detector with respect to the complete reading of the whole 105k pixels. The pixels are sequentially analog-to-digital (A/D) converted with a rate of 5 or 10 MHz and then several hundreds of events can be supported per second. These are by far sufficient for a pathfinder mission but an improvement is requested for a large observatory, in which case many thousands of counts per second are expected.

A further reduction of data will be performed in orbit by BEE. The ROI is the rectangular area which contains the pixels which triggered but has a large a margin of 10 or 20 pixels: then it is for the large part composed of pixels which didn't collect any charge. The average number of hit pixels depends on the energy of the absorbed photon but it

For each photon						*TOT*	For each pixel		*TOT*	**TOT**
Time	Energy	RVC		RL			RPC	RPH		
		x	y	x	y					
24	8	16	16	8	8	*80*	16	8	*1104*	
GEM		ASIC chip								**1184**

Table 6.1: Detailed division of the bits required to describe each track. It is assumed that each track hits 46 pixels in average.

is of the order of one hundred, against the several hundreds of the ROI. The amount of data required to describe the track can be reduced without losing any information by suppressing the pixels which didn't collect any charge, namely those with a conversion number below a certain threshold. This procedure is called zero-suppression and, since it is performed after the A/D conversion, it doesn't reduce the dead time of the detector. However it is of fundamental importance for the space use to reduce the amount of telemetry required to transmit the complete track.

In Table 6.1 a preliminary estimate of the bits of information necessary per absorbed photon is reported. The time and the energy of the event should be derived by the analog signal of the GEM; otherwise they are calculated from the trigger and the total charge collected by pixels respectively as currently done in laboratory. The timing is performed at a few μs level and a word of 24 bit=16×10^6 is used to tag the events within each second. An additional bit is introduced each second, after that the counter is reset. This procedure requires by far less telemetry than the use of a single word which would be $\sim$48 bit long to tag the events for the whole duration of the mission at the μs level.

The ROI of each track is characterized by its ROI Vertex Coordinates (RVC, the coordinate of the lowest left vertex) and its ROI Length (RL, length of the rectangle containing the track). The position of each hit pixel within the ROI is referred to the RVC and is detected with a single coordinate, called RPC (ROI Pixel Coordinate). The charge collected by each pixel is digitalized with a resolution specified by the ROI Pixel Height (RPH).

The instrument produces an amount of information proportional to the flux of the source. An average of 46 hit pixels per track is derived from Monte Carlo simulations for a power law spectrum of index 2.05, corresponding to the spectrum of the Crab nebula. This source will be often used as reference in the future and in this case it is expected that each track requires about 1 kbit of data.

This can be a quite large amount of data. A few hundreds of counts per second are expected for a strong source like the Crab nebula in the pathfinder scenario. Long observations even of strong sources are planned to achieve the scientific objectives presented in Sec. 6.5 and then about a few hundreds of kbit/s of data should be continuously transferred to Earth. This is beyond the capabilities of the S-Band omnidirectional antennas which can download about 500 kbit/s of data during the visibility with the on-ground station in a low Earth orbit (LEO, height between a few hundred and $\sim$2000 km). If both the station and the orbit are equatorial, namely inclined only a few degrees, a contact occurs each orbit and lasts about 10 minutes, while the orbit is about 100 minutes: then

the average downlink is 50 kbit/s. Moreover some contacts may be intentionally not used since the same antenna of the ground station could be shared among many satellites to reduce the costs of the mission. Then the contact may be impossible in case of contemporary visibility of more than one satellite.

The real-time transmission of the complete amount of data for strong sources would require at least the X band, included directional antennas: however this solution is much more complex and then expensive of the S-Band antennas. The approach of the low-cost missions presented in Sec. 6.3 (and possible even in the large observatory scenario) is to anyway use omnidirectional antennas but to transmit data to Earth in two modalities. The first consists in the download of the whole informations of the tracks alternating the observation of strong sources with that of faint objects. Data are saved in a (large) on-board memory and eventually downloaded during the subsequent observations. The mass memory should be of the order of 2 Gbyte, sufficient to store 1 day of observation with a rate of 200 counts/s.

The second modality is to perform the reconstruction of the track on-board. It requires a quite powerful computer since the analysis must be performed in real-time but the analyzed data would require an amount of telemetry a factor $\sim$10 lower. In this case the large part of the information of the track is filtered and it is downloaded only:

- the time, the energy and the impact point of the absorbed photon, to perform imaging, spectroscopy and timing;
- the emission angle, the size and other descriptors of the track (including a quality parameter) to measure the polarization.

The capability of on-board analysis is a requirement in both pathfinder and large observatory missions but it is used only when the data fill the on-board memory. Indeed the on-ground reconstruction is preferable since allows to perform subsequent refined analyzes: nevertheless on-board track reconstruction will be used for long and uninterrupted observations of strong sources or for very bright transient objects.

The on-board reconstruction is performed by an unit separated from the detector and the BEE, called Control Electronics (CE). It also manages the scientific payload and the communication with the spacecraft.

6.1.2 Calibration sources and filter wheel

The GPD will be calibrated in flight with polarized and unpolarized sources to verify periodically the performances of the mixture in terms of gains, linearity and modulation factor. The design of a small polarized source suitable for space use was already presented in Sec. 3.4: it is able to produce simultaneously nearly completely polarized photons at 2.622 and 5.899 keV by means of Bragg diffraction at 45°. X-ray photons are produced with a single Fe^{55} radioactive source which irradiates a lithium floride crystal and at the same time extracts the fluorescence of chlorine from a thin PVC film.

Two unpolarized sources will be used: the first is another Fe^{55} nuclide which will illuminate the whole detector to check the uniformity of the instrument and provide a calibration point at 5.899 keV. A second radioactive source of cadmium will be exploited

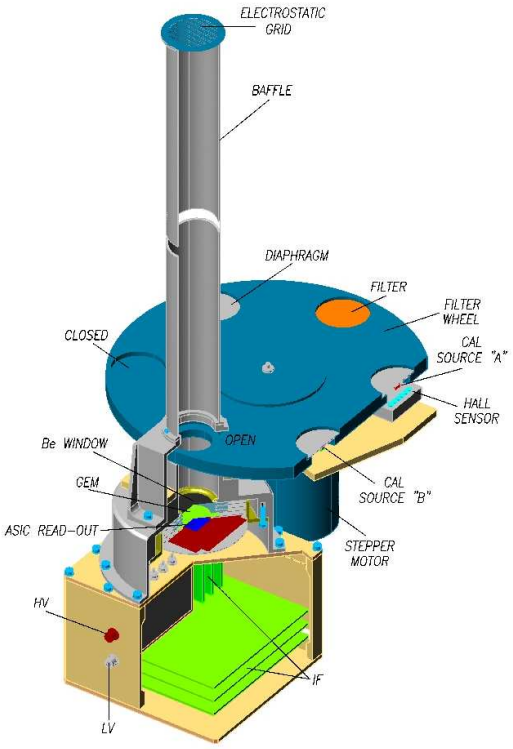

Figure 6.1: Concept design of the GPD and the filter wheel.

to extract the fluorescence by a copper target at 8.04 keV. These two energies allow to verify the value and the linearity of the gain in the gas, which could be changed during the mission to react to the possible aging of the mixture.

These three calibration sources are mounted in a rotating filter wheel (see Fig. 6.1), whose different positions allow for the different calibrations. A closed position, one with a diaphragm and one with a gray filter, namely a thin absorber film made of beryllium, are also inserted: the first is used during the launch to protect the instrument and allows for the measurement of the internal background. The diaphragm could be used to exclude possible strong sources in the field of view of fainter objects and eventually the gray filter could be exploited in case of very strong transient sources to reduce the dead time by partially absorbing low energy photons.

6.1.3 Resources

The weight and the power requested by the GPD are very limited. The version currently working in our laboratory, which includes the detector and the BEE, weights 1.6 Kg and absorbs about 5 W: slightly higher resources, reported in Table 6.2, are requested for the space use since many electronics components must be specifically built for operation in this environment. The column "Quantity" in the Table specifies how many items are

Function	Quantity	Power (W)	Mass (kg)
Detector	n	—	0.4
BEE	n	12.9	3.5
CE	1	15.3	4.0
Filter wheel	n	—	2.9
TOT (n=3)		54.0	24.7

Table 6.2: Resources in terms of power and weight requested for the space use of the GPD.

required in case of multiple detectors: the case $n = 3$ is taken as example since it is the configuration of PolariX (see Sec. 6.3.1). Indeed the use of more than one instrument can be convenient: the construction of many small optics is economically preferable with respect to a single telescope of equivalent area and in the case of GPD this is performed without any substantial degradation of the scientific performances of the instrument (see Sec. 6.2.1).

6.2 Grazing incidence X-ray optics

Grazing incidence X-ray optics have had a huge importance for the development of X-ray astronomy. They have been used for two main reasons: firstly they allow to resolve extended sources and confused regions; secondly they strongly increase the signal to noise ratio, since the flux of the source is indeed to be compared only with the background inside the point spread function of the optics.

The reflection of X-rays occurs only when the grazing angle is below a certain critical angle θ_c which depends on the reflecting material and can be expressed as (Giacconi et al., 1969):

$$\cos\theta_c = 1 - \delta \quad \Longrightarrow \quad \theta_c \simeq \sqrt{2\delta} \tag{6.1}$$

where δ is a small quantity related to the real part of the index of reflection. It can be calculated from (Compton and Allison, 1963):

$$\delta = \frac{2\pi r_0 c^2}{\omega^2}\left[N + \sum_H N_H \frac{\omega_H^2}{\omega^2}\ln\left|\frac{\omega^2-\omega_H^2}{\omega_H^2}\right|\right], \tag{6.2}$$

where ω and ω_H are the frequencies associated to radiation and photoabsorption edges of the material. N is the electron density and N_H is that associated to the edge which basically takes into account the number of electrons per orbital.

In Fig. 6.2 the theoretical efficiency of reflection for different grazing angles and materials is reported: it is larger for heavier materials, smaller grazing angles and longer wavelengths and is significantly reduced near the edges since the competitive contribution of photoabsorption. Measurements in general are in good agreement with theory if the surface is smooth enough.

X-ray optics are composed of nested and concentric mirrors or shells (see Fig. 6.3a), the total area being the sum of their contributions. X-rays are typically reflected two

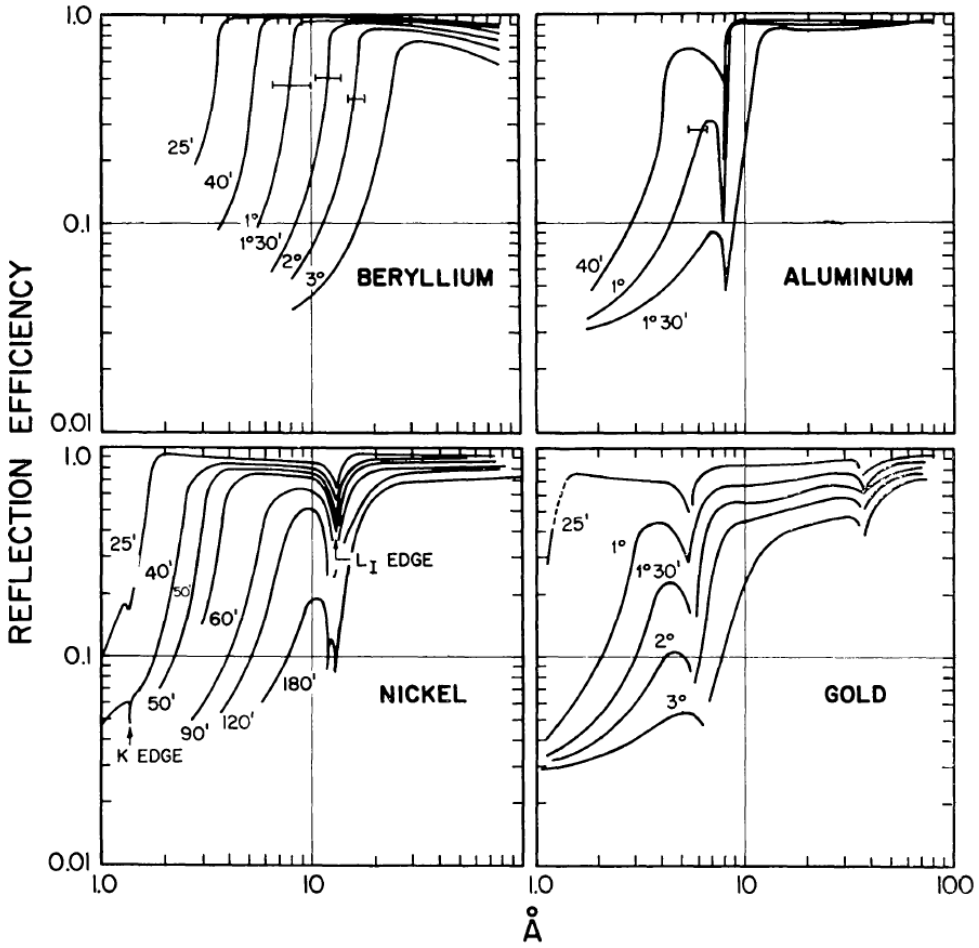

Figure 6.2: Theoretical efficiency of reflection for different materials and grazing incidence angles (Giacconi et al., 1969).

times, firstly by a paraboloid and secondly by a hyperboloid surface to reduce the focal length (see Fig. 6.3b). The critical angle is roughly proportional to the square root of the density of the reflecting material and for this reason a heavy and malleable material as gold is used.

Reflection occurs only for grazing angles of a few degrees and hence each shell focuses the photons only impinging on an annular region A which is proportional to the square of the radius of the mirror, $A \propto r^2$. High energy radiation is characterized by a smaller critical angle because θ_c is roughly proportional to the wavelength of the photons: then it is reflected effectively only by inner shells where the grazing angles are smaller. Unfortunately these mirrors can contribute less to the total area, being the radius smaller: in summary inner mirrors reflect both low and high energy photons while outer shells, which contribute more to the total area, are effective only for low energy radiation. This actually causes a fast decrease of the effective area with energy and for this reason the

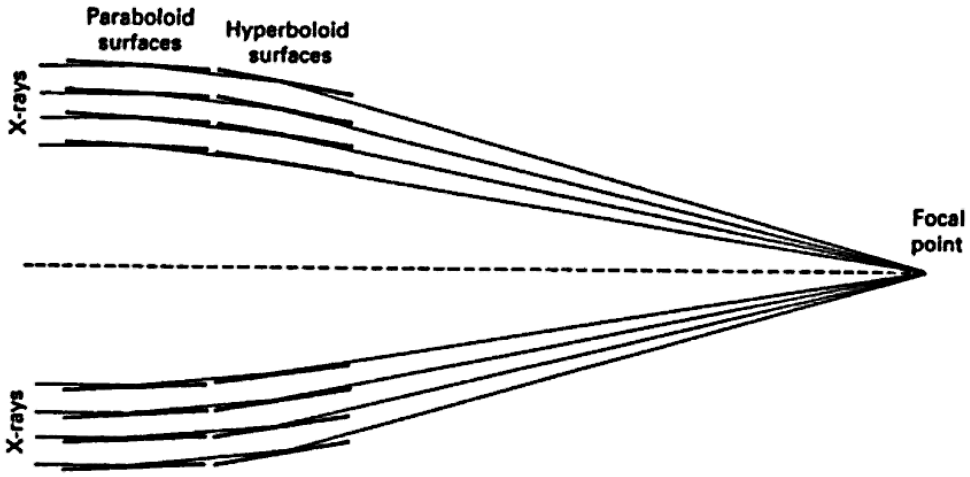

(a)

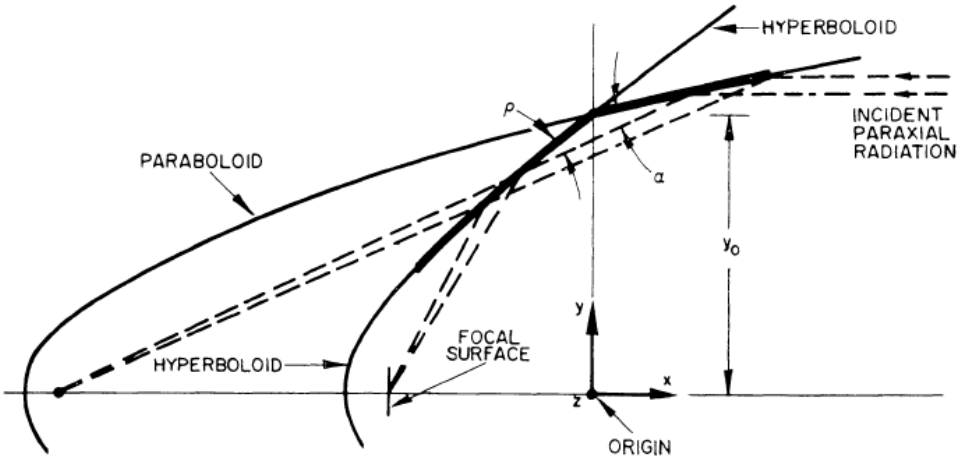

(b)

Figure 6.3: (**a**) Section of an X-ray optics. Photons are reflected by nested and concentric mirrors (Tucker and Giacconi, 1985). (**b**) Two reflections occur to shorten the focal length; generally these are on a paraboloid and a hyperboloid surfaces (Giacconi et al., 1969).

first applications of X-ray optics, e.g. *Einstein* (Giacconi et al., 1979), have been in the soft X-ray range.

The high energy response of the X-ray optics can be increased by increasing the focal length. In this case the grazing angles are smaller and hence even the outer shells give a contribution to the reflection of high energy radiation. However a longer focal length requires higher resources in term of costs, weights and space available in the fairing of the launcher. This approach has been followed by modern missions, e.g. *BeppoSAX* (Boella et al., 1997), *XMM-Newton* (Jansen et al., 2001) and *Chandra* (Weisskopf et al., 2002), to extend the response up to ∼10 keV.

In the near future a further increase in the high energy response will be achieved with multi-layer coatings (Pareschi and Cotroneo, 2003). In this case the shells are composed of alternating layers of materials with high and low atomic number of gradually changing thickness. This technique provides an effective reflection at angles up to 3 times those of mono-layer surfaces and the focusing of X-rays up to 60-80 keV can be achieved, the high energy limit being the K-edge of the high Z material. Recently a few groups are performing calculations and experiments to extend the performance of optics up to 200 keV and more (Jensen et al., 2007). At low energy the response would be affected by the photoabsorption of the high Z material but this issue could be overcome with carbon overcoating (Pareschi et al., 2004). Multi-layer optics are exploited in many new missions, as for example *Astro-H* (formerly *NeXT*, Takahashi et al., 2008), *NuSTAR* (Koglin et al., 2005) and *SIMBOL-X* (Ferrando et al., 2005, 2008).

6.2.1 The use with the GPD

The use of the current version of the GPD requires an X-ray optics for two main reasons. Firstly it is an imaging device and then the use of a telescope makes the background negligible and allows to resolve extended sources. The actual angular resolution of the GPD depends both on the point spread function of the telescope and its focal length because the inclined penetration of photons in the gas cell causes an additional blurring of the order of (see Fig. 6.4):

$$b \leq 1 \text{ cm} \frac{r}{f}, \tag{6.3}$$

where f is the focal length and r the radius of the shell. For a pathfinder mission $f \sim 3$ m, $r \sim 15$ cm and then $b \leq 500\ \mu m$.

The X-ray optics is also required to collect a sufficient number of photons to perform an accurate measurement in a reasonable observation time. The minimum detectable polarization (see Sec. 2.4) can easily be expressed as a function of the number of absorbed photons N_{ph} (cf. 2.30):

$$\text{MDP} = \frac{4.29}{\mu\sqrt{N_{ph}}}. \tag{6.4}$$

A detection at the 1% level requires:

$$N_{ph} = \left(\frac{4.29}{\mu \text{ MDP}}\right)^2 = 143 \times 10^3, \tag{6.5}$$

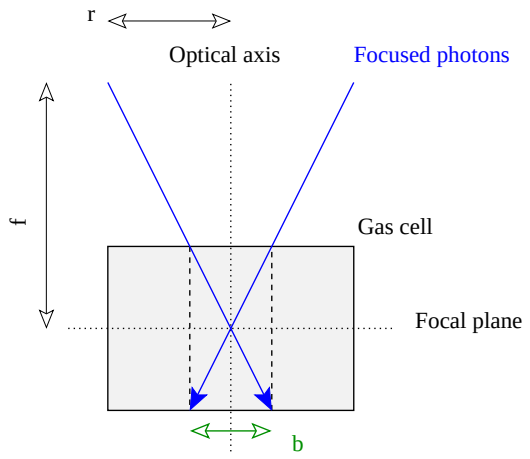

Figure 6.4: Blurring due to the inclined penetration of photons in the gas cell.

where an average value of $\mu = 0.30$ is used, which is a reasonable value for a power law spectrum like that of the Crab Nebula between 2 and 10 keV. The flux of this source is about 3.5 counts/s cm^2 and the area of the current GPD is 15×15 mm^2, with an average efficiency of 0.15. The time required to perform a measurement at the 1% level is then 120×10^3 s, i.e. more than one day, which is a quite long observation time since the Crab Nebula is one of the brightest object in the X-ray sky.

The background has been neglected in Eq. 6.4 since in general it will be negligible. In the case of X-rays instruments in space it can be expressed as the sum of two contributions. The first is called internal background and is caused by the passage of cosmic particles in the active area of the detector, which is the gas cell for the GPD. An estimate of this contribution can be derived from previous experiments: in particular one of the four proportional counters of the *Wisconsin Soft X-ray Astronomy Instrument* on-board OSO-8 mission was filled with a mixture 90% neon and 10% CO_2 (Bunner, 1978), which is rather similar to that used with the GPD. In that case a flux $\mathcal{F}_i$ of 1.5 and 1.0×10^{-4} counts/(cm^2 s keV) was measured in the energy bands 1.6-3.0 keV and 3.0-6.0 keV respectively.

The GPD is an imaging device and then the flux of the sources must be compared only with the background in the point spread function of the telescope. It can be safely assumed that, including the inclined penetration of photons in the gas cell, it corresponds to a circle of radius smaller than r_i=500 μm. The internal background is then:

$$B_i = \int_{E_{min}}^{E_{max}} \mathcal{F}_i(E) \pi r_i^2 \, dE \lesssim 3.9 \times 10^{-6} \text{ counts/s.} \tag{6.6}$$

where the integration is performed between 2 and 10 keV and the spectrum measured by Bunner (1978) is linearly extended above 6 keV.

The second source of background is the diffuse emission. The X-ray sky is uniformly very luminous in the X-rays, possibly because of distant and unresolved AGNs. The

spectrum of the diffuse background can be retrieved from literature and is (Zombeck, 1990):

$$\mathcal{I}(E) = 8.5E^{-0.40}\text{keV cm}^2\text{ s}^{-1}\text{ keV}^{-1}\text{ sr}^{-1}. \tag{6.7}$$

Then the diffuse background in the instrument is:

$$B_d = \int_{E_{min}}^{E_{max}} \mathcal{I}(E)\pi r_i^2\ \Delta\Omega\ dE, \tag{6.8}$$

where $\Delta\Omega$ is the solid angle which correspond to the point spread function of the optics. It is approximately:

$$\Delta\Omega = 2\pi\left(1 - \cos\arctan\frac{r_i}{f}\right), \tag{6.9}$$

where f is the focal length of the telescope. A larger solid angle and then a higher background is subtended in the point spread function if the focal length is shorter. Among the mission proposed and presented below, the telescope of EXP^2 (see Sec. 6.3.2) is the more compact, f=2.1 m (see Table 6.3), and in this case B_i=1.1$\times$10^{-8} counts/s.

The background of the GPD is then largely dominated by the internal contribution but this is still much lower than the fluxes of the sources accessible to X-ray polarimetry. These are reported in Table 6.8 for some objects which could be actually observed with the GPD. The fainter source accessible, at least with a small mission, will be probably Sgr B2 (see Sec. 1.4.9) since in this case a nearly completely polarized emission is expected and then a polarization could be measured even if a relatively small number of photons are collected. The flux of Sgr B2 is 1.3$\times$10^{-3} counts/s and hence about a factor 500 higher than the expected internal background.

The absence of a significant background allows to sum the data from a cluster of small telescopes without a significant loss of sensitivity with respect to a single large optics. This is very important for small missions since a large collecting area can be reached with many identical units. An X-ray optics is composed of tens of shells and a relevant part of the costs is the manufacture of the superpolished mandrels which are the "matrix" over which each shell is deposited. After that the mandrels are manufactured, the replica of identical shells is a relatively simple and inexpensive operation. Then the duplication of small optics with a limited number of shells is relatively cheap task and is convenient if the detector requires small resources in terms of weight and power consumption as the GPD.

Note that it is well-known that grazing incidence reflection can modify the polarization of the incident radiation. Unfortunately this argument is scarcely discussed in literature for X-ray optics and only a theoretical study dedicated to the telescope of the *Advanced X-ray Astrophysics Facility*, the current Chandra mission, was retrieved. It is presented in details in the Appendix B but basically the result is that the reflection doesn't affect the plane of polarization, at least for on-axis sources. A small change in the degree of polarization can instead occur but this is of the order of one part per 10^3. This accuracy is out of the capabilities of the current generation of X-ray polarimeters: the effect would be of the order of 0.01% in the case of a source polarized 10% and in almost all astrophysical contexts a lower degree of polarization and consequently a lower effect is expected. Then it will be neglected in the following.

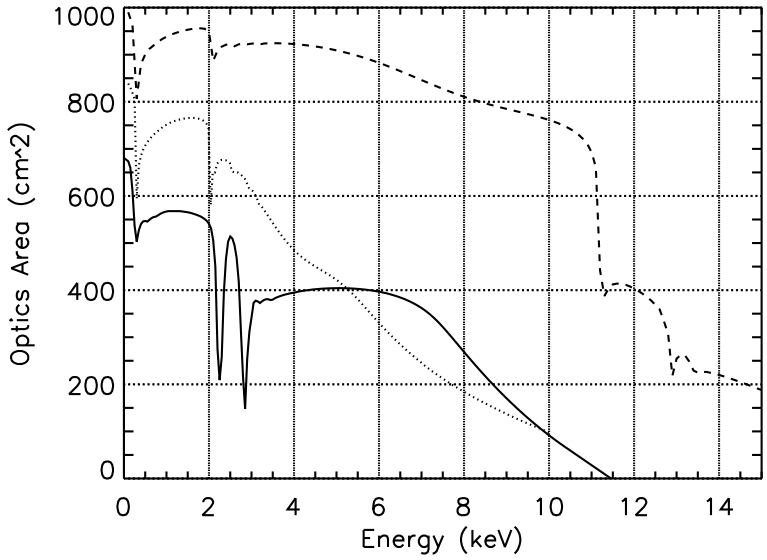

Figure 6.5: Comparison of the area of the telescopes of pathfinder missions. PolariX is the solid line, EXP^2 is the dotted and IXPE is the dashed.

6.3 Pathfinder missions

Pathfinders are designed to be small and low-cost missions. The polarimetry in the X-ray sky is almost unexplored and then they are intended to be versatile tools not optimized for a certain scientific objective. Nevertheless they are expected to be a breakthrough in the study of the X-ray astrophysical sources (see Sec. 6.5).

All the pathfinders could be launched in a few years and this suggests as baseline the use of the current version of the GPD, filled with the standard 20% helium and 80% DME mixture at 1 atm and 1 cm thick. However the pathfinders are not completely equivalent and the main differences are the optics and the profile of the mission. Each telescope is chosen on the basis of the resources available since their volume, weight and cost is the most demanding part of the scientific payload of these missions. Moreover some pathfinders, i.e. PolariX and IXPE, are dedicated to X-ray polarimetry while EXP^2 is onboard a mission whose primary scientific objective is a survey in the hard X-ray band. Then it could be used only during pointed observation, i.e. during the $\sim$50% of time.

A quite large collecting area is generally achieved with a small cluster of telescopes and that of the different smalls missions is compared in Fig. 6.5. For comparison the effective area of XMM-Newton is $\sim$1500 cm^2 at 2 keV and $\sim$1000 cm^2 at 6 keV (Jansen et al., 2001). However their cost is not prohibitive for a small mission because a high quality in term of angular resolution is not required. Indeed the focal length are generally of the order of a few meters and the inclined penetration of photons produces a blurring $\gtrsim$ 10 arcsec.

The baseline is the use of a GPD per optics but two detectors could be inserted in each focal plane if enough resources are available. They would be filled with slightly dif-

ferent mixtures and alternatively used, allowing for the optimization of the instrument to the specific observation and to completely cover the energy band pass of the optics. Indeed the baseline 20% helium and 80% DME mixture provides the better sensitivity in the energy range 2-10 keV but this mixture is the best "in average". An improvement for specific soft or hard sources could be achieved with different mixtures and then the possibility to change the detector only in this cases is attractive (see Sec. 6.5.2). Note that the use of different sealed GPDs is preferable with respect to that of a refilling system since the former strategy is more reliable and moreover provides a redundancy in a critical part of the scientific payload.

In Table 6.3 are compared the main characteristics of the instruments on board the pathfinders and that of XPOL on-board IXO, which will be presented as a large mission in Sec. 6.4.

6.3.1 PolariX

PolariX (*Polari*metro *X*, which in Italian means "X-ray polarimeter") is a small mission proposed to the Italian space agency (ASI, Agenzia Spaziale Italiana) and dedicated to X-ray polarimetry (Costa et al., 2006). PolariX was selected for a phase A study at the end of 2007 in competition with four other proposals: the study finished in December 2008 and currently PolariX is waiting for the downselection to two approved missions. If selected it will be launched in mid 2014.

The institutes and the industries involved are all Italian. The Principal Investigator is the IASF/INAF of Rome (Istituto di Astrofisica Spaziale e Fisica Cosmica/Istituto Nazionale di Astrofisica) which will also build the control electronics. The Osservatorio Astronomico of Brera (OAB/INAF) is responsible of the optics and eventually the focal plane is developed by the INFN of Pisa (Istituto Nazionale di Fisica Nucleare). The spacecraft is built by the Thales Alenia Space of Turin from the bus of SIMBOL-X, the ground segment is managed by the Telespazio of Rome and scientific support is provided by the University of Rome "Roma Tre".

The design is driven by the budget available which is of 50 millions of euro. This requires the use of technology with high readiness level and, when possible, already tested for space use. The current GPD is included in the former class.

A key characteristics of PolariX is the use of the three telescopes already built for the Jet-X instrument (see Fig. 6.6), supposed to fly on-board *Spectrum X-ray Gamma* which however has never been launched. They has been already calibrated and an Half Energy Width (HEW) of $\sim$15 arcsec was measured (Citterio et al., 1996). Moreover the good operations in space is already verified by the use of a further unit, the spare, in the *X-ray Telescope* instrument on-board the *Swift* satellite (Burrows et al., 2005). The total area of the three telescopes is reported in Fig. 6.5 and the quite long focal length (f = 3.5 m) allows to reach an angular resolution (HEW) of 24 arcsec, including the inclined penetration in the gas cell.

An exploded view of PolariX is reported in Fig. 6.7. Note that the mechanical structure which supports the optics (MIRRORS WHEEL in the Figure) can host three or five telescopes. The mandrels of the Jet-X optics are still available and then further units could

	$\mathcal{D}$	#	Area cm^2 at 3.5 keV	f cm	Ang. Res. arcsec	fov $arcmin^2$	E keV	ΔE keV at 6 keV	τ μs	T ks
Pathfinder missions										
PolariX	✓	3	380	350	24	∼15×15	2-10	20%	8	15.7
EXP^2 on-board HXMT		2	542	210	40	∼25×25	2-10	20%	8	10.7
IXPE	✓	3	924	400	30	∼19×19	2-15	20%	8	6.4
Large observatory										
XPOL on-board IXO		1	9378	2000	5	∼2.6×2.6	2-10	20%	8	0.75

$\mathcal{D}$: Mission dedicated to X-ray polarimetry
#: Number of telescopes
f: Focal length
Ang. Res.: Angular resolution (HEW)
E: Energy range
ΔE: Spectral resolution
τ: Time resolution
T: Time required for reaching an MDP of 1% for the Crab nebula between 2 and 10 keV

Table 6.3: Comparison of the main characteristics of the X-ray photoelectric polarimeters inserted in pathfinder missions and on-board IXO.

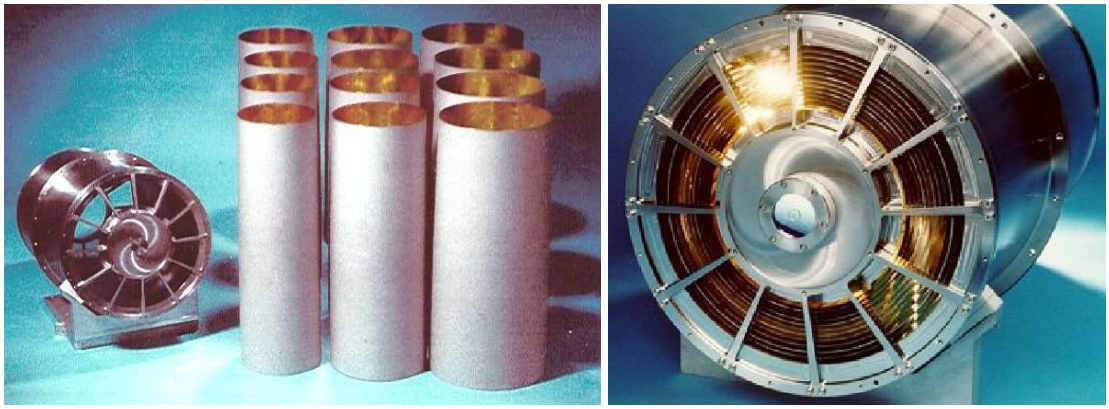

(a) (b)

Figure 6.6: One of the three units of the Jet-X telescopes still available. (**a**) Shells and mechanical structure (spider). (**b**) Optics mounted (Citterio et al., 1996).

be built with a modest cost. For this reason the design of PolariX is focused on the use of three telescopes, but it can host also two further optics.

The GPD and the filter wheel are contained in a box (see Fig.6.8a). The former is thermally controlled by a Peltier and a temperature between 10°C and 20°C with a maximum oscillation of ± 1°C is maintained to assure the stability of the gain and the performances of the GPD. The BEE and the high voltage power supplies are placed in a dedicated box near the GPD (see Fig. 6.8b) at a distance below $\sim$20 cm to maintain the noise low.

The X-ray sky in the 2-10 keV energy range is particularly luminous and a baffle is used to remove the stray light which could be transmitted by the lightshield tube (see Fig. 6.7). It also supports an electrostatic grid on the top which is maintained at high voltage to protect the window of the GPD. It is at $\sim$-2 kV to generate the drift field in the gas cell and could be damaged by the high flux of low energy protons producing secondary X-rays and overloading the HV power supply.

In Table 6.4 the masses of PolariX are summarized and its weight is well below the capabilities of the Vega launcher, included by ASI in the budget of the mission. PolariX will be placed in a low equatorial orbit (LEO) with an altitude of 505 km and an inclination below 5°: in this configuration the maximum load of the Vega launcher is about 2200 kg against the less than 1000 kg expected for PolariX. The LEO orbit is chosen to reduce the background since the magnetic field of the Earth effectively shields the cosmic particles at these altitudes.

At any moment the sky in the direction orthogonal to the Sun ± 20° is accessible to PolariX, this limit being required to maintain a sufficient exposure of the solar panel. The Earth occults the observed source for a large fraction of time ($\sim$50%) if it is not orthogonal to the orbit of the satellite and then the observation of a different source during the occultation could almost double the available observation time. This possibility (Smart Pointing) is inserted in the baseline of the mission and requires a dedicated on-board control and a very reliable AOCS (Attitude and Orbit Control Systems).

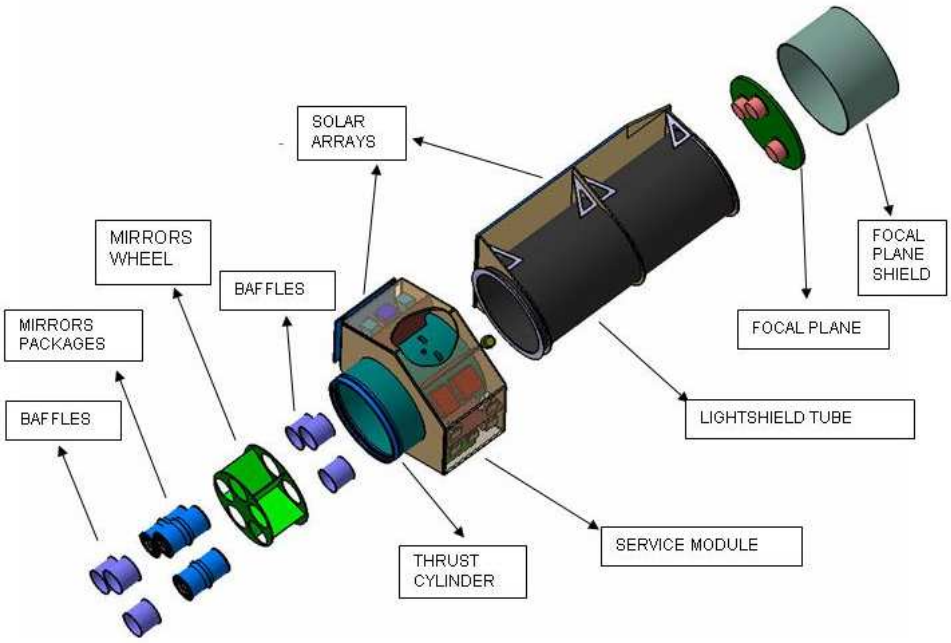

Figure 6.7: Exploded view of PolariX (image credit: Thales Alenia Space of Turin).

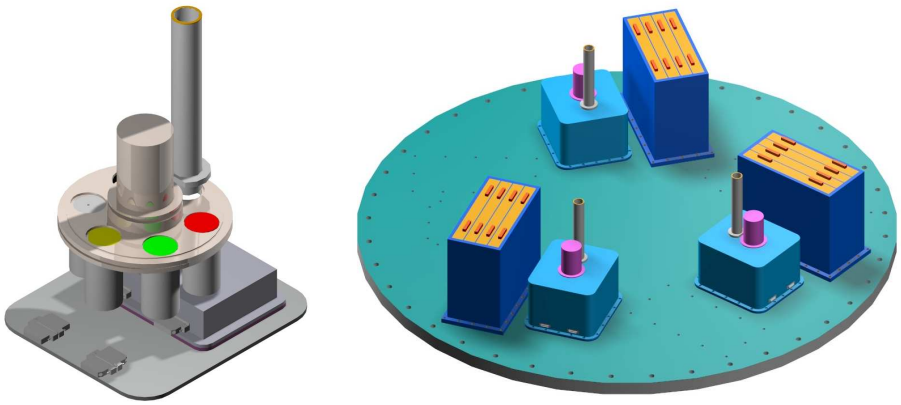

(a) **(b)**

Figure 6.8: Focal plane of PolariX. (**a**) Box which contains the GPD and the filter wheel. (**b**) Layout of the focal plane. The box which contains the HV power supplies and the BEE is in orange (images credit: INFN of Pisa).

Function	Mass (kg)	Margin	Margin (kg)	Mass (kg)
Focal Plane	24.7	20%	5	30
Telescopes	237	20%	47	281
Payload Electronics	9	20%	2	11
Total Payload				**322**
AOCS	60	7%	4	64
TT&C	9	11%	1	10
Data Handling	20	10%	2	22
EPS	94	12%	11	106
Structure subsystem	130	20%	26	156
Thermal control	38	10%	4	42
Total Service Module				**400**
		TOT + 20% margin and launcher adapter		*911*

Table 6.4: Mass of the PolariX satellite. AOCS is the Attitude and Orbit Control Systems and TT&C refers to Telecommanding, Tracking and Communications. Eventually EPS is Electrical Power Systems.

Data are downloaded from the ASI space station in Malindi and subsequently transmitted to the Mission Operation Center located at Fucino. Eventually they are collected in the PolariX Science Data Center developed and managed under the responsibility of the IASF/INAF of Rome.

PolariX is intended to be an observatory dedicated to the Italian and worldwide scientific community and hence the 75% of its observation time is open to the community as Guest Observer Program. The ground and user segment are illustrated in Fig. 6.9.

The duration of the PolariX mission is limited to 1.5 years to reduce the cost of the mission, but the orbit decay could allow to extend the mission up to a few years.

6.3.2 EXP^2 on-board HXMT

HXMT (*Hard X-ray Modulation Telescope*, Li, 2007) is a Chinese space mission devoted to study hard X-ray emission of astrophysical sources with three instruments, the *Low*, *Medium* and *High Energy telescopes*, LE, ME and HE respectively, which provide energy response between 1 and 250 keV. Each instrument is composed of smaller modules which are slat-collimated and their main characteristics are reported in Table 6.5. The launch is scheduled in a few years.

The main scientific objective of the HXMT mission is an all-sky survey, performed by exploiting the direct demodulation technique (Li and Wu, 1994) with the phoswich detectors of the HE telescope. An Italian contribution could be carried out in the optimization of their electronics which would benefit of the expertise of the Italian team which already built the *Phoswich Detection System* instrument on board BeppoSAX (Frontera et al., 1997). Pointed observations are foreseen to study X-ray binaries and Supernova remnants for about a half of observation time.

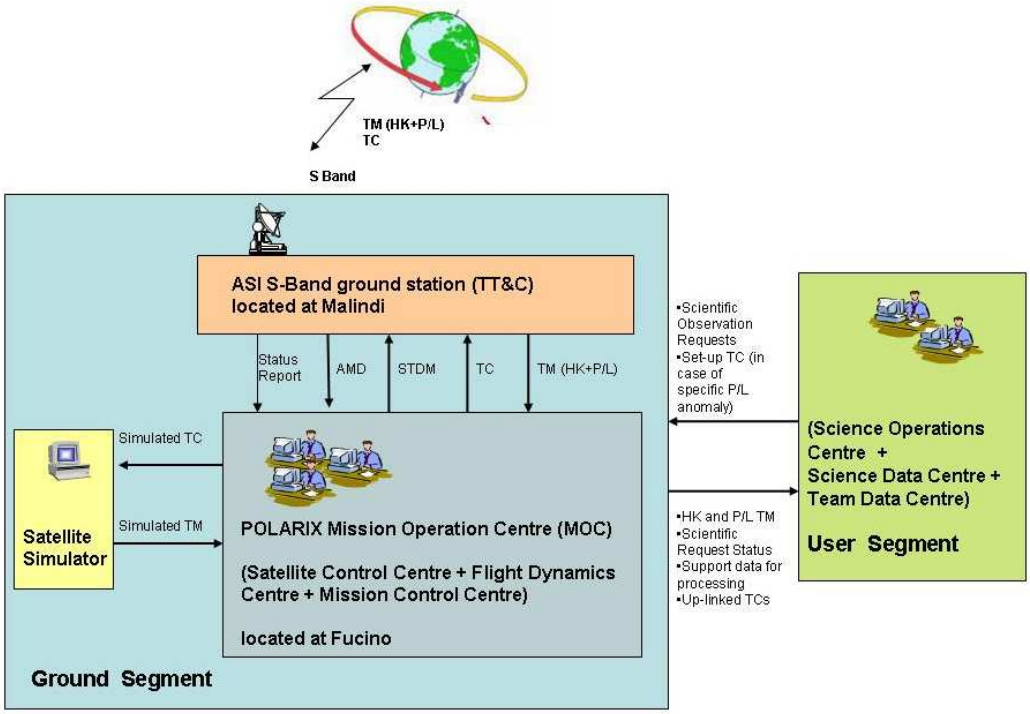

Figure 6.9: Drawing of the ground and user segment of PolariX.

	LE	ME	HE
Detectors	SCD	Si-PIN	NaI/CsI
Total Area (cm^2)	384	952	5000
Energy Range (keV)	1-15	5-30	20-250
Time Resolution (μs)	1000	20	25
Energy Resolution	8% @ 6 keV	15% @ 20 keV	19% @ 60 keV
FoV of one module	$5.7° \times 1.1°$	$5.7° \times 1.1°$	$5.7° \times 1.1°$
Number of modules	3	3	18
Angular resolution		$<5'$	
Source location		$<1'$	
Sensitivity (3σ, 10^5 s, counts/(cm^2 s keV)	4.4×10^{-5}	2.6×10^{-5}	3×10^{-7}

Table 6.5: Main characteristics of the instruments on-board HXMT.

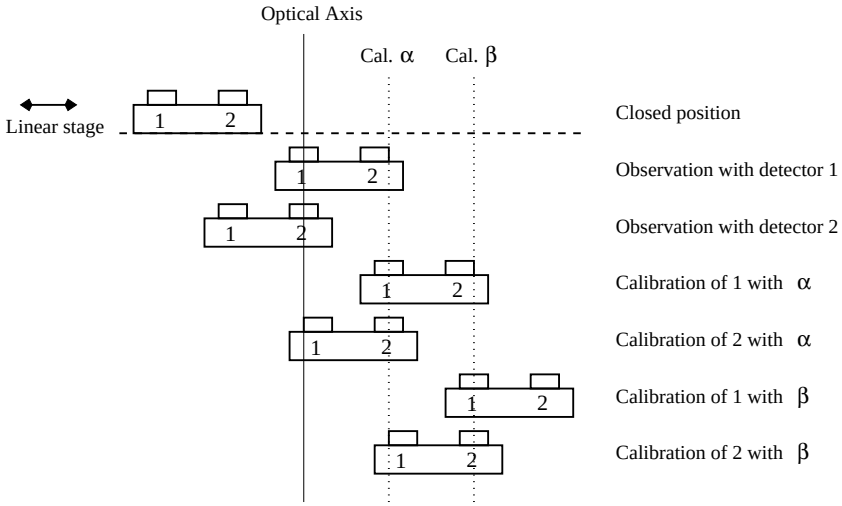

Figure 6.10: Operating modes of the linear stage in case of the combination with the functions of the filter wheel. Only two calibration sources (α and β) are shown for clarity.

Hard X-ray emission and polarimetry are often related since non thermal processes can emerge both with hard tails and polarized radiation. An high degree of polarization also suggests the geometry of the system, being related to the presence of an uniform magnetic field, an asymmetric distribution of matter or the direction of accelerated particles. Instead the presence of a (hard) non-thermal emission and the lack of any polarization is the signature of disordered or symmetric systems, because the magnetic field is randomly distributed or photons are scattered on spherical distributions of matter.

EXP^2 (*Efficient X-ray Photoelectric Polarimeter*) allows to join the study of the polarization to that of hard X-rays performed with HXMT (Costa et al., 2007; Soffitta et al., 2008). The institutes involved in this project are the same as PolariX, namely the IASF/INAF of Rome, the OAB/INAF for the optics, the INFN of Pisa for the detector and the University of Rome "Roma Tre" for scientific support.

The focal plane instrumentation shares many similarities with PolariX. The current version of the GPD is used to accomplish to the ambitious schedule of HXMT but in this case each focal plane includes two detectors filled with the standard and a softer mixtures. They are alternatively used to match at best the spectrum of the observed source thanks to a linear stage which moves the appropriate instrument in the focal plane. This function could be joined to that of the filter wheel (see Sec. 6.1.2): calibration sources could be placed above the linear stage and the detectors are calibrated when one of them is placed below it (see Fig. 6.10). However in this configuration some possibilities of the filter wheel, e.g. gray filter and diaphragm, would not be available.

The design of the optics is driven by the resources available. The most stringent constraints are the weight available ($\sim$110 kg) and the volume in the fairing of the launcher which has a length $\sim$2.5 m. The latter makes it impossible the use of telescopes already built, e.g. the Jet-X optics whose focal length is 3.5 m, but the construction of devoted tele-

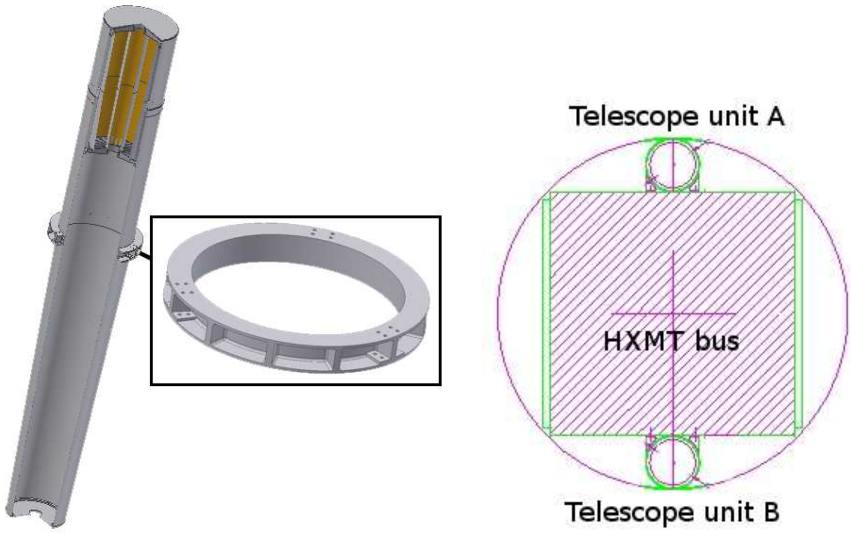

(a) (b)

Figure 6.11: (**a**) A telescope unit (credit: OAB/INAF). (**b**) Mounting of the two modules of EXP^2 on the side of the bus of HXMT.

scopes can be performed with the modern technology which allows better performances. An iridium coating could be used to increase the critical angle with respect to the gold at high energy while a carbon overcoating could be exploited to "fill" the reflectivity decrease at ∼3 keV caused by the M-edges of gold and iridium. Indeed this is the energy range where the GPD is particularly sensitive. In case of problems in the deposition of the iridium or carbon, the schedule of HXMT could be anyhow respected since the most demanding part of the manufacture of the telescope are the mandrels and they can be built regardless of the coating. Gold is then a safe alternative solution in case the iridium or carbon coatings fail.

EXP^2 is composed of two identical telescopes with a focal length of 2.1 m, each of 30 shells with diameter ranging from 9 to 27 cm. The application of the iridium and carbon coatings to inners mirrors could be difficult and hence this is done only on the 22 outer shells which contributes most to the total area, reported in Fig. 6.5. The estimated weight of the optics is 100 kg but it could be reduced by decreasing the thickness of a least a number of shells from 200 μm to 100 μm. This would imply a controlled loss of angular resolution and preliminary tests suggests a HEW<30 arcsec. Then the angular resolution of the GPD would be of the order of 40 arcsec including the effect of inclined penetration in the gas cell.

The optics and the focal plane instruments are mounted in a tube which provides the mechanical support of the telescope and the interface with the bus of HXMT. The tubes are mounted on the side of the spacecraft with a flange (see Fig. 6.11).

EXP^2 has been approved by ASI which is currently negotiating its inclusion on-board HXMT with the Chinese space agency.

Number of telescopes	3
Shells per telescope	30
Focal length	4.0 m
Shell diameter	142-274 mm
Shell thickness	145-224 μm
Mean grazing angle	15.3-29.4 arcmin
Angular resolution	<30 arcsec HEW
Telescopes mass	27.5 kg per telescope

Table 6.6: Main characteristics of the three identical telescopes of IXPE (Weisskopf et al., 2008).

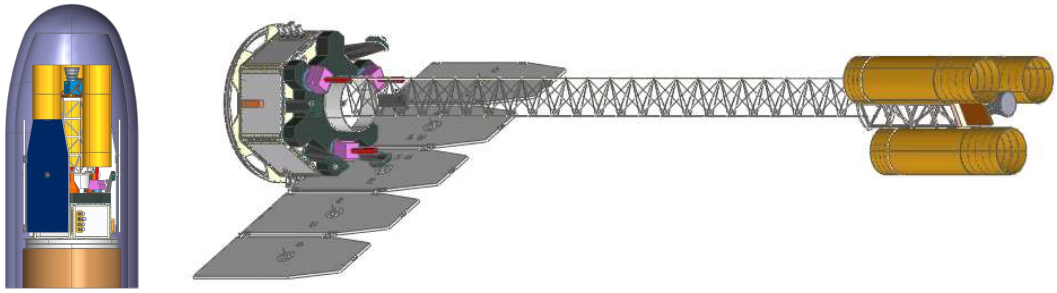

(a) **(b)**

Figure 6.12: (**a**) IXPE in the fairing of the Pegasus XL launcher. (**b**) A drawing of the satellite after that the extensible bench has been deployed (images credit: M. C. Weisskopf).

6.3.3 IXPE

The *Imaging X-ray Polarimetry Explorer* (IXPE, Weisskopf et al., 2008) is a small mission proposed to the National Aeronautics and Space Administration (NASA) which was not selected since an analogous mission based on the TPC (see Sec. 2.5) was preferred. Nevertheless it is very interesting because the large area at high energy allows to appreciate the performances of the GPD filled with a heavy mixture (see Sec. 6.5.2). The Italian institutes involved in IXPE were the IASF/INAF of Rome, the INFN of Pisa and the University of Rome "Roma Tre". They had the responsibility of the focal plane instruments and the calibration sources, while the Marshall Space Flight Center was responsible for the optics and the spacecraft.

Three telescopes were included in the IXPE payload and their characteristics are summarized in Table 6.6. They have a large total area (see Fig. 6.5) and a long focal length, achieved with the use of an extensible bench. A drawing of IXPE inside the fairing of the Pegasus XL launcher selected by NASA for the small missions is reported in Fig. 6.12a: only after the launch the optics are deployed (see Fig. 6.12b). The expected weight of IXPE is 214 kg and this is well below the maximum weight which could be carried by the launcher in a LEO orbit.

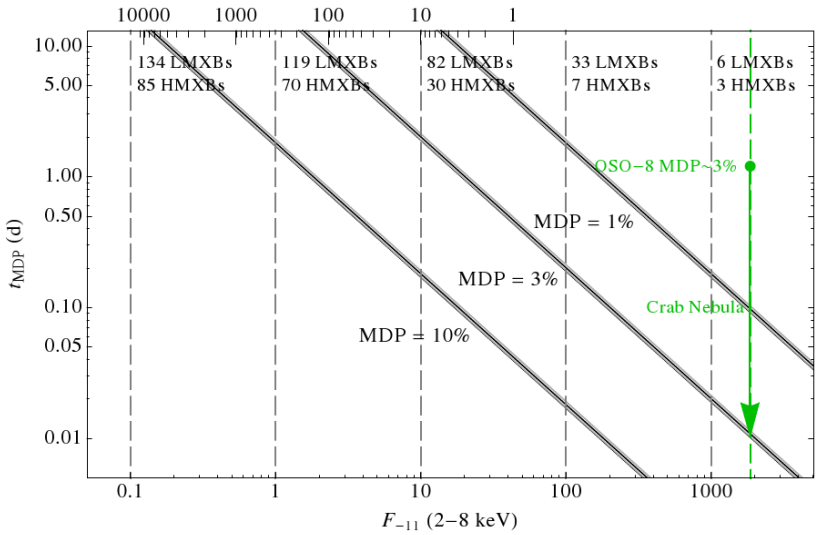

Figure 6.13: Observation time (in days) required to reach a certain MDP with IXPE as a function of the flux (in unit of 10^{-11} erg/(cm^2 s)). The number of HMXBs and LMXBs above various flux levels are also reported while the top axis provides the number of extragalactic sources corresponding to each flux. The green point represents the sensitivity of the polarimeter on-board OSO-8 (Weisskopf et al., 2008).

The observation time required to reach a certain MDP is reported in Fig. 6.13 as a function of the flux of the source. The number of HMXBs and LMXBs above various flux levels are also reported, while the top axis provides the number of extragalactic sources corresponding to each flux. IXPE would be able to perform polarimetry of tens of sources. The duration of the mission would be longer than one year and it would be divided into two phases: the first one would be dedicated to a survey of ∼40 objects, including 4 PWNe, 4 other pulsars, 12 LMXBs, 6 HMXBs, 8 blazars and 6 other AGNs, while the subsequent phase would be exploited to perform more detailed studies on the most interesting sources (Weisskopf et al., 2008).

6.4 Large observatory scenario

The continuous development of space instrumentation has allowed an enormous improvement in the X-ray astronomy. The study of the (near) Universe has been possible thanks to the recent observatories like Chandra and XMM-Newton which exploits X-ray telescopes with an area of the order of 0.1 m^2. The distant Universe will be studied thanks to the next generation observatories but the intrinsic faintness of the sources requires optics of the order of 1 m^2, i.e. at least a order of magnitude larger than current telescopes.

XEUS (*X-ray Evolving Universe Spectrometer*) was the European project aimed to the observation of the distant Universe with three main scientific objectives (Arnaud et al., 2008). The first was to study the formation and the growing of supermassive black holes:

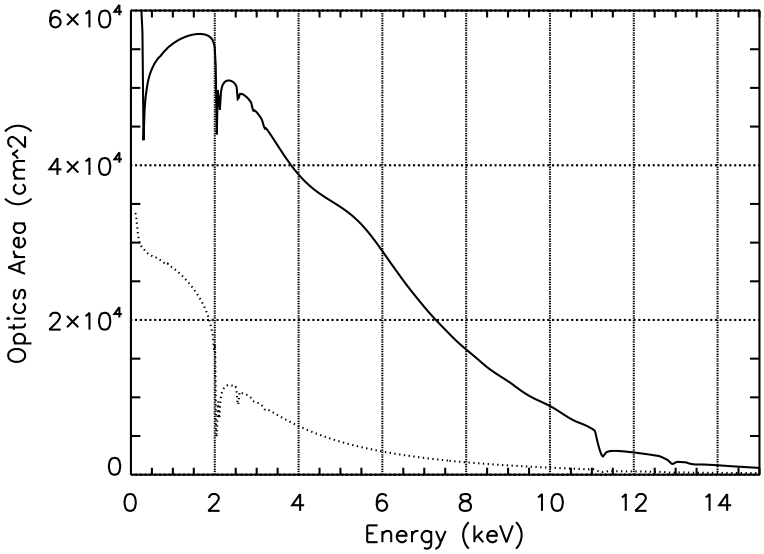

Figure 6.14: Comparison between the optics area of XEUS (solid line) and IXO (dotted line).

XEUS was designed to detect them at z >10 and to census the Compton-thick AGNs. Moreover it could investigate the feedback of supermassive black holes on the host galaxies and eventually its high energy resolution at the level of one eV could provide for the first time the possibility to derive the redshift by the X-ray data alone.

The study of large scale structures was another scientific objective of XEUS. It could trace their evolution thanks to the observation of the hot gas which is heated in gravitational wells produced by dark matter. The large collecting area, the excellent spectral and the good angular resolution allowed to study the Warm Hot Intergalactic Medium which should contain a significant fraction of the barionic matter of the Universe. XEUS could perform detailed analyzes of the composition of intracluster medium to investigate the role of the feedback from supernovae and supermassive black holes.

Eventually XEUS was designed to study the behavior of matter under extreme conditions. These included the strong gravitational field near galactic and extragalactic black holes and the extreme physics related to the neutron stars, which are ideal laboratories of particle and nuclear physics since in these systems huge magnetic fields and densities several times that nuclear are encountered.

XEUS was characterized by a telescope of 5 m^2 (see Fig. 6.14) with an angular resolution better than 5 arcsec. A silicon micro-pore optics was used in place of the classical technology which is based on grazing incidence reflection on shells because the former provides a ratio between mass and collecting area more than an order of magnitude better. A focal length of 35 m was achieved with two satellites in formation flight, placed in orbit in the second Lagrangian point by a single Ariane launcher.

There were two main instruments in the focal plane of XEUS. The first was the *Narrow Field Instrument*, a spectrometer based on an array of Transition Edge Sensors which can provide an energy resolution at the level of one eV on a field of view of 1.6×1.6 $arcmin^2$.

The *Wide Field Imager* was instead based on silicon pixels arrays and offered a moderately high spectroscopy (30-150 eV) on a large field of view, 7×7 arcmin^2.

Three smaller instruments supplemented the main devices. The *Hard X-ray Imager* could extend the imaging capability of the WFI up to 40 keV with a field of view of 7×7 arcmin^2. The *High Time Resolution Spectrometer* was devoted to single photon spectroscopy for bright point sources at high counting rate. Eventually the *X-ray polarimeter* (XPOL) was dedicated to polarimetry of galactic and extragalactic sources and is described in Sec. 6.4.1.

The XEUS mission was selected by the European Space Agency (ESA) for a phase A study to be launched in ∼2020. Afterwards ESA and NASA decided to merge the XEUS and the Constellation-X missions (Hornschemeier et al., 2005) since their overlapping scientific objectives and the common shortage of founds: the resultant mission has been called IXO, *International X-ray Observatory*.

The design of IXO has not been defined yet but its scientific requirements are reported in Table 6.7. The current hypothesis is to reduce the area of the telescope and its focal length to 20 m to exploit an extensible bench in place of the formation flight configuration, strongly reducing the costs. The area of the current design of IXO is compared with that of XEUS in Fig. 6.14.

XPOL is currently in the baseline instruments of IXO.

6.4.1 XPOL on-board IXO/XEUS

XPOL (*X*-ray *Pol*arimeter) is the photoelectric polarimeter based on the GPD on-board IXO/XEUS (Bellazzini et al., 2006a; Costa et al., 2008). The construction of further generation of the ASIC chip is the only improvement required with respect to the current instrument: it would not be able to sustain the rate expected in the focus of the large IXO optics because several thousands of counts per second are expected for a strong source like the Crab nebula against a current read-out capability of some hundreds.

Currently a standard helium-DME mixture is assumed as baseline for XPOL even if there is room for a further improvement, since the launch of IXO is scheduled in more than ten years. The focal plane layout is based on that of pathfinder missions with a filter wheel which is used to put in front of detector calibration sources and/or diaphragms. The detector is controlled, powered and read-out by the Back End Electronics which is placed near the detector. Data are transmitted to the Control Electronics where are forwarded to telemetry or stored in the mass memory in case of high rate (∼100 mCrab). In the latter case they are analyzed on-board so that only a subset of the informations are eventually transmitted to Earth. The mass memory is 16 Gbyte, dimensioned to store 30 ks of observation of a strong source.

The inclusion of the GPD in the focal plane of IXO didn't require many resources since they are essentially that reported in Table 6.2 with n =1. At the contrary XPOL can greatly extend the multi-purpose capabilities of an international observatory like IXO because it allows to measure the polarization of X-ray sources alongside large throughput spectroscopy, timing and imaging.

The observation time dedicated to XPOL should be ∼10% of the total and then the

Mirror effective area	
3 m^2 @ 1.25 keV	Black hole evolution, cosmic feedback, EoS, large scale structures
0.65 m^2 @ 6 keV (1 m^2 goal)	EoS, strong gravity
150 cm^2 @ 30 keV (350 cm^2 goal)	Cosmic acceleration, strong gravity
Spectral resolution	
ΔE = 2.5 eV within 2×2 $arcmin^2$ (0.3-7 keV)	Black hole evolution, large scale structures
ΔE = 10 eV within 5×5 $arcmin^2$ (0.3-7 keV)	
ΔE <150 eV @ 6 keV within 18 $arcmin^2$ diameter (0.1-15 keV)	Missing baryons using background AGNs
$E/\Delta E$=3000 with an area of 10^3 cm^2 for point sources (0.3-1 keV)	
ΔE=1 keV within 8×8 $arcmin^2$ (10-40 keV)	
Mirror angular resolution	
≤5 arcsec HEW (0.1-10 keV)	Black hole evolution, cosmic feedback, large scale structures, missing baryons
30 arcsec HEW (10-40 keV, 5 arcsec goal)	Black hole evolution
Count rate	
1 Crab with >90% throughput, ΔE <200 eV (0.1-15 keV)	EoS, strong gravity
Polarimetry	
1% MDP on 1 mCrab in 100 ks (2-6 keV)	AGNs geometry, strong gravity
Astrometry	
1 arcsec at 3σ confidence	Black hole evolution
Absolute timing	
50 μs	Neutron studies

Table 6.7: Scientific requirements of the IXO mission. The driver of the constrain is also specified.

use of the large optics of IXO is in part compensated by the lower observation time (see Sec. 6.5). However the main scientific driver for XPOL is the long focal length ($f \geq$20 m): a high angular resolution (5 arcsec) is expected including the effect of the inclined penetration of photons in the gas cell and this is a large improvement which can't be achieved by any pathfinder mission. It makes possible the polarimetry of faint sources which must be resolved from close diffuse emission, like jets or the fine structures of the PWNe (see Sec. 6.5).

6.5 Scientific objectives

X-ray polarimetry is an almost unexplored science and the objectives of future instruments are fundamentally based on the literature and the expectations that have been developed since the beginning of X-ray astronomy. Then the missions based on the GPD, especially pathfinders, are designed to be versatile and address at best to many different scientific topics; nevertheless many "guaranteed" results can be identified. The GPD has a sensitivity that allows to reach a minimum detectable polarization below 1% and in many cases the polarization at this level is a direct consequence of well-defined and accepted models or theories: even a non-detection would imply a significant discovery.

Both galactic and bright extragalactic sources are accessible to small missions, while faint extragalactic objects could be systematically studied with the polarimeter on-board IXO. Specific expectations are performed for a subset of interesting actual sources and the results are derived both in the pathfinder and IXO scenarios. PolariX is assumed as benchmark of the former since this is the small mission in the most advanced phase at the moment. Long observations (up to $\sim$10 days) can be planned for pathfinders because the telescope is dedicated to X-ray polarimetry, while in the case of IXO only $\sim$10% of the observation time could be reasonably reserved to XPOL and consequently the longest pointings are of the order of a few days.

The minimum detectable polarization for each source is estimated with Eq. 2.30 (see Sec. 2.4):

$$\mathrm{MDP} = \frac{4.29}{\epsilon \mu F} \sqrt{\frac{B + \epsilon F}{ST}}, \tag{6.10}$$

where F and B are the source and the background fluxes in a selected energy range, ϵ is the detector efficiency, S the collecting area and T the observation time. This assumes the lack of any systematic effects, taking into account Poisson fluctuations alone.

The flux of the sources is calculated from their actual spectra, retrieved from the literature and parameterized with an XSPEC model. The modulation factor of the GPD is derived with the Monte Carlo software (see Sec. 2.4) and the products $\epsilon\mu F$ and ϵF are calculated taking into account the finite energy resolution of the instrument. The value of these functions at an energy E is gaussian smeared according to the energy resolution with a procedure performed by XSPEC, the modulation factor being introduced by means of a multiplicative tabulated model. Both the internal and the diffuse background are considered in the calculation of the MDP but their contributions are generally negligible (see Sec. 6.2.1).

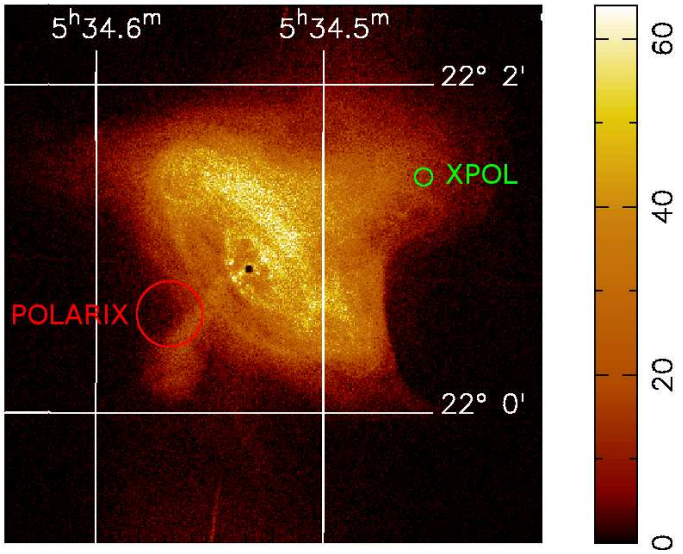

Figure 6.15: Comparison of the HEW of PolariX and XPOL. The structures of the Crab nebula would be clearly resolved (image from Weisskopf et al., 2000)

The MDP for some representative sources is reported in Table 6.8. The results are integrated in the 2-10 keV energy range and an observation time of 100 ks (∼1 day) and 10 ks (∼3 hours) is assumed in the pathfinder and large observatory scenarios respectively. The MDP for particularly faint sources, e.g. the M87 knot A or Sgr B2, can be scaled for a longer observation time T_1 from that reported in the Table MDP_0:

$$\mathrm{MDP}_1 = \mathrm{MDP}_0 \sqrt{\frac{T_0}{T_1}}, \tag{6.11}$$

where T_0 is 100 ks or 10 ks for the pathfinder and large observatory scenario respectively.

The use of the GPD on-board IXO allows an improvement in the sensitivity of an order of magnitude with respect to pathfinder missions because the same results are achieved in one tenth of the observation time. Since the background is always negligible, in principle the same results as XPOL could be achieved by a pathfinder mission with a 10 times longer observation. However the source must be assumed stationary, while the large part of sources in X-ray sky are extremely variable, and observations much longer than ∼10 days are difficult to be planned. Then only the large optics of IXO opens the way for the systematic measurement of a large number of faint extragalactic sources.

Moreover the high angular resolution of XPOL (5 arcsec) can be very efficiency exploited in the study of diffuse sources. The Half Energy Width of XPOL is superimposed on the Crab nebula in Fig. 6.15 and allows to finely resolve all its sub-structures. The HEW of PolariX (24 arcsec) is also reported for comparison. Note that both the point spread function and the inclined penetration of photons in the cell gas are taken into account (Fabiani et al., 2009).

	Class	**PolariX**, T=100 ks flux (c/s)	flux (mCrab)	MDP (%)	**XPOL**, T=10 ks flux (c/s)	MDP (%)	Reference
Crab nebula	PWN	145.637	1000.00	0.4	3586.349	0.3	
Cas A	CCO	0.014	0.09	42.2	0.345	28.4	Mereghetti et al. (2002)
4U0142+614	AXP	0.722	4.96	6.8	18.823	4.4	Rea et al. (2007)
SGR 1900+14 (quiescence)	SGR	0.112	0.77	12.2	2.604	8.8	
Cyg X-1	HMXB	159.550	1095.53	0.5	4132.423	0.3	Cui et al. (1998)
X0115+63	HMXB	74.757	513.31	0.5	1798.438	0.4	Santangelo et al. (1999)
GRS 1915+105 (thermal state)	LMXB	62.044	426.02	0.5	1416.332	0.4	McClintock et al. (2006)
GX339-4	LMXB	95.751	657.47	0.5	2447.624	0.4	
Her X-1	LMXB	5.660	38.86	1.7	129.706	1.3	dal Fiume et al. (1998)
Holm 9 XMM1	ULX	0.027	0.19	27.9	0.663	19.6	Winter et al. (2006)
IC0342 XMM2	ULX	0.014	0.09	40.1	0.332	28.0	Winter et al. (2006)
M81 XMM1	ULX	0.013	0.09	42.1	0.324	28.5	Winter et al. (2006)
IC4329A	Seyfert 1	0.690	4.73	5.6	16.798	3.9	
Fairall 9	Seyfert 1	0.162	1.11	11.9	3.997	8.2	
MCG-6-30-15	Seyfert 1	0.390	2.68	7.8	9.645	5.4	Tanaka et al. (1995)
Centaurus A	Seyfert 2	0.455	3.13	4.7	8.828	3.8	
Circinus galaxy	Seyfert 2	0.039	0.27	19.8	0.861	15.2	
MCG-5-23-16	Seyfert 2	0.491	3.37	6.6	11.940	4.7	
3C 279	Quasar	0.030	0.20	26.8	0.723	18.8	Giommi et al. (2002)
1ES 1101-232	BL Lac	0.253	1.74	9.7	6.274	6.7	
BL Lac	BL Lac	0.066	0.45	18.5	1.617	12.8	Giommi et al. (2002)
Mrk 421 (typical)	BL Lac	0.851	5.84	5.6	21.524	3.8	
Mrk 501 (outburst)	BL Lac	1.510	10.36	3.7	36.404	2.6	
M87 knot A	Jet	not resolved			0.163	39.4	Perlman and Wilson (2005)
Sgr B2	RN	0.001	0.01	65.7	0.013	68.9	Sidoli et al. (2001)

Table 6.8: Minimum detectable polarization for some representative sources. The PolariX mission is a benchmark for the pathfinder scenario. A flux of 1000 mCrab corresponds between 2 and 10 keV to 1 Crab=2.3×10^{-8} erg/(cm^2 s). The spectra of the sources are retrieved by the literature as specified in the column "Reference".

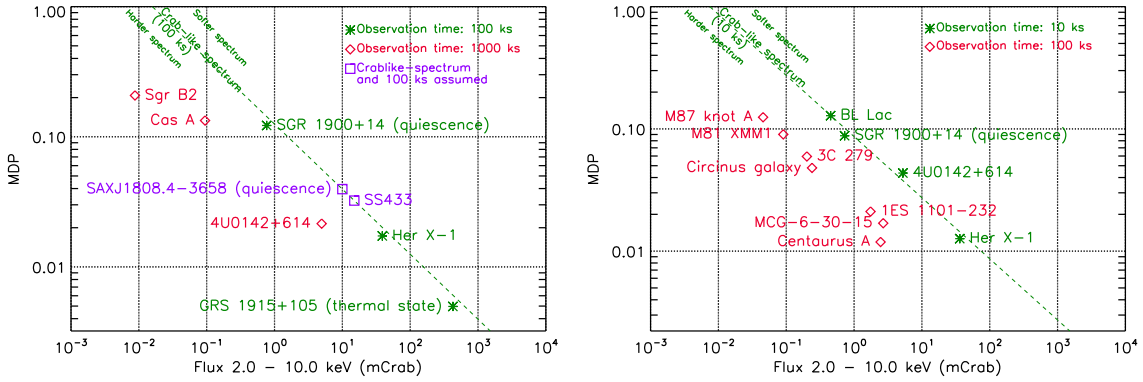

Figure 6.16: Dependence of the MDP on the flux of the source for PolariX (**a**) and XPOL (**b**). Some sources belonging to different classes are reported as example.

XPOL is also able to measure the polarization of galactic and extragalactic jets, which are expected to be highly polarized (see Sec. 1.4.8), allowing for distinguishing the origin of the emission. A MDP of 8.8% can be reached in the case of the knot A of M87 for an observation of 200 ks.

The dependence of the MDP with the flux is reported graphically in Fig. 6.16. The flux is expressed in mCrab, where 1 mCrab = 2.3×10^{-11} erg/(cm^2 s) in the energy range 2-10 keV, and the spectrum of the Crab Nebula is assumed as reference. A lower MDP can be reached for harder sources being equal the flux because in this case the counts are distributed at higher energy where the modulation factor of the GPD is larger.

The Eq. 6.10 can also be reversed to obtain the observation time required to reach a determined MDP for a certain source. The results are presented in Fig. 6.17.

6.5.1 Observation of peculiar sources

The MDP provides the lower limit to the degree of polarization which is measurable for a certain source and hence it is a hint of the possibilities opened by the instrument. However the MDP can't be used to compare the results of an observation with the expectations of a model and then a small Monte Carlo software is used to simulate the observation of some specific sources.

The rate and the observation time are used to derive the number of collected counts in a certain energy band, while the shape of the spectrum is exploited to calculate the average modulation factor $\bar{\mu}$ in that energy interval. The expected degree of polarization $\mathcal{P}$ as a function of energy is defined by the model assumed and synthetic modulation curves are generated with a modulation equal to the product of $\bar{\mu}$ by $\mathcal{P}$. A Poisson-distributed noise is summed in each angular bin of the modulation curve which is eventually fitted with a $\cos^2$ function. The measured degree and angle of polarization and their errors are estimated as the mean of the fit parameters on several hundreds of synthetic curves generated in each energy band. Obviously this procedure takes into account statistical

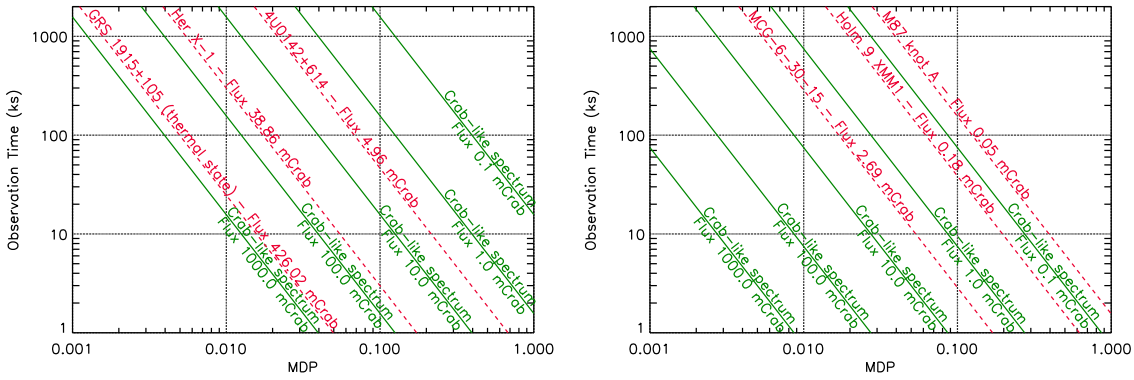

(a) **(b)**

Figure 6.17: Observation time required to reach a certain MDP as a function of the flux of the source for PolariX (**a**) and XPOL (**b**).

fluctuations alone.

An example of the results were published by Dovčiak, Muleri, Goosmann, Karas, and Matt (2008) which extended the study of Connors et al. (1980) already presented in Sec. 1.4.6. The degree and the plane of polarization are calculated in the case of a geometrically thin but optically thick accretion disk surrounding a galactic black hole. Thermal disk emission is polarized by scatterings in a semi-infinite atmosphere whose optical depth is varied between 0.5 to infinity. Gravitation effects are fully taken into account: they causes a rotation of the plane of polarization and the sum of photons produced in different regions of the disk. This in turn implies a reduction of the polarization degree because X-rays are locally polarized parallel or orthogonal to the plane of the disk but the polarization is summed incoherently because of gravitational bending.

The degree and the angle of polarization measured by an external observer are reported in Fig. 6.18. It is assumed that the mass of the black hole is M=14 $M_\odot$ and the accretion rate is $\dot{M}$=1.4×10^{18} g s^{-1}; different optical depths τ and inclinations of the observer θ_0 are considered. X-rays at higher energies are produced closer to the central black hole and hence the gravitational effects of depolarization and rotation of the plane of polarization are larger. The net result is a degree and an angle of polarization strongly dependent on energy (see Fig. 6.18), this effect being larger in the case of Kerr black holes because an accretion disk co-rotating with the black hole is truncated closer to the central compact source than in the Schwarzschild case. As a matter of fact the amplitude of the rotation of the plane of polarization is considered one of the most sensitive probe for the measurement of black holes spin.

The observability of these effects is investigated in both pathfinder and large observatory scenarios. The Galactic black hole system and micro-quasar GRS 1915+105 is used as benchmark: this source is very bright in the thermal state and the inclination of 70° (Mirabel and Rodriguez, 1994) favors a high degree of polarization (cf. Fig. 6.18). The spectrum assumed corresponds to a low-luminosity thermal state (McClintock et al., 2006), $\mathcal{L} \lesssim 0.3\ \mathcal{L}_{Edd}$, which minimizes the contamination by non-thermal phenomena

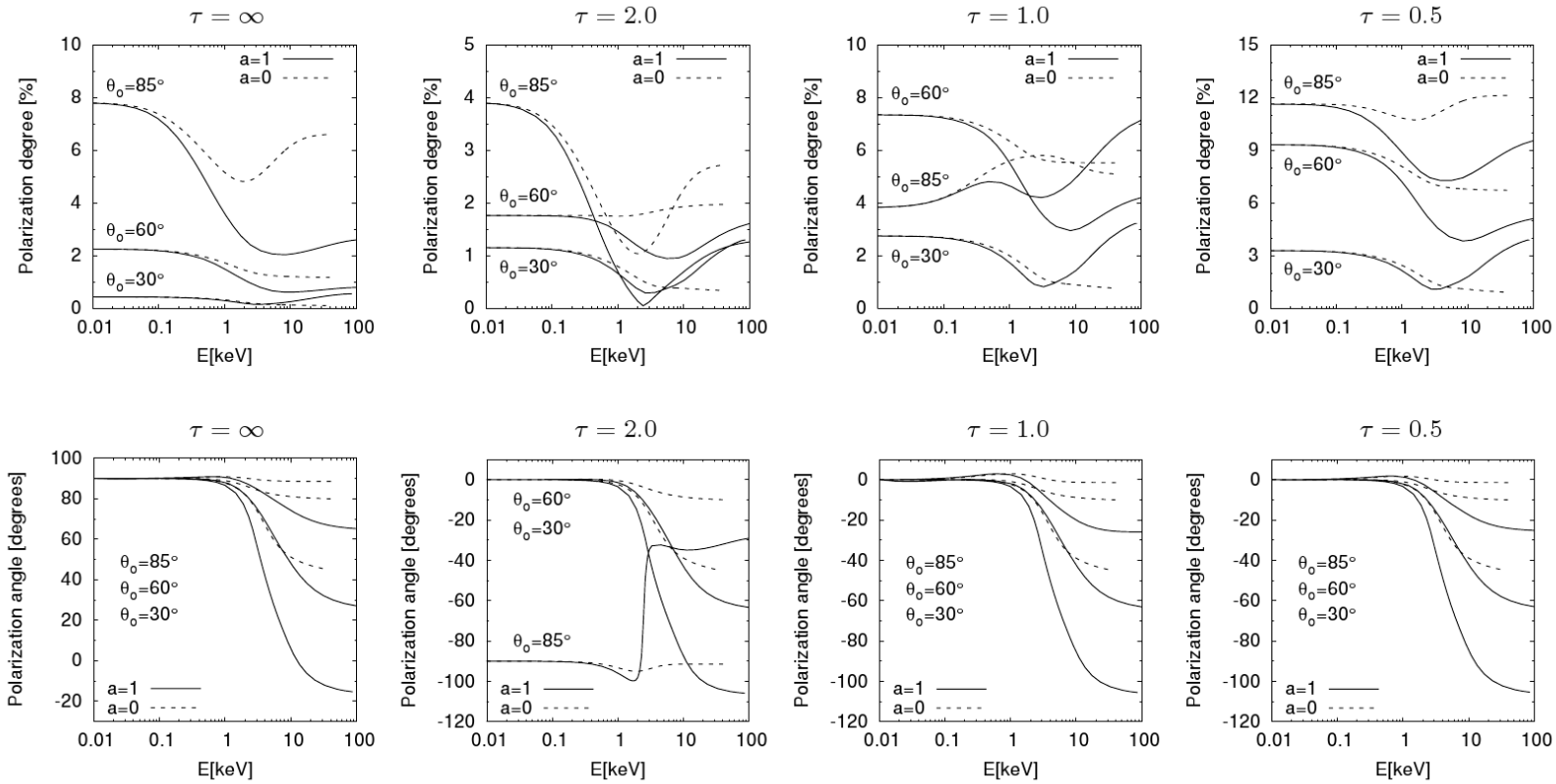

Figure 6.18: Polarization expected in the case of thermal emission of galactic black holes. The dependence of the degree and the plane of polarization with energy are in the top and bottom panels respectively. The optical depth is infinity, 2.0, 1.0 and 0.5 from left to right. The observer inclination θ_0 is 30°, 60° and 85°. Schwarzschild and Kerr black holes are dashed and solid lines respectively. The mass of the black hole is M=14 $M_\odot$ and the accretion rate $\dot{M}$=1.4×10^{18} g s^{-1} (Dovčiak et al., 2008).

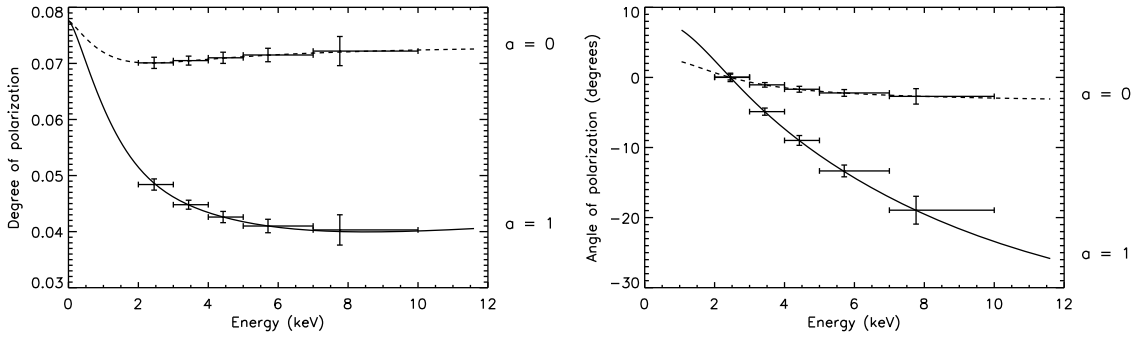

(a) **(b)**

Figure 6.19: Simulated 1 Ms observation of GRS 1915+105 with PolariX. The energy dependence of the degree and angle of polarization are in (**a**) and (**b**). The solid and dashed curves refer to the case of a Kerr and a Schwarzschild black hole respectively. $\tau = 1.0$ and $\theta_0 = 70°$. Errors are at the 1-σ level. Note that the angle of polarization is set to zero at low energy since the actual inclination of the accretion disk is not known.

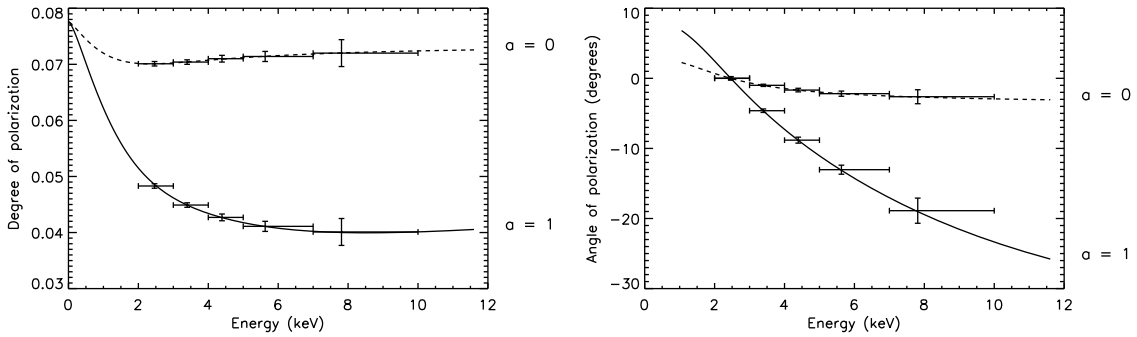

(a) **(b)**

Figure 6.20: The same as Fig. 6.7 but for XPOL and an observation of 200 ks.

which are not taken into account in the model. The dependence of the polarization with energy is that calculated for τ=1, θ_0=70°, a mass of the black hole M=14 $M_\odot$ and an accretion rate $\dot{M}$=1.4×10^{18} g s^{-1} (McClintock et al., 2006). The results for an observation of 1 Ms and 200 ks with PolariX and XPOL are reported in Fig. 6.19 and Fig. 6.20 respectively. The variation with energy is easily observed for both degree and angle of polarization and the Kerr and Schwarzschild cases can be clearly discriminated.

The origin of X-ray emission from the molecular cloud Sgr B2 was already discussed in Sec. 1.4.9 (Sunyaev et al., 1993; Koyama et al., 1996; Revnivtsev et al., 2004). A strong limit on the angular position of the source which illuminated Sgr B2 in the past could be obtained with the GPD (see Fig. 6.21). A Monte Carlo simulation provides a 2.4° error in the measurement of the polarization plane for a 1 Ms observation with PolariX and this corresponds to the 1-σ error in the determination of the angular position of the

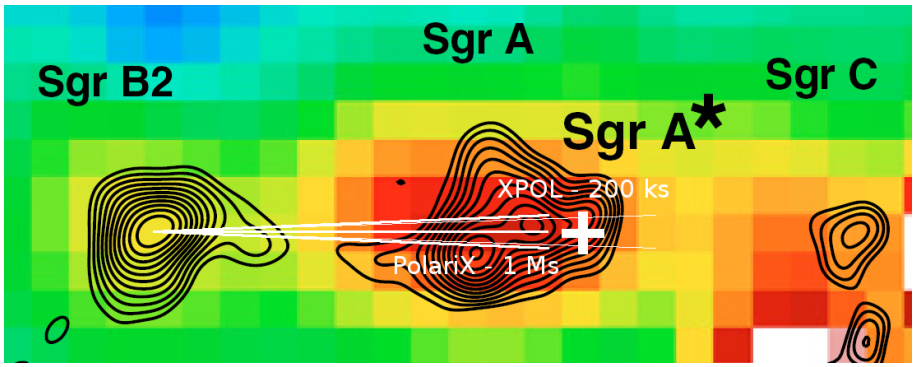

Figure 6.21: Monte Carlo simulations of Sgr B2 observation with PolariX and XPOL lasting 1 Ms and 200 ks respectively. A polarization degree of 70% is assumed. Errors are at the 1-σ level.

external source. A polarization of 70% is assumed since a very high degree of polarization is expected on the basis of numerical calculations (Churazov et al., 2002). Instead an analogous observation with XPOL lasting 200 ks provides an error of 1.88° (see Fig. 6.21).

X-ray polarimetry could be a powerful probe to test quantum gravity theories (see Sec. 1.4.11). The vacuum is expected to be birefringent in the context of quantum loop gravity (Gambini and Pullin, 1999) and this would cause a rotation of the plane of polarization as the photons propagate from distant sources (Mitrofanov, 2003). Observations of blazars are the best candidates for these studies, since they are very bright and a high degree of polarization is expected (see Sec. 1.4.8; Celotti and Matt, 1994; Poutanen, 1994). Despite these sources could present intrinsic variations of the polarization, they could be distinguished from an actual signature of quantum gravity birefringence because is expected that the rotation is proportional to the distance (cf. Eq. 1.41):

$$\Delta\phi(E) \simeq \chi E_{keV}^2 D_{ly} \tag{6.12}$$

and then a correlation with the distance for different objects emerges in case of an actual effects.

PolariX is able to measure the polarization of a small number of blazars. As an example, 1ES 1101-232 is a blazar at z=0.186 and a MDP of 9.7% can be reached with a 100 ks observation in the energy range 2-10 keV (see Table 6.8): then the measurement of a possible rotation of the plane of polarization with energy could be possible within several days. XPOL can achieve an analogous result in an observation time of $\sim$1 day, making possible a survey of different blazars to search for a possible rotation of the polarization correlated with the distance of the objects.

In Fig. 6.22 is reported the effect of the quantum gravity birefringence on the direction of polarization which would be measured with a 200 ks observation of 1ES 1101-232 by XPOL. A constant polarization degree of 20% is assumed: a fit with a constant function would be rejected up to a limit $\chi \sim 10^{-10}$, which is an order of magnitude lower than current upper limits (see Sec. 1.4.11).

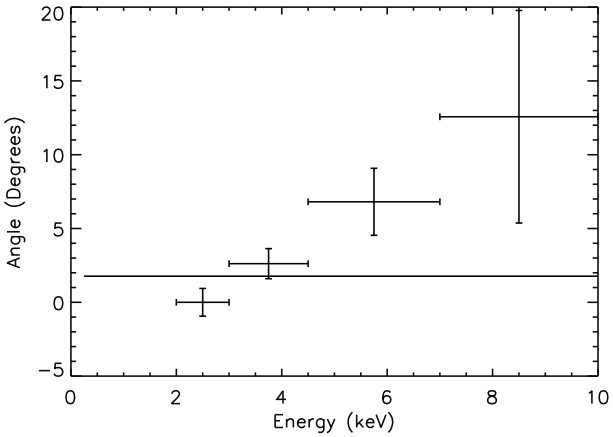

Figure 6.22: Rotation of the plane of polarization induced by the vacuum birefringence which is expected in the case of loop quantum gravity. A 200 ks observation of the blazar 1ES 1101-232 with XPOL and a polarization degree of 20% are assumed. The fit with a constant function (solid line) can be rejected up to $\chi \sim 10^{-10}$. Errors are at 1-σ level.

6.5.2 High energy optimization

A mixture 20% helium and 80% DME provides the best polarimetric sensitivity between 2 and 10 keV and indeed this is the current baseline configuration of the GPD, exploited in both pathfinder and large observatory scenarios. However when a large area is available at high energy ($\gtrsim$6 keV) it could be better exploited with detectors filled with mixtures of argon, which provide a higher sensitivity and allow to extend the energy range of the GPD above 10 keV.

Mixtures based on argon can be used only above 6 keV since only in this case the photoelectron has an energy higher than that of the Auger electron, the latter being 3.206 keV when the photon is absorbed by the K-shell. Then argon polarimeters can't be used in place of helium ones in the contex of a versatile and all-purpose explorer mission: however they could temporarily replace the baseline detectors in the focus of the telescope. GPDs filled with argon mixtures could be used for a wide number of sources which emit hard spectra, e.g.:

- black holes binaries, to improve the spectro-polarimetric capabilities of the GPD;
- highly absorbed sources, e.g. Circinus Galaxy or Sgr B2;
- sources whose emission is expected to be more polarized at higher energy, e.g. AGNs;
- sources with cyclotron lines, e.g. X0115+63.

In this Section the scientific performances of the GPD when it is filled with mixtures of argon are discussed. The three optics of the IXPE mission are taken as a realistic example because its telescopes maintain a very large area up to 11 keV (see Fig. 6.5). In addition to

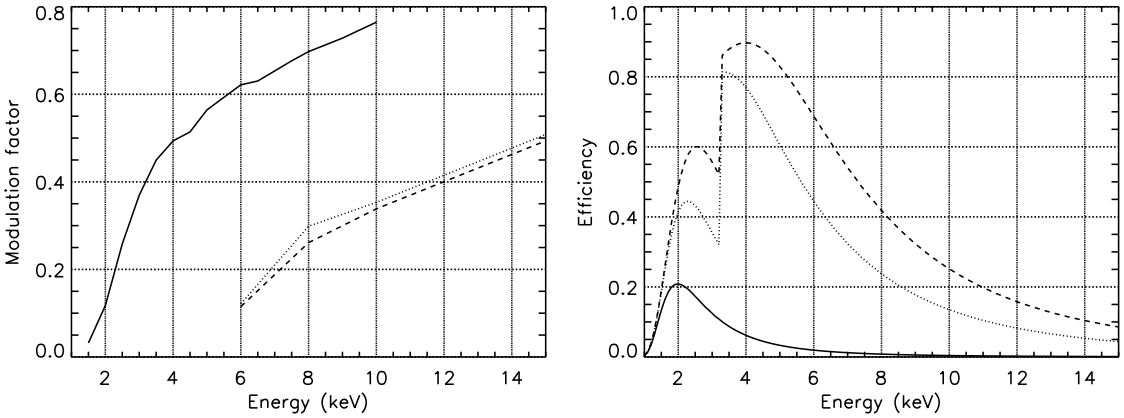

(a) (b)

Figure 6.23: Comparison of the modulation factor (**a**) and efficiency (**b**) for heavy mixtures. Solid line refers to the baseline mixture composed of 20% He and 80% DME at 1 atm and a gas cell 1 cm thick. Dotted and dashed lines refer to 60% Ar and 40% DME at 2 atm and gas thickness 1 or 2 cm respectively. A 50 μm beryllium window is included in the efficiency.

the baseline helium mixture, two mixtures 60% argon and 40% DME at a pressure 2 atm but with an absorption region 1 or 2 cm thick are considered. Their behavior is studied with the Monte Carlo software and the detailed results are presented in Chapter 8.

The modulation factors of these three mixtures are compared in Fig. 6.23a. μ is significantly lower in the case of argon and this is expected since tracks are shorter and more scattered by atomic nuclei. However their efficiency is much larger (see Fig. 6.23b) and this allows a significant improvement of the quality factor above 6 keV, reported in Fig. 6.24.

The minimum detectable polarization for the three mixtures considered is reported in Table 6.9 for five benchmark sources which are representative of the classes of astrophysical objects listed above. The MDP is derived with Eq. 6.10 in different energy bands and the flux and the average modulation factor in each energy interval are also reported in the Table. The former is proportional to the efficiency of the mixture, while the average modulation factor $\bar{\mu}$ provides the amplitude of the expected modulation, which is proportional to the product of $\bar{\mu}$ by the actual degree of polarization. $\bar{\mu}$ is weighted with the spectrum of the source.

The MDP between 6 and 10 keV is halved with the use of argon mixtures (see Table 6.9). This is achieved thanks to the higher number of collected photons, the fluxes being a factor $\sim$30 higher, even if the larger statistic is partially balanced by the lower modulation factor. Furthermore the use of argon mixtures opens the way for measurements above 10 keV thus extending the scientific objectives of the GPD, the case of the transient X-ray pulsar X0115+63 being an interesting example. A cyclotron absorption line at about 12 keV has been detected in the spectrum of this source (Wheaton et al., 1979; Santangelo et al., 1999): it should be highly polarized and a very important probe for the study of the emission geometry in X-ray pulsars (Meszaros et al., 1988). Energy resolved

	He + DME			Ar + DME 1 cm			Ar + DME 2 cm		
E (keV)	Flux (c/s)	$\bar{\mu}$	MDP (%)	Flux (c/s)	$\bar{\mu}$	MDP (%)	Flux (c/s)	$\bar{\mu}$	MDP (%)
Crab Nebula, T=100 ks									
2 - 3	237.3	0.2216	0.40	—	—	—	—	—	—
3 - 6	92.3	0.4551	0.31	—	—	—	—	—	—
6 - 10	5.36	0.6593	0.89	142.6	0.2127	0.53	239.0	0.1965	0.45
10 - 15	—	—	—	12.6	0.3892	0.98	23.9	0.3746	0.74
GRS1915+105, T=1 Ms									
2 - 3	79.4	0.2455	0.20	—	—	—	—	—	—
3 - 4	41.4	0.4276	0.16	—	—	—	—	—	—
4 - 6	22.1	0.5347	0.17	—	—	—	—	—	—
6 - 10	4.09	0.6548	0.32	107.5	0.2032	0.20	188.6	0.1966	0.16
10 -15	—	—	—	5.03	0.3818	0.50	9.51	0.3673	0.38
Circinus Galaxy, T=1 Ms									
2 - 3	0.0491	0.2343	8.3	—	—	—	—	—	—
3 - 6	0.0364	0.4732	4.8	—	—	—	—	—	—
6 - 10	0.0056	0.6674	8.6	0.151	0.2303	4.8	0.257	0.2127	4.0
10 -15	—	—	—	0.026	0.3944	6.7	0.050	0.3800	5.1
Sgr B2, T=1 Ms									
2-10	0.0030	0.5872	13.4	—	—	—	—	—	—
6 -15	—	—	—	0.0391	0.2051	10.6	0.0651	0.1920	8.8
X0115+35, T=100 ks									
6-11	—	—	—	109.9	0.2178	0.59	184.9	0.2017	0.49
11-15	—	—	—	1.06	0.4127	3.2	2.03	0.3984	2.4

Table 6.9: Comparison of the MDP for the three mixtures considered and some representative sources, belonging to classes of objects whose study would benefit of the use of a harder polarimeter. The Crab Nebula is a reference source. The baseline mixture He+DME refers to a mixture 20% helium and 80% DME at 1 atm and 1 cm thick. Ar+DME mixtures assume 40% argon and 60% DME at 2 atm and the gas cell is 1 or 2 cm thick. T is the observation time dedicated to each mixture and $\bar{\mu}$ the average modulation factor weighted with the spectrum of the source.

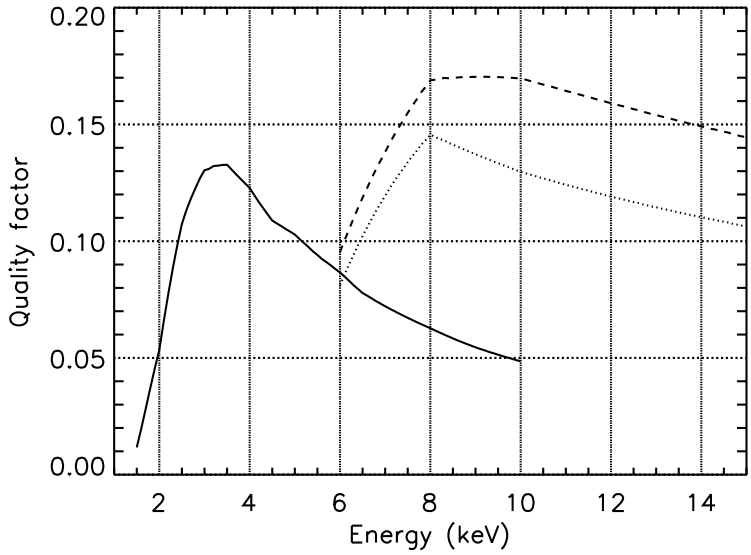

Figure 6.24: Comparison of the quality factor $\mu\sqrt{\epsilon}$. The mixtures are the same as Fig. 6.23.

polarimetry would be accessible to GPDs filled with mixtures of argon (see Table 6.9) and a phase-resolved analysis should be possible for a reasonable long observation time.

Measurements above 10 keV would also increase the spectro-polarimetric capabilities of the GPD. This is of primary importance in many contexts: for example it provides a more powerful probe to investigate the spin of galactic black holes since in a wider energy range the expected rotation of the plane of polarization is larger (see Sec. 6.5.1). In Table 6.10 are reported the errors in the determination of the angle of polarization in different energy bands for the case of GRS 1915+105, assuming a 1 Ms observation of IXPE and three configurations:

1. 3 detectors (one per optics) filled with the baseline He-DME mixture at a pressure 1 atm and with an absorption region 1 cm thick (baseline configuration);

2. 3 baseline detectors alternatively replaced by three detectors filled with 60% argon and 40% DME, at a pressure 2 atm and a gas cell 1 cm thick;

3. the same as the case 2, but the thickness of the absorption region of the polarimeters based on argon is 2 cm.

When the observation time is divided between polarimeters based on helium and argon, a significant improvement is achieved: with a modest reduction of sensitivity below 6 keV, the measurement in the energy band 6-10 keV is more accurate and that between 10 and 15 keV is feasible.

The results obtained with argon mixtures are very promising. A gas cell 2 cm thick systematically provides better performances even if the larger thickness implies a lower angular resolution because of the inclined penetration of photons in the gas cell. The

	He+DME, 1 Ms	He+DME (500 ks) and **Ar+DME 1 cm (500 ks)**	He+DME (500 ks) and **Ar+DME 2 cm (500 ks)**
Energy keV	Angular Error °	Angular Error °	Angular Error °
2.0 - 3.0	0.38	0.54	0.54
3.0 - 4.0	0.33	0.46	0.46
4.0 - 6-0	0.38	0.54	0.54
6.0 - 10.0	0.76	**0.65**	**0.54**
10.0 - 15.0	—	**1.65**	**1.24**

Table 6.10: Comparison of the spectro-polarimetric capabilities of the three configurations considered, assuming a 1 Ms observation of GRS 1915+105 with IXPE. The 1-σ errors in the measurement of the plane of polarization are reported in the Table. The observation time is divided between helium and argon-based instruments if two types of detectors are present. The results obtained with the mixtures of argon are in bold. A Kerr black hole and $\tau = 1$ are assumed.

actual use of heavy mixtures on-board next missions largely depends on the telescope: the difficulties and the higher costs deriving from two detectors alternatively replaced in the focal plane are balanced only if a sufficient area above 6 keV is available.

Chapter 7

Photoelectric polarimetry with large field of view

The GPD has been always regarded as a focal plane instrument and then it has been proposed to be included on the next generation space-borne missions together with a grazing incidence optics (see Chapter 6). Despite this essential use of photoelectric polarimeters has not been accomplished yet, new possibilities are already emerging. In this Chapter a new application of the GPD and photoelectric polarimeters in general is explored, namely the feasibility of an instrument with a large field of view.

A polarimeter able to monitor continuously a large part of the sky would make accessible the study of transient sources, which are very common objects in the high energy sky. In particular the study of the prompt emission of GRBs would be of primary importance (see Sec. 1.4.10) and this provides an obvious and strong scientific justification of this application, which is even more interesting since the absence of an X-ray optics would make the instrument simple, light and inexpensive.

The area of the current version of the GPD is 15×15 mm^2 and hence it is too small to collect the large number of photons required to perform measurements of polarization without the use of an X-ray optics. However new detectors of larger area are currently under development and they could be placed side by side so that an area of many cm^2 would be achieved with several units. The TPC (see Sec. 2.5) also has been proposed as large field of view instrument (Hill et al., 2007), since its large quantum efficiency can be exploited to design instruments even with a modest area.

In this Chapter is discussed the capability to preserve the sensitivity of photoelectric polarimeters in the case of inclined beams, this problem obviously being at the bases of the construction of devices with large field view. Both polarized and unpolarized radiation is considered to analyze the possible decrease of performances and the emergence of spurious effects. Methods and algorithms to control the severe systematic effects which originate at angles above $\sim20^\circ$ are presented through a consistent analytical treatment, simulations and measurements.

The work presented in this Chapter was partially published by Muleri et al. (2008b), but the bases of this analysis and the first attempts to correct the systematic effects which emerge were already discussed by Muleri (2005).

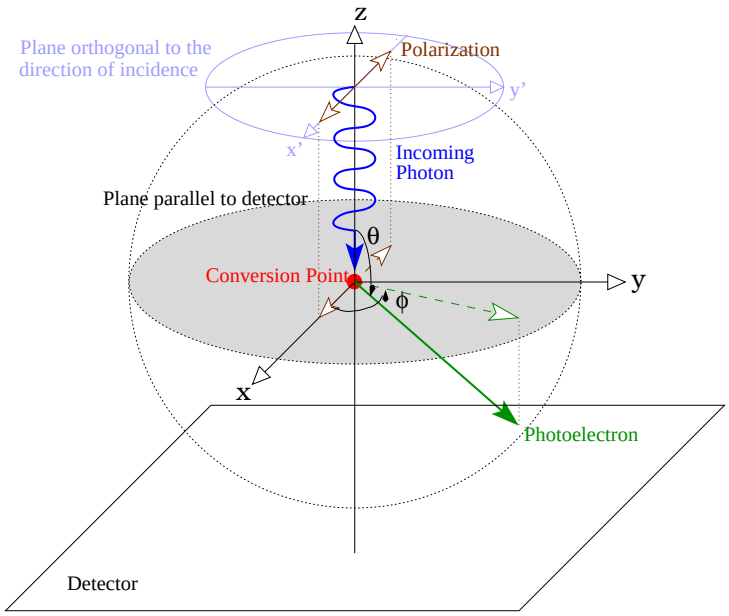

Figure 7.1: Definition of the angles of emission of a photoelectron.

7.1 Analysis of the photoelectric differential cross section

The photoelectric effect and its sensitivity to the polarization of the absorbed photon were already discussed in Sec. 2.1 and Sec. 2.1.1 respectively. Here a brief review is outlined for clarity, stressing the arguments necessary to the subsequent discussion.

The direction of emission of a photoelectron carries memory of the polarization of the absorbed photon. The probability that a photoelectron is emitted in a certain direction is modulated with a $\cos^2\phi$ function, where ϕ is the azimuthal angle between the direction of emission and polarization (see Fig. 7.1).

Inner orbitals with spherical symmetry, namely 1s and 2s, give the larger contribution to photoelectric absorption in the working condition of the GPD. This is true also for other photoelectric polarimeters, e.g. TPC, and hence outer orbitals are neglected in the following discussion. In this hypothesis the differential cross section of the photoelectric effect is:

$$\frac{d\sigma}{d\Omega} \propto \frac{\sin^2\theta\cos^2\phi}{(1+\beta\cos\theta)^4}, \tag{7.1}$$

where θ is the angle between the direction of the photon and that of the photoelectron (see Fig. 7.1).

The Eq. 7.1 includes the relativistic correction $1/(1+\beta\cos\theta)^4$, where β is the velocity of the emitted electron in units of the speed of light. If this relativistic correction is neglected, $d\sigma/d\Omega \propto \sin^2\theta\cos^2\phi$ and then the photoelectrons are emitted preferentially into the plane perpendicular to the direction of incidence, $\theta = \pi/2$. A complete symmetry between the emission above and below this plane is present, namely the directions $\theta = \bar{\theta}$

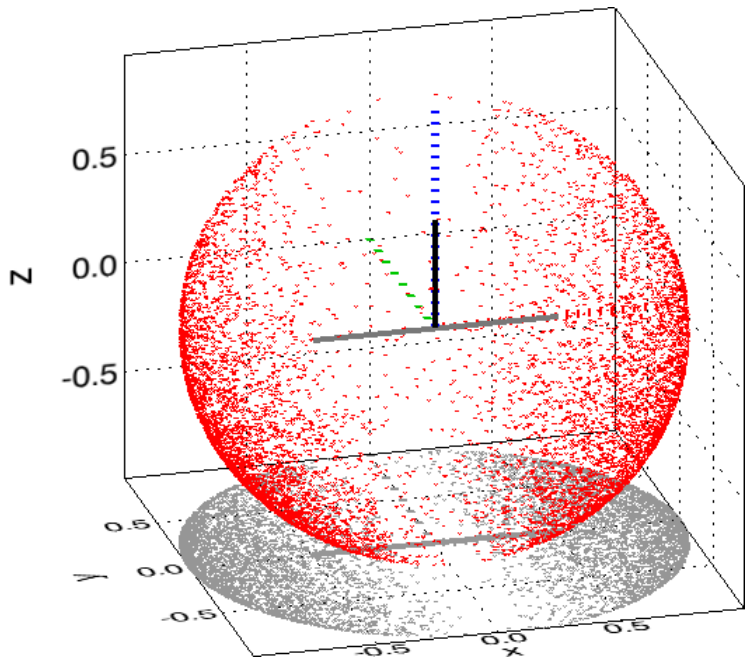

Figure 7.2: Forward folding due to the relativistic correction. The incident direction of (polarized) photons is the black solid line, while that of polarization is gray. The photons are absorbed in the center of the sphere of unit radius, in the point (0,0,0), and the directions of emission of photoelectrons are traced with the red points on the sphere. Note that they are more common in the semi-space $z < 0$. The projection of the plot on the xy plane is also shown. The red, green and blue dashed lines are respectively the x', y' and z' axes (see below). The energy of photoelectrons is 50 keV to show the forward folding more clearly.

are equivalent to those $\theta = -\bar{\theta}$.

The relativistic correction brakes this symmetry since it makes more probable the emission in the semi-space opposite with respect to the incident direction of photons. This causes an effect of "forward folding" which is shown in Fig. 7.2. The photons are absorbed in the center of the sphere of unit radius, in the point (0,0,0), and the directions of emission of photoelectrons are represented by the lines which join the red points and the center. The effect of the forward folding is to concentrate the photoelectrons in the semi-space $z < 0$ and indeed the red points are distributed preferentially in this region.

The most probable angle of emission significantly differs from $\pi/2$ at energies above a few keV: in Fig. 7.3 the probability distribution of angles θ as a function of energy is reported, the most probable angle of emission being:

$$\theta_m = \cos^{-1}\left(\frac{3 - \sqrt{9 + 16\beta^2}}{2\beta}\right). \tag{7.2}$$

An X-ray polarimeter derives the polarization of the absorbed photons from the initial direction of emission of photoelectrons. Actually it measures the projections of the

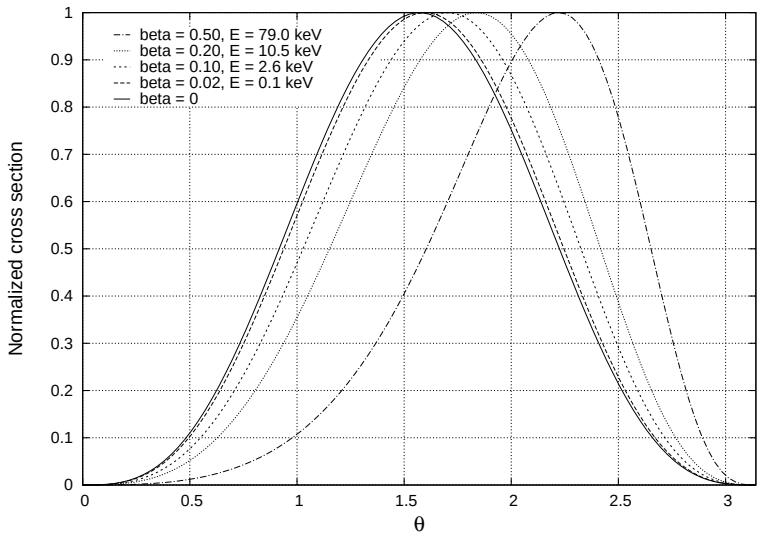

Figure 7.3: Forward folding of the angle of emission of photoelectrons θ for different values of their velocity β.

directions of emission on its plane (xy, see Fig. 7.1) which correspond to the gray points in Fig. 7.2. Their azimuthal distribution is not changed by the relativistic correction and it still follows a $\cos^2$ function: no photoelectrons are emitted orthogonally to the direction of polarization and this can be easily verified.

Photoelectrons are emitted according to the angular dependence specified by Eq. 7.1. This formula holds in a frame of reference $x'y'z'$ defined in such a way that z'-axis is coincident with the direction of incident photons and x' represents the direction of polarization. The frame of reference xyz is instead that of the detector (see Fig. 7.4): these two frames are coincident only if the photons are incident orthogonally to the detector.

The modulation of the emission directions of photoelectrons ℓ_i on a certain plane will be hereafter called "intrinsic", $\mathcal{M}_0$. It is different from the actual modulation measured by an instrument, $\mathcal{M}$, and is very important to understand the difference between these two quantities. The first depends only on the differential cross section of the photoelectric effect and it corresponds to the histogram of the projections on a plane of the directions ℓ_i. Instead the actual modulation curve is always measured on the plane of the detector and takes into account all the possible errors in the process of measurement of ℓ_i, including the propagation of the photoelectrons in the gas, the scattering on the atomic nuclei, the diffusion of pairs and so on. For this reason the actual modulation factor measured with an instrument is always below 100%, while the intrinsic modulation is always 100% in the plane orthogonal to the incident photons.

The intrinsic modulation can be calculated on the plane $x'y'$ or in that xy and they will be identified by $\mathcal{M}'_0(\phi')$ and $\mathcal{M}_0(\phi)$ respectively. The intrinsic modulation in $x'y'$ can be derived from the angular dependence expressed by Eq. 7.1: it must be only integrated over θ'. This takes into account that the directions characterized by the same ϕ'

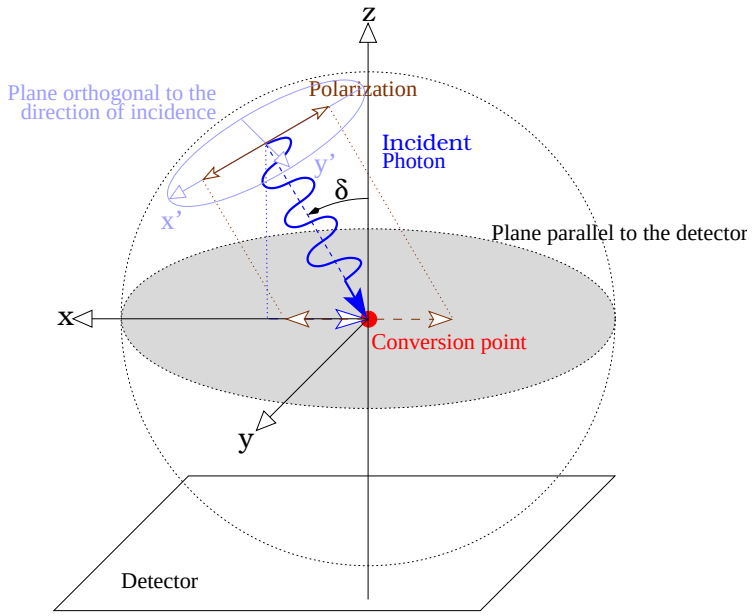

Figure 7.4: Definition of the frame of reference $x'y'z'$ and xyz.

are summed when projected on the plane $x'y'$ and falls in the same bin of the histogram of emission directions. Then:

$$^{pol}\mathcal{M}'_0(\phi') = \frac{d\sigma'}{d\phi'} \propto \int_0^\pi \frac{\sin^2\theta' \cos^2\phi'}{(1+\beta\cos\theta')^4} \sin\theta' d\theta' \propto \cos^2\phi', \tag{7.3}$$

where the term $\sin\theta'$ derives from $d\Omega' = \sin\theta' d\theta' d\phi'$.

In the same way, if photons are unpolarized:

$$^{unpol}\mathcal{M}'_0(\phi') = \frac{d\sigma'}{d\phi'} \propto \int_0^\pi \frac{\sin^2\theta'}{(1+\beta\cos\theta')^4} \sin\theta' d\theta' \propto 1. \tag{7.4}$$

The frame of reference $x'y'z'$ and xyz are coincident in the case of radiation which is incident orthogonally to the detector and hence the intrinsic modulation in these frames are equal:

$$\mathcal{M}_0(\phi) \equiv \mathcal{M}'_0(\phi'). \tag{7.5}$$

This result obviously holds for both polarized and unpolarized photons.

The emission direction of photoelectrons is reconstructed correctly with a certain probability: in general it depends on the energy but is identical in every azimuthal direction in the hypothesis that the polarimeter has negligible systematic effects. Then the modulation $\mathcal{M}(\phi)$ measured by the detector is proportional to the intrinsic one (in the frame of reference of the detector) and a constant is added to take into account the errors in the process of measurement, i.e. the probability to reconstruct the direction of emission

incorrectly:

$$\mathcal{M}(\phi) = M \cdot \mathcal{M}_0(\phi) + C \quad \text{with} \quad \begin{cases} {}^{pol}M_0(\phi) &= \cos^2\phi \\ {}^{unpol}M_0(\phi) &= 1 \end{cases} \tag{7.6}$$

where M and C are constants. Eq. 7.6 is the usual function used to fit the modulation of the histogram of the photoelectrons direction.

The modulation factor μ, namely the amplitude of the response of the instrument for completely polarized photons, can be derived from Eq. 7.6 (see Sec. 1.1.2):

$$\mu = \frac{\max\{\mathcal{M}\} - \min\{\mathcal{M}\}}{\max\{\mathcal{M}\} + \min\{\mathcal{M}\}} = \frac{M}{M + 2 \cdot C}, \tag{7.7}$$

but note that the last passage is allowed only if the $\mathcal{M}_0(\phi)$ function is normalized to unity.

7.2 Intrinsic modulation for inclined photons

The photons are incident nearly perpendicularly to the plane of the detector if a photoelectric polarimeter is used as narrow field instrument with an X-ray optics. The actual angle of incidence is determinated by the reflecting material of each shell and the geometry of the telescope but it is always of the order of a few degrees, namely rather small. Moreover any systematic effect possibly related to the inclined incidence of photons is reduced for symmetry reasons, since each shell concentrates the radiation from an annular region and in each point of the focal plane photons come from a conic region corresponding to this annular region (see Fig. 7.5). Hence every azimuthal systematics is averaged and, even if the average is not perfect out of the optical axis, this is an effect at the second order. Instead for instruments with large field of view photons coming from the same source are all incident with a large and identical inclination (see Fig. 7.5) and then the systematic effects are not azimuthally averaged but are summed in phase.

In the following the case of polarized and unpolarized radiation inclined at an angle $\delta \gtrsim 20°$ is analyzed, but only the simple situation of photons inclined around an axis orthogonal to the direction of polarization is considered. In particular this study is limited within the following assumptions (see Fig. 7.4):

1. the direction of polarization is along the x axis;
2. the inclination of an angle δ is performed around y axis.

The intrinsic modulation is derived even in this case with the same procedure presented in Sec. 7.1 but in this case there is an important difference, namely the frame $x'y'z'$ and xyz are not identical.

The plane $x'y'$ is by definition orthogonal to the incident direction of photons and then the intrinsic modulation $\mathcal{M}'_0$ is identical to Eq. 7.3:

$${}^{pol}\mathcal{M}'_0(\phi') = \frac{d\sigma'}{d\phi'} \propto \int_0^{\pi} \frac{\sin^2\theta' \cos^2\phi'}{(1 + \beta\cos\theta')^4} \sin\theta' d\theta' \propto \cos^2\phi'. \tag{7.8}$$

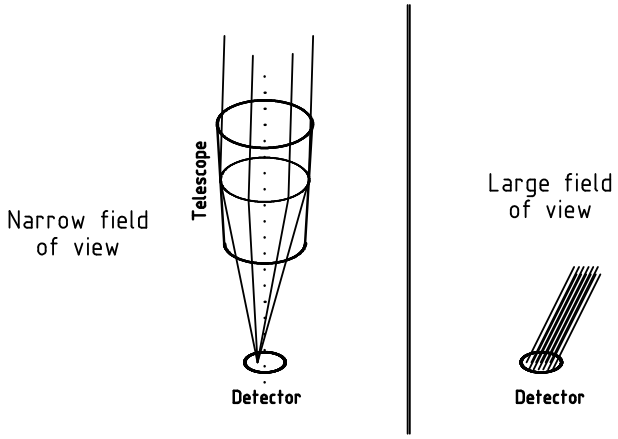

Figure 7.5: Differences between narrow and large field of view use of an instrument. Any systematic effect related to the inclined incidence of photons are averaged in the first case both for the lower inclination and symmetry reasons.

However the functions:

$$\left.\frac{d\sigma'}{d\Omega'}\right|_{pol} \propto \frac{\sin^2\theta'\cos^2\phi'}{(1+\beta\cos\theta')^4} \tag{7.9}$$

$$\left.\frac{d\sigma'}{d\Omega'}\right|_{unpol} \propto \frac{\sin^2\theta'}{(1+\beta\cos\theta')^4} \tag{7.10}$$

must be expressed in xyz to calculate the intrinsic modulation in the frame of the detector. This can be performed by applying a rotation to the coordinates:

$$\begin{pmatrix} x' \\ y' \\ z' \end{pmatrix} = \begin{pmatrix} \cos\delta & 0 & -\sin\delta \\ 0 & 1 & 0 \\ \sin\delta & 0 & \cos\delta \end{pmatrix} \times \begin{pmatrix} x \\ y \\ z \end{pmatrix} \Longrightarrow \begin{cases} x' = x\cos\delta - z\sin\delta \\ y' = y \\ z' = x\sin\delta + z\cos\delta \end{cases} \tag{7.11}$$

From the definition of θ and ϕ follows that (see Fig. 7.1):

$$\begin{cases} x = r\sin\theta\cos\phi \\ y = r\sin\theta\sin\phi \\ z = r\cos\theta \end{cases} \quad \text{and} \quad \begin{cases} x' = r'\sin\theta'\cos\phi' \\ y' = r'\sin\theta'\sin\phi' \\ z' = r'\cos\theta' \end{cases} \tag{7.12}$$

A rotation doesn't change the distances, namely $r = r'$. The numerator and the denominator of Eq. 7.9 and Eq. 7.10 can then be transformed as:

$$\sin\theta'\cos\theta' = \frac{x'}{r'} = \frac{x\cos\delta - z\sin\delta}{r} = \sin\theta\cos\phi\cos\delta - \cos\theta\sin\delta \tag{7.13}$$

$$\cos\theta' = \frac{z'}{r} = x\sin\delta + z\cos\delta = \sin\theta\cos\phi\sin\delta + \cos\theta\cos\delta \tag{7.14}$$

$$\sin^2\theta' = \frac{x'^2 + y'^2}{r'^2} = (\sin\theta\cos\phi\cos\delta - \cos\theta\sin\delta)^2 + (\sin\theta\sin\phi)^2 \tag{7.15}$$

Then:

$$\left.\frac{d\sigma}{d\Omega}\right|_{pol} \propto \frac{\left(\sin\theta\sin\phi\cos\delta-\cos\theta\sin\delta\right)^2}{\left(1+\beta\sin\theta\cos\phi\sin\delta+\cos\theta\cos\delta\right)^4} \tag{7.16}$$

$$\left.\frac{d\sigma'}{d\Omega'}\right|_{unpol} \propto \frac{\left(\sin\theta\cos\phi\cos\delta-\cos\theta\sin\delta\right)^2+\left(\sin\theta\sin\phi\right)^2}{\left(1+\beta\sin\theta\cos\phi\sin\delta+\cos\theta\cos\delta\right)^4} \tag{7.17}$$

The analytical integration of these functions in θ is not easy and hence the relativistic correction is approximated at its first order:

$$\frac{1}{\left(1+\beta\cos\theta\right)^4} \approx 1-4\beta\cos\theta. \tag{7.18}$$

The integration of Eq. 7.16 and Eq. 7.17 is straightforward with this approximation and the result is:

$$\begin{aligned} {}^{pol}\mathcal{M}_0(\phi,\delta,\beta) &= \left[-\frac{3}{2}\pi\beta\sin\delta\cos^2\delta\right]\cos^3\phi+\left[\frac{4}{3}\cos^2\delta\right]\cos^2\phi+ \\ &+ \left[\frac{\pi}{2}\beta\left(2\sin\delta-3\sin^3\delta\right)\right]\cos\phi+\left[\frac{2}{3}\sin^2\delta\right] \end{aligned} \tag{7.19}$$

$$\begin{aligned} {}^{unpol}\mathcal{M}_0(\phi,\delta,\beta) &= \left[\frac{3}{2}\pi\beta\sin^3\delta\right]\cos^3\phi+\left[-\frac{4}{3}\sin^2\delta\right]\cos^2\phi+ \\ &+ \left[\pi\beta\left(\frac{3}{2}\sin\delta\cos^2\delta-2\sin\delta\right)\right]\cos\phi+\left[2-\frac{2}{3}\cos^2\delta\right] \end{aligned} \tag{7.20}$$

The functions ${}^{pol}\mathcal{M}_0(\phi,\delta,\beta)$ and ${}^{unpol}\mathcal{M}_0(\phi,\delta,\beta)$ are quite complex however they depend only on the parameters β and δ, namely on the energy and inclination of the photons. When δ=0 both functions are proportional to the those reported in Eq. 7.6, obtained when photons are incident perpendicularly to the detector, the constant of proportionality being required to take into account the functions ${}^{pol}\mathcal{M}_0(\phi,\delta,\beta)$ and ${}^{unpol}\mathcal{M}_0(\phi,\delta,\beta)$ are not normalized to unity.

The systematic effects which emerge for inclined photons can depend on the relativistic correction or not. It is never negligible in the context of X-ray polarimetry, $\beta \approx$0.11 for E=3 keV, but it is interesting to discuss the two contributions individually. If $\beta = 0$, Eq. 7.19 and Eq. 7.20 become:

$${}^{pol}\mathcal{M}_0(\phi,\delta,\beta=0) = \left[\frac{4}{3}\cos^2\delta\right]\cos^2\phi+\left[\frac{2}{3}\sin^2\delta\right] \tag{7.21}$$

$${}^{unpol}\mathcal{M}_0(\phi,\delta,\beta=0) = \left[-\frac{4}{3}\sin^2\delta\right]\cos^2\phi+\left[2-\frac{2}{3}\cos^2\delta\right] \tag{7.22}$$

These functions are very different from those obtained in the case of photons orthogonal to the detector and the first important difference is the presence of a constant term in

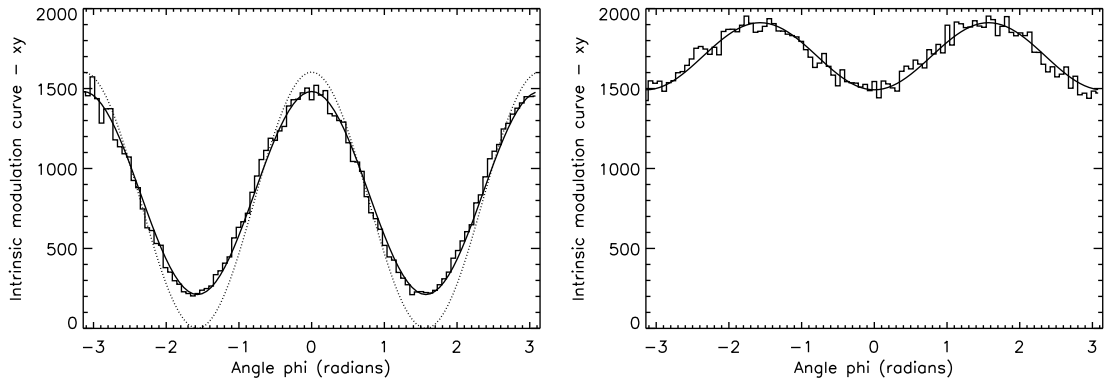

(a) **(b)**

Figure 7.6: Intrinsic modulation curves $\mathcal{M}_0$ on the plane xy in the case of polarized (**a**) and unpolarized (**b**) radiation. The relativistic correction is neglected, $\beta = 0$, and the inclination δ is -30°. Dashed curve is a fit with a $\cos^2$ function. Solid line is the corresponding $\mathcal{M}_0$ function, i.e. ${}^{pol}\mathcal{M}_0$ in (**a**) and ${}^{unpol}\mathcal{M}_0$ in (**b**). The value of δ is fixed and only the normalization is changed in the fit. Note the constant term in (**a**) and the modulation which appears in (**b**). Both are caused by the systematics presented in this Chapter.

the intrinsic modulation even for completely polarized photons. Indeed in the direction orthogonal to that of polarization:

$$ {}^{pol}\mathcal{M}_0(\phi = 90°, \delta, \beta = 0) = \frac{2}{3}\sin^2\delta \neq 0 \quad \text{if} \quad \delta \neq 0. \tag{7.23}$$

Hence a complete modulation of the intrinsic response is never achieved for inclined photons since emission of photoelectrons is intrinsically expected even in the direction orthogonal to polarization when $\delta \neq 0$. Note that the introduction of the relativistic correction doesn't affect this result.

An even more dramatic effect is present in the case of ${}^{unpol}\mathcal{M}_0(\phi, \delta, \beta = 0)$ since a $\cos^2$ term proportional to $\sin^2\delta$ emerges. This spurious modulation has the same signature as polarized radiation and then it would be indistinguishable from an actual polarized on-axis signal. Its amplitude μ_s is:

$$ \mu_s = \frac{\max\left\{{}^{unpol}\mathcal{M}_0\right\} - \min\left\{{}^{unpol}\mathcal{M}_0\right\}}{\max\left\{{}^{unpol}\mathcal{M}_0\right\} + \min\left\{{}^{unpol}\mathcal{M}_0\right\}} = \frac{1}{2}\left(1 - \cos^2\delta\right). \tag{7.24}$$

Note that this expression is correct only if the relativistic correction is neglected.

The intrinsic modulation curves in the case of polarized and unpolarized radiation are reported in Fig. 7.6a and Fig. 7.6b respectively. Obviously they are calculated in the plane of the detector xy since in the $x'y'$ plane they always follow a $\cos^2$ function, the modulation being not complete only if the absorption of non spherically symmetric shells is considered.

In Fig. 7.6 it is assumed that δ=-30° and $\beta = 0$. In the case of polarized radiation a fit with a $\cos^2$ function is not satisfactory (dotted line in Fig. 7.6a) since a costant term is

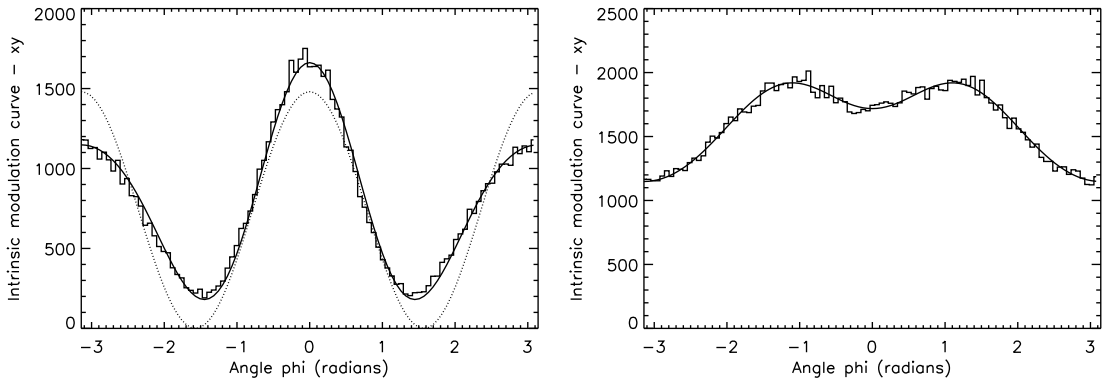

Figure 7.7: The same as Fig. 7.6 but including the relativistic correction. It causes the asymmetry between the peaks in (**a**) and (**b**), cf. Fig. 7.6. The energy of the photoelectrons is $E = 20$ keV ($\beta = 0.27$).

clearly present. Solid line is instead the function ${}^{pol}\mathcal{M}_0(\phi, \delta = -30°, \beta = 0)$: note that its shape is fixed since both δ and β are fixed and only the normalization can change. A clear $\cos^2$ spurious modulation appears in the case of unpolarized photons, reported in Fig. 7.6b: in the case δ=-30°, μ_s=12.5% (cf. Eq 7.24).

The systematic effects not related to the relativistic correction correspond to even powers of $\cos^2\phi$, i.e. $\cos^2$ and $\cos^0$: hence they add a constant term but the modulation remains periodic of 180°. Instead the terms which depend on β, which are proportional to $\sin\delta$ and then are null only if δ=0, are odd functions (see Eq. 7.19 and Eq. 7.20). These terms introduce a contribution which is periodic of 360° and are related to a front-back asymmetry: the direction ϕ=$\bar{\phi}$ is no more equivalent to $\bar{\phi}$+180°.

The effects of the relativistic terms on the intrinsic modulation are shown in Fig. 7.7 for δ=-30°. Polarized and unpolarized radiation is considered in Fig. 7.7a and Fig. 7.7b respectively: the energy of photoelectrons is 20 keV (β=0.27) to show more clearly the asymmetry induced by the combined effect of the inclined absorption and the relativistic correction. A clear asymmetry appears between the peaks corresponding to the direction of polarization in case of completely polarized radiation (see in Fig. 7.7a) and a $\cos^2$ fit would be not acceptable and anyhow reduce the amplitude of the modulation, namely the sensitivity of the instrument. The case of unpolarized radiation in Fig. 7.7b is even more interesting: the asymmetry related to the relativistic correction allows to distinguished, at least in principle, the spurious modulation from inclined unpolarized photons and an actual polarized signal on axis. Indeed the $\cos^2$ shape of the modulation found in Eq. 7.22 is significantly modified by the relativistic terms.

Inclined systematic effects can be globally visualized with a plot similar to that reported in Fig. 7.2. In that case no photoelectrons are projected in the y direction, namely in the direction orthogonal to that of polarization, while in case of inclined photons there is emission even in this direction (see Fig. 7.8). Moreover the emission on the left is more probable than that on the right (see again Fig. 7.8) and this induces the asymmetry be-

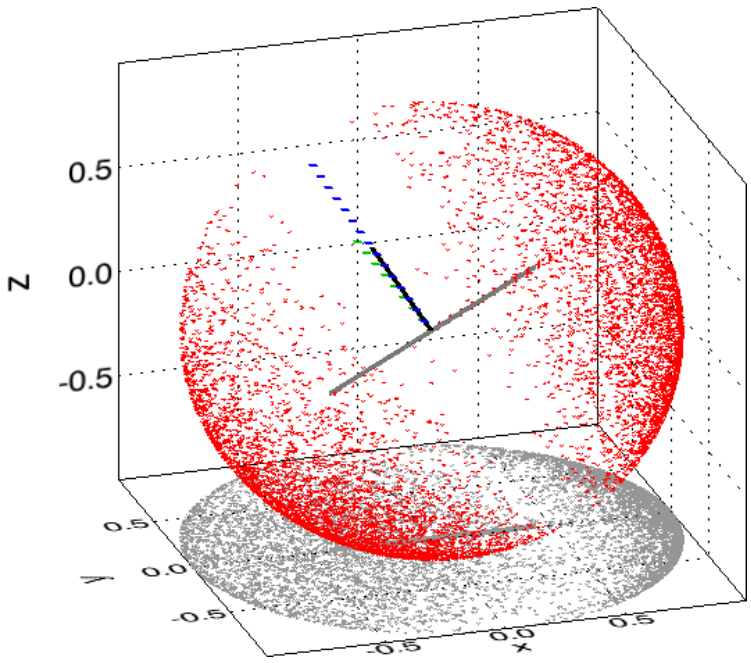

Figure 7.8: The same as Fig. 7.2, but for photons which are inclined of -30°. Note that in this case there are tracks of photoelectrons which are projected along the y axis, namely orthogonally to the direction of polarization. Note also the different intensities of projections on the left and right, which indicate a different probability of emission.

tween the peaks of the modulation curve.

It's worth to stress that the systematic effects found above are not related to changes in the differential cross section of photoelectric absorption and least of all caused by errors in the measurement of the initial direction of photoelectrons, since they have not been considered yet. The changes in the intrinsic response are the direct consequence of the procedure of measurement which is sensitive only to the projection of the emission direction on a plane. Therefore it is unavoidable for all the instruments as the GPD and (at least) the current version of the TPC.

7.3 Instrumental modulation

The actual modulation measured by the instrument $\mathcal{M}(\phi, \delta, \beta)$ is proportional to the intrinsic one in the frame of detector and then (cf. Eq. 7.6):

$$\mathcal{M}(\phi) = M \cdot \mathcal{M}_0(\phi - \phi_0, \delta, \beta) + C, \tag{7.25}$$

where the angular phase is added for completeness.

The a priori knowledge of the inclination and energy of photons, namely δ and β, is assumed in the following: they will be indicated with $\bar{\delta}$ and $\bar{\beta}$ and establish the shape of

the intrinsic modulation curve used to fit the histogram of initial directions so that only the normalization can be changed.

In the case of polarized radiation the function $\mathcal{M}_0(\phi)$ in Eq. 7.25 is:

$$\mathcal{M}_0(\phi,\bar{\delta},\bar{\beta}) = \left\{ \frac{1}{\frac{4}{3} - \frac{2}{3}\sin^2\bar{\delta} + \frac{\pi\bar{\beta}}{2}\left|\sin\bar{\delta}\right|} \left[{}^{pol}\mathcal{M}_0(\phi,\bar{\delta},\bar{\beta})\right] \right\}. \tag{7.26}$$

where the factor $\frac{4}{3} - \frac{2}{3}\sin^2\delta + \frac{\pi\beta}{2}\left|\sin\delta\right|$ is introduced to normalize to unity the intrinsic modulation ${}^{pol}\mathcal{M}_0$ found in the previous Section. Then the modulation factor can be calculated with the usual formula:

$$\mu = \frac{M}{M + 2\cdot C}. \tag{7.27}$$

Note that Eq. 7.26 is a generalization of the $\cos^2$ function used in case of photons orthogonal to the detector and if δ=0 (cf. Eq. 7.19):

$${}^{pol}\mathcal{M}_0(\phi,\bar{\delta}=0,\bar{\beta}) = \left\{ \frac{1}{\frac{4}{3}} \left[\frac{4}{3}\cos^2\phi\right] \right\} = \cos^2\phi. \tag{7.28}$$

In case of unpolarized radiation:

$$\mathcal{M}_0(\phi,\bar{\delta},\bar{\beta}) = \left\{ {}^{unpol}\mathcal{M}_0(\phi,\bar{\delta},\bar{\beta}) \right\}, \tag{7.29}$$

where the function $\mathcal{M}_0$ is not normalized.

The Eq. 7.25 is the function that should be used to fit actual data in case of inclined beams and this is verified in two cases. The first is that of polarized radiation at 3.7 keV inclined at δ=-40°; instead systematic effects in case of unpolarized photons are studied with a beam at 5.9 keV inclined at δ=-30°. Both Monte Carlo simulations and measurements are used assuming a mixture of helium 30% and DME 70%, a gas pressure 1 atm and an absorption region 1 cm thick.

7.3.1 Monte Carlo simulations

Synthetic modulation curves for inclined photons can be obtained with the Monte Carlo software (see Sec. 2.2.2), which include the effects of propagation of the photoelectrons in the gas and the errors in the reconstruction of their original direction of emission. Hence the response of the instrument must be fitted with the function $\mathcal{M}(\phi)$ reported in Eq. 7.25.

The modulation obtained for polarized radiation at 3.7 keV and inclined at δ=-40° is shown in Fig. 7.9. The histogram of emission directions is fitted with the usual $\cos^2$ function, $\mathcal{M}(\phi) = M\cdot\cos^2(\phi-\phi_0)+C$, and the correct ${}^{pol}\mathcal{M}_0$ curve: the results are reported in Fig. 7.9a and in Fig. 7.9b respectively, while the parameters of the fits are listed in Table 7.1. For comparison the result of a $\cos^2$ fit in the case of photons orthogonal to the detector is also reported in the Table.

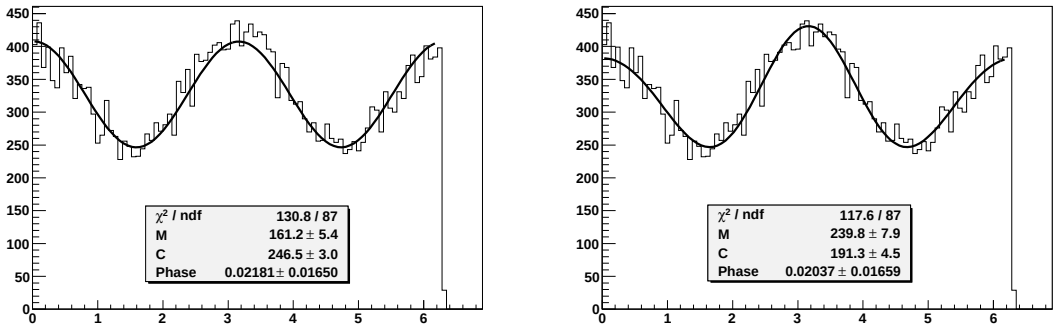

(a) **(b)**

Figure 7.9: Fit to the synthetic modulation curve for 3.7 keV polarized photons which are inclined -40°. A $\cos^2$ and the correct ${}^{pol}\mathcal{M}_0$ functions are used in (**a**) and (**b**) respectively, the parameters of the fits being reported in Table 7.1. Note that the angle ϕ is between 0 and 2π for a different definition with respect to Fig. 7.6 and Fig. 7.7.

E keV	δ °	$\mathcal{M}$	M	C	ϕ_0 rad	μ	χ^2_r
Polarized photons							
3.7	0	$\cos^2$	276.4±5.3	189.9±2.7	0.009±0.009	0.4212±0.0058	0.90
3.7	-40	$\cos^2$	161.2±5.4	246.5±3.0	0.022±0.017	0.2464±0.0066	1.50
3.7	-40	${}^{pol}\mathcal{M}$	239.8±7.9	191.3±4.5	0.020±0.017	0.3852±0.0097	1.35
Unpolarized photons							
5.9	0	$\cos^2$	6.0±5.4	324.5±3.3	0.715±0.447	0.0092±0.0082	1.11
5.9	-30	$\cos^2$	38.6±5.4	307.4±3.3	-1.557±0.070	0.0590±0.0078	2.56
5.9	-30	${}^{unpol}\mathcal{M}$	154.7±12.2	121.4±16.3	0.009±0.051	—	1.29

Table 7.1: Fit to synthetic modulation curves for polarized and unpolarized photons. $\mathcal{M}$ is the function used for the fit (see Eq. 7.25), μ the amplitude of the modulation calculated with the Eq. 7.27. It corresponds to the modulation factor in case of polarized radiation but is not defined in case of ${}^{unpol}\mathcal{M}$. χ^2_r is the reduced χ^2. About 30×10^3 counts are considered in each simulation. The number of degrees of freedom of the fits is 87.

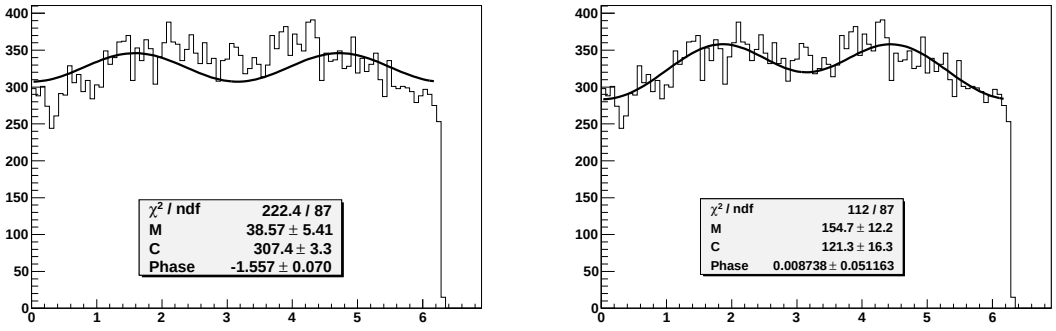

(a) **(b)**

Figure 7.10: The same as Fig. 7.9, but for unpolarized photons with energy 5.9 keV and δ=-30°. The modulation is completely caused by the systematic effects presented in this Chapter.

If the $\cos^2$ function is used to fit the histogram of emission directions for inclined photons, the modulation factor μ and hence the amplitude of the response is strongly reduced with respect to the case of orthogonal photons. Indeed it decreases from $\sim 42\%$ to $\sim 24\%$ (see Table 7.1) and moreover the quality of the fit also gets worse, namely the reduced χ^2 increases. Instead the function ${}^{pol}\mathcal{M}_0$ allows to maintain the sensitivity to the polarization, i.e. a large modulation factor, $\sim 38\%$, even at large angle. This has a simple interpretation: μ is calculated with the usual formula (Eq. 7.27), but the correct intrinsic modulation ${}^{pol}\mathcal{M}_0$ takes into account that a part of the constant term is unavoidable. Since it is not due to errors in the process of measurement, the value of the constant term C is lower than in the $\cos^2$ case.

Simulations are performed also with unpolarized radiation at 5.9 keV. The modulation curve obtained for a beam inclined at δ=-30° is fitted with a $\cos^2$ function in Fig. 7.10a, while the fit with the function ${}^{unpol}\mathcal{M}_0$ is reported in Fig. 7.10b. The results are in Table 7.1. A significant spurious modulation emerges for inclined photons, being absent in the case of radiation orthogonal to the detector. A $\cos^2$ fit provides a modulation ~6% and, since the modulation factor at this energy for the GPD is about 60%, a polarization degree of 10% would be measured if systematic effects are neglected. Moreover note that the ${}^{unpol}\mathcal{M}_0$ functions provides a by far better fit to the modulation curve.

7.3.2 Measurements

The measurement of the systematic effects which emerge for inclined beams is possible thanks to the facility described in Chapter 4. The 105k pixels, 50μm pitch, sealed version of the Gas Pixel Detector is used, the gas cell being filled with 30% helium and 70% DME mixture at 1 atm and 1 cm thick. Data are selected on the basis of the third momentum of the tracks (see Sec. 2.2.1) and only those with $M_3 > 1.3$ are analyzed.

The prototype version of the Bragg source is used: radiation at 3.692 keV is produced

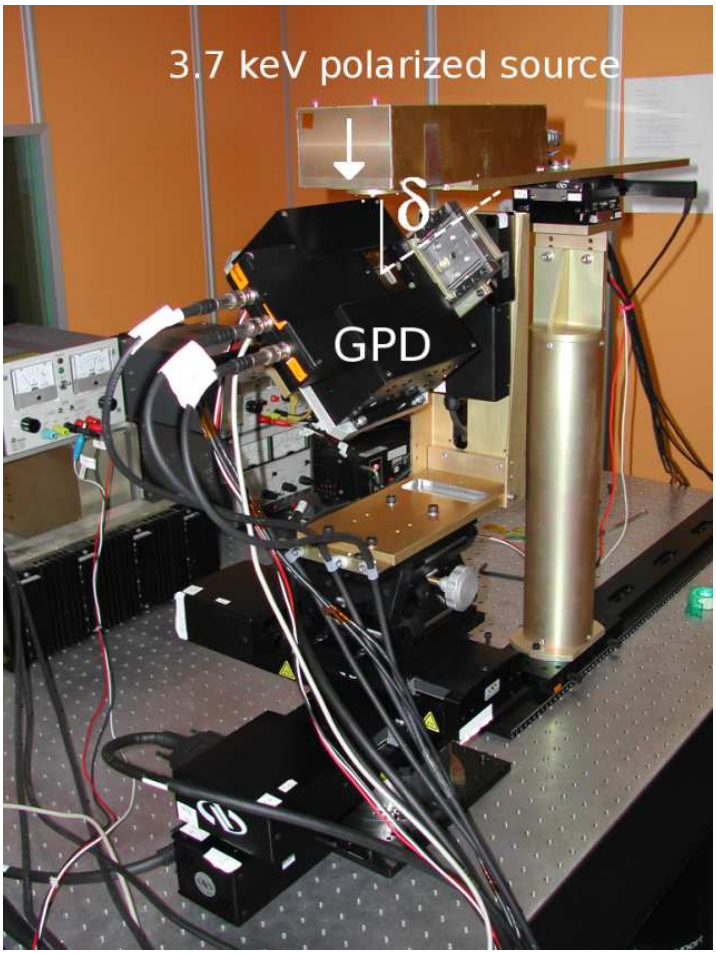

Figure 7.11: The setup used to perform the measurements at large angle of inclination.

by means of diffraction of the calcium Kα line on an aluminum crystal (see Chapter 3). The setup is shown in Fig. 7.11.

The results for polarized radiation and δ=-40° are reported in Fig. 7.12: the fit with the $\cos^2$ and ${}^{pol}\mathcal{M}$ functions are in Fig. 7.12a and Fig. 7.12b respectively, while the parameters of the fits are in Table 7.2. Measurements essentially confirm the results obtained with the Monte Carlo software: the modulation factor is strongly reduced if the usual $\cos^2$ function is used for inclined photons, decreasing from 46% on axis to 23% (see Table 7.2). Moreover the fit is not statistically acceptable. Instead the fit with the function ${}^{pol}\mathcal{M}_0$ allows to recover 80% of the on-axis modulation factor at -40°.

Unpolarized radiation is produced with a Fe^{55} radioactive source. It emits both 5.899 and 6.490 keV unpolarized photons but they are not spectrally resolved by the instrument. The lines at 5.899 keV is more than 10 times stronger than that at 6.490 keV and then the latter is neglected in this context. The modulation curve when δ=-30° is reported in Fig. 7.13: a significant spurious modulation appears as expected. The fit with a $\cos^2$

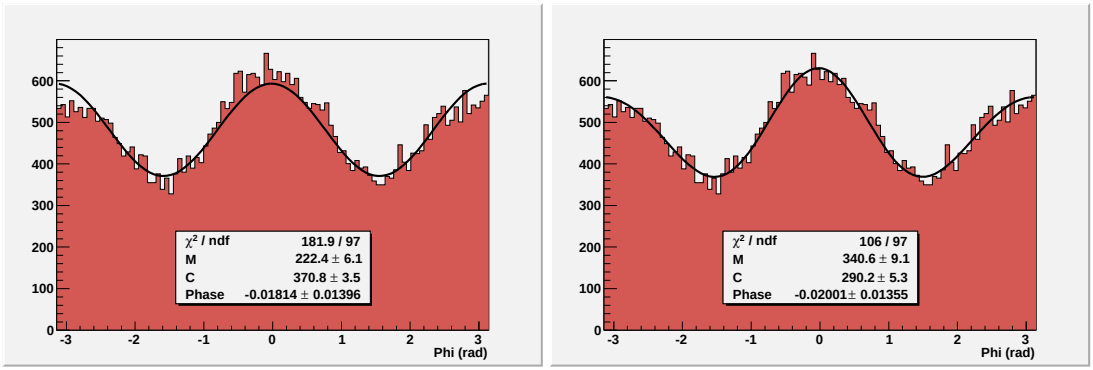

(a) **(b)**

Figure 7.12: Measured modulation curve for 3.692 keV polarized photons. It is fitted with a $\cos^2$ and the correct ${}^{pol}\mathcal{M}_0$ functions in (**a**) and (**b**) respectively. δ=-40° and the parameters of the fits are reported in Table 7.2. Only tracks with $M_3 > 1.3$ are analyzed.

E keV	δ °	$\mathcal{M}$	M	C	ϕ_0 rad	μ	χ^2_r
Polarized photons							
3.692	0	$\cos^2$	292.3±4.9	170.6±2.5	-0.012±0.008	0.4614±0.0055	1.22
3.692	-40	$\cos^2$	222.4±6.1	370.8±3.5	-0.018±0.014	0.2307±0.0052	1.88
3.692	-40	${}^{pol}\mathcal{M}$	340.6±9.1	290.2±5.3	-0.020±0.014	0.3698±0.0075	1.09
Unpolarized photons							
5.899	0	$\cos^2$	12.9±4.7	265.7±2.8	0.488±0.180	0.0238±0.0084	1.16
5.899	-30	$\cos^2$	125.5±10.5	1301.3±6.3	1.524±0.004	0.0460±0.0037	5.08
5.899	-30	${}^{unpol}\mathcal{M}$	496.4±23.5	70.6±31.3	-0.041±0.031	—	1.95

Table 7.2: Fit to measured modulation curves for polarized and unpolarized photons. The field are the same as Table 7.1. The number of degrees of freedom of the fits is 97.

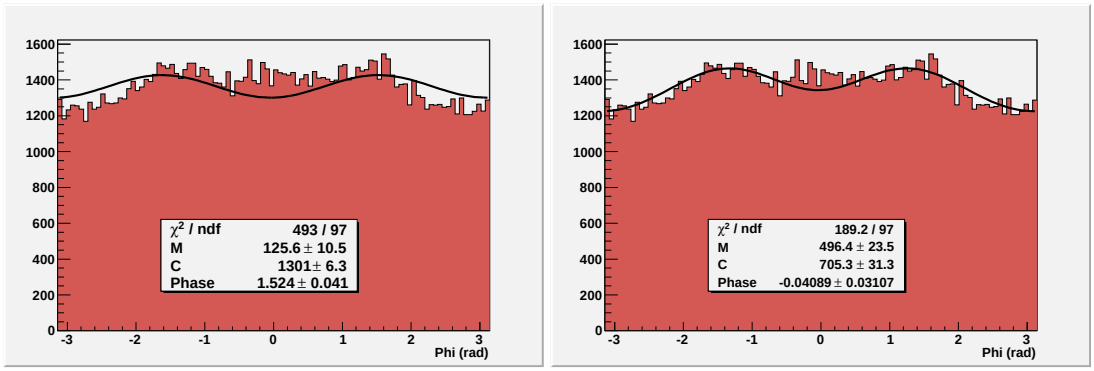

(a) **(b)**

Figure 7.13: The same as Fig. 7.12, but for unpolarized photons with energy 5.9 keV and δ=-30°.

function (see Fig. 7.13a) provides an amplitude of 5% (see Table 7.2).

The function ${}^{unpol}\mathcal{M}$ fits rather well the measured modulation, even if a significant excess is present around $\phi \approx 0$. This is possibly due to border effects caused by the inclined penetration of photons in the gas cell: when they are absorbed near the beryllium window or the GEM, the electric field can be insufficient or not uniform and consequently a part of the charge or even tracks may be lost. This effect is azimuthally uniform if photons are incident orthogonally to the detector but emerges very clearly for inclined photons. In Fig. 7.14a the map of the reconstructed absorption points is reported for the measurement at δ=-30° with the unpolarized source of Fe^{55} . It is diaphragmed and collimated so that its image on the detector is circular with diameter 5 mm: however photons are absorbed at different depths in the cell gas and then the inclined penetration distributes the image on a strip along the x axis (see Fig. 7.14b). The left-hand part of the strip is absorbed near the window, while the right-hand one is absorbed near the GEM: as a consequence the modulation curves for the regions $x < -4$ mm and $x > 4.5$ mm are very different and are reported in Fig. 7.15a and Fig. 7.15b respectively. In the first case the emission is strongly inhibited for $\phi \approx 0$, namely toward positive x, since tracks hit the window in this direction; instead in the right-hand part of the strips the emission is suppressed toward left, namely in the direction of GEM.

The systematic effect related to the partial collection of charges has been neglected in the study presented in this Chapter even if it is obviously present in the case of measurements. It has been implicitly assumed that border effects are averaged when the whole image is analyzed and the consistency among theoretical analysis, simulations and actual data supports this hypothesis. Nevertheless border effects could explain the excess at $\phi \approx 0$ reported in Fig. 7.13b: photoelectrons extracted from 5.899 and 6.490 keV photons produced by the Fe^{55} source have long paths in the helium mixture ($\sim 300\mu m$) and hence a partial loss of charge is possible. In this case tracks are in large part removed with a cut on the spectrum which is performed in the analysis of data acquired with the Fe^{55} source, however the relativistic correction may introduce an asymmetry between

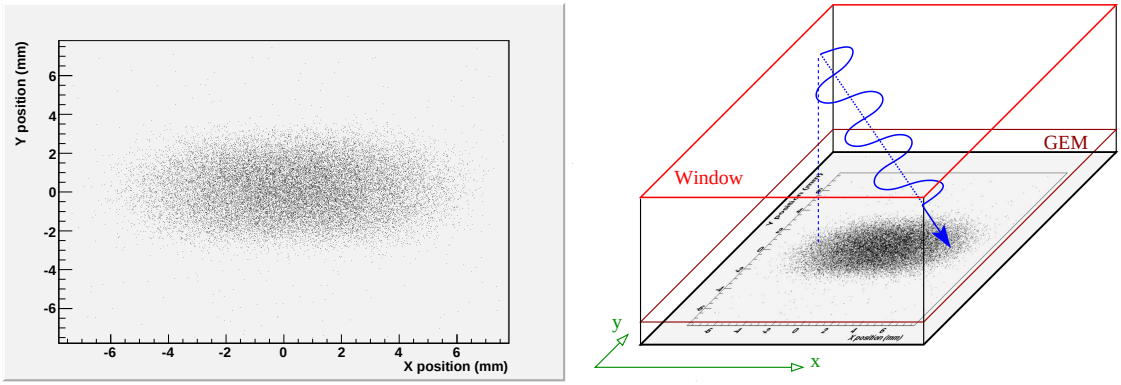

(a) **(b)**

Figure 7.14: (**a**) Image of the circular Fe^{55} source when it is inclined at δ=-30°. Its diameter is 5 mm but the absorbed photons are distributed on a strip because of the inclined penetration in the gas cell (**b**).

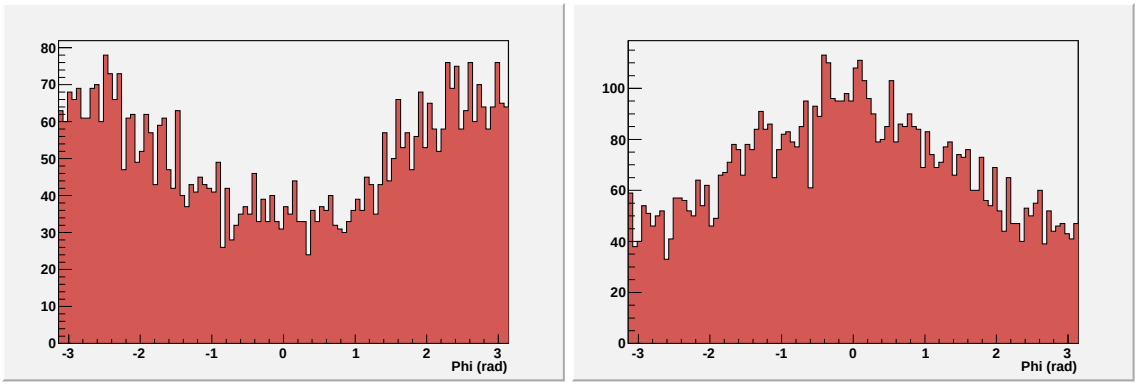

(a) **(b)**

Figure 7.15: Modulation curves of the regions x <-4 mm (**a**) and x >4.5 mm (**b**) of the image reported Fig. 7.14a.

the charge losses near the GEM and the window. In particular the forward folding can reduce the effect in the latter case and increase that close to the GEM, thus explaining the origin of the excess at $\phi \approx 0$ in Fig. 7.13b.

7.4 On the feasibility of a polarimeter with a large field of view

The results presented in this Chapter strongly suggest that the construction of a photoelectric polarimeter with a large field of view is not an easy generalization of its "traditional" use as focal plane instrument. When radiation is incident not orthogonally to the detector significant changes in the intrinsic response of the device emerge and they must be accurately studied and taken into account to built a reliable instrument.

The theory and the tools presented have been proved effective in the control of the large systematic effects arising up to several tens of degrees. They can be taken into account if the inclination and the energy of incident photons is known and these informations could be easily obtained with the GPD. It has imaging capability and hence the use of a coded mask could provide the direction of incidence of radiation at the expense of $\sim$50% of the flux. Moreover the even moderate energy resolution of the GPD would be sufficient to obtain a reasonable estimate of the velocity β of the photoelectrons.

However this study can actually neither prove nor disprove the feasibility of photoelectric polarimeters with large field of view. The agreement between analytic functions, Monte Carlo results and measured modulation curves is promising but the analysis presented here is limited in the simplest geometry. The inclination of radiation selects a preferred direction on the plane of the detector which is the azimuthal angle of the incidence direction. The phase of the systematic effects which emerge brings memory of it. In the case studied the direction of polarization is parallel to this special direction (see Fig. 7.4) and hence the modulation produced by polarized photons is "summed in phase" with the systematic effects. This allows to retain a certain degree of symmetry thus strongly simplifying the geometry of the problem. However the modulation curve is affected by two degrees of freedom in the general case. The first is the angle of polarization ϵ and the second the azimuthal direction of incidence α (see Fig. 7.16). Each produces an effect with a different phase and a possible degeneracy between these two angles may emerge.

Note that the systematic effects presented in this Chapter emerge clearly only if it is not assumed that the modulation curve is periodic of 180°, namely if the histogram of emission directions is not folded on 180°. Moreover the analysis of the asymmetries in the complete azimuthal response of the polarimeter is of fundamental importance to distinguish between systematic effects produced by inclined unpolarized photons and actual polarized signals on axis.

The discussion presented above has been performed in the particular case of photoelectric polarimeters, but it is possible that similar systematics affect scattering devices also. Indeed the differential cross section in Thomson limit, where a larger intrinsic modulation is expected, is (cf. 1.20):

$$\frac{d\sigma_T}{d\Omega} = r_0^2 \left(1 - \sin^2\theta \cos^2\phi\right), \tag{7.30}$$

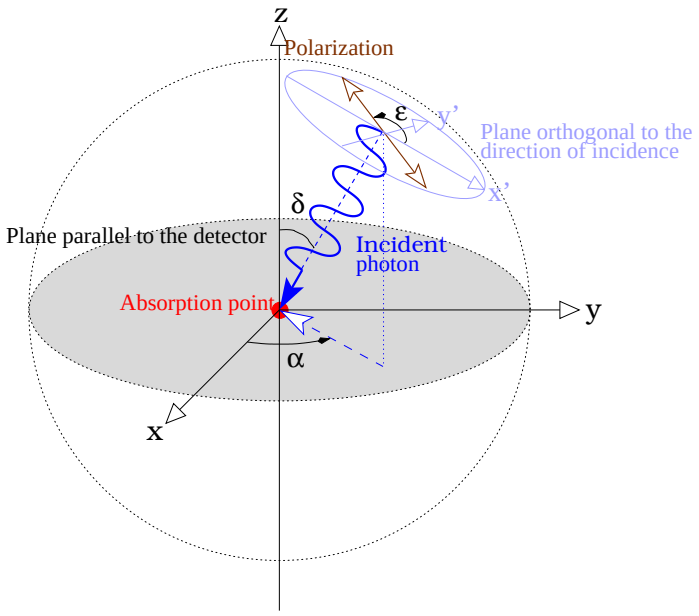

Figure 7.16: Definition of the geometry of the photoabsorption at large angles in the general case.

thus having a similar angular dependence as the photoelectric cross section without the relativistic correction. The systematic effects which may be caused by the inclined incidence of photons on scattering polarimeters will be soon investigated.

Chapter 8

High energy sensitivity of the GPD

The energy range of the GPD is basically selected by the choice of the mixture filling the gas cell (see Sec. 2.4). A mixture helium 20% and DME 80% is the current baseline because it is sensitive between 2 and 10 keV and then allows to exploit an energy band where astrophysical compact sources are in general very bright and a "traditional" X-ray optics can be easily used. However the use of the GPD at higher energies doesn't require substantial changes in the design of the instrument and as a matter of fact mixtures of neon or argon have been already used with the current prototype.

This Chapter is dedicated to the study of mixtures "heavier" than baseline. Their modulation factors are derived from Monte Carlo simulations (see Sec. 2.2.2) to study the sensitivity of the GPD in the context of possible future missions devoted to the polarimetry in the hard X-ray range, namely above 10 keV.

In the near future a sufficient collecting area to perform polarimetry will be accessible even in this energy range thanks to multilayer optics, which make possible the reflection of photons up to 60-80 keV (see Sec. 6.2). Missions which include telescopes based on this technology are currently under development and many have passed a certain level of selection, e.g. *Astro-H* (formerly *NeXT*, Takahashi et al., 2008), *NuSTAR* (Koglin et al., 2005) and *SIMBOL-X* (Ferrando et al., 2005, 2008). They will be dedicated to imaging and spectroscopy.

The use of heavy mixtures with the GPD was already studied in Sec. 6.5.2 but in that context mixtures of argon are used to increase the versatility of pathfinder missions, discussing the inclusion of detectors devoted to higher energy alongside baseline ones, the observation time being shared between instruments optimized for different energies. In this Chapter a more "extreme" solution is discussed, namely a mission completely dedicated to hard X-ray polarimetry.

The work presented in this Chapter was published by Muleri et al. (2006).

8.1 Monte Carlo simulations

The simulations are based on the Monte Carlo software already presented in Sec. 2.2.2. This software has been usually used at lower energies but the algorithm which describes

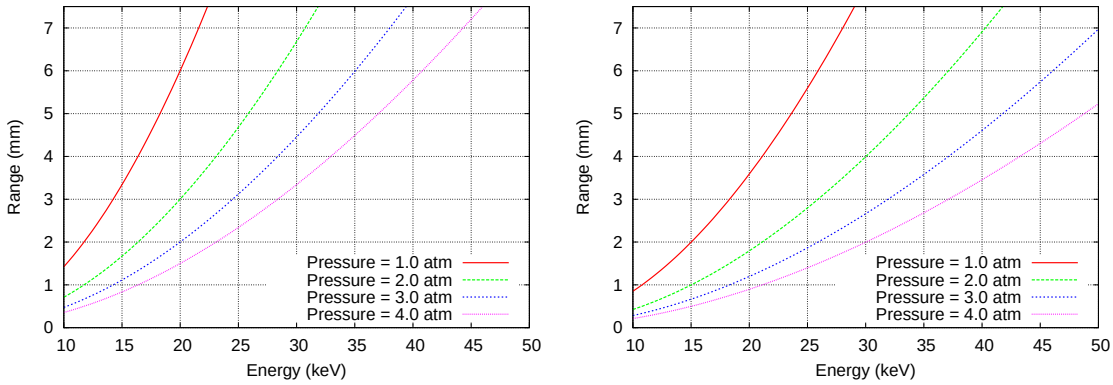

Figure 8.1: (**a**) Approximate electron range in a mixture neon 80% and DME 20% at different pressures. (**b**) The same as (**a**) but for the mixture argon 60% and DME 40% (**b**) (range from Zombeck, 1990).

the propagation of the electrons in the gas, which is the most critical part of the program, is even better determined at energies above a few keV (Joy, 1995).

The current detector made of 105k pixels at 50μm pitch is considered, while the mixture, the pressure and the thickness of the gas cell are freely changed. Neon and argon mixtures with a small percentage of DME (20% and 40% respectively) at 1, 2, 3 and 4 atm are considered. The gas cell thickness is 1,2 or 3 cm and each simulation is performed with 25×10^3 photons incident orthogonally to the detector. A support, e.g. a grid or a larger thickness, may be required to assure the mechanical resistance of the current 50 μm beryllium window in case of pressure higher than 1 atm but, even if this would decrease the transparency to X-rays, it is neglected in this context.

Tracks are analyzed only if secondary charges are completely collected on the active surface of the detector and this defines the upper limit to the energy range of the simulations presented. It is assumed that photons are absorbed in the center of the GPD and, since its area is 15×15 mm^2, the range of the photoelectrons must be less than $\sim$7.5 mm to be completely absorbed in the gas cell. The approximate electron range in the mixtures of neon and argon considered is reported in Fig. 8.1a and Fig. 8.1b respectively and this provides a raw upper limit to the high energy use of the GPD. The actual maximum energy also depends on the thickness of the gas cell since secondary charges are diffused in a larger area if the drift distance is longer.

Simulations are performed above a lower limit which is about twice the energy of the K-shell edge of the principal component of the mixture, namely neon or argon, to distinguish photoelectrons from Auger emission. The energy of the orbital 1s for some elements is in Table 8.1 together with the fluorescence yields for the K and L-shells. Note that mixtures of krypton and xenon could be used with the GPD to extend the response up to several tens of keV but their high fluorescence yield could make more difficult the analysis of photoelectrons tracks. The emission of a single ionizing particle makes

Element	E_{1s} (keV)	P_K (%)	P_L (%)
Neon	0.870	1.50	—
Argon	3.206	12.0	∼0.02
Krypton	14.33	65.2	∼2.0
Xenon	34.59	88.8	∼8.0

Table 8.1: K shell edge and fluorescence yield of K and L-shells for some elements (Krause, 1979).

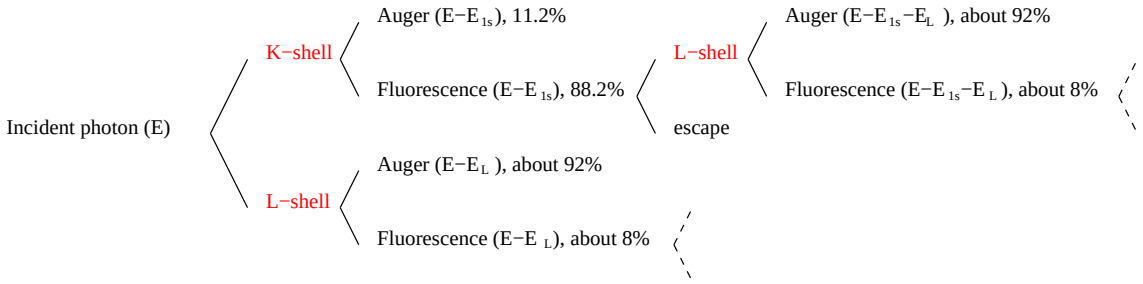

Figure 8.2: Possible branches of photon interaction with krypton atoms when the energy $E > E_{1k}$.

possible a more accurate determination of the initial direction of photoelectrons and the absence of the Auger emission would also allow to accept photons of energy just above the K-shell edge. However the interaction of radiation with the atoms of the mixture would proceed via different branches (see Fig. 8.2), making more difficult the reconstuction of the tracks "history". If a photon is absorbed by the K-shell, a fluorescence photon is produced in place of Auger electron in more than half of cases. It is emitted with an energy slightly less than that corresponding to K-edge and hence it can be absorbed only by a L-shell of another atom or escape from the detector. In the first case (or if the incident photon is initially absorbed by the L-shells) a low energy Auger electron is often produced since the fluorescence yield in this case is rather low.

The only "interesting" track is that of the photoelectron which is emitted after the first interaction, since it is the only which carries memory of the polarization of the original photon. Then it must be distinguished in a background of tracks produced by the low energy Auger electrons and the measurement of the original photon energy should include the secondary tracks generated after the primary interaction. This requires an approach more elaborated than that performed with the usual mixtures of helium, neon or argon, when the emission of a photoelectron is basically always followed by that of a single Auger electron. For this reason mixtures of xenon and krypton are not considered in this Chapter. In addition scattering polarimeters (see Sec. 1.2) could be an effective alternative to photoelectric instruments filled with xenon and krypton since the scattering is competitive with photoabsorption at energies above several tens of keV. Then the very hard X-ray polarimetry should be discussed by comparing these two techniques.

8.1.1 Mixtures of neon

Neon mixtures at 1 atm have been extensively studied in the 2-10 keV energy range and both Monte Carlo and measurements were performed before adopting the helium mixtures as baseline. Then a safe solution for extending the response of the GPD at higher energies could be the use of neon mixtures at high pressure.

Simulations for neon 80% and DME 20% at pressure 1, 2, 3 and 4 atm and for gas cell 1, 2 and 3 cm thick are performed for photons at energy 2, 3, 4, 5, 6, 8, 10, 12, 15, 20, 25, 30 and 35 keV. The modulation and the quality factor (see Sec. 2.4) are in Fig. 8.3 and numerical values of μ are in Appendix A.

The peak of the quality factor is higher and is reached at higher energies if the gas pressure or its thickness is increased. For example the quality factor of a mixture 1 cm thick peaks at 4 keV if the pressure is 1 atm and it is about 0.13 at this energy. Instead the maximum value of $\mu\sqrt{\epsilon}$ is above 0.15 at 6 keV and 4 atm. For the extreme case of a gas cell 3 cm thick, it reaches 0.18 at 7 keV and 4 atm.

As expected, the modulation factor decreases if the efficiency is higher, both the increase of the pressure and the cell thickness producing a similar effect. However the higher quality factor suggests that the small decrease of the modulation factor is largely balanced by the increasing of the efficiency, since in this case more counts are collected and consequently statistical fluctuations are lower.

8.1.2 Mixtures of argon

Simulations for argon 60% and 40% DME are performed at 6, 8, 10, 15, 20, 25, 30, 35, 40, 45 and 50 keV. The pressure and the thickness of the gas cell are 1, 2, 3 and 4 atm and 1, 2 and 3 cm respectively. The results are reported in Fig. 8.4 and the numerical values of the modulation factor are reported in Appendix A.

The same dependence on the pressure and cell thickness discussed in the case of the neon mixtures is observed. The modulation factor basically is inversely related with the efficiency: if the one is increased the other decreases but the sensitivity, namely the quality factor, is higher. Note that argon mixtures achieve a higher quality factor with respect to the neon ones, the peak is reached at higher energies and is generally wider.

8.2 Scientific performances

X-ray polarimetry above 10 keV is very attractive. A higher degree of polarization is often expected at higher energies because in this case non-thermal components typically are predominant and the scattering plays a more important role. Neon and argon mixtures could open the way for measurements in this energy range. The choice of the gas pressure and thickness allows to shift the energy range of the instrument to tune it with the band-pass of the telescope. The usual decrease of the telescope area with energy and that of the fluxes of astrophysical sources can be recovered, at least partially, by the higher performances of heavier mixtures which reach higher quality factors. For example it is 0.13 for a mixture neon 80% and DME 20% (1 atm and 1 cm) but reaches $\sim$0.20 for

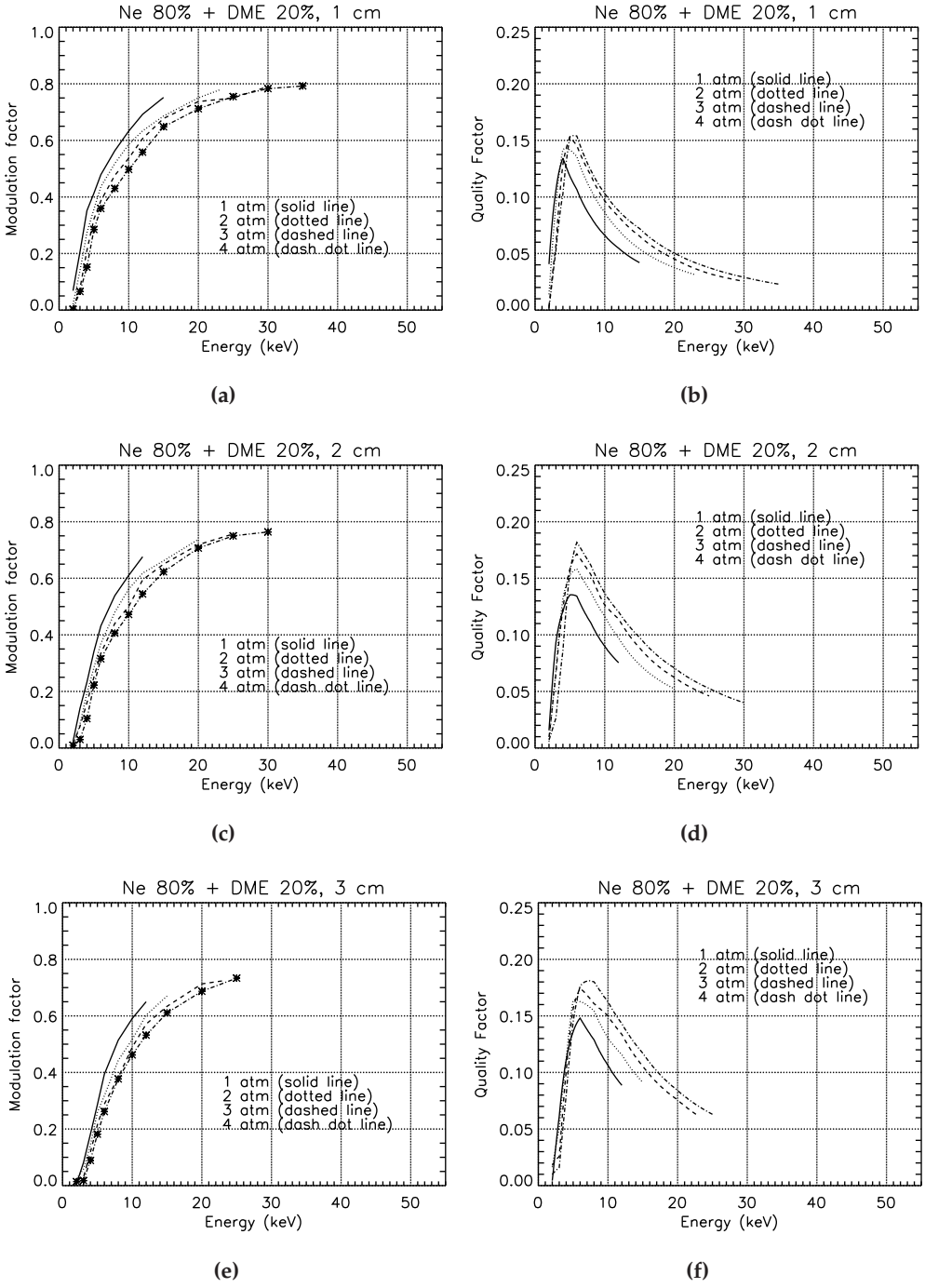

Figure 8.3: Dependence of the modulation (**a**, **c**, **e**) and quality factor $\mu\sqrt{\epsilon}$ (**b**, **d**, **f**) on the photon energy for the mixture neon 80% and DME 20%. Solid, dotted, dashed and dot-dashed curves correspond to pressure 1, 2 3 and 4 atm respectively. The thickness of the gas cell is 1 cm (**a**, **b**), 2 cm (**c**, **d**) and 3 cm (**e**, **f**). The efficiency in the quality factor includes a 50 μm beryllium window.

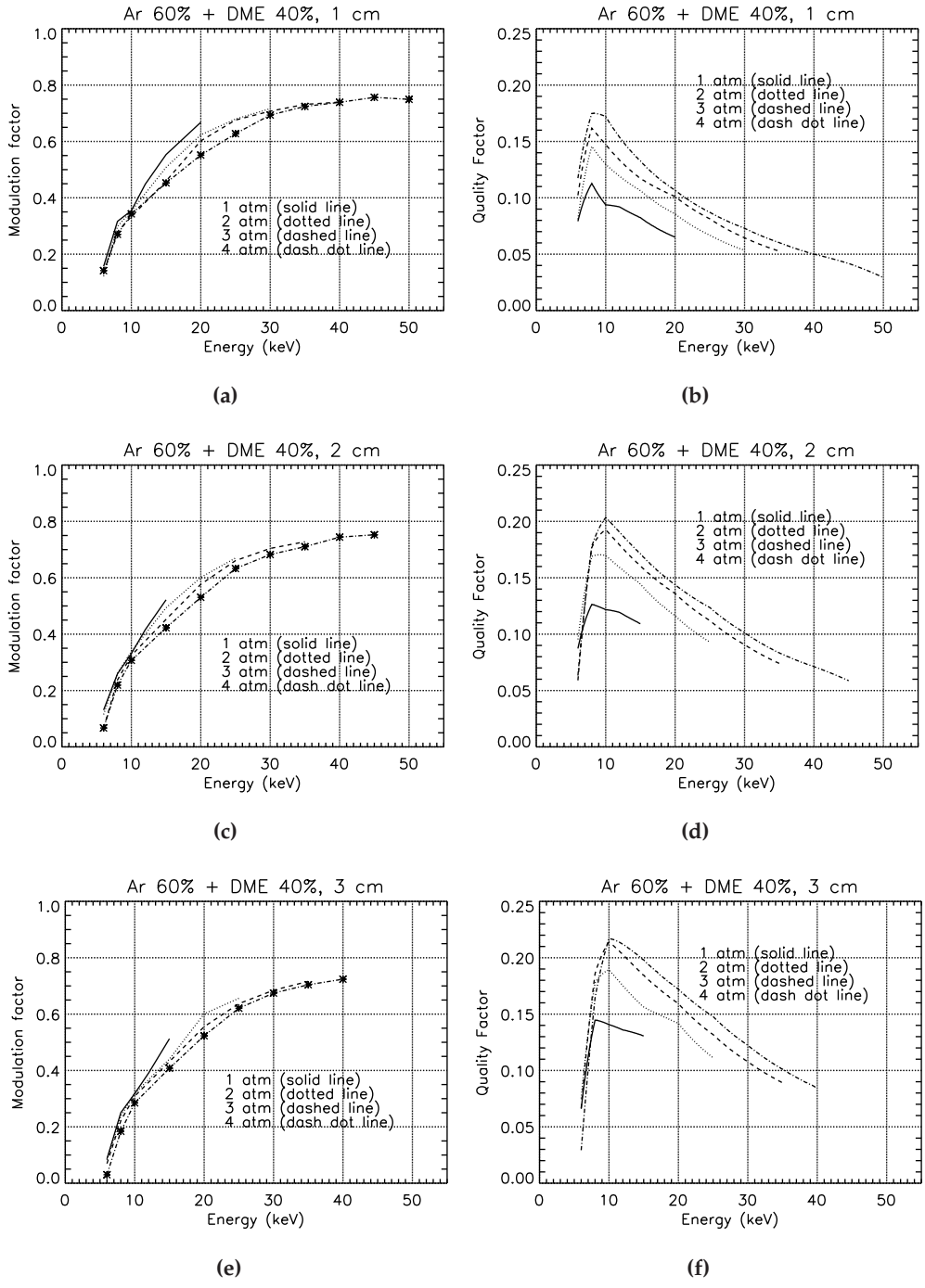

Figure 8.4: The same as Fig. 8.3, but for the mixture argon 60% and DME 40%.

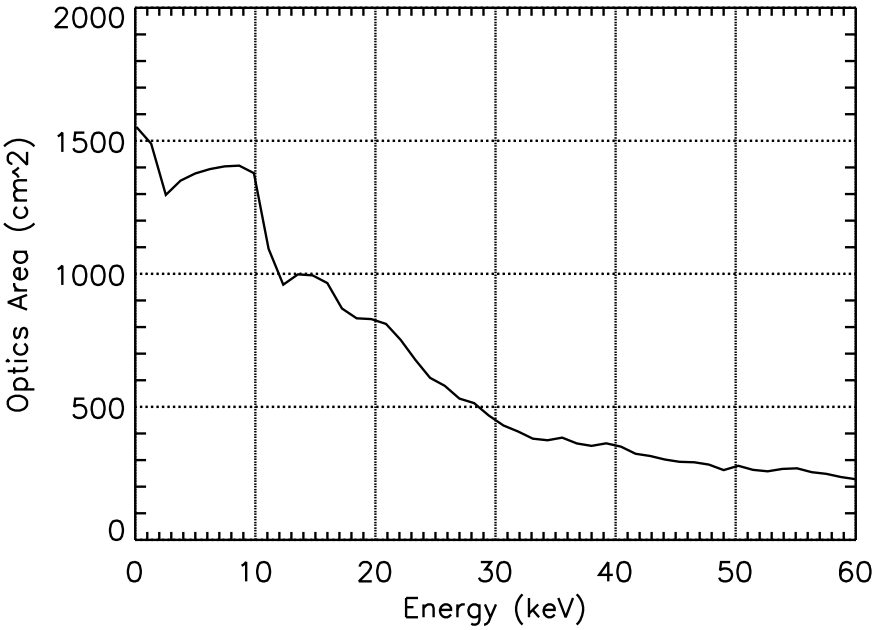

Figure 8.5: Area of one of the telescope designs of SIMBOL-X. Its main characteristics are in Table 8.2.

the mixture of argon at 2 atm and 2 cm thick. Only minor changes are required to use the current prototype of the GPD with mixtures of neon or argon, even if some technical issues, such as the possibility of GEM discharges, could emerge if both a heavy mixture and high pressure are used.

8.2.1 The case study of SIMBOL-X

SIMBOL-X is an Italian-French space mission devoted to hard X-rays which will exploit multilayer optics to operate between 0.5 and 80 keV (Ferrando et al., 2005, 2008). Two detectors, developed with the contribution of German laboratories, are in the focal plane (Laurent et al., 2008): the Low Energy Detector, a silicon drift detector providing imaging and moderately high spectroscopy between 0.5 and 20 keV, and the High Energy Detector, based on CdTe crystals and covering the energy band up to 80 keV. A focal length of $\sim$20 m is achieved with a formation flight configuration.

The telescope of SIMBOL-X is taken as a realistic example of the capabilities of multilayer optics to study the scientific performances of the GPD at high energy. Its design has not been established yet and then a preliminary one is assumed. The area of the optics is in Fig. 8.5 and its main characteristics in Table 8.2.

A mixture argon 60% and DME 40% at 3 atm and 2 cm thick is selected among those presented in Sec. 8.1: this provides a trade-off between good performances and a reasonable instrumental configuration. In the context of pathfinder missions (see Sec. 6.5.2) a more conservative solution was considered, namely a mixture at 2 atm and a gas cell 1 or

Focal length:	20 m
Maximum diameter:	70 cm
Weight:	215 kg
Field of view:	12.7×12.7 arcmin^2

Table 8.2: Main characteristics of the telescope design assumed for SIMBOL-X.

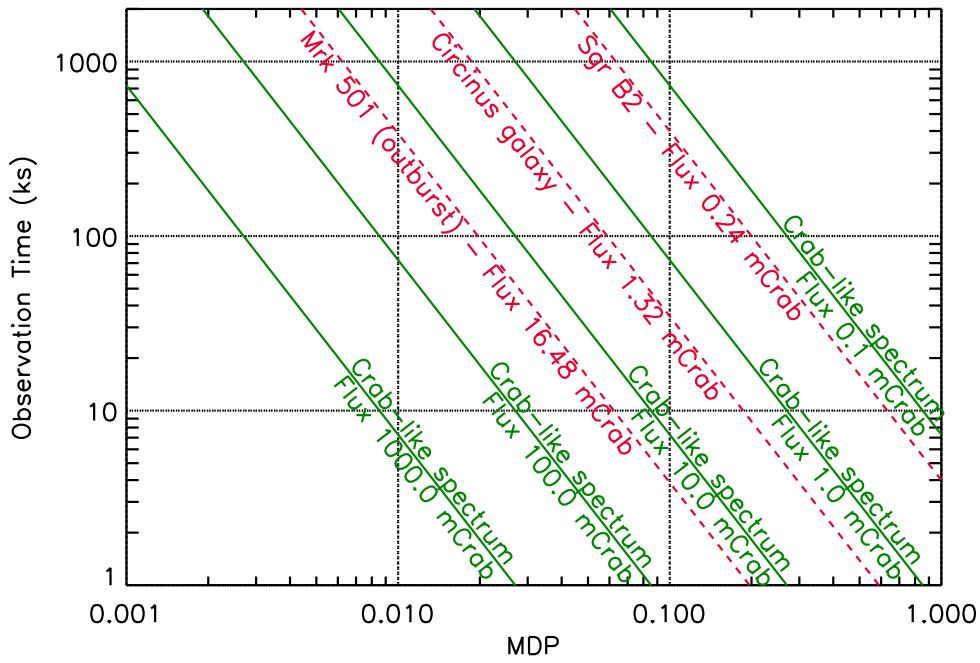

Figure 8.6: Observation time required to reach a certain MDP as a function of the flux of the source. The flux is expressed in mCrab and is integrated between 6 and 35 keV. In this energy range 1 Crab=2.47×10^{-8} erg/(cm^2 s).

2 cm thick, because these missions are expected to be launched in a few years and then a higher degree of readiness is required.

The observation time required to reach a certain Minimum Detectable Polarization (MDP, see Sec. 2.4) is reported in Fig. 8.6 as a function of the 6-35 keV flux of the source expressed in mCrab, where 1 mCrab=2.47×10^{-11} erg/(cm^2 s) in this energy band. Some very attractive results are achievable. The case of the highly obscured molecular cloud Sgr B2 was already discussed in Sec. 1.4.9 and its observability was studied in both pathfinder and large observatory scenarios in Sec. 6.5.1. An MDP below 10% with an observation of 1 Ms would be reached in the context of a SIMBOL-X like mission with the argon mixture, corresponding to an error in the measurement of the plane of polarization of 0.85° in the same hypothesis assumed in Sec. 6.5.1, namely a degree of polarization of 70%. This about one third of the error box expected in the pathfinder scenario between 2 and 10 keV for the same observation time.

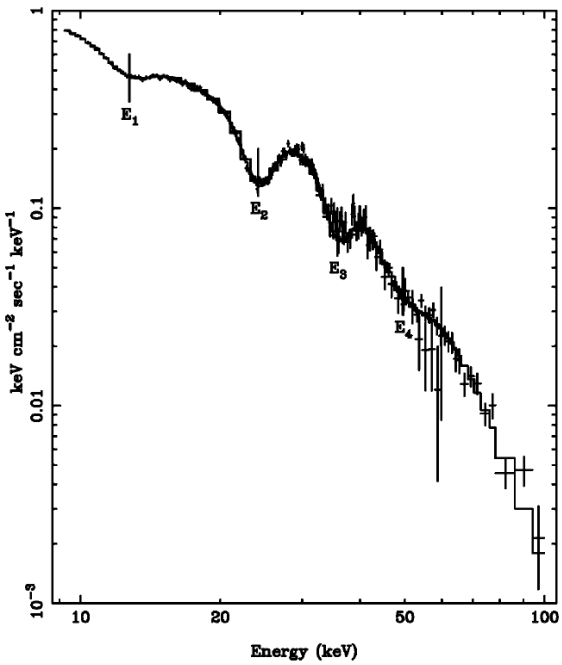

Figure 8.7: Spectrum of the X-ray pulsar X0115+63. Four cyclotron lines are present. Their energy and width is in Table 8.3 (Santangelo et al., 1999).

Mrk 501 is one of the closest (z=0.034) and brightest BL Lacertae objects at all wavelengths. Its emission could be explained with synchrotron self Compton production (see Sec. 1.4.8) and in this case a high degree of polarization ($\mathcal{P}$ >10%) is expected. An observation of 1 day could easily detect polarization at this level.

The transient X-ray pulsar X0115+63 shows 4 cyclotron lines between 12 and 50 keV (Santangelo et al., 1999). Its spectrum is reported in Fig. 8.7 and the energy and the width of the lines are in Table 8.3. Polarimetry of the first two lines could be performed with argon mixtures and this would be of primary importance in the study of accretion physics on X-ray pulsars (Meszaros et al., 1988).

The MDP in six energy bands is reported in Table 8.4 for an observation of 100 ks,

	Energy (keV)	σ (keV)
1^{st}	12.78±0.08	1.52±0.14
2^{nd}	24.0±0.07	1.94±0.11
3^{rd}	35.00±0.35	1.98±0.4
4^{th}	49.8±1.4	4.8±2.0

Table 8.3: Energy and standard deviation of the cyclotron lines of X0115+63. They are fitted with a cut-off power law plus gaussian lines (Santangelo et al., 1999).

Energy (keV)	Flux (c/s)	MDP (%)
6.0 - 8.0	278.3	0.61
8.0 - 11.0	119.0	0.45
11.0 - 15.0	8.07	1.23
15.0 - 21.0	7.83	0.96
21.0 - 27.0	0.085	7.6
27.0 - 35.0	0.177	4.6

Table 8.4: MDP for an observation of 100 ks of X0115+63. The energy bands are chosen taking into account both the resolution of the instrument and the energy of the lines.

where the intervals are chosen to spectrally resolve the cyclotron lines taking into account the energy resolution of the instrument ($\sim$20% at 6 keV).

Conclusions

The main objective of this thesis was the development of the GPD toward the use in space on-board future satellite missions and this purpose was pursued by means of four main original contributions. The first was the construction of a facility able to produce monochromatic polarized and unpolarized photons (see Chapter 3 and Chapter 4), which has been basically used with the GPD but also to perform measurements with other instruments. The first characterization of silicon detectors aimed to build a low resource but sensitive all sky monitor was an example.

Unpolarized radiation is readily produced with radioactive sources or X-ray tubes, both being available on sale; instead the construction of the polarized source and the mechanical assembly of the facility are original. Both a prototype and an improved version of the polarized source have been built: they are based on Bragg diffraction and share essentially the same design. Unpolarized photons are incident at nearly 45° on a crystal, the angle of incidence and diffraction being established thanks to capillary plates that provide good collimation with limited size. Only the component polarized orthogonally to the plane of incidence is effectively diffracted and this implies that the output radiation results highly polarized. This is an "opposite" use of the same technique that has been traditionally used for the measurement of X-ray polarization, even in astronomy though, unfortunately, with meagre results.

The main difference between the prototype and the improved version of the Bragg source is the generator of unpolarized photons which in the latter case is an X-ray tube much more powerful (and cumbersome). Another significant difference is that the crystal is mounted on a manual stage which allows tilt regulation and an optimal alignment of the incident photons and the crystal, implying an increase both of the flux and the degree of polarization of output radiation. Instead an important property of the prototype source is that it is small and portable.

Different commercial crystals were selected so that nearly monochromatic and polarized radiation can be produced at 1.65, 2.04, 2.293, 2.61, 2.691, 3.692, 4.511, 8.048 keV and integer multiplies. While at 1.65, 2.04 and 2.61 keV the diffraction of continuum photons is used, a larger flux and a precise knowledge of the degree of polarization is achieved at 2.293, 2.691, 3.692, 4.511 and 8.048 keV because in this case the fluorescence emission of the X-ray tube is in accordance with the Bragg energy at nearly 45°. About a half of the incident monochromatic flux is diffracted and the knowledge of the energy of incident radiation allows the precise calculation of the degree of polarization of diffracted photons.

The Bragg diffraction was also exploit to design a very small and portable polarized calibration source which exploits a single radioactive Fe^{55} nuclide to produce polarized photons at 2.622 and 5.899 keV. It will be part of the scientific payload of space missions together with the GPD so that in-flight calibration even with polarized photons could be performed.

Polarized and unpolarized sources are mounted on a mechanical assembly which was designed and built to accomplish the complete characterization of the GPD. Three main classes of measurements drove its development: the first was the study of the relation between the plane and the measured angle of polarization; the second was the possibility to map all the active surface of the instrument with narrow polarized and unpolarized beams and investigate the imaging capabilities of the GPD; the third was the study of possible systematic effects due to the absorption of inclined photons.

The detector is moved, rotated or inclined with respect to the incident photons with high accuracy by eight motorized stages so that the plane of polarization of the beam on the instrument, its position and inclination can be changed. A resolution of 0.5 μm is achieved in the position of the spot on the detector, while the inclination and the rotation are performed at minimum steps of 1 and 0.2 arcsec respectively. The size and the aperture of the beam are controlled with diaphragms and capillary plates. An automatic software was developed within this thesis to perform long and consecutive measurements: it can manage all the movements so that any measurement can be performed without the intervention of the user.

The second topic of this thesis was the characterization of two important aspects of the GPD. The first was the response to polarized radiation at energies of a few keV where the maximum sensitivity was expected on the basis of Monte Carlo simulations, used because a calibration source at these energies was missing. For the first time the prototype Bragg source allowed an actual measurement and the good agreement between expected and measured performances has definitely proved the feasibility of the X-ray polarimetry with the GPD (see Chapter 5).

The characterization of the angular reconstruction of the GPD was the second important measurement performed within this thesis (see Chapter 5). The facility allows to accurately control the plane of polarization of the beam and its relation with the measured angle of polarization was investigated. The preliminary results has shown that some (small) systematic effects emerge: residuals from the expected linear behavior are present with a particularly puzzling azimuthal periodicity of 180°. The nature of these effects has not been clarified yet but further investigations will be soon performed. However they don't affect substantially the readiness and the reliability of the instrument.

The definition of the GPD perspectives of measurement was the third subject of this thesis (see Chapter 6). Proposals of missions which include the GPD were submitted to space agencies in Italy, Europe and United States and three of four have passed a certain level of selection, currently waiting for the possible implementation to the launch. This thesis contributed to their design but also (and above all) to the definition of the scientific objectives, two different scenarios being considered. The first was that of small and low-cost missions possibility devoted to X-ray polarimetry: these pathfinders are designed to be extremely versatile to accomplish at best the wealth of expectations presented in

Chapter 1.

Among pathfinders PolariX is the mission in the most advanced state of development: it is a completely Italian project dedicated to X-ray polarimetry making use of GPD and if selected it will be launched in mid 2014. Polarization at the level of 1% could be measured for galactic or bright extragalactic sources in a few days of observation: this allows to perform polarimetry of objects belonging to different classes and hence answer to many of the expectations of X-ray polarimetry. Moreover the unique sensitivity of the GPD suggests that unexpected results could also be achieved: after all polarimetry is unexplored yet and the X-ray sky has usually reserved many surprises.

The second analyzed scenario is that of a large observatory. The GPD is in the baseline of the International X-ray Observatory, the next large X-ray mission expected to be launched in $\sim$2020 thanks to the joint efforts of space agencies in Europe, United States and Japan. It will able to perform polarimetry of even faint extragalactic sources with an angular resolution not achievable by small missions.

In the context of pathfinders and IXO scenarios the minimum polarization detectable above statistical fluctuations is estimated for many actual sources belonging to different classes and even more refined simulations are performed in some cases to discuss the possible observability of specific effects. This is, for example, the case of gravitational effects which influence the polarization of thermal emission produced by an accretion disk around a galactic black hole. The results, derived in collaboration with the Astronomical Institute and Academy of Sciences of the Czech Republic and University of Rome "Roma Tre", were published in a dedicated paper.

The last subject of this thesis was the exploration of new applications of the GPD. The first was presented in Chapter 7 and consists in its use as large field of view instrument to study, for example, GRBs, magnetars and the other transient sources. This application was already proposed even for competitive photoelectric polarimeters but this thesis contributed with a completely original study of the systematic effects which emerge when inclined photons are photoabsorbed in a gas, considering both polarized and unpolarized radiation. The problem is consistently analyzed with an extendible analytical treatment, simulations and measurements and this analysis, although incomplete, is of primary importance for the possible realization of any photoelectric polarimeters with large field of view.

Severe systematic effects arise when the inclination is greater than about 20°. They basically emerge because photoelectric polarimeters measure only the projection of the photoelectron emission direction on a plane and hence they are sensitive only to their azimuthal behavior. Deep changes in the shape of the intrinsic response of the instrument are discovered for both polarized and unpolarized photons. They consist in a significant reduction, 50% at 40°, of the amplitude of the response for polarized radiation and a strong spurious signal which emerges when unpolarized photons are incident not orthogonally to the detector. In both cases the azimuthal response is no more symmetric on 180° because the relativistic correction to the differential cross section of the photoelectric effect breaks the symmetry of the emission when photons are inclined.

The sensitivity to polarization could be, at least in principle, recovered with the methods and the algorithms presented in this thesis but this was verified only in the simplest

geometry. Actually the study presented can not yet prove the feasibility of photoelectric polarimeters with large field of view. However it strongly suggests that this use of the GPD is not an easy generalization of that in the focal plane and this conclusion is also true for any currently available photoelectric polarimeter. Moreover similar systematics could also emerge in the case of scattering devices with large field of view.

Another attractive application of the GPD could be its use at higher energy, namely above 10 keV (see Chapter 8). This possibility was investigated with Monte Carlo simulations replacing the baseline mixture of helium with ones of neon or argon at high pressure (1, 2, 3 and 4 atm) and thick gas cells (1, 2 and 3 cm). They were analyzed up to energies of $\sim$35 keV and more. Assuming a multilayer optics such as that of the mission SIMBOL-X the expected performances are rather encouraging and a sensitivity able to perform X-ray polarimetry of obscured objects and cyclotron lines can be reached with observations of the order of one day. This proves that photoelectric polarimetry with the GPD could be a very interesting opportunity even in the hard X-rays.

This thesis has hopefully shown to the reader that the development of X-ray polarimetry, the last unexplored branch of X-ray astronomy, will be of the primary interest. Its purpose has been also to prove that the GPD offers an actual opportunity to unveil this exciting window on the world of compact sources. Thanks also to the work carried out in this thesis, a pathfinder mission making use of GPD could be launched in a few years and this would eventually open the way for polarimetry even in the X-rays after a half century wait.

Acknowledgments

Many people supported me during this thesis. First of all, I would like to thank Enrico Costa and Paolo Soffitta. They followed my PhD work with true interest and above all gave me much freedom in my researches and its approach. Hopefully the results have balanced the risks.

Ronaldo Bellazzini and his group at the INFN of Pisa have developed the Gas Pixel Detector for several years. This thesis would not be possible without this beautiful device.

Angela Bazzano encouraged me and patiently read this manuscript. Giorgio Matt provided scientific support when needed, Antonella Tarana that for the "administration" of the PhD.

A small period of this thesis was spent in Prague. I thank Vladimr Karas and Michal Dovčiak for that nice week. I hope that it was the first of a series of successful collaborations.

Luigi Stella ran a very nice course of High Energy Astrophysics. It gave me the bases and the interest for understanding a large part of what is presented in Chapter 1.

I would like to thank the "residents" of the room 1C06, who is here now, who left some months ago and who appears in the late afternoon. They enjoy my pleasant presence each day and this requires a certain amount of patience. The other colleagues at the IASF of Rome, and in particular the members of the High Energy group, fall in the same lucky category. Despite they are a bit farther from my desk, the canteen is too small to avoid debates.

This thesis would not be written without my laptop. It was so nice to break well before its deadline.

Eventually I thank my family, and in particular my parents. They prove each day with their example the spontaneity and the importance of all kind of hard works. Now I see the importance of writing articles and cleaning our laboratory. I thank my next to no one friends and my one-hundred-four-months-old girlfriend Ambra. I would not be so proud to finish this work without her patient. Yes, I request a lot of patience!

Appendices

Appendix A

Modulation factor for some mixtures

The modulation factor and the efficiency of the baseline mixture (20% helium and 80% DME, pressure 1 atm and gas cell 1 cm thick) adopted throughout this thesis are reported in Table A.1. The efficiency is calculated from the absorption coefficient retrieved from XCOM database[1].

The modulation factor of the mixtures discussed in Chapter 8 are in Table A.2 and Table A.3 for the mixtures of neon and argon respectively.

μ is calculated with the Monte Carlo software presented in Sec. 2.2.2. Its results have been basically confirmed with measurements performed in the context of this thesis (see Sec. 5.1). Data selection is not performed.

[1] It is accessible from *http://physics.nist.gov/PhysRefData/Xcom/html/xcom1.html*.

Energy (keV)	μ	ϵ
1.5	0.0319	0.1334
2.0	0.1172	0.2083
2.5	0.2582	0.1730
3.0	0.3694	0.1246
3.5	0.4496	0.0872
4.0	0.4936	0.0619
4.5	0.5141	0.0448
5.0	0.5644	0.0332
5.5	0.5931	0.0252
6.0	0.6216	0.0194
6.5	0.6304	0.0152
7.0	0.6533	0.0122
7.5	0.6764	0.0099
8.0	0.6975	0.0081
9.0	0.7283	0.0056
10.0	0.7648	0.0040

Table A.1: Modulation factor μ of the baseline mixture helium 20% and DME 80% calculated with the Monte Carlo software. The gas pressure is 1 atm and its thickness 1 cm; no cuts on data are applied. The efficiency ϵ is also reported. Simulations in the case of the baseline mixture were originally performed by INFN of Pisa.

	Gas cell thickness 1 cm				Gas cell thickness 2 cm				Gas cell thickness 3 cm			
E (keV)	1 atm	2 atm	3 atm	4 atm	1 atm	2 atm	3 atm	4 atm	1 atm	2 atm	3 atm	4 atm
2.0	0.0685	0.0206	0.0050	0.0028	0.0231	0.0076	0.0137	0.0098	0.0063	0.0230	0.0251	0.0139
3.0	0.2055	0.1389	0.0760	0.0657	0.1398	0.0842	0.0760	0.0299	0.0809	0.0584	0.0286	0.0176
4.0	0.3517	0.2737	0.2112	0.1516	0.2328	0.1946	0.1597	0.1035	0.1819	0.1442	0.1185	0.0888
5.0	0.4130	0.3570	0.3217	0.2848	0.3410	0.2842	0.2504	0.2222	0.2859	0.2595	0.2145	0.1818
6.0	0.4789	0.4364	0.3867	0.3590	0.4318	0.3693	0.3351	0.3151	0.3938	0.3175	0.2883	0.2616
8.0	0.5634	0.5181	0.4762	0.4300	0.5385	0.4798	0.4402	0.4059	0.5143	0.4429	0.3826	0.3770
10.0	0.6327	0.5858	0.5368	0.4973	0.6103	0.5622	0.5003	0.4719	0.5906	0.5163	0.4890	0.4620
12.0	0.6924	0.6339	0.6066	0.5582	0.6761	0.6181	0.5946	0.5444	0.6500	0.6026	0.5710	0.5319
15.0	0.7517	0.6861	0.6775	0.6479	—	0.6617	0.6500	0.6227	—	0.6700	0.6337	0.6106
20.0	—	0.7502	0.7372	0.7117	—	0.7375	0.7189	0.7066	—	—	0.7132	0.6870
23.0	—	0.7781	—	—	—	—	—	—	—	—	0.7239	—
25.0	—	—	0.7500	0.7549	—	—	0.7566	0.7499	—	—	—	0.7333
30.0	—	—	0.7903	0.7830	—	—	—	0.7638	—	—	—	—
35.0	—	—	—	0.7923	—	—	—	—	—	—	—	—

Table A.2: Modulation factor for the mixture 80% neon and 20% DME calculated with the Monte Carlo software. The pressure is 1, 2, 3 or 4 atm and the cell gas thickness 1,2 or 3 cm. No cuts on data is performed.

	Gas cell thickness 1 cm				Gas cell thickness 2 cm				Gas cell thickness 3 cm			
E (keV)	1 atm	2 atm	3 atm	4 atm	1 atm	2 atm	3 atm	4 atm	1 atm	2 atm	3 atm	4 atm
6.0	0.1565	0.1215	0.1337	0.1417	0.1308	0.1150	0.0652	0.0670	0.0863	0.0831	0.0697	0.0300
8.0	0.3164	0.2986	0.2798	0.2703	0.2592	0.2611	0.2373	0.2191	0.2502	0.2382	0.2218	0.1839
10.0	0.3545	0.3530	0.3331	0.3429	0.3312	0.3383	0.3245	0.3068	0.3181	0.3188	0.3091	0.2848
12.0	0.4483	—	—	—	0.4157	—	—	—	0.3909	—	—	—
15.0	0.5535	0.5081	0.4595	0.4528	0.5218	0.4936	0.4525	0.4225	0.5126	0.4403	0.4315	0.4078
20.0	0.6680	0.6234	0.6021	0.5515	—	0.6014	0.5768	0.5306	—	0.6008	0.5554	0.5230
25.0	—	0.6794	0.6760	0.6276	—	0.6700	0.6609	0.6327	—	0.6561	0.6370	0.6208
30.0	—	0.7163	0.7074	0.6936	—	—	0.7041	0.6824	—	—	0.6847	0.6745
35.0	—	—	0.7315	0.7243	—	—	0.7278	0.7102	—	—	0.7161	0.7041
40.0	—	—	0.7397	0.7389	—	—	—	0.7442	—	—	—	0.7238
45.0	—	—	—	0.7564	—	—	—	0.7526	—	—	—	—
50.0	—	—	—	0.7494	—	—	—	—	—	—	—	—

Table A.3: The same as Table A.2 but for the mixture argon 60% and DME 40%.

Appendix B

Polarization induced by grazing incidence optics

Reflection on grazing incidence optics can affect the polarization of collected photons. This issue is scarcely discussed in the literature: only Chipman et al. (1992) performed a theoretical study based on Fresnel equations and Mueller calculus dedicated to the telescope subsystem of the *Advanced X-ray Astrophysics Facility* (AXAF, Weisskopf et al., 1996). This work was afterwards corrected by Sanchez Almeida and Martinez Pillet (1993) (see also Chipman et al., 1993). The results are described below together with the theoretical framework in which they are inserted.

B.1 Attenuation and retardance

Grazing-incidence reflection can modify the state of polarization of incident radiation introducing a linear attenuation and/or a linear retardance (Chipman, 1989). The former causes a partial absorption of the radiation, while the latter a rotation of the plane of polarization.

Incident photons can be considered as the superimposition of two linearly polarized components, in this context conveniently defined in the plane perpendicular and parallel to the plane of reflection, s and p respectively (see Fig. B.1). The Fresnel coefficients a_s and a_p characterize the reflection in the two planes: they are complex quantities and their modules give the ratio between the electric field of the reflected and the incident radiation, while their phases δ provide the phase shift caused by the reflection.

The coefficients a_s and a_p depend on the angle of reflection and the complex refractive index of the material n. They are calculated from the Fresnel equations:

$$a_s \equiv |a_s| \exp(\imath\delta_s) = \frac{\cos\phi - \left(n^2 - \sin^2\phi\right)^{\frac{1}{2}}}{\cos\phi + \left(n^2 - \sin^2\phi\right)^{\frac{1}{2}}} \tag{B.1}$$

$$a_p \equiv |a_p| \exp(\imath\delta_p) = \frac{n^2\cos\phi - \left(n^2 - \sin^2\phi\right)^{\frac{1}{2}}}{n^2\cos\phi + \left(n^2 - \sin^2\phi\right)^{\frac{1}{2}}} \tag{B.2}$$

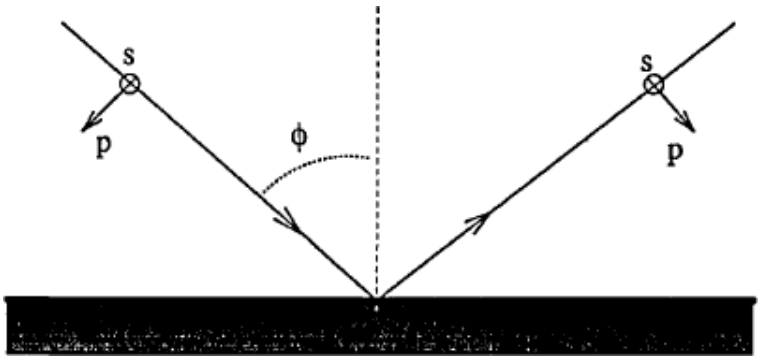

Figure B.1: Geometry of grazing-incidence reflection (Sanchez Almeida and Martinez Pillet, 1993).

where $n = n_0 - \imath k$ ($\imath = \sqrt{-1}$) and ϕ is the incidence angle measured from the normal to the surface (see Fig. B.1). Note that grazing incidence reflection occurs for $\phi \approx$90°.

The linear diattenuation $\mathcal{D}$ is defined from the modules of the Fresnel coefficients:

$$\mathcal{D} = \frac{||a_s|^2 - |a_p|^2|}{|a_s|^2 + |a_p|^2} \tag{B.3}$$

and expresses the differential absorption of the two components s and p which are orthogonally polarized. For example an optical element acts as a perfect polarizer if $\mathcal{D}$=1 since in this case only the s or the p component is transmitted. If $\mathcal{D} = 0$ the optical element transmits the incident radiation regardless of polarization and consequently the polarization state of incident radiation is not changed.

In Fig. B.2 the modules and phases of the Fresnel coefficients are plotted for n=0.91-$\imath$0.04, that is the value for gold at about 0.1 keV. The limit for grazing incidence is $\phi \rightarrow$90° and in this case $a_s/a_p \sim$1. Indeed $|a_p|/|a_s| \rightarrow 1$ and then the reflection occurs with the same efficiency independently from the state of polarization of the incident radiation ($\mathcal{D}$=0), and moreover the direction of the electric field doesn't change, $\delta_s, \delta_p \rightarrow$180° and hence the phase is rotated of an irrelevant factor 180°.

This is a general result and is not affected by the particular value of metal refractive index. Indeed for $\phi \approx 90°$ Fresnel equations become (cf. Eq. B.2):

$$a_s \approx a_p \approx -1. \tag{B.4}$$

B.2 The Mueller calculus

The study of propagation of polarized light through an optical system can be conveniently performed using the Mueller calculus (see, for example, Tinbergen, 1996). In this approach optical elements are represented as 4×4 matrices which operate on Stokes vectors (see Sec. 1.1.1). As an example the Mueller matrix of an ideal linear polarizer with

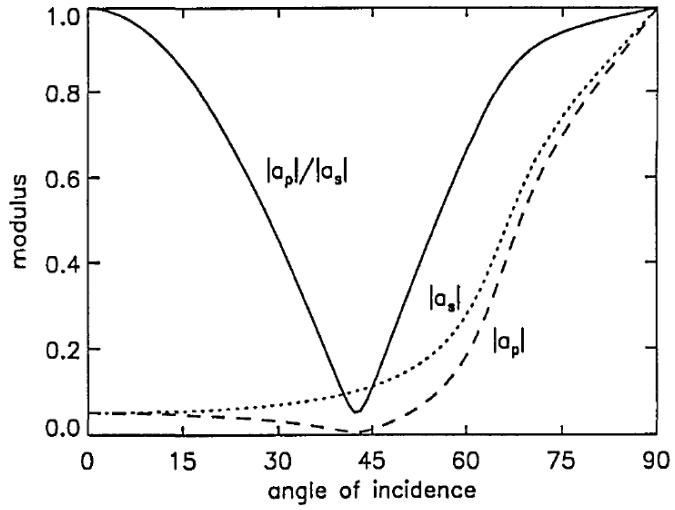

(a)

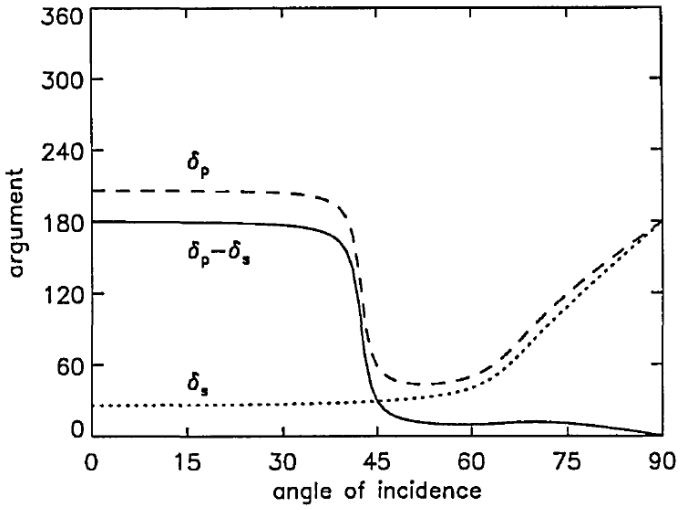

(b)

Figure B.2: Modules (**a**) and phases (**b**) of the Fresnel coefficients as a function of the angle of incidence in case of reflection on gold. For $\phi \rightarrow 90°$, $|a_p|/|a_s| \rightarrow 1$ and $\delta_p - \delta_s \rightarrow 0$ (Sanchez Almeida and Martinez Pillet, 1993).

horizontal transmission axis is:

$$\mathcal{M} = \begin{bmatrix} \frac{1}{2} & \frac{1}{2} & 0 & 0 \\ \frac{1}{2} & \frac{1}{2} & 0 & 0 \\ 0 & 0 & 0 & 0 \\ 0 & 0 & 0 & 0 \end{bmatrix}, \tag{B.5}$$

and if this matrix is applied on the Stokes vector which represents unpolarized radiation:

$$\begin{bmatrix} I \\ Q \\ U \\ V \end{bmatrix}_{trans.} = \begin{bmatrix} \frac{1}{2} & \frac{1}{2} & 0 & 0 \\ \frac{1}{2} & \frac{1}{2} & 0 & 0 \\ 0 & 0 & 0 & 0 \\ 0 & 0 & 0 & 0 \end{bmatrix} \begin{bmatrix} 1 \\ 0 \\ 0 \\ 0 \end{bmatrix} = \begin{bmatrix} \frac{1}{2} \\ \frac{1}{2} \\ 0 \\ 0 \end{bmatrix} = \frac{1}{2} \begin{bmatrix} 1 \\ 1 \\ 0 \\ 0 \end{bmatrix}. \tag{B.6}$$

As expected, the intensity of transmitted radiation is halved and the beam result linearly polarized in the horizontal direction

B.3 Mueller matrix for single reflection telescopes

X-ray telescope are not diffraction-limited and this greatly simplifies the Mueller matrix of the system because in this case the measured Stokes vector involves the integration over the whole diffraction pattern. In the case of a single diffraction telescope, the Mueller matrix for on-axis sources is (Sanchez Almeida and Martinez Pillet, 1992):

$$\begin{bmatrix} H_+ + H_- & 0 & 0 & 0 \\ 0 & H_+ & 0 & 0 \\ 0 & 0 & H_+ & 0 \\ 0 & 0 & 0 & H_+ - H_- \end{bmatrix}, \tag{B.7}$$

where:

$$H_+ = \int_0^\infty |h_+(q)|^2 q dq \tag{B.8}$$

$$H_- = \int_0^\infty |h_-(q)|^2 q dq \tag{B.9}$$

The functions $h_+(q)$ and $h_-(q)$ are:

$$h_+(q) = \int_0^1 \left[A_\rho(x) + A_\theta(x)\right] J_0(xq) x dx \tag{B.10}$$

$$h_-(q) = \int_0^1 \left[A_\rho(x) - A_\theta(x)\right] J_2(xq) x dx \tag{B.11}$$

$$q = \frac{k\rho R}{f} \tag{B.12}$$

where k is the wave number of the radiation, R and f are the radius of the mirror and the focal length of the telescope respectively, ρ and θ are the radial coordinate with respect

to the optical axis and the azimuthal angle in the focal plane. J_i is the Bessel function of order i and eventually A_ρ and A_θ are the Fresnel coefficients in the radial and in the azimuthal directions respectively. They are defined as:

$$A_\rho(x) = \begin{cases} 0 & \text{for } 0 \leq x \leq \epsilon \\ a_p & \text{for } \epsilon \leq x \leq 1 \end{cases} \tag{B.13}$$

$$A_\theta(x) = \begin{cases} 0 & \text{for } 0 \leq x \leq \epsilon \\ a_s & \text{for } \epsilon \leq x \leq 1 \end{cases} \tag{B.14}$$

where x is the distance from the optical axis normalized to the radius of the mirror r and ϵ takes into account that grazing incidence reflection occurs in an annular region: it is the ratio between the internal and external radii of this annular aperture.

An optical system which doesn't change the state of polarization of incident radiation is characterized by $A_\rho = A_\theta$. Indeed in this case $h_- = 0$ (cf. Eq. B.11) and its Mueller matrix reduces to be proportional to the identity matrix (cf. Eq. B.7). Thus the presence of a non-zero $|h_-|$ function involves polarization effects whose magnitudes depend on the ratio of H_+ and H_-.

Note that the Mueller matrix of an X-ray telescope is diagonal for on-axis sources (see Eq. B.7). In this case it doesn't produce crosstalk between different types of polarization:

- an unpolarized radiation doesn't become polarized. This can be derived also from the axial symmetry of the system;
- if incident radiation is polarized, some change in the degree of polarization may occur but the direction of polarization doesn't change.

For example consider incident radiation which is linearly polarized in the x direction. The Stokes vector of the reflected photons is:

$$\begin{aligned} \begin{bmatrix} I \\ Q \\ U \\ V \end{bmatrix}_{Refl.} &= \begin{bmatrix} H_+ + H_- & 0 & 0 & 0 \\ 0 & H_+ & 0 & 0 \\ 0 & 0 & H_+ & 0 \\ 0 & 0 & 0 & H_+ - H_- \end{bmatrix} \times \begin{bmatrix} 1 \\ 1 \\ 0 \\ 0 \end{bmatrix} = \\ &= \begin{bmatrix} H_+ + H_- \\ H_+ \\ 0 \\ 0 \end{bmatrix} = (H_+ + H_-) \begin{bmatrix} 1 \\ \frac{H_+}{H_+ + H_-} \\ 0 \\ 0 \end{bmatrix} \\ &\approx (H_+ + H_-) \begin{bmatrix} 1 \\ 1 - \frac{H_-}{H_+} \\ 0 \\ 0 \end{bmatrix}. \end{aligned} \tag{B.15}$$

The last approximation holds if $H_+ \gg H_-$ as expected. Then the effect of grazing incidence reflection for on-axis sources is a slight change of the degree of polarization of order $H_-/H_+ \ll 1$.

B.4 Estimate for the AXAF telescope

The Mueller matrix can be obtained if the telescope geometry is defined. The incident angle ϕ and hence the Fresnel coefficients can be calculated from the knowledge of the mirrors curvature and material; in turn the coefficients a_ρ and a_θ allow the calculation of h_-, h_+, H_-, H_+ and then of the Mueller matrix of the telescope.

Sanchez Almeida and Martinez Pillet (1993) calculate that for the AXAF telescope:

$$\frac{H_-}{H_+} \approx 4.7 \times 10^{-5}. \tag{B.16}$$

This derives from the assumption of a focal length of 10 m and 6 shells whose diameters ranges from 0.6 to 1.2 m. $\epsilon \approx 0.93$, ϕ falls between $89.09°$ to $89.56°$ and eventually $n = 0.91 - \imath 0.04$ (Chipman et al., 1992).

Hence single reflection mirrors introduce a change of the degree of polarization of $\sim 5 \times 10^{-5}$. X-ray telescopes focus photons through two reflections and Sanchez Almeida and Martinez Pillet (1993) evaluate that elements in the Mueller matrix are increased by a factor 2^2 in this case. Then they conclude that the AXAF telescope causes a change of the polarization degree of reflected photons between 10^{-3} and 5×10^{-5}.

This result is obtained for a telescope with a long focal length, f=10 m, which favors small grazing-incidence angles and then a smaller effect. However this estimate is rather encouraging: an accuracy of one part per 10^3 is (unfortunately) out of the capabilities of the current generation of X-ray polarimeters because, for example, if the radiation is polarized at the 1% level the effect of the grazing incidence optics is of the order of 0.001%. Then it can be safely neglected in the context of the GPD.

List of scientific publications

List of scientific publications presented within this thesis:

2009

- **F. Muleri**, P. Soffitta, R. Bellazzini, A. Brez, E. Costa, M. Frutti, M. Mastropietro, M. Minuti, E. Morelli, M. Pinchera, A. Rubini, and G. Spandre. *A Versatile Facility for the Calibration of X-ray Polarimeters*. In Proc. of Polarimetry days in Rome: Crab status, theory and prospects (2009)

- S. Fabiani, F. Lazzarotto, R. Bellazzini, A. Brez, E. Costa, S. Di Cosimo, **F. Muleri**, A. Rubini, P. Soffitta, and G. Spandre. *The Study of PWNe with a photoelectric polarimeter*. In Proc. of Polarimetry days in Rome: Crab status, theory and prospects (2009)

- M. Feroci, L. Amati, L. A. Antonelli, V. Bonvicini, E. Costa, E. Del Monte, I. Donnarumma, Y. Evangelista, F. Fiore, F. Fuschino, G. L. Israel, G. Labanti, I. Lapshov, F. Lazzarotto, M. Marisaldi, M. Mastropietro, E. Morelli, **F. Muleri**, F. Nicastro, M. Orlandini, L. Pacciani, F. Perotti, M. Rapisarda, A. Rashevsky, A. Rubini, P. Soffitta, A. Vacchi, G. Zampa, and N. Zampa. *A Light and Effective Wide Field Monitor for Gamma Ray Bursts and Transient Sources*. In Proc. of The Sixth Huntsville Gamma-Ray Burst Symposium 2008 (2009)

2008

- **F. Muleri**, P. Soffitta, L. Baldini, R. Bellazzini, J. Bregeon, A. Brez, E. Costa, M. Frutti, L. Latronico, M. Minuti, M. B. Negri, N. Omodei, M. Pesce-Rollins, M. Pinchera, M. Razzano, A. Rubini, C. Sgró, and G. Spandre. *Low energy polarization sensitivity of the Gas Pixel Detector*. Nuclear Instruments and Methods in Physics Research A, 584:149 (2008)

- M. Dovčiak, **F. Muleri**, R. W. Goosmann, V. Karas, and G. Matt. *Thermal disc emission from a rotating black hole: X-ray polarization signatures*. MNRAS, 391:32 (2008)

- **F. Muleri**, P. Soffitta, R. Bellazzini, A. Brez, E. Costa, M. Frutti, M. Mastropietro, E. Morelli, M. Pinchera, A. Rubini, and G. Spandre. *A versatile facility for the calibration of x-ray polarimeters with polarized radiation*. In Proc. of SPIE, volume 7011-84 (2008)

- **F. Muleri**, P. Soffitta, R. Bellazzini, A. Brez, E. Costa, S. Fabiani, M. Frutti, M. Minuti, M. B. Negri, M. Pinchera, A. Rubini, and G. Spandre. *The Gas Pixel Detector as an X-ray photoelectric polarimeter with a large field of view*. In Proc. of SPIE, volume 7011-88 (2008)

- E. Costa, R. Bellazzini, J. Bregeon, A. Brez, M. Frutti, S. Di Cosimo, L. Latronico, F. Lazzarotto, G. Matt, M. Minuti, E. Morelli, **F. Muleri**, M. Pinchera, M. Razzano, A. Rubini, P. Soffitta, and G. Spandre. *XPOL: a photoelectric polarimeter onboard XEUS*. In Proc. of SPIE, volume 7011, page 70110F-1 (2008)

- P. Soffitta, R. Bellazzini, G. Tagliaferri, E. Costa, G. Pareschi, S. Basso, V. Cotroneo, M. Frutti, F. Lazzarotto, **F. Muleri**, A. Rubini, G. Spandre, A. Brez, L. Baldini, J. Bregeon, M. Minuti, G. Matt, and F. Frontera. *X-ray polarimetry on-board HXMT*. In Proc. of SPIE, volume 7011, page 701128-1 (2008)

2007

- **F. Muleri**, P. Soffitta, R. Bellazzini, A. Brez, E. Costa, S. Fabiani, M. Frutti, M. Minuti, M. B. Negri, P. Pascale, A. Rubini, G. Sindoni, and G. Spandre. *A very compact polarizer for an X-ray polarimeter calibration*. In Proc. of SPIE, volume 6686, page 668610 (2007)

- E. Costa, R. Bellazzini, G. Tagliaferri, L. Baldini, S. Basso, J. Bregeon, A. Brez, O. Citterio, V. Cotroneo, F. Frontera, M. Frutti, G. Matt, M. Minuti, **F. Muleri**, G. Pareschi, G. C. Perola, A. Rubini, C. Sgró, P. Soffitta, and G. Spandre. *An x-ray polarimeter for HXMT mission*. In Proc. of SPIE, volume 6686, page 66860Z-1 (2007)

2006

- **F. Muleri**, R. Bellazzini, E. Costa, P. Soffitta, F. Lazzarotto, M. Feroci, L. Pacciani, A. Rubini, E. Morelli, L. Baldini, F. Bitti, A. Brez, F. Cavalca, L. Latronico, M. M. Massai, N. Omodei, M. Pinchera, C. Sgró, G. Spandre, G. Matt, G. C. Perola, O. Citterio, G. Pareschi, V. Cotroneo, D. Spiga, and R. Canestrari. *An x-ray polarimeter for hard x-ray optics*. In Proc. of SPIE, volume 6266, page 62662X (2006)

- R. Bellazzini, L. Baldini, F. Bitti, A. Brez, F. Cavalca, L. Latronico, M. M. Massai, N. Omodei, M. Pinchera, C. Sgró, G. Spandre, E. Costa, P. Soffitta, G. Di Persio, M. Feroci, **F. Muleri**, L. Pacciani, A. Rubini, E. Morelli, G. Matt, and G. C. Perola. *A photoelectric polarimeter for XEUS: a new window in x-ray sky*. In Proc. of SPIE, volume 6266, page 62663Z (2006)

- E. Costa, R. Bellazzini, P. Soffitta, **F. Muleri**, M. Feroci, M. Frutti, M. Mastropietro, L. Pacciani, A. Rubini, E. Morelli, L. Baldini, F. Bitti, A. Brez, F. Cavalca, L. Latronico, M. M. Massai, N. Omodei, M. Pinchera, C. Sgró, G. Spandre, G. Matt, G. C. Perola, G. Chincarini, O. Citterio, G. Tagliaferri, G. Pareschi, and V. Cotroneo. *POLARIX: a small mission of x-ray polarimetry*. In Proc. of SPIE, volume 6266, page 62660R (2006)

Bibliography

S. L. Adler. Photon splitting and photon dispersion in a strong magnetic field. *Annals of Physics*, 67:599, 1971. 14

G. Amelino-Camelia, J. Ellis, N. E. Mavromatos, D. V. Nanopoulos, and S. Sarkar. Tests of quantum gravity from observations of γ-ray bursts. Nature, 393:763, 1998. 39

R. R. J. Antonucci and J. S. Miller. Spectropolarimetry and the nature of NGC 1068. ApJ, 297:621, 1985. 2

M. Arnaud, X. Barcons, D. Barret, M. Bautz, R. Bellazzini, J. Bleeker, H. Böhringer, T. Boller, W. N. Brandt, M. Cappi, F. Carrera, A. Comastri, E. Costa, T. Courvoisier, P. de Korte, T. Dwelly, A. Fabian, K. Flanagan, R. Gilli, R. Griffiths, G. Hasinger, J. Kaastra, S. Kahn, R. Kelley, H. Kunieda, K. Makishima, G. Matt, M. Mendez, K. Mitsuda, K. Nandra, T. Ohashi, M. Page, G. Palumbo, M. Pavlinsky, S. Sciortino, A. Smith, L. Strüder, T. Takahashi, M. Türler, M. Turner, Y. Ueda, C. Vignali, J. Vink, R. Warwick, M. Watson, R. Willingale, and S. N. Zhang. XEUS: the physics of the hot evolving universe. *Experimental Astronomy*, page 24, 2008. 144

W. Bambynek, B. Crasemann, R. W. Fink, H.-U. Freund, H. Mark, C. D. Swift, R. E. Price, and P. V. Rao. X-Ray Fluorescence Yields, Auger, and Coster-Kronig Transition Probabilities. *Reviews of Modern Physics*, 44:716, 1972. 42, 43

R. Bellazzini, F. Angelini, L. Baldini, A. Brez, E. Costa, G. Di Persio, L. Latronico, M. M. Massai, N. Omodei, L. Pacciani, P. Soffitta, and G. Spandre. Novel gaseus X-ray polarimeter: data analysis and simulation. In *Proc. of SPIE*, volume 4843, page 383, 2003. 49

R. Bellazzini, L. Baldini, F. Bitti, A. Brez, F. Cavalca, L. Latronico, M. M. Massai, N. Omodei, M. Pinchera, C. Sgró, G. Spandre, E. Costa, P. Soffitta, G. Di Persio, M. Feroci, F. Muleri, L. Pacciani, A. Rubini, E. Morelli, G. Matt, and G. C. Perola. A photoelectric polarimeter for XEUS: a new window in x-ray sky. In *Proc. of SPIE*, volume 6266, page 62663Z, 2006a. 146

R. Bellazzini, G. Spandre, M. Minuti, L. Baldini, A. Brez, F. Cavalca, L. Latronico, N. Omodei, M. M. Massai, C. Sgro', E. Costa, P. Soffitta, F. Krummenacher, and R. de Oliveira. Direct reading of charge multipliers with a self-triggering CMOS analog chip

with 105 k pixels at 50 μm pitch. *Nuclear Instruments and Methods in Physics Research A*, 566:552, 2006b. 47, 48, 49, 58, 113

R. Bellazzini, L. Baldini, A. Brez, F. Cavalca, L. Latronico, M. M. Massai, M. Minuti, N. Omodei, M. Pesce-Rollins, C. Sgró, G. Spandre, E. Costa, and P. Soffitta. Gas pixel detectors. *Nuclear Instruments and Methods in Physics Research A*, 572:160, 2007a. 69, 113

R. Bellazzini, G. Spandre, M. Minuti, L. Baldini, A. Brez, L. Latronico, N. Omodei, M. Razzano, M. M. Massai, M. Pesce-Rollins, C. Sgró, E. Costa, P. Soffitta, H. Sipila, and E. Lempinen. A sealed Gas Pixel Detector for X-ray astronomy. *Nuclear Instruments and Methods in Physics Research A*, 579:853, 2007b. 59, 60, 114

M. J. Berger and S. M. Seltzer. Studies in Penetration of Charged Particles in Matter. *Nuclear Science Series Report*, 39:205, 1964. 54

G. F. Bignami, P. A. Caraveo, A. D. Luca, and S. Mereghetti. The magnetic field of an isolated neutron star from X-ray cyclotron absorption lines. Nature, 423:725, 2003. 22

J. K. Black, R. G. Baker, P. Deines-Jones, J. E. Hill, and K. Jahoda. X-ray polarimetry with a micropattern TPC. *Nuclear Instruments and Methods in Physics Research A*, 581:755, 2007. 64, 66, 67

G. Boella, R. C. Butler, G. C. Perola, L. Piro, L. Scarsi, and J. A. M. Bleeker. BeppoSAX, the wide band mission for X-ray astronomy. A&AS, 122:299, 1997. 131

S. V. Bogovalov and D. V. Khangoulian. On the origin of the torus and jet-like structures in the centre of the Crab Nebula. MNRAS, 336:L53, 2002. 16

R. Browning. Universal elastic scattering cross sections for electrons in the range 1–100 kev. *Applied Physics Letters*, 58(24):2845, 1991. 53

N. Bucciantini, L. del Zanna, E. Amato, and D. Volpi. Polarization in the inner region of pulsar wind nebulae. A&A, 443:519, 2005. 16

A. N. Bunner. Soft X-ray results from the Wisconsin experiment on OSO-8. ApJ, 220:261, 1978. 132

D. N. Burrows, J. E. Hill, J. A. Nousek, J. A. Kennea, A. Wells, J. P. Osborne, A. F. Abbey, A. Beardmore, K. Mukerjee, A. D. T. Short, G. Chincarini, S. Campana, O. Citterio, A. Moretti, C. Pagani, G. Tagliaferri, P. Giommi, M. Capalbi, F. Tamburelli, L. Angelini, G. Cusumano, H. W. Bräuninger, W. Burkert, and G. D. Hartner. The Swift X-Ray Telescope. *Space Science Reviews*, 120:165, 2005. 135

J. Byrne and N. Howarth. The K-shell fluorescence yield and atomic shell structure effects. *Journal of Physics B Atomic Molecular Physics*, 3:280, 1970. 42

V. Canuto. Radiative Opacities and Compton Scattering in Strong Magnetic Fields. ApJ, 160:L153, 1970. 10

V. Canuto, J. Lodenquai, and M. Ruderman. Thomson scattering in a strong magnetic field. Phys. Rev. D, 3:2303, 1971. 10, 12

A. Celotti and G. Matt. Polarization Properties of Synchrotron Self-Compton Emission. MNRAS, 268:451, 1994. 34, 155

G. A. Chanan, R. Novick, and E. H. Silver. Further comments on the effects of vacuum birefringence on the polarization of X-rays emitted from magnetic neutron stars. ApJ, 228:L71, 1979. 15

S. Chandrasekhar. On the Radiative Equilibrium of a Stellar Atmosphere. IX. ApJ, 103: 165, 1946. 28

S. Chandrasekhar. *Radiative transfer*. Oxford, Clarendon Press, 1950. 28

K. S. Cheng, C. Ho, and M. Ruderman. Energetic Radiation from Rapidly Spinning Pulsars. II. VELA and Crab. ApJ, 300:522, 1986a. 19

K. S. Cheng, C. Ho, and M. Ruderman. Energetic radiation from rapidly spinning pulsars. I - Outer magnetosphere gaps. II - VELA and Crab. ApJ, 300:500, 1986b. 19

R. A. Chipman. Polarization analysis of optical systems. *Optical Engineering*, 28:90, 1989. 203

R. A. Chipman, D. M. Brown, and J. P. McGuire, Jr. Polarization aberration analysis of the Advanced X-ray Astrophysics Facility Telescope assembly. Appl. Opt., 31:2301, 1992. 203, 208

R. A. Chipman, D. M. Brown, and J. P. McGuire, Jr. Erratum: Polarization aberration analysis of the advanced x-ray astrophysics facility telescope assembly [Appl. Opt. 31, 2301-2313 (1992)]. Appl. Opt., 32:4236, 1993. 203

E. Churazov, R. Sunyaev, and S. Sazonov. Polarization of X-ray emission from the Sgr B2 cloud. MNRAS, 330:817, 2002. 37, 155

O. Citterio, S. Campano, P. Conconi, M. Ghigo, F. Mazzoleni, E. Poretti, G. Conti, G. Cusumano, B. Sacco, H. Brauninger, W. Burkert, R. Egger, C. M. Castelli, and R. Willingale. Characteristics of the flight model optics for the JET-X telescope onboard the Spectrum-X-Gamma satellite. In *Proc. of SPIE*, volume 2805, page 56, 1996. 135, 137

W. Coburn and S. E. Boggs. Polarization of the prompt γ-ray emission from the γ-ray burst of 6 December 2002. Nature, 423:415, 2003. 38, 40

A. H. Compton and S. K. Allison. *X-rays in Theory and Experiment*. D. Van Nostrand Co., New York, 1963. 128

P. A. Connors, R. F. Stark, and T. Piran. Polarization features of X-ray radiation emitted near black holes. ApJ, 235:224, 1980. 30, 31, 69, 152

S. Corbel, R. P. Fender, A. K. Tzioumis, J. A. Tomsick, J. A. Orosz, J. M. Miller, R. Wijnands, and P. Kaaret. Large-Scale, Decelerating, Relativistic X-ray Jets from the Microquasar XTE J1550-564. *Science*, 298:196, 2002. 33, 34

E. Costa, M. Frutti, F. Pica, L. Piro, A. Rubini, P. Soffitta, E. Massaro, G. Matt, and G. Medici. Performances of lithium scatterers for X-ray polarimetry. In *Proc. of SPIE*, volume 1344, page 23, 1990. 69

E. Costa, F. Frontera, J. Heise, M. Feroci, J. in't Zand, F. Fiore, M. N. Cinti, D. Dal Fiume, L. Nicastro, M. Orlandini, E. Palazzi, M. Rapisarda#, G. Zavattini, R. Jager, A. Parmar, A. Owens, S. Molendi, G. Cusumano, M. C. Maccarone, S. Giarrusso, A. Coletta, L. A. Antonelli, P. Giommi, J. M. Muller, L. Piro, and R. C. Butler. Discovery of an X-ray afterglow associated with the γ-ray burst of 28 February 1997. Nature, 387:783, 1997. 38

E. Costa, P. Soffitta, R. Bellazzini, A. Brez, N. Lumb, and G. Spandre. An efficient photoelectric X-ray polarimeter for the study of black holes and neutron stars. Nature, 411: 662, 2001. 45, 46

E. Costa, R. Bellazzini, P. Soffitta, F. Muleri, M. Feroci, M. Frutti, M. Mastropietro, L. Pacciani, A. Rubini, E. Morelli, L. Baldini, F. Bitti, A. Brez, F. Cavalca, L. Latronico, M. M. Massai, N. Omodei, M. Pinchera, C. Sgró, G. Spandre, G. Matt, G. C. Perola, G. Chincarini, O. Citterio, G. Tagliaferri, G. Pareschi, and V. Cotroneo. POLARIX: a small mission of x-ray polarimetry. In *Proc. of SPIE*, volume 6266, page 62660R, 2006. 135

E. Costa, R. Bellazzini, G. Tagliaferri, L. Baldini, S. Basso, J. Bregeon, A. Brez, O. Citterio, V. Cotroneo, F. Frontera, M. Frutti, G. Matt, M. Minuti, F. Muleri, G. Pareschi, G. C. Perola, A. Rubini, C. Sgro, P. Soffitta, and G. Spandre. An x-ray polarimeter for HXMT mission. In *Proc. of SPIE*, volume 6686, page 66860Z–1, 2007. 141

E. Costa, R. Bellazzini, J. Bregeon, A. Brez, M. Frutti, S. Di Cosimo, L. Latronico, F. Lazzarotto, G. Matt, M. Minuti, E. Morelli, F. Muleri, M. Pinchera, M. Razzano, A. Rubini, P. Soffitta, and G. Spandre. XPOL: a photoelectric polarimeter onboard XEUS. In *Proc. of SPIE*, volume 7011, page 70110F–1, 2008. 146

S. Covino, D. Lazzati, G. Ghisellini, P. Saracco, S. Campana, G. Chincarini, S. di Serego, A. Cimatti, L. Vanzi, L. Pasquini, F. Haardt, G. L. Israel, L. Stella, and M. Vietri. GRB 990510: linearly polarized radiation from a fireball. A&A, 348:L1, 1999. 38

W. Cui, K. Ebisawa, T. Dotani, and A. Kubota. Simultaneous ASCA and RXTE Observations of Cygnus X-1 during its 1996 State Transition. ApJ, 493:L75, 1998. 150

D. dal Fiume, M. Orlandini, G. Cusumano, S. del Sordo, M. Feroci, F. Frontera, T. Oosterbroek, E. Palazzi, A. N. Parmar, A. Santangelo, and A. Segreto. The broad-band (0.1-200 keV) spectrum of HER X-1 observed with BeppoSAX. A&A, 329:L41, 1998. 150

J. K. Daugherty and A. K. Harding. Electromagnetic cascades in pulsars. ApJ, 252:337, 1982. 18

A. J. Dean, D. J. Clark, J. B. Stephen, V. A. McBride, L. Bassani, A. Bazzano, A. J. Bird, A. B. Hill, S. E. Shaw, and P. Ubertini. Polarized Gamma-Ray Emission from the Crab. *Science*, 321:1183, 2008. 7, 8, 40

L. Del Zanna, E. Amato, and N. Bucciantini. Axially symmetric relativistic MHD simulations of Pulsar Wind Nebulae in Supernova Remnants. On the origin of torus and jet-like features. A&A, 421:1063, 2004. 16

L. Del Zanna, D. Volpi, E. Amato, and N. Bucciantini. Simulated synchrotron emission from pulsar wind nebulae. A&A, 453:621, 2006. 16, 17

M. Dovčiak, V. Karas, and G. Matt. Polarization signatures of strong gravity in active galactic nuclei accretion discs. MNRAS, 355:1005, 2004. 32

M. Dovčiak, F. Muleri, R. W. Goosmann, V. Karas, and G. Matt. Thermal disc emission from a rotating black hole: X-ray polarization signatures. MNRAS, 391:32, 2008. 152, 153

R. C. Duncan and C. Thompson. Formation of very strongly magnetized neutron stars - Implications for gamma-ray bursts. ApJ, 392:L9, 1992. 21

J. Dyks and B. Rudak. Two-Pole Caustic Model for High-Energy Light Curves of Pulsars. ApJ, 598:1201, December 2003. 19

J. Dyks, A. K. Harding, and B. Rudak. Relativistic Effects and Polarization in Three High-Energy Pulsar Models. ApJ, 606:1125, 2004. 20

H. Eberhard and N. Werner. *The Elementary Process of Bremsstrahlung*. World Scientific, 2004. 75, 95

R. F. Egerton. *Electron EnergyLoss Spectroscopy in the Electron Microscope*. New York: Plenum Press, 1986. 53

H. Euler and B. Kockel. Über die Streuung von Licht an Licht nach der Diracschen Theorie. *Naturwissenschaften*, 23:246, April 1935. 14

K. D. Evans, R. Hall, and M. Lewis. The calibration of Bragg X-ray analyser crystals for use as polarimeters in X-ray astronomy. *Space Science Instrumentation*, 3:163, 1977. 72

A. C. Fabian, S. Vaughan, K. Nandra, K. Iwasawa, D. R. Ballantyne, J. C. Lee, A. De Rosa, A. Turner, and A. J. Young. A long hard look at MCG-6-30-15 with XMM-Newton. MNRAS, 335:L1, 2002. 32

S. Fabiani, F. Lazzarotto, R. Bellazzini, A. Brez, E. Costa, S. Di Cosimo, F. Muleri, A. Rubini, P. Soffitta, and G. Spandre. The Study of PWNe with a photoelectric polarimeter. In *Proc. of Polarimetry days in Rome: Crab status, theory and prospects*, 2009. 149

R. Fender. *Jets from X-ray binaries*, page 381. Compact stellar X-ray sources, 2006. 33

M. Feroci, L. Amati, L. A. Antonelli, V. Bonvicini, E. Costa, E. Del Monte, I. Donnarumma, Y. Evangelista, F. Fiore, F. Fuschino, G. L. Israel, G. Labanti, I. Lapshov, F. Lazzarotto, M. Marisaldi, M. Mastropietro, E. Morelli, F. Muleri, F. Nicastro, M. Orlandini, L. Pacciani, F. Perotti, M. Rapisarda, A. Rashevsky, A. Rubini, P. Soffitta, A. Vacchi, G. Zampa, and N. Zampa. A Light and Effective Wide Field Monitor for Gamma Ray Bursts and Transient Sources. In *Proc. of The Sixth Huntsville Gamma-Ray Burst Symposium 2008*, 2009. 89

P. Ferrando, A. Goldwurm, P. Laurent, O. Limousin, J. Martignac, F. Pinsard, Y. Rio, J. P. Roques, O. Citterio, G. Pareschi, G. Tagliaferri, F. Fiore, G. Malaguti, U. Briel, G. Hasinger, and L. Strüder. SIMBOL-X: a formation-flying mission for hard-x-ray astrophysics. In O. Citterio and S. L. O'Dell, editors, *Proc. of SPIE*, volume 5900, page 195, 2005. 131, 181, 187

P. Ferrando, M. Arnaud, U. Briel, E. Cavazutti, R. Clédassou, J. L. Counil, F. Fiore, P. Giommi, A. Goldwurm, O. Lamarle, P. Laurent, F. Lebrun, G. Malaguti, S. Mereghetti, G. Micela, G. Pareschi, M. Piermaria, J. P. Roques, and G. Tagliaferri. The Simbol-X mission. *Memorie della Societa Astronomica Italiana*, 79:19, 2008. 131, 181, 187

M. Forot, P. Laurent, I. A. Grenier, C. Gouiffès, and F. Lebrun. Polarization of the Crab Pulsar and Nebula as Observed by the INTEGRAL/IBIS Telescope. ApJ, 688:L29, 2008. 8

F. Frontera, E. Costa, D. dal Fiume, M. Feroci, L. Nicastro, M. Orlandini, E. Palazzi, and G. Zavattini. The high energy instrument PDS on-board the BeppoSAX X–ray astronomy satellite. A&AS, 122:357, 1997. 139

D. C. Gabuzda, P. Y. Kochenov, T. V. Cawthorne, and R. I. Kollgaard. Intraday polarization variability outside the VLBI core of the active galactic nucleus 0716+714. MNRAS, 313:627, 2000. 36

B. M. Gaensler and P. O. Slane. The Evolution and Structure of Pulsar Wind Nebulae. ARA&A, 44:17, 2006. 15

R. Gambini and J. Pullin. Nonstandard optics from quantum space-time. Phys. Rev. D, 59(12):124021, 1999. 39, 155

N. Gehrels, C. L. Sarazin, P. T. O'Brien, and et al. A short γ-ray burst apparently associated with an elliptical galaxy at redshift z = 0.225. Nature, 437:851, 2005. 38

P. K. Ghosh. *Introduction to Photoelectron Spectroscopy*. John Wiley & Sons, 1983. 44

R. Giacconi, W. P. Reidy, G. S. Vaiana, L. P. van Speybroeck, and T. F. Zehnpfennig. Grazing-Incidence Telescopes for X-Ray Astronomy. *Space Science Reviews*, 9:3, 1969. 128, 129, 130

R. Giacconi, G. Branduardi, U. Briel, A. Epstein, D. Fabricant, E. Feigelson, W. Forman, P. Gorenstein, J. Grindlay, H. Gursky, F. R. Harnden, J. P. Henry, C. Jones, E. Kellogg, D. Koch, S. Murray, E. Schreier, F. Seward, H. Tananbaum, K. Topka, L. Van Speybroeck, S. S. Holt, R. H. Becker, E. A. Boldt, P. J. Serlemitsos, G. Clark, C. Canizares, T. Markert, R. Novick, D. Helfand, and K. Long. The Einstein /HEAO 2/ X-ray Observatory. ApJ, 230:540, 1979. 131

P. Giommi, M. Capalbi, M. Fiocchi, E. Memola, M. Perri, S. Piranomonte, S. Rebecchi, and E. Massaro. A Catalog of 157 X-ray Spectra and 84 Spectral Energy Distributions of Blazars Observed with BeppoSAX. In P. Giommi, E. Massaro, and G. Palumbo, editors, *Blazar Astrophysics with BeppoSAX and Other Observatories*, page 63, 2002. 150

I. N. Gnedin, G. G. Pavlov, and I. A. Shibanov. The effect of vacuum birefringence in a magnetic field on the polarization and beaming of X-ray pulsars. *Pis ma Astronomicheskii Zhurnal*, 4:214, 1978. 15

J. Granot. The Most Probable Cause for the High Gamma-Ray Polarization in GRB 021206. ApJ, 596:L17, 2003. 38

J. Granot and A. Königl. Linear Polarization in Gamma-Ray Bursts: The Case for an Ordered Magnetic Field. ApJ, 594:L83, 2003. 38

J. Greiner, S. Klose, K. Reinsch, H. Martin Schmid, R. Sari, D. H. Hartmann, C. Kouveliotou, A. Rau, E. Palazzi, C. Straubmeier, B. Stecklum, S. Zharikov, G. Tovmassian, O. Bärnbantner, C. Ries, E. Jehin, A. Henden, A. A. Kaas, T. Grav, J. Hjorth, H. Pedersen, R. A. M. J. Wijers, A. Kaufer, H.-S. Park, G. Williams, and O. Reimer. Evolution of the polarization of the optical afterglow of the γ-ray burst GRB030329. Nature, 426: 157, 2003. 38, 39

A. Guinier. *X-Ray Diffraction: In Crystals, Imperfect Crystals, and Amorphous Bodies*. Dover Publications; Reprint edition (June 7, 1994), 1994. 70

F. Haardt and L. Maraschi. A two-phase model for the X-ray emission from Seyfert galaxies. ApJ, 380:L51, 1991. 32

F. Haberl. The magnificent seven: magnetic fields and surface temperature distributions. Ap&SS, 308:181, 2007. 21

F. Haberl, A. D. Schwope, V. Hambaryan, G. Hasinger, and C. Motch. A broad absorption feature in the X-ray spectrum of the isolated neutron star RBS1223 (1RXS J130848.6+212708). A&A, 403:L19, 2003. 22

A. K. Harding. Pulsar gamma-rays - Spectra, luminosities, and efficiencies. ApJ, 245:267, 1981. 18

A. K. Harding, M. S. Strickman, C. Gwinn, R. Dodson, D. Moffet, and P. McCulloch. The Multicomponent Nature of the Vela Pulsar Nonthermal X-Ray Spectrum. ApJ, 576:376, 2002. 18

S. Heinz, N. S. Schulz, W. N. Brandt, and D. K. Galloway. Evidence of a Parsec-Scale X-Ray Jet from the Accreting Neutron Star Circinus X-1. ApJ, 663:L93, 2007. 33

W. Heitler. *Quantum theory of radiation*. International Series of Monographs on Physics, Oxford: Clarendon, 1954, 3rd ed., 1954. 5, 41, 43

B. L. Henke, E. M. Gullikson, and J. C. Davis. X-Ray Interactions: Photoabsorption, Scattering, Transmission, and Reflection at E = 50-30,000 eV, Z = 1-92. *Atomic Data and Nuclear Data Tables*, 54:181, 1993. 72, 73, 74, 97

J. S. Heyl and N. J. Shaviv. Polarization evolution in strong magnetic fields. MNRAS, 311:555, 2000. 20, 21

J. S. Heyl and N. J. Shaviv. QED and the high polarization of the thermal radiation from neutron stars. Phys. Rev. D, 66(2):023002, 2002. 22, 24

J. S. Heyl, N. J. Shaviv, and D. Lloyd. The high-energy polarization-limiting radius of neutron star magnetospheres - I. Slowly rotating neutron stars. MNRAS, 342:134, 2003. 22

J. E. Hill, S. Barthelmy, J. K. Black, P. Deines-Jones, K. Jahoda, T. Sakamoto, P. Kaaret, M. L. McConnell, P. F. Bloser, J. R. Macri, J. S. Legere, J. M. Ryan, B. R. Smith, Jr., and B. Zhang. A burst chasing x-ray polarimeter. In *Proc. of SPIE*, volume 6686, page 66860Y–12, 2007. 66, 68, 161

A. E. Hornschemeier, N. E. White, and H. Tananbaum. The Frontier in X-ray Spectroscopy: NASA's Constellation-X Mission. In *X-ray Diagnostics of Astrophysical Plasmas: Theory, Experiment, and Observation*, volume 774 of *American Institute of Physics Conference Series*, page 383, 2005. 146

J. P. Hughes, K. S. Long, and R. Novick. A search for X-ray polarization in cosmic X-ray sources. ApJ, 280:255, 1984. 8

H. Iskef, J. W. Cunningham, and D. E. Watt. Projected ranges and effective stopping powers of electrons with energy between 20 eV and 10 keV. *Physics in Medicine and Biology*, 28:535, 1983. 56

K. Jahoda, J. H. Swank, A. B. Giles, M. J. Stark, T. Strohmayer, W. Zhang, and E. H. Morgan. In-orbit performance and calibration of the Rossi X-ray Timing Explorer (RXTE) Proportional Counter Array (PCA). In *Proc. of SPIE*, volume 2808, page 59, 1996. 124

B. T. Jannuzi, P. S. Smith, and R. Elston. The optical polarization properties of X-ray-selected BL Lacertae objects. ApJ, 428:130, 1994. 34

F. Jansen, D. Lumb, B. Altieri, J. Clavel, M. Ehle, C. Erd, C. Gabriel, M. Guainazzi, P. Gondoin, R. Much, R. Munoz, M. Santos, N. Schartel, D. Texier, and G. Vacanti. XMM-Newton observatory. I. The spacecraft and operations. A&A, 365:L1, 2001. 131, 134

C. P. Jensen, S. Romaine, R. Bruni, F. E. Christensen, and Z. Zhong. Optical constants in the hard X-ray/soft gamma ray range of selected materials for multilayer reflectors. In *Proc. of SPIE*, volume 6688, page 66880V, 2007. 131

D. C. Joy. *Monte Carlo Modeling for Electron Microscopy and Microanalysis*. Oxford University Press, 1995. 53, 54, 182

DC Joy and S. Luo. An empirical stopping power relationship for low-energy electrons. *Scanning*, 11(4):176–180, 1989. 54

P. Kaaret. X-ray clues to viability of loop quantum gravity. Nature, 427:287, 2004. 40

E. Kalemci, S. E. Boggs, C. Kouveliotou, M. Finger, and M. G. Baring. Search for Polarization from the Prompt Gamma-Ray Emission of GRB 041219a with SPI on INTEGRAL. ApJS, 169:75, 2007. 38

G. Kanbach. Gamma-Ray Pulsars. In W. Becker, H. Lesch, and J. Trümper, editors, *Neutron Stars, Pulsars, and Supernova Remnants*, page 91, 2002. 18

G. Kanbach, A. Słowikowska, S. Kellner, and H. Steinle. New optical polarization measurements of the Crab pulsar. In T. Bulik, B. Rudak, and G. Madejski, editors, *Astrophysical Sources of High Energy Particles and Radiation*, volume 801 of *American Institute of Physics Conference Series*, page 306, 2005. 8

O. Kargaltsev and G. G. Pavlov. Pulsar Wind Nebulae in the Chandra Era. In C. Bassa, Z. Wang, A. Cumming, and V. M. Kaspi, editors, *40 Years of Pulsars: Millisecond Pulsars, Magnetars and More*, volume 983 of *American Institute of Physics Conference Series*, page 171, 2008. 15

V. M. Kaspi, M. S. E. Roberts, and A. K. Harding. *Isolated neutron stars*, page 279. Compact stellar X-ray sources, 2006. 19

C. F. Kennel and F. V. Coroniti. Confinement of the Crab pulsar's wind by its supernova remnant. ApJ, 283:694, 1984a. 15

C. F. Kennel and F. V. Coroniti. Magnetohydrodynamic model of Crab nebula radiation. ApJ, 283:710, 1984b. 15

J. E. Koglin, F. E. Christensen, W. W. Craig, T. R. Decker, C. J. Hailey, F. A. Harrison, C. Hawthorn, C. P. Jensen, K. K. Madsen, M. Stern, G. Tajiri, and M. D. Taylor. NuSTAR hard x-ray optics. In *Proc. of SPIE*, volume 5900, page 266–275, 2005. 131, 181

S. S. Komissarov and Y. E. Lyubarsky. The origin of peculiar jet-torus structure in the Crab nebula. MNRAS, 344:L93, 2003. 16, 17

K. Koyama, Y. Maeda, T. Sonobe, T. Takeshima, Y. Tanaka, and S. Yamauchi. ASCA View of Our Galactic Center: Remains of Past Activities in X-Rays? PASJ, 48:249, 1996. 35, 36, 154

M. O. Krause. Atomic radiative and radiationless yields for K and L shells. *Journal of Physical and Chemical Reference Data*, 8:307, 1979. 183

D. Lai and W. C. Ho. Polarized X-Ray Emission from Magnetized Neutron Stars: Signature of Strong-Field Vacuum Polarization. *Physical Review Letters*, 91(7):071101, 2003. 24, 25, 26

D. Lai and W. C. G. Ho. Resonant Conversion of Photon Modes Due to Vacuum Polarization in a Magnetized Plasma: Implications for X-Ray Emission from Magnetars. ApJ, 566:373, 2002. 24

P. Laurent, P. Lechner, M. Authier, U. Briel, C. Cara, S. Colonges, P. Ferrando, J. Fontignie, E. Kendziorra, O. Limousin, J. Martignac, A. Meuris, L. Ravera, and Y. Rio. The Simbol-X focal plane. *Memorie della Societa Astronomica Italiana*, 79:32, 2008. 187

D. Lazzati. Polarization in the prompt emission of gamma-ray bursts and their afterglows. *New Journal of Physics*, 8:131, 2006. 38

T.-P. Li. HXMT: A Chinese High-Energy Astrophysics Mission. *Nuclear Physics B Proceedings Supplements*, 166:131, 2007. 139

T.-P. Li and M. Wu. Reconstruction of objects by direct demodulation. Ap&SS, 215:213, 1994. 139

J. Lodenquai, V. Canuto, M. Ruderman, and S. Tsuruta. Photon Opacity in Surfaces of Magnetic Neutron Stars. ApJ, 190:141, 1974. 13

K. S. Long, G. A. Chanan, W. H.-M. Ku, and R. Novick. The linear X-ray polarization of Scorpius X-1. ApJ, 232:L107, 1979. 8

M. S. Longair. *High energy astrophysics. Vol.1: Particles, photons and their detection*. Cambridge University Press, March 1992. 45

Y. E. Lyubarsky. On the structure of the inner Crab Nebula. MNRAS, 329:L34, 2002. 16

M. Lyutikov, V. I. Pariev, and R. D. Blandford. Polarization of Prompt Gamma-Ray Burst Emission: Evidence for Electromagnetically Dominated Outflow. ApJ, 597:998, 2003. 38

L. Maccione, S. Liberati, A. Celotti, J. G. Kirk, and P. Ubertini. Gamma-ray polarization constraints on Planck scale violations of special relativity. *Arxiv*, 0809.0220, 2008. 40

A. Martocchia and G. Matt. Iron Kalpha line intensity from accretion discs around rotating black holes. MNRAS, 282:L53, 1996. 32

G. Matt, A. C. Fabian, and R. R. Ross. X-Ray Photoionized Accretion Discs - Ultraviolet and X-Ray Continuum Spectra and Polarization. MNRAS, 264:839, 1993. 32

J. E. McClintock and R. A. Remillard. *Black hole binaries*, page 157. Compact stellar X-ray sources, 2006. 28

J. E. McClintock, R. Shafee, R. Narayan, R. A. Remillard, S. W. Davis, and L.-X. Li. The Spin of the Near-Extreme Kerr Black Hole GRS 1915+105. ApJ, 652:518, 2006. 150, 152, 154

S. McGlynn, D. J. Clark, A. J. Dean, L. Hanlon, S. McBreen, D. R. Willis, B. McBreen, A. J. Bird, and S. Foley. Polarisation studies of the prompt gamma-ray emission from GRB 041219a using the spectrometer aboard INTEGRAL. A&A, 466:895, 2007. 38

S. Mereghetti, A. Tiengo, and G. L. Israel. The X-Ray Source at the Center of the Cassiopeia A Supernova Remnant. ApJ, 569:275, 2002. 150

P. Meszaros. Radiation from accreting magnetized neutron stars. *Space Science Reviews*, 38:325, 1984. 27

P. Meszaros. *High-energy radiation from magnetized neutron stars*. University of Chicago Press, 1992. 10

P. Meszaros and J. Ventura. Vacuum-Polarization Effects on Thomson Cross Sections in a Magnetized Plasma. *Physical Review Letters*, 41:1544, 1978. 10, 12, 14

P. Meszaros and J. Ventura. Vacuum polarization effects on radiative opacities in a strong magnetic field. Phys. Rev. D, 19:3565, 1979. 10, 12, 13

P. Meszaros, R. Novick, A. Szentgyorgyi, G. A. Chanan, and M. C. Weisskopf. Astrophysical implications and observational prospects of X-ray polarimetry. ApJ, 324:1056, 1988. 1, 28, 29, 157, 189

J. M. Miller. Relativistic X-Ray Lines from the Inner Accretion Disks Around Black Holes. ARA&A, 45:441, 2007. 31

G. Miniutti, A. C. Fabian, R. Goyder, and A. N. Lasenby. The lack of variability of the iron line in MCG-6-30-15: general relativistic effects. MNRAS, 344:L22, 2003. 32

I. F. Mirabel and L. F. Rodriguez. A Superluminal Source in the Galaxy. Nature, 371:46, 1994. 152

I. G. Mitrofanov. Astrophysics (communication arising): A constraint on canonical quantum gravity? Nature, 426:139, 2003. 40, 69, 155

F. Muleri. Un Polarimetro Fotoelettrico per Astronomia a Raggi X. Master's thesis, Università di Roma "La Sapienza", 2005. 52, 161

F. Muleri, R. Bellazzini, E. Costa, P. Soffitta, F. Lazzarotto, M. Feroci, L. Pacciani, A. Rubini, E. Morelli, L. Baldini, F. Bitti, A. Brez, F. Cavalca, L. Latronico, M. M. Massai, N. Omodei, M. Pinchera, C. Sgró, G. Spandre, G. Matt, G. C. Perola, O. Citterio, G. Pareschi, V. Cotroneo, D. Spiga, and R. Canestrari. An x-ray polarimeter for hard x-ray optics. In *Proc. of SPIE*, volume 6266, page 62662X, 2006. 181

F. Muleri, P. Soffitta, R. Bellazzini, A. Brez, E. Costa, S. Fabiani, M. Frutti, M. Minuti, M. B. Negri, P. Pascale, A. Rubini, G. Sindoni, and G. Spandre. A very compact polarizer for an X-ray polarimeter calibration. In *Proc. of SPIE*, volume 6686, page 668610, 2007. 70

F. Muleri, P. Soffitta, L. Baldini, R. Bellazzini, J. Bregeon, A. Brez, E. Costa, M. Frutti, L. Latronico, M. Minuti, M. B. Negri, N. Omodei, M. Pesce-Rollins, M. Pinchera, M. Razzano, A. Rubini, C. Sgró, and G. Spandre. Low energy polarization sensitivity of the Gas Pixel Detector. *Nuclear Instruments and Methods in Physics Research A*, 584:149, 2008a. 113

F. Muleri, P. Soffitta, R. Bellazzini, A. Brez, E. Costa, S. Fabiani, M. Frutti, M. Minuti, M. B. Negri, M. Pinchera, A. Rubini, and G. Spandre. The Gas Pixel Detector as an X-ray photoelectric polarimeter with a large field of view. In *Proc. of SPIE*, volume 7011, page 70112A–1, 2008b. 161

F. Muleri, P. Soffitta, R. Bellazzini, A. Brez, E. Costa, M. Frutti, M. Mastropietro, E. Morelli, M. Pinchera, A. Rubini, and G. Spandre. A versatile facility for the calibration of X-ray polarimeters with polarized and unpolarized controlled beams. In *Proc. of SPIE*, volume 7011, page 701127–1, 2008c. 89

M. P. Muno, F. K. Baganoff, W. N. Brandt, S. Park, and M. R. Morris. Discovery of Variable Iron Fluorescence from Reflection Nebulae in the Galactic Center. ApJ, 656:L69, 2007. 35

H. Murakami, K. Koyama, and Y. Maeda. Chandra Observations of Diffuse X-Rays from the Sagittarius B2 Cloud. ApJ, 558:687, 2001a. 35

H. Murakami, K. Koyama, M. Tsujimoto, Y. Maeda, and M. Sakano. ASCA Discovery of Diffuse 6.4 KEV Emission near the Sagittarius C Complex: A New X-Ray Reflection Nebula. ApJ, 550:297, 2001b. 35

Y. Nakamura and S. Shibata. Polarization of the Crab Nebula with disordered magnetic components. MNRAS, 381:1489, 2007. 16

R. Novick. Stellar and Solar X-Ray Polarimetry. *Space Science Reviews*, 18:389, 1975. 1, 5, 6, 8, 62

R. Novick, M. C. Weisskopf, R. Berthelsdorf, R. Linke, and R. S. Wolff. Detection of X-Ray Polarization of the Crab Nebula. ApJ, 174:L1, 1972. 7

R. Novick, M. C. Weisskopf, J. R. P. Angel, and P. G. Sutherland. The effect of vacuum birefringence on the polarization of X-ray binaries and pulsars. ApJ, 215:L117, 1977. 14

B. Paczynski. Are Gamma-Ray Bursts in Star-Forming Regions? ApJ, 494:L45, 1998. 38

G. Pareschi and V. Cotroneo. Soft (0.1 - 10 kev) and hard (¿10 kev) x-ray multilayer mirrors for the XEUS astronomical mission. In *Proc. of SPIE*, volume 5168, page 53, 2003. 131

G. Pareschi, V. Cotroneo, D. Spiga, D. Vernani, M. Barbera, M. A. Artale, A. Collura, S. Varisco, G. Grisoni, G. Valsecchi, and B. Negri. Astronomical soft x-ray mirrors reflectivity enhancement by multilayer coatings with carbon overcoating. In *Proc. of SPIE*, volume 5488, page 481, 2004. 131

G. G. Pavlov and V. E. Zavlin. Polarization of Thermal X-Rays from Isolated Neutron Stars. ApJ, 529:1011, 2000. 21, 22, 23

G. G. Pavlov, D. Sanwal, G. P. Garmire, and V. E. Zavlin. The Puzzling Compact Objects in Supernova Remnants. In P. O. Slane and B. M. Gaensler, editors, *Neutron Stars in Supernova Remnants*, volume 271 of *Astronomical Society of the Pacific Conference Series*, page 247, 2002. 21

E. S. Perlman and A. S. Wilson. The X-Ray Emissions from the M87 Jet: Diagnostics and Physical Interpretation. ApJ, 627:140, 2005. 34, 35, 150

J. Poutanen. Relativistic jets in blazars: Polarization of radiation. ApJS, 92:607, 1994. 34, 155

B. Povh, K. Rith, C. Scholz, and F. Zetsche. *Particles and Nuclei: An Introduction to the Physical Concepts*. Springer, 2008. 56

V. Radhakrishnan and D. J. Cooke. Magnetic Poles and the Polarization Structure of Pulsar Radiation. Astrophys. Lett., 3:225, 1969. 19

N. Rea, E. Nichelli, G. L. Israel, R. Perna, T. Oosterbroek, A. N. Parmar, R. Turolla, S. Campana, L. Stella, S. Zane, and L. Angelini. Very deep X-ray observations of the anomalous X-ray pulsar 4U0142+614. MNRAS, 381:293, 2007. 150

M. J. Rees. Expected polarization properties of binary X-ray sources. MNRAS, 171:457, 1975. 1, 8, 30, 69

M. J. Rees and J. E. Gunn. The origin of the magnetic field and relativistic particles in the Crab Nebula. MNRAS, 167:1, 1974. 16

M. G. Revnivtsev, E. M. Churazov, S. Y. Sazonov, R. A. Sunyaev, A. A. Lutovinov, M. R. Gilfanov, A. A. Vikhlinin, P. E. Shtykovsky, and M. N. Pavlinsky. Hard X-ray view of the past activity of Sgr A* in a natural Compton mirror. A&A, 425:L49, 2004. 36, 37, 154

S. Rosswog and M. Bruggen. *Introduction to High-Energy Astrophysics*. Cambridge University Press, 2007. 37

M. A. Ruderman and P. G. Sutherland. Theory of pulsars - Polar caps, sparks, and coherent microwave radiation. ApJ, 196:51, 1975. 18

G. B. Rybicki and A. P. Lightman. *Radiative processes in astrophysics*. New York, Wiley-Interscience, 1979. 2, 86

J. Sanchez Almeida and V. Martinez Pillet. Instrumental polarization in the focal plane of telescopes. A&A, 260:543, 1992. 206

J. Sanchez Almeida and V. Martinez Pillet. Polarizing properties of grazing-incidence X-ray mirrors - Comment. Appl. Opt., 32:4231, 1993. 203, 204, 205, 208

A. Santangelo, A. Segreto, S. Giarrusso, D. dal Fiume, M. Orlandini, A. N. Parmar, T. Oosterbroek, T. Bulik, T. Mihara, S. Campana, G. L. Israel, and L. Stella. A BEPPOSAX Study of the Pulsating Transient X0115+63: The First X-Ray Spectrum with Four Cyclotron Harmonic Features. ApJ, 523:L85, 1999. 150, 157, 189

F. Sauli. Principles of Operation of Multiwire Proportional and Drift Chambers. *Lectures given in Academic Training Program of CERN, 1975-1976*, 77-09, 1977. 55

F. Sauli. GEM: A new concept for electron amplification in gas detectors. *Nuclear Instruments and Methods in Physics Research A*, 386:531, 1997. 45

S. Y. Sazonov and R. A. Sunyaev. Scattering in the inner accretion disk and the waveforms and polarization of millisecond flux oscillations in LMXBs. A&A, 373:241, 2001. 27

E. J. Schreier, E. Feigelson, J. Delvaille, R. Giacconi, J. Grindlay, D. A. Schwartz, and A. C. Fabian. Einstein observations of the X-ray structure of Centaurus A - Evidence for the radio-lobe energy source. ApJ, 234:L39, 1979. 33

N. I. Shakura and R. A. Syunyaev. Black holes in binary systems. Observational appearance. A&A, 24:337, 1973. 28

S. Shibata, H. Tomatsuri, M. Shimanuki, K. Saito, and K. Mori. On the X-ray image of the Crab nebula: comparison with Chandra observations. MNRAS, 346:841, 2003. 16

L. Sidoli, S. Mereghetti, A. Treves, A. N. Parmar, R. Turolla, and F. Favata. X-ray emission from the giant molecular clouds in the Galactic Center region and the discovery of new X-ray sources. A&A, 372:651, 2001. 150

E. H. Silver, H. L. Kestenbaum, K. S. Long, R. Novick, R. S. Wolff, and M. C. Weisskopf. Search for X-ray polarization in the Crab pulsar. ApJ, 225:221, 1978. 8

E. H. Silver, A. Simonovich, S. E. Labov, R. Novick, P. E. Kaaret, C. Martin, T. Hamilton, M. C. Weisskopf, R. F. Elsner, J. W. Beeman, G. A. Chanan, G. Manzo, E. Costa, G. C. Perola, and G. W. Fraser. Bragg crystal polarimeters. In *Proc. of SPIE*, volume 1160, page 598, 1989. 71

P. Soffitta, R. Bellazzini, G. Tagliaferri, E. Costa, G. Pareschi, S. Basso, V. Cotroneo, M. Frutti, F. Lazzarotto, F. Muleri, A. Rubini, G. Spandre, A. Brez, L. Baldini, J. Bregeon, M. Minuti, G. Matt, and F. Frontera. X-ray polarimetry on-board HXMT. In *Proc. of SPIE*, volume 7011, page 701128–1, 2008. 141

R. F. Stark and P. A. Connors. Observational test for the existence of a rotating black hole in CYG X-1. Nature, 266:429, 1977. 30

T. H. Stix. *The Theory of Plasma Waves*. McGraw-Hill, 1962. 9

T. Strohmayer and L. Bildsten. *New views of thermonuclear bursts*, page 113. Compact stellar X-ray sources, 2006. 27

R. A. Sunyaev and L. G. Titarchuk. Comptonization of low-frequency radiation in accretion disks Angular distribution and polarization of hard radiation. A&A, 143:374, 1985. 28, 30

R. A. Sunyaev, M. Markevitch, and M. Pavlinsky. The center of the Galaxy in the recent past - A view from GRANAT. ApJ, 407:606, 1993. 35, 154

T. Takahashi, R. Kelley, K. Mitsuda, H. Kunieda, R. Petre, N. White, T. Dotani, R. Fujimoto, Y. Fukazawa, K. Hayashida, M. Ishida, Y. Ishisaki, M. Kokubun, K. Makishima, K. Koyama, G. M. Madejski, K. Mori, R. Mushotzky, K. Nakazawa, Y. Ogasaka, T. Ohashi, M. Ozaki, H. Tajima, M. Tashiro, Y. Terada, H. Tsunemi, T. G. Tsuru, Y. Ueda, N. Yamasaki, S. Watanabe, and the NeXT team. The NeXT Mission. In *Proc. of SPIE*, volume 7011-25, 2008. 131, 181

Y. Tanaka, K. Nandra, A. C. Fabian, H. Inoue, C. Otani, T. Dotani, K. Hayashida, K. Iwasawa, T. Kii, H. Kunieda, F. Makino, and M. Matsuoka. Gravitationally Redshifted Emission Implying an Accretion Disk and Massive Black-Hole in the Active Galaxy MCG:-6-30-15. Nature, 375:659, 1995. 150

T. M. Tauris and E. P. J. van den Heuvel. *Formation and evolution of compact stellar X-ray sources*, page 623. Compact stellar X-ray sources, 2006. 26

C. Thompson and R. C. Duncan. The soft gamma repeaters as very strongly magnetized neutron stars - I. Radiative mechanism for outbursts. MNRAS, 275:255, 1995. 21

J. Tinbergen. *Astronomical Polarimetry*. Cambridge University Press, 1996. 2, 204

J. S. Toll. *The Dispersion Relation for Light and its Application to Problems Involving Electron Pairs*. PhD thesis, Princeton University, 1952. 14

W.-Y. Tsai and T. Erber. Propagation of photons in homogeneous magnetic fields: Index of refraction. Phys. Rev. D, 12:1132, August 1975. 14

W. Tucker and R. Giacconi. *The X-ray universe*. Harvard University Press, 1985. 130

C. M. Urry and P. Padovani. Unified Schemes for Radio-Loud Active Galactic Nuclei. PASP, 107:803, 1995. 32

M. H. van Kerkwijk and D. L. Kaplan. Isolated neutron stars: magnetic fields, distances,and spectra. Ap&SS, 308:191, 2007. 21

M. H. van Kerkwijk, D. L. Kaplan, M. Durant, S. R. Kulkarni, and F. Paerels. A Strong, Broad Absorption Feature in the X-Ray Spectrum of the Nearby Neutron Star RX J1605.3+3249. ApJ, 608:432, 2004. 22

S. Vaughan and A. C. Fabian. A long hard look at MCG-6-30-15 with XMM-Newton- II. Detailed EPIC analysis and modelling. MNRAS, 348:1415, 2004. 32

J. Ventura. Scattering of light in a strongly magnetized plasma. Phys. Rev. D, 19:1684, 1979. 9, 11, 12

J. Ventura, W. Nagel, and P. Meszaros. Possible vacuum signature in the spectra of X-ray pulsars. ApJ, 233:L125, 1979. 12, 24

K. Viironen and J. Poutanen. Light curves and polarization of accretion- and nuclear-powered millisecond pulsars. A&A, 426:985, 2004. 27

E. Waxman. Astronomy: New direction for γ-rays. Nature, 423:388, 2003. 40

M. C. Weisskopf, G. G. Cohen, H. L. Kestenbaum, K. S. Long, R. Novick, and R. S. Wolff. Measurement of the X-ray polarization of the Crab Nebula. ApJ, 208:L125, 1976. 7

M. C. Weisskopf, E. H. Silver, H. L. Kestenbaum, K. S. Long, and R. Novick. A precision measurement of the X-ray polarization of the Crab Nebula without pulsar contamination. ApJ, 220:L117, 1978. 7

M. C. Weisskopf, S. L. O'dell, and L. P. van Speybroeck. Advanced X-Ray Astrophysics Facility (AXAF). In *Proc. of SPIE*, volume 2805, page 2, 1996. 203

M. C. Weisskopf, J. J. Hester, A. F. Tennant, R. F. Elsner, N. S. Schulz, H. L. Marshall, M. Karovska, J. S. Nichols, D. A. Swartz, J. J. Kolodziejczak, and S. L. O'Dell. Discovery of Spatial and Spectral Structure in the X-Ray Emission from the Crab Nebula. ApJ, 536: L81, 2000. 16, 149

M. C. Weisskopf, B. Brinkman, C. Canizares, G. Garmire, S. Murray, and L. P. Van Speybroeck. An Overview of the Performance and Scientific Results from the Chandra X-Ray Observatory. PASP, 114:1, 2002. 16, 131

M. C. Weisskopf, R. F. Elsner, D. Hanna, V. M. Kaspi, S. L. O'Dell, G. G. Pavlov, and B. D. Ramsey. The prospects for X-ray polarimetry and its potential use for understanding neutron stars. *Paper Presented at the 363rd Heraeus Seminar in Bad Honef, Germany. Springer Lecture Notes, submitted*, 2006. 1, 41

M. C. Weisskopf, R. Bellazzini, E. Costa, B. D. Ramsey, S. L. ODell, R. Elsner, G. Pavlov, G. Matt, V. Kaspi, A. Tennant, P. Coppi, K. Wu, and O. H. W. Siegmund. An imaging x-ray polarimetry mission. In *Proc. of SPIE*, volume 7011-57, 2008. 143, 144

W. A. Wheaton, J. P. Doty, F. A. Primini, B. A. Cooke, C. A. Dobson, A. Goldman, M. Hecht, S. K. Howe, J. A. Hoffman, and A. Scheepmaker. An absorption feature in the spectrum of the pulsed hard X-ray flux from 4U0115 + 63. Nature, 282:240, 1979. 157

N. E. White, F. Nagase, and A. N. Parmar. The properties of X-ray binaries. In W. H. G. Lewin, J. van Paradijs, and E. P. J. van den Heuvel, editors, *X-ray binaries*, page 1, 1995. 26

D. C. B. Whittet. *Dust in the Galactic Environment*. CRC Press, 2003. 2

R. A. M. J. Wijers, P. M. Vreeswijk, T. J. Galama, E. Rol, J. van Paradijs, C. Kouveliotou, T. Giblin, N. Masetti, E. Palazzi, E. Pian, F. Frontera, L. Nicastro, R. Falomo, P. Soffitta, and L. Piro. Detection of Polarization in the Afterglow of GRB 990510 with the ESO Very Large Telescope. ApJ, 523:L33, 1999. 38

D. R. Willis, E. J. Barlow, A. J. Bird, D. J. Clark, A. J. Dean, M. L. McConnell, L. Moran, S. E. Shaw, and V. Sguera. Evidence of polarisation in the prompt gamma-ray emission from GRB 930131 and GRB 960924. A&A, 439:245, 2005. 38

A. S. Wilson and Y. Yang. Chandra X-Ray Imaging and Spectroscopy of the M87 Jet and Nucleus. ApJ, 568:133, 2002. 34

C. Winkler, T. J.-L. Courvoisier, G. Di Cocco, N. Gehrels, A. Giménez, S. Grebenev, W. Hermsen, J. M. Mas-Hesse, F. Lebrun, N. Lund, G. G. C. Palumbo, J. Paul, J.-P. Roques, H. Schnopper, V. Schönfelder, R. Sunyaev, B. Teegarden, P. Ubertini, G. Vedrenne, and A. J. Dean. The INTEGRAL mission. A&A, 411:L1, 2003. 7

L. M. Winter, R. F. Mushotzky, and C. S. Reynolds. XMM-Newton Archival Study of the Ultraluminous X-Ray Population in Nearby Galaxies. ApJ, 649:730, 2006. 150

S. E. Woosley. Gamma-ray bursts from stellar mass accretion disks around black holes. ApJ, 405:273, 1993. 38

J. J. Yeh. *Atomic Calculation of Photoionization Cross–Sections and Asymmetry Parameters*. Gordon and Breach Science Publishers, 1993. 41, 42, 45, 53

J. J. Yeh and I. Lindau. Atomic Subshell Photoionization Cross Sections and Asymmetry Parameters: $1 \leq Z \leq 103$. *Atomic Data and Nuclear Data Tables*, 32:1, 1985. 53

M. V. Zombeck. *Handbook of space astronomy and astrophysics*. Cambridge University Press, 2nd ed., 1990. 133, 182